Solid-Liquid Interface Studies of Titania and Nanocarbon Materials

CHENBO WANG

Supervised by Professor John S Foord



A thesis submitted in conformity with the requirements for the degree of Doctor of Philosophy in Theoretical and Physical Chemistry

University of Oxford

Department of Chemistry

Linacre College

Michaelmas 2019

Declaration

All research works reported in this thesis has not previously been accepted in substance for any degree and is not being concurrently submitted in candidature for any degree. This thesis is conducted by the author unless stated otherwise. All materials from other sources has been properly and fully acknowledged.

Chenbo Wang

Dedicated to my parents.

Acknowledgements

This doctorate dissertation would never have been completed without the constant guidance, support and advice from my supervisor, Prof. John S. Foord. Therefore, I must express my most sincere gratitude and utmost respect. His inexhaustible passion and profound patience have deeply inspired me to complete my study and stay enthusiastic in my future career and life. I also wish to express my gratitude for Professor Russell G Egdell, for guiding me through my first year of D.Phil. study. I would like to thank Dr. Robert Jacobs, and Dr. Ashley Shepherd in the Surface Analysis Facility for helping me with surface analysis technics.

I am thankful to all the members in the JSF research group, past and present. Their friendship and knowhow have encouraged and assisted me throughout my doctoral journey. Throughout my doctoral studies, I would like to specially express my greatest appreciation to:

Dr Jingping Hu, Dr Emina Hadzifejzovic, Dr Luyun Jiang and Dr Martin Lopez our group postdocs. Dr Liang Chen, Dr Patrick Gan, Dr Sirikarn Wisetsuwannaphum, Dr Christos Mavrokefalos and Dr Johanna Larsson our past group members. Dr. Hiu-Ming (Thomas) Lau, Dr. Xiao-Sheng Cai, Ella Bentin, Yi-Fan Wang, and Yue (Scarlet) Ma.

I am indebted to my family and friends for their endless support, compassion and encouragement. Most special thanks to my parents. Without their support and great encouragement, I could not have overcome all the difficulties.

Abstract

Modifying TiO_2 has been of great interest for applications in photocatalytic degradation of organic pollutants, production of hydrogen from water and photovoltaic applications. The chemical composition of TiO_2 can be altered by doping by which the titanium and/or oxygen component is replaced. Doping alters the material's optical properties, but sometimes at the cost of undesirable consequences.

A novel 2-propanol/HNO_3 based one pot sol-gel evaporation method was developed and optimized for rapid growth of highly N doped TiO_2 nanoparticles. With the adaptation of CasaXPS software, a novel MB absorption spectrum peak deconvolution technic is proposed. Total absorption area yields better pseudo-first-order reaction linearity than using maximum absorption peak height (MB monomer) was found to be a better indicator of MB degradation. This is especially true for exotic absorption spectra change with uneven peak reduction rate.

Photocatalytic degradation of MB by N-doped TiO_2 takes place via the sequential decomposition of methyl groups from MB to azure A/B/C and further mineralisation. N-doping enables photocatalytic response under visible spectrum. Samples prepared using 2 mL concentrated nitric acid in 25 mL 2-propanol solution (0.5 M Ti concentration) and annealed at 300 °C for 10 hrs yield best photocatalytic results under visible spectrum irradiation.

Using a dip-coating method Sn doped anatase TiO_2 thin film grown on 5%Nb:$SrTiO_3$ (001) substrate and Sn doped rutile TiO_2 thin film grown on FTO substrate are achieved. Doping

level of up 15% were achieved with anatase TiO_2 thin film epitaxial growth while maintaining host anatase structure. Sn doped anatase and rutile thin film as a photoanode material were investigated using a three-electrode setup. 10% Sn doped anatase thin film showed better photocurrent performance under UV while 1% Sn doped rutile anatase thin film performed better under simulated one sun illumination and visible spectrum. The main contribution to PEC performance is still due to the UV spectrum. The overall increase in photocurrent should be due to an increase in photoactive sites caused by Sn doping.

The underlying principle of water oxidation and reduction using a semiconductor photoanode/cathode-based PEC device was explored, and the reason for RHE scale is explained with multiple examples of PEC designs. This serves as a standard model in interpreting electrochemical data of photoanode/photocathode in a three-electrode setup.

Rice husk waste material can be used as a potential biomass-derived carbon material for EDLC electrode. Two different-sized bimetallic Co/Mn MOFs were grown in the channels of cRHs for improved EDLC performance. A drop-coating method was devised for EDLC testing using smaller material quantity. cRHs fabricated under different carbonisation conditions were tested with 400 °C carbonised in nitrogen (**#4**) showing best specific capacitance of 11.54 F/g. Carbonized metal acetate precursor derived MOFs sample **#4 ACT** yields a consistent specific capacitance of around 30 F/g irrespective of scan rate.

Preface

This thesis is a collection of four selected chemistry projects conducted by the author during his PhD studies at University of Oxford. All the four project chapters are interrelated as they all involve studying electrochemical interface.

Chapter 1 introduces background of semiconductor physics, electrochemical reaction and the electrode-electrolyte interface. It is then followed by application in PEC electrolytic water splitting, AOPs photodegradation of dyes and EDLC application.

Chapter 2 introduces the relevant experimental techniques used in sample growth and characterisations. The basic concepts and methodologies involved in the characterisation process are explained.

Chapter 3 studies the nitrogen doping effect on anatase TiO_2 for MB degradation applications. The results are being prepared for publishing in scientific journal.

Chapter 4 studies the doping effect of Sn on anatase TiO_2 thin films for PEC applications.

Chapter 5 further investigates the Sn doping advantages on rutile TiO_2 for PEC applications. The combine results of chapter 4 and 5 are being prepared for publishing in scientific journal.

Chapter 6 studies the EDLC performance of carbonized Mn/Co MOFs@cRHs. The results of this project have been published in the following scientific journal:

Kim, Hyunuk, Muhammad Sohail, Chenbo Wang, Martin Rosillo-Lopez, Kangkyun Baek, Jaehyoung Koo, Myung Won Seo, Seyoung Kim, John S. Foord, and Seong Ok Han. 2019. "Facile One-Pot Synthesis of Bimetallic Co/Mn-MOFs@Rice Husks, and Its Carbonization for Supercapacitor Electrodes." Scientific Reports 9 (1): 8984. https://doi.org/10.1038/s41598-019-45169-0.

Chapter 7 concludes the thesis

Table of Contents

Declaration.....III

Acknowledgements V

Abstract.....VI

Preface VIII

Table of Contents X

Abbreviations XV

Chapter 1 Introduction.....1

1.1 Semiconductor physics.....1

1.1.1 Energy band and band gap 2

1.1.2 Fermi level and voltage.....5

1.1.3 Intrinsic semiconductor.....6

1.1.4 Doped semiconductor.....9

1.2 Electrochemical potential and thermodynamics.....10

1.2.1 Electrochemical potential.....11

1.2.2 Nernst equation 12

1.2.3 Electrode Potential 13

1.2.4 Electrochemical equilibrium 16

1.2.5 Reversible, Irreversible, spontaneous and equilibrium 18

1.3 Semiconductor photo-electrochemistry.....21

1.3.1 Electrical double layers 22

1.3.2 Metal-metal interface 24

1.3.3 Semiconductor-metal interface 26

1.3.4 Semiconductor-electrolyte interface 31

1.4 Photoelectrochemical Cell 39
1.4.1 PEC basics 39
1.4.2 Band diagram 41
1.4.3 PEC configurations 43
1.5 Doped TiO_2 for advanced oxidation processes 45
1.5.1 Rise of TiO_2 45
1.5.2 Advanced oxidation processes 46
1.5.3 Modified TiO_2 47
1.6 Electrical double-layer capacitor 49
1.6.1 EDL Interface 49
1.6.2 EDLC electrodes 50
1.6.3 Carbon-based EDLC electrodes 52
1.7 Thesis outline 54
Reference 56

Chapter 2 Experimental Techniques 62

2.1 Introduction 62
2.2 Material synthesis 62
2.2.1 Dip-coating 62
2.2.2 Thermal evaporation 64
2.2.3 Mn/Co bi-metallic MOFs 65
2.3 Electrochemical characterisation 66
2.3.1 Overview of electrode processes 66
2.3.2 PEC setup and photoelectrode preparation 71
2.3.3 EDLC electrode preparation 74
2.3.4 Electrochemical method 75
2.4 Physical characterisation 78
2.4.1 X-ray diffraction 78

2.4.2 X-ray photoelectron spectroscopy 79
2.4.3 Scanning Electron Microscopy 83
2.5 Methylene blue degradation 84
2.5.1 Photocatalytic degradation of methylene blue 84
2.5.2 Methylene blue spectrum deconvolution 85
Reference 91

Chapter 3 Nitrogen-Doped TiO_2 Powder: A Methylene Blue Degradation Study 93

3.1 Introduction 93
3.2 Experimental 95
3.3 Results and discussion 96
3.3.1 Process optimisation 96
3.3.2 Effect of annealing temperature 103
3.3.3 Effect of HNO_3 concentration 111
3.3.4 Deconvolution of methylene blue absorption spectra 118
3.3.5 Direct hole oxidation of methylene blue on N-doped TiO_2 surface 127
3.3.6 Interpretation of methylene blue degradation results with hypsochromic shift 134
3.3.7 Sb/N co-doped TiO_2 138
3.4 Conclusion 142
Reference 146

Chapter 4 Sn-Doped Anatase TiO_2 Thin Film 150

4.1 Introduction 150
4.2 Experimental 151
4.3 Results and discussion 152

4.3.1 Feasibility of using Sn-doped anatase TiO_2 photoanode in PEC characterisation....152
4.3.2 Light on/off experiment....159
4.3.3 Semiconductor-electrolyte interface under illumination....161
4.3.4 PEC performance comparison....173
4.3.5 Potential PEC setups....180
4.4 Conclusions....184
References....186

Chapter 5 Sn-Doped Rutile TiO_2 Thin Film....189

5.1 Introduction....189
5.2 Experimental....190
5.3 Results and discussion....191
5.3.1 Physical characterisation of Sn-doped TiO_2 thin film....191
5.3.2 Light on/off experiment....196
5.3.3 PEC performance comparison....198
5.3.4 Rutile and anatase results compared....206
5.3.5 Mott-Schottky plot....209
5.4 Conclusions....212
Reference....214

Chapter 6 Mn/Co modified carbonised rice husks for EDLCs....216

6.1 Introduction....216
6.2 Experimental....217
6.2.1 Ball milling....217
6.2.2 Drop-coating....218
6.3 Results and discussion....218
6.3.1 Electrolyte selection with GC electrode....218

6.3.2 Improvements of using Nafion® cover 221
6.3.3 Carbonised rice husk 227
6.3.4 Mn/Co modified cRHs 230
6.6 Conclusion 242
Reference 244

Chapter 7 Conclusions 247

7.1 N doped TiO_2 powder 247
7.2 Sn doped TiO_2 thin films 248
7.3 Carbonised Co/Mn MOFs modified cRHs 249

Abbreviations

Abbreviations	Meaning
MO	Molecular orbital
VB	Valence band
CB	Conduction band
SHE	Standard hydrogen electrode
EDL	Electrical double layer
IHP	Inner Helmholtz plane
OHP	Outer Helmholtz plane
KPFM	Kelvin probe force microscope
AFM	Atomic force microscopy
SCL	Space charge layer
PEC	Photoelectrochemical cell
PPCPs	Pharmaceutical and personal care products
AOPs	Advanced oxidation processes

DSSCs	Dye-sensitized solar cells
EDLC	Electrical double-layer capacitor
UV-Vis	Ultraviolet-visible
XES	X-ray emission spectroscopy
XAES	X-ray induced Auger electron spectroscopy
GCE	Glassy carbon electrode
CV	Cyclic voltammetry
XRD	X-ray diffraction
XPS	X-ray photoelectron spectroscopy
SEM	Scanning electron microscopy
EIS	Electrochemical impedance spectroscopy
MWNTs	Multi-walled carbon nanotubes
SWNTs	Single-walled carbon nanotubes
RHE	Reversible hydrogen electrode
ITO	Indium tin oxide

FTO	Fluorine-doped tin oxide
MB	Methylene blue
AB	Azure B
AA	Azure A
AC	Azure C
Th	Thionine
DI	Deionized
MOFs	Metal–organic frameworks
cRHs	Carbonized rice husks

Chapter 1 Introduction

This chapter covers some of the background information related to solid-liquid interfaces. In the first three sections, relevant semiconductor physics and electrochemistry concepts are explained leading to the overview of photo-electrochemistry on solid-liquid interfaces. The following three sections provide the literature reviews on photoelectrochemical cells (PECs), advanced oxidation processes (AOPs), and electrical double-layer capacitors (EDLCs) which are the three key applications used in this thesis. The final section presents an outline of the thesis.

1.1 Semiconductor physics

A semiconductor is a material that has the electrical conductivity between that of a conductor and an insulator. Some common examples are GaN[1], silicon[2], germanium[3], TiO_2[4] and SnO_2[5] which are widely used in LEDs[6], solar cells[7], transistors[8], gas sensors[9], amongst others. Semiconductor devices have a range of useful electric properties such as directional current passthrough, variable resistance, photovoltaic effect and exotic current voltage responses. The useful electronic properties of semiconductors arise from the unique electronic band structure of the material. In solid-state physics, the electronic band structure of a solid material describes the range of energies that an electron within the solid may have which is explained by band theory.

1.1.1 Energy band and band gap

In a single, isolated atom, electrons occupy atomic orbitals which have discrete energy levels. When two or more atoms come together to form a molecule, their atomic orbitals overlap forming a molecular orbital (MO). The Pauli exclusion principle dictates that no two electrons can have the same set of quantum numbers in a molecule (or atom). When two identical atoms combine to form a molecule, each atomic orbital split into two MOs of different energy, allowing the electrons in the former atomic orbitals to occupy the new orbital structure without having the same energy.

Similarly, if a large number N of identical atoms group together to form a solid, due to Pauli exclusion principle, each atomic orbital splits into N discrete MOs, each with a different energy. The number of atoms in a macroscopic solid is a very large (~10^{22}), therefore the number of orbitals is also very large, thus newly formed orbitals are very closely spaced in energy (of the order of 10^{-22} eV). The energy of adjacent orbitals is so close that they can be considered as a continuum, an energy band. However, the MO will not be distributed uniformly over all energy levels. There will be regions where no MOs are present thus forming a gap between energy bands where no electrons may reside. In the case of a semiconductor, the band structure consists of a highest energy (electron) filled band known as the valence band, a lowest empty band known as the conduction band and a gap in between called the band gap.

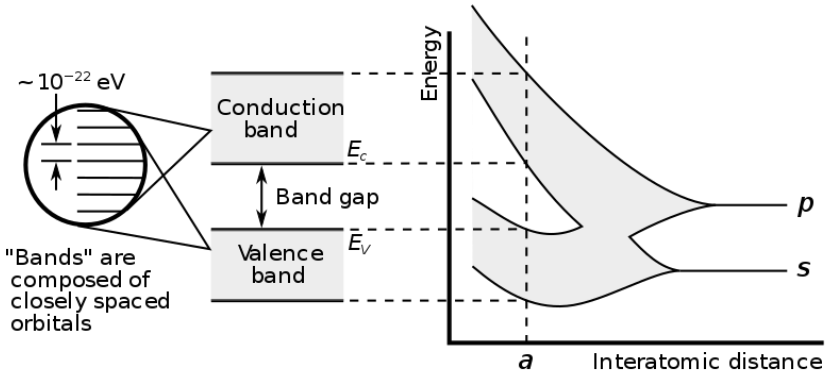


Figure 1.1. Formation of the valence and conduction bands in a diamond crystal from carbon atoms.[10]

The bonding in metal oxide semiconductors is somewhat different in nature. Due to the higher electronegativity of oxygen, in a metal oxide semiconductor, the valence electrons are fully or partially transferred from the metal to the oxygen. The bonding character of metal oxides is therefore somewhat ionic. By constructing a MO diagram from the individual atomic energy levels, we can identify a qualitative band picture.

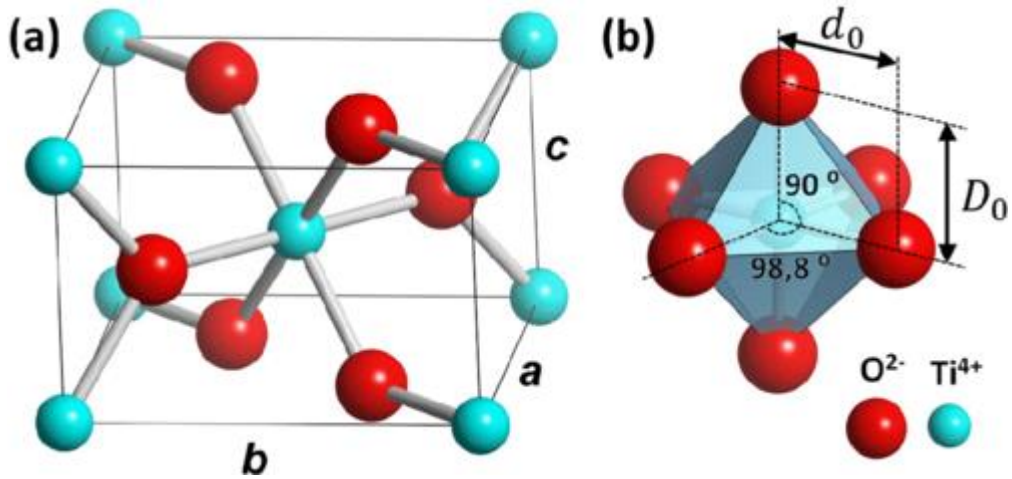


Figure 1.2. Ball and stick models of (a) rutile TiO_2 unit cell and (b) single TiO6 octahedron.[11]

In rutile TiO_2 for example (figure 1.2), Ti atoms are surrounded by six O atoms, forming a distorted octahedron. Therefore, Ti 3d orbitals will split into two sets of orbitals: d_{z^2}, $d_{x^2-y^2}$ orbitals belong to e_g, and d_{xz}, d_{xy}, d_{yz} orbitals belong to t_{2g} (x, y and z axis are along the Ti-O bond). The O atoms are surrounded by three Ti atoms in a planar geometry, thus sp^2

hybridization of the O atom forms three bonds (p_x, p_y and s orbitals) in the plane and one bond (p_z) perpendicular to the plane. According to Sorantin and Schwarz's study[12], two Ti e_g orbitals combining with four Ti sp^3 orbitals form six σ metal-ligand bonds pointing towards the six O atoms along axis direction. The Ti d_{yz} orbitals form π bond with the O p_z orbital, while the Ti d_{xz} and dxy orbitals have σ non-bonding with O atoms. Ti t_{2g} orbitals form π or σ bonds with adjacent Ti atoms, this Ti-Ti bonding is expected to be very weak owing to the large distance between Ti atoms.

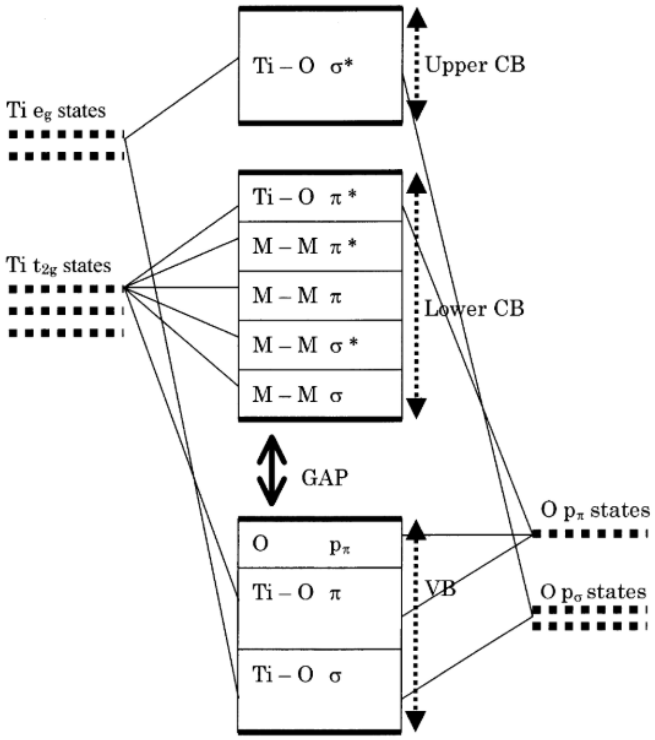


Figure 1.3. The bonding diagram of the TiO_2 perfect crystal (rutile) proposed by Soratin and Schwarz.[12]

In figure 1.3, the valence band (VB) can be decomposed into three parts: the σ bonding of the O p_σ and Ti e_g states in the lower energy region; the π bonding of the O p_π and Ti e_g

states in the middle energy region; and the O p_π states in the higher energy region. The bottom of the lower conduction band (CB) consists of metal-metal interactions due to the π or σ bonding of the Ti t_{2g}-Ti t_{2g} states. At the top of the lower CB, the rest of the Ti t_{2g} states are anti-bonding with the O p_π states. The upper CB consists of the σ anti-bonding between the O p_σ and Ti e_g states.

1.1.2 Fermi level and voltage

In band theory, the Fermi level can be a hypothetical energy level of an electron, such that at thermodynamic equilibrium this energy level would have a 50% chance of being occupied at any given time. The Fermi level does not necessarily correspond to an actual energy level, nor does it require the existence of a band structure. The Fermi level (electrochemical potential) for the electrons of a material is the thermodynamic work required to add one electron to the material.

Differences in Fermi level can be measured simply with a voltmeter. When the leads of a voltmeter are attached to two points in a circuit, the displayed voltage is a measurement of the total work transferred when a unit charge is allowed to move from one point to the other. Therefore, the observed voltage difference ($V_A - V_B$) between two points, *A* and *B*, is related to the electrochemical potential difference ($\overline{\mu_A} - \overline{\mu_B}$) in Fermi level by: $V_A - V_B = -(\overline{\mu_A} - \overline{\mu_B})/e$, where e is the electric charge of an electron. (see section 1.2.1)

When two points are in good electrical contact, electrons will move from high Fermi level to low Fermi level. Eventually, Fermi level in both points will reach the same value and the

whole system is in equilibrium. So, for an electrically connected system at equilibrium, the voltage between any two points will be zero; a constant Fermi level is present throughout all the connected parts. (no electromagnetic force or field)

1.1.3 Intrinsic semiconductor

Conductors, semiconductors and insulators all have electronic band structures. The difference in conductivity is closely related to filling of states as well as state delocalization. A good conductor such as metals have many partially filled states in one energy band that the Fermi level sits inside the energy band. Insulators and semiconductors, by contrast, have little to no partially filled states such that the Fermi level sits inside a band gap. The band gap in the semiconductor is much smaller compared to the band gap of the insulator. For a semiconductor, the band gap is small enough that at room temperature (298 K) the thermal energy is capable of promoting some electrons across the band gap creating partially filled states in both valence band conduction band.

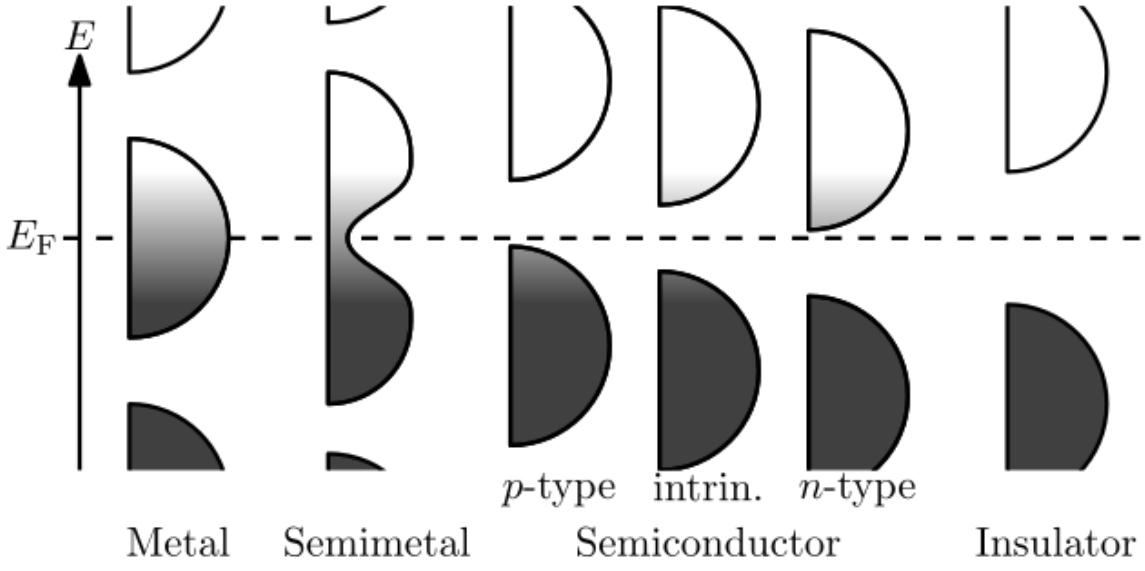


Figure 1.4. Filling of the electronic states in various types of materials at equilibrium where height is energy, width is the density of available states for a certain energy in the material. The shade follows Fermi-Dirac distribution with dark for filled states and white for empty states, and Fermi level (E_f) is shown as dashed line.[13]

The energy distribution of electrons in a solid follows Fermi-Dirac distribution:

$$f(E) = \frac{1}{1+exp[(E-E_f)/kT]} \tag{1.1.1}$$

where k is Boltzmann's constant, T is the absolute temperature, E_f is the Fermi level, E is the energy of the electron, function f(E) gives the percentage of occupied levels with an energy of E. The Fermi level have a 50% chance of being occupied by an electron at any time. At absolute zero the function f(E) become a sharp cutoff at energy E_f with completely filled level below E_f and completely empty level above E_f.

Fermi-Dirac distribution function f(E) give the percentage of occupied levels, the density of states (DOS) function N(E) gives the number of allowed levels, thus the density of electrons per unit energy n(E) can be obtained by multiplying the two functions:

$$n(E) = N(E)f(E) \tag{1.1.2}$$

Since holes correspond to empty states that are not occupied by electrons, so that the hole density per unit energy p(E) equals:

$$p(E) = N(E)[1 - f(E)] \tag{1.1.3}$$

Carrier density in an intrinsic semiconductor is obtained by integrating the above-mentioned equations over all possible energies. Electrons in the conduction band are taken from the bottom of the conduction band E_C to the top of the conduction band, holes in the valence band are taken from the top of the valence band E_V to the bottom of the valence band:

$$n_0 = \int_{E_C}^{\infty} n(E)dE \tag{1.1.4}$$

$$p_0 = \int_{-\infty}^{E_V} p(E)dE \tag{1.1.5}$$

where n_0 and p_0 are electron and hole density respectively. While this integral cannot be solved at non-zero temperatures, we can obtain an approximate analytical solution by replacing the Fermi distribution function with a simple exponential function. However, this relation is only valid for non-degenerate semiconductors in which the Fermi level is at least 3kT away from either band edges. The analytical solution:

$$n_0 = N_C \, exp\left[\left(E_f - E_C\right)/kT\right] \tag{1.1.6}$$

$$p_0 = N_V \, exp\left[\left(E_V - E_f\right)/kT\right] \tag{1.1.7}$$

$$N_C = 2\left[\frac{2\pi m_e^* kT}{h^2}\right]^{3/2} \tag{1.1.8}$$

$$N_V = 2\left[\frac{2\pi m_h^* kT}{h^2}\right]^{3/2} \tag{1.1.9}$$

where N_C and N_V are effective DOS in the conduction band and valence band respectively, m_e^* and m_h^* are the effective mass of electrons and holes respectively. E_C is the conduction band minimum, E_V is the valence band maximum and E_f is the Fermi level. Multiplying through by n_0 and p_0 the Fermi level component is eliminated. Using the law of mass action, intrinsic carrier density n_i can be obtained that is independent of the Fermi level:

$$n_0 p_0 = N_C N_V \, exp[(E_V - E_C)/kT] = n_i^2 \tag{1.1.10}$$

For a perfectly stoichiometric solid at ground state, there are no electrons in the conduction band (no holes in the valence band). At elevated temperatures, the number electrons excited

into the conduction band equals to the number of holes left in the valence band which is identified as intrinsic carrier density n_i:

$$n_0 = p_0 = n_i \tag{1.1.11}$$

Since the DOS in the valence and conduction bands are equal in an intrinsic semiconductor, the Fermi level must be placed midway in the energy gap (consider equivalent mass of electron and hole are the same):

$$E_f = \frac{(E_V+E_C)}{2} + \frac{1}{2}kTln\left(\frac{N_V}{N_C}\right) = \frac{(E_V+E_C)}{2} + \frac{3}{4}kTln\left(\frac{m_h^*}{m_e^*}\right) \cong \frac{(E_V+E_C)}{2} \tag{1.1.12}$$

1.1.4 Doped semiconductor

Semiconductors for practical applications are often doped with impurities (dopant), mainly with the aim to improve the conductivity. Doped semiconductors are called extrinsic semiconductors, which contain impurities added into the crystal structure. Based on the type of impurities, extrinsic semiconductors are classified into n-type and p-type semiconductors. N-type impurities are electron donors releasing a mobile electron into the conduction band. P-type impurities are electron acceptors, creating a mobile vacancy called a hole in the valence band that behaves like a positively charged particle.

For the Group IV semiconductors such as diamond, silicon and germanium, pentavalent impurities such as phosphorus, arsenic, antimony etc. are electron donors (n-type dopant) and trivalent impurities such as boron, gallium, indium, aluminium etc. are electron acceptors (p-type dopant). Take phosphorus doped silicon (n-type semiconductor) for example. Phosphorus has five valence electrons and silicon has four valence electrons. The

four valence electrons of phosphorus atom form covalent bonds with the four neighbouring silicon atoms, leaving the fifth valence electron of the phosphorus atom unable to form covalent bond. Thus, the fifth valence electron of phosphorus atom is free to move. However, this does not mean the doped semiconductor become negatively charged, charge neutrality is maintained as the immobile phosphorus atom is positively charged while the donor electron moves "freely" in the semiconductor crystal. Similarly, a p-type semiconductor would be boron doped silicon, since the boron atom has three valence electrons—one less than silicon. This creates a "broken bond" (hole) during the formation of covalent bonds with the four neighbouring silicon atoms. Thus, the hole is free to move in the semiconductor crystal.

1.2 Electrochemical potential and thermodynamics

Electrochemistry studies the relationship of chemical processes and electricity. Electricity is a measurable and quantitative phenomenon that is well suited for precision data collection using advanced electronics apparatus. Chemical reactions where electrons are transferred between chemical species are called oxidation-reduction (redox) reactions. In electrochemistry, the redox reactions are separated artificially by an electric circuit. Some of the measurements used in electrochemistry are somewhat similar to the ones used in electrical engineering: voltage, current, capacitance, resistivity etc. In recent years, the study of surface science has stemmed from both electrochemistry and solid-state physics perspectives and have proven to be equally fruitful. This field of study has impacted many technologies including microelectronics, sensors, solar cells, energy storage and much more.

In this thesis, it is strongly recommended to distinguish the subtle differences in terminologies used across solid state physics and electrochemistry. For example, the symbol E is used as the Fermi level (electrochemical potential), an energy term in units of J/mol and electrode potential, a potential term in volts; symbol Φ is used by work function, an energy term and electrostatic potential in solids, a potential term.

1.2.1 Electrochemical potential

In electrochemistry and solid-state physics both the chemical potential and the electrochemical potential of the electrons are used to describe the thermodynamic equilibrium of electrons. The chemical potential of a certain species, part of which may be due to potentials associated with "external" force fields such as electric potential energy, gravitational potential energy, while the rest would be due to "internal" factors such as density, temperature, etc. The phrase "chemical potential" sometimes means "total chemical potential", but that is not always true.

In electrochemistry, the term "chemical potential" means internal chemical potential, while the term “electrochemical potential” is used to mean total chemical potential.[14] In solid-state physics, the definitions are normally compatible with this[15], but occasionally the definitions are swapped[16]. Here, it is clarified that the term “chemical potential” used in this thesis means the internal, nonelectrical chemical potential that is the "electrochemical potential" minus the local electric potential energy. The electrochemical potential ($\bar{\mu_i}$) can be expressed as:

$$\bar{\mu_i} = \mu_i + zFE \tag{1.2.1}$$

where z is the valency (charge) of the species, F is the Faraday constant in C/mol, E is the electrostatic potential in V, μ_i is the chemical potential in J/mol. In previous section, Fermi level is known as the electrochemical potential of electrons in a semiconductor. When a potential bias (V_{bias}) is applied to the metal electrode, the Fermi level is consequently shifted by the amount of zFV_{bias}.

1.2.2 Nernst equation

The reduction potential (also known as redox potential) is a measure of the tendency of a chemical species to acquire electrons and therefore be reduced. The reduction potential is measured in volts. The more positive the reduction potential, the greater the species' affinity for electrons and tendency to be reduced. In electrochemistry, the Nernst equation relates the reduction potential of an actual electrochemical reaction to the standard reduction potential.

The Nernst equation is derived from the standard changes in the Gibbs free energy concerning electrochemical reaction. It was named after Walther Nernst, a German physical chemist who formulated the equation.[17] For any electrochemical redox reaction in the form of:

$$Ox + ze^{-} \rightarrow Red \tag{1.2.2}$$

The electrochemical potential E is defined as the change in Gibbs free energy per coulomb of charge transferred:

$$\Delta G = -zFE \tag{1.2.3}$$

where F is the Faraday constant, z is the number of charges transferred (electron is negatively charged). Thermodynamics dictates that actual free energy change ΔG is related to the free energy change under standard state ΔG^0 by the relationship:

$$\Delta G = \Delta G^0 + RTlnQ \tag{1.2.4}$$

where Q is the reaction quotient. Replacing Gibbs free energy change ΔG with -zFE leads to the Nernst equation:

$$E = E^0 - \frac{RT}{zF} lnQ = E^0 + \frac{RT}{zF} ln\left(\frac{a_{ox}}{a_{red}}\right) \tag{1.2.5}$$

where E is reduction potential in V, E^0 is the standard reduction potential in V, R is the universal gas constant in J/(mol·K), F is the Faraday constant in C/mol, a_{red} and a_{ox} are the chemical activity for reduced and oxidized species measured with respect to the standard state (1 mol/L for solutes, 1 atm for gases), z is the number of electrons transferred in the redox reaction.

1.2.3 Electrode Potential

In an electrochemical cell, such as the galvanic cell (a battery that is discharging), the overall redox reaction can be broken down into two half-cell reactions: reduction reaction on the cathode (with redox potential $E_{cathode}$) and oxidation reaction on the anode (with redox potential E_{anode}). The potential difference between the two electrode equals the overall cell potential:

$$E_{cell} = E_{cathode} - E_{anode} \tag{1.2.6}$$

Electric potential difference between the pair of electrodes generates electricity and the overall cell potential can be measured using a voltmeter. However, there is no simple way

to accurately measure the potential of an individual electrode (the electrode potential in isolation). Although it is impossible to measure the potential of any electrode directly, artificially introducing a reference electrode with an agreed upon potential value can decouple the individual electrode from the pair.

The standard hydrogen electrode (SHE) is a good reference electrode which forms the basis of the thermodynamic reference of reduction potentials. Being the universal reference electrode, the standard electrode potential of SHE (E_{SHE}) is designated to be 0 V at 298 K. For any electrode potential that is not yet known, it can be paired up with the SHE and obtain the potential by measuring galvanic cell potential. Using such a process, any unknown electrode potential can be obtained by pairing up with an electrode with known electrode potential.

The physical definition of "absolute" electrode potential was a debated question back in 1970s, and Trasatti[18] showed that Galvani potential difference cannot be regarded as an absolute electrode potential. In the 1980s, with increasing interesting on the electrolyte-semiconductor interface, the relation between the reduction potential on the vacuum scale and the so-called Fermi level in solution are debated[19–22]. It is agreed[23] that the reduction potential on this vacuum scale is equivalent to the chemical (not the electrochemical) potential of the electron in the solution; and the Fermi level in the solution can be related to the reduction potential in the vacuum. (detailed discussion in section 1.1.3) In order to determine the reduction potential (electric potential in unit V) on the vacuum scale (energy in J/mol), the absolute electrode potential is required.

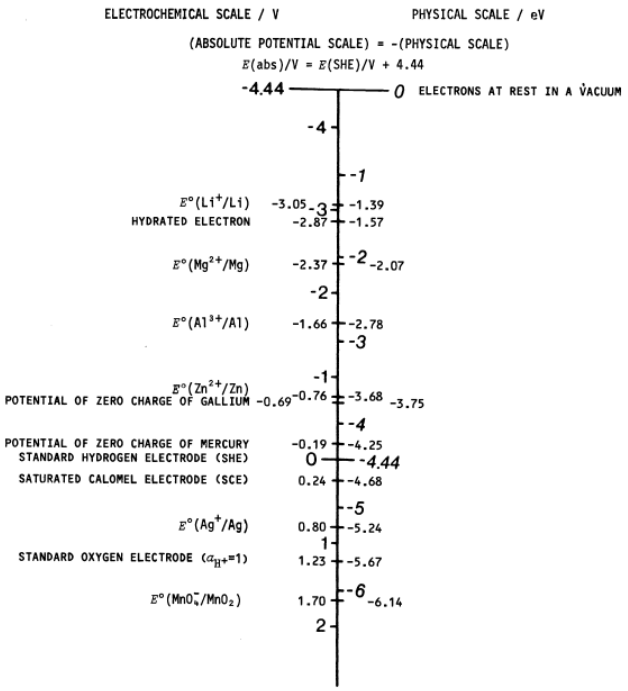


Figure 1.5. Conversion of relative reference electrode potentials into electronic energies for aqueous systems. Reproduced from Trasatti[19].

The reduction potential of a redox couple in an electrolyte with respect to the vacuum energy level is not accurately known. Empirical estimates absolute electrode potential of SHE to be 4.44 ± 0.02 V at 298 K [24], which forms basis for comparison with all other electrode reactions. For any electrode X at 25 °C:

$$\psi_X^{abs} = 4.44\,V + E_X^{SHE} \tag{1.2.7}$$

where ψ_X^{abs} is absolute electrode potential of X using vacuum as reference in V, and E_X^{SHE} is the measured electrode potential relative to the SHE in V. An important note is that the more positive the electrode potential, the more negative it is on the vacuum scale (figure 1.5), this is due to charge of electron is negative.

1.2.4 Electrochemical equilibrium

The Nernst equation shows that a half-cell potential will change by 59 mV (298 K) per 10-fold change in the concentration of a substance involved in a single-electron redox reaction. When applied in electrochemical equilibria by plotting the phase diagram of the potential vs pH, Pourbaix diagram is obtained.

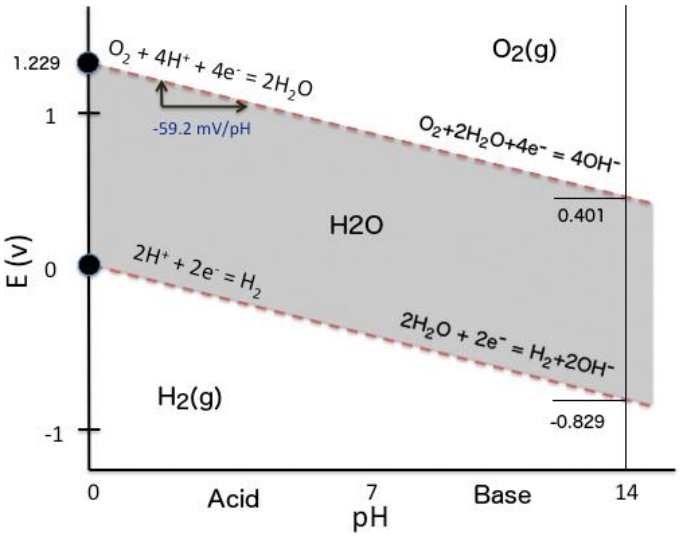


Figure 1.6. Pourbaix diagram for water, including equilibrium regions for water, oxygen and hydrogen at standard conditions. The vertical scale is the electrode potential relative to SHE potentials, the horizontal scale is the pH of the electrolyte.[25]

The Nernst equation can be used to show the relationship between the reduction potential change and the shift in the electrochemical equilibrium. Take the SHE as an example, at equilibrium:

$$H^+ + e^- \rightleftarrows 0.5H_2 \tag{1.2.8}$$

In terms of electrochemical expression:

$$\bar{\mu}_{H^+} + \bar{\mu}_{e^-} = 0.5\bar{\mu}_{H_2} \tag{1.2.9}$$

where $\bar{\mu}_{H^+}$, $\bar{\mu}_{e^-}$, and $\bar{\mu}_{H_2}$ are the electrochemical potential of hydrogen ion in solution, electron in the electrode and hydrogen gas respectively. In ideal circumstances, the chemical potential term can be expanded:

$$\mu_{H^+} = \mu^0_{H^+} + RTln(\frac{[H^+]}{1}) \tag{1.2.10}$$

$$\mu_{H_2} = \mu^0_{H_2} + RTln(\frac{P_{H_2}}{1}) \tag{1.2.11}$$

In electrochemical potential terms:

$$\bar{\mu}_{H^+} = \mu_{H^+} + zFE_{solution} = \mu^0_{H^+} + RTln(\frac{[H^+]}{1}) + FE_{solution} \tag{1.2.12}$$

$$\bar{\mu}_{H_2} = \mu_{H_2} = \mu^0_{H_2} + RTln(\frac{P_{H_2}}{1}) \tag{1.2.13}$$

$$\bar{\mu}_{e^-} = \mu_{e^-} + zFE_{electrode} = \mu_{e^-} - FE_{electrode} \tag{1.2.14}$$

Substituting the electrochemical potentials in equation 1.2.9 with the expanded terms in equations 1.2.12, 1.2.13 and 1.2.14:

$$\mu^0_{H^+} + RTln(\frac{[H^+]}{1}) + FE_{solution} + \mu_{e^-} - FE_{electrode} = 0.5(\mu^0_{H_2} + RTln\left(\frac{P_{H_2}}{1}\right)) \tag{1.2.15}$$

Rearranging the above equation, the Nernst equation is obtained:

$$E_{electrode} - E_{solution} = \frac{\Delta\mu^0}{F} + \frac{RT}{F} ln\left(\frac{[H^+]}{P^{0.5}_{H_2}}\right) \tag{1.2.16}$$

$$\Delta\mu^0 = \mu_{e^-} + \mu^0_{H^+} - 0.5\mu^0_{H_2} \tag{1.2.17}$$

It can be predicted that potential $E_{electrode} - E_{solution}$ will become more positive as H^+ concentration increases (hydrogen gas pressure constant).

1.2.5 Reversible, Irreversible, spontaneous and equilibrium

In thermodynamics, the Gibbs free energy is a thermodynamic potential that can be used to calculate the maximum of reversible work that may be performed by a thermodynamic system at a constant temperature and pressure. The Gibbs free energy is defined as:[26]

$$G = H - TS \tag{1.2.18}$$

Where H is enthalpy, T is temperature and S is entropy. Thus, the change in Gibbs free energy at constant pressure and temperature can be written as:

$$\Delta G = \Delta H - T\Delta S \tag{1.2.19}$$

At constant pressure, ΔH = q (irrespective of reversibility), and TΔS = q_{rev} (reversible heat flow). Equation 1.2.19 can be reduced to:

$$\Delta G = q - q_{rev} \tag{1.2.20}$$

Thus, ΔG is the difference between the heat released during a process (via a reversible or an irreversible path) and the heat released for the same process in a reversible manner. Under the special condition in which a process occurs reversibly, q = q_{rev} the Gibbs free energy change is zero. Thus, ΔG=0, the system is at equilibrium.

For a process which ΔG≠0, the heat released during a process for a system give rise to entropy change of the surroundings:

$$\Delta H_{sys} = -T\Delta S_{sur} \tag{1.2.21}$$

The second law of thermodynamics states that in any spontaneous process, the entropy of the universe increases:

$$\Delta S_{univ} = \Delta S_{sur} + \Delta S_{sys} > 0 \tag{1.2.22}$$

Substituting ΔS_{sur} in the above equation lead to:

$$-\frac{\Delta H_{sys}}{T} + \Delta S_{sys} > 0 \quad (1.2.23)$$

Multiplying both sides with -T lead to:

$$\Delta H_{sys} - T\Delta S_{sys} < 0 \quad (1.2.24)$$

Equation 1.2.24 is the Gibbs free energy change of system. Therefore, for a spontaneous process Gibbs free energy decreases.

In an electrochemical cell (Galvanic cell), the maximum amount of work that can be produced is equal to the product of overall cell potential and total charge transferred. Thus, the Gibbs free energy change becomes:

$$\Delta G = -nFE_{GC} \quad (1.2.25)$$

where n is the molar number of electrons transferred, F is the Faraday constant, and E_{GC} is the overall cell potential. For the process occurs spontaneously, $\Delta G < 0$, overall electrochemical cell potential is positive, $E_{GC} > 0$.

The Gibbs free energy change and the reaction quotient are related by the following equation:

$$\Delta G = \Delta G^0 + RTlnQ \quad (1.2.26)$$

Where ΔG is Gibbs free energy change, ΔG^0 is the standard Gibbs free energy change (all reactants and products are in their standard states), Q is the reaction quotient.

Equilibrium constant K describes a reaction that is at equilibrium, whereas Q describes a reaction that is not at equilibrium. When the reaction is at equilibrium (Q = K), the driving

force behind a chemical reaction is zero (ΔG = 0). Thus, the above equation 1.2.26 is converted to:

$$\Delta G^0 = -RTlnK \tag{1.2.27}$$

Inserting equation 1.2.27 back into equation 1.2.26, standard Gibbs free energy (ΔG^0) can be replaced by the equilibrium constant (K):

$$\Delta G = -RTlnK + RTlnQ = RTln\frac{Q}{K} \tag{1.2.28}$$

If the products and reactants are in their standard states. When Q < K, from equation 1.2.28 ΔG < 0 and from equation 1.2.25 $E_{GC} > 0$, the reaction is spontaneous in the forward direction. Conversely, when Q > K, from equation 1.2.28 ΔG > 0 and from equation 1.2.25 $E_{GC} < 0$, the reaction is spontaneous in the reverse direction. When Q =K, the system is at equilibrium with ΔG = 0 and $E_{GC} = 0$.

In conclusion:

Table 1.1. Criteria for the spontaneity of a process

ΔG	E_{GC}	Q/K	Direction of reaction
< 0	> 0	< 1	Spontaneous in forward direction
= 0	= 0	= 1	System at equilibrium
> 0	< 0	> 1	Nonspontaneous (spontaneous in reverse direction)

In electrochemistry, half reactions for corresponding electrode potentials are often written as reversible reactions. This can cause confusion between spontaneous reactions and reversibility. Take water electrolysis as an example. On the cathode of the electrolytic cell:

$$2H^+ + 2e^- \rightleftarrows H_2(g) \tag{1.2.29}$$

On the anode of the electrolytic cell:

$$2OH^- \rightleftarrows H_2O + 2e^- + 0.5O_2(g) \tag{1.2.30}$$

Theoretically without any overpotential, cathodic reaction will occur at 0 V vs SHE (pH=0), anodic reaction will occur at 1.23 V vs SHE (pH=0). Since water electrolysis is an electrolytic cell rather than galvanic cell, the overall cell potential is negative (-1.23 V), which amounts to Gibbs free energy change of +237 kJ per mol of hydrogen produced. Thus, the overall water electrolysis process is nonspontaneous (reverse reaction is spontaneous).

In any spontaneous process, the path between reactants and products is irreversible. Chemical systems are reversible only in equilibrium condition. So why for an overall irreversible process (water electrolysis) can be split into two reversible half-cell reactions? The half-cell reaction under electrochemical investigation is generally performed at equilibrium condition (i.e. little to none overpotential). Thus, it can be considered as reversible at such conditions.

1.3 Semiconductor photo-electrochemistry

Nowadays semiconductors play a critical role in modern technology, especially in environmental science such as production of clean energy, sensor technology and energy storage. Unlike metal and carbon materials which are good electrical conductors,

semiconductors have low conductivity usually well below that of the electrolyte. Due to the difference in electronic structure, a semiconductor electrode interacts differently with the electrolyte compared to conventional metal (or carbon) electrodes. The study of semiconductor-electrolyte interface has both fundamental and practical reasons: how does the electronic structure of electrode influence behaviour of electrochemical interface and effect electrochemical reactions? The interface of a semiconductor-electrolyte has similarities and differences with semiconductor-metal and metal-electrolyte interface. It is instructive to examine all these interfaces in order to understand the unique properties of the semiconductor-electrolyte interface.

1.3.1 Electrical double layers

It is well known that an electrical double layer (EDL) structure appears on the surface of a charged object when it is exposed to an electrolyte. The model which gave rise to the term EDL was first put forward in 1853 by Helmholtz. In the Helmholtz model, it is assumed that no electron transfer reactions across the electrode-electrolyte interface were to occur. Due to electrical attraction generated by the charged electrode surface, ions with opposite charge are adsorbed on the electrode surface and form a monolayer of ions that compensates charges of the electrode.[27] There are two parallel layers of charges at the interface, hence the name electrical double layer.

Later, Gouy and Chapman took a step further. They considered that instead of a monolayer of ions coated on the electrode surface, it is made of a diffuse layer of ions. In the diffuse layer, ions are drawn towards the electrode surface via Coulombic force and can move rather

freely. They derived the Poisson–Boltzmann equation by assuming ions are point charges while neglecting non-Coulombic interactions. Gouy-Chapman theory can give reasonable predictions for monovalent ions at low concentration (< 0.2 M) and potential (< 80 mV). However, ignoring size of the ion causes Poisson–Boltzmann equation to yield an unrealistically high concentration of ions very close to the electrode which lead to an overestimation of EDL capacitance.[28]

The limitation in the Gouy-Chapman model was partially addressed by Stern[29]. In this model, Helmholtz model and the Gouy-Chapman model are combined. In the first layer closest to the electrode, ions are chemically adsorbed on the surface (Stern layer). In the second layer screening the first layer, ions are drawn towards the surface via Coulombic force (Diffuse layer). Later, Grahame[30] divided the Stern layer further into two sub-layers: an inner layer consists of specifically adsorbed ions and their solvent molecules, and an outer layer consists of solvated ions. The inner Helmholtz layer is between the charged surface and the inner Helmholtz plane (IHP). The region extending beyond the IHP to the outer Helmholtz plane (OHP) is the outer Helmholtz layer. Usually, the solvation molecules in the inner Helmholtz layer will strongly be oriented compared with those in outer Helmholtz layer.

The EDL is the result of the change in electric potential near a surface. With an electrode, it is possible to regulate the surface charge by applying an external electric potential, conversely, a change in electrolyte will affect potential drop in EDL.

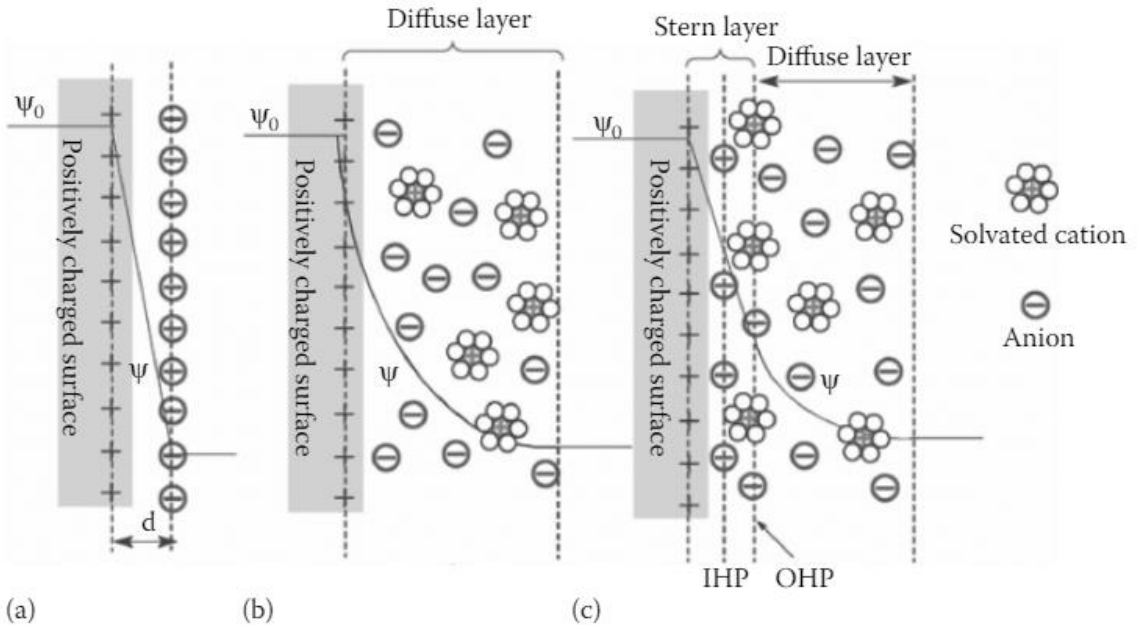


Figure 1.7. Models of the electrical double-layer at a positively charged surface: (a) the Helmholtz model; (b) the Gouy–Chapman model; and (c) the Stern model, showing the IHP and OHP. The IHP refers to the closest approach of specifically adsorbed ions (generally anions) and the OHP refers to that of the non-specifically adsorbed ions. The OHP is also the plane where diffuse layer begins. d is the double-layer distance described by the Helmholtz model. ψ_0 and ψ are the potentials at the electrode surface and the electrode interface, respectively. Reproduced from Zhang.[31]

1.3.2 Metal-metal interface

The energy difference from the Fermi level to the vacuum level is called the work function (Φ), and different material have different work functions. When two metals are electrically isolated from each other, an arbitrary potential difference may exist between them (figure 1.8).

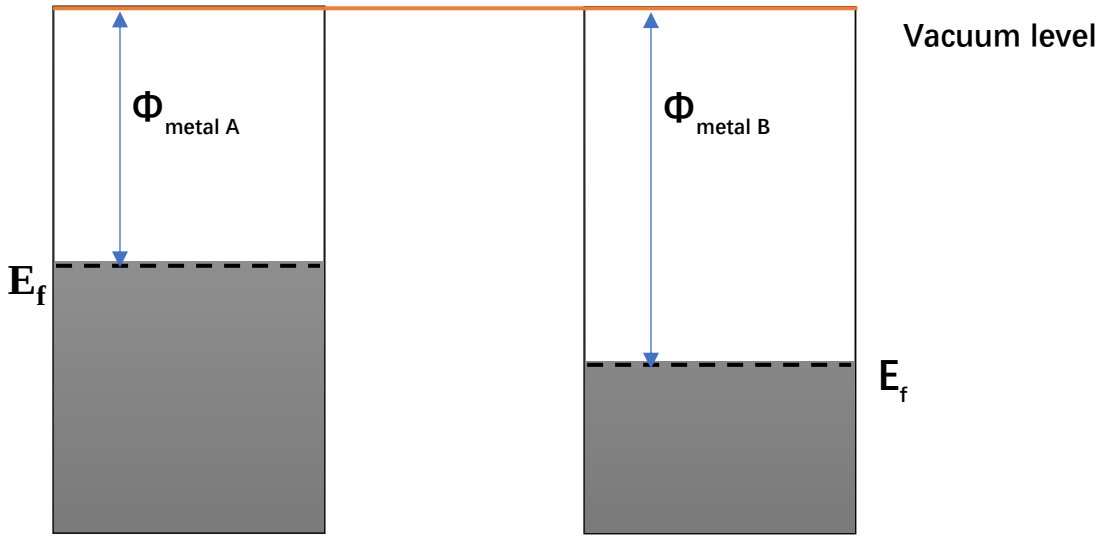


Figure 1.8. Two metals A and B in isolation with work functions of $\Phi_{metal\ A}$ and $\Phi_{metal\ B}$ respectively. Metal A has a smaller work function than metal B.

When two different metals come into electrical contact, in accordance with thermodynamics, the Fermi level must be constant throughout the entire connected system. (see section 1.1.2) Electrons in metal A is at higher energy level than those in metal B. During contact, electrons are transferred from metal A to metal B and occupy the empty energy levels above metal B's Fermi level. Due to the transfer of electrons, a net positive charge occurs on metal A's side and net negative charge on metal B's side. Thus, an electric potential difference is established at the interface. The electric potential is related to work function difference between the two metals. The electric potential difference of two materials in electric contact is called Volta potential, which is the potential difference between a point close to the surface of the first material, and a point close to the surface of the second material.[32] (figure 1.9)

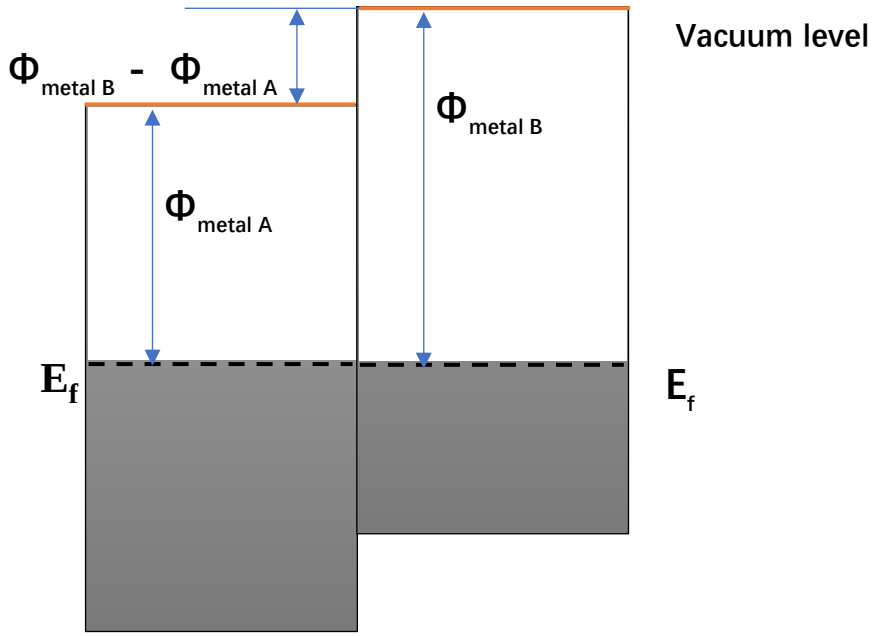


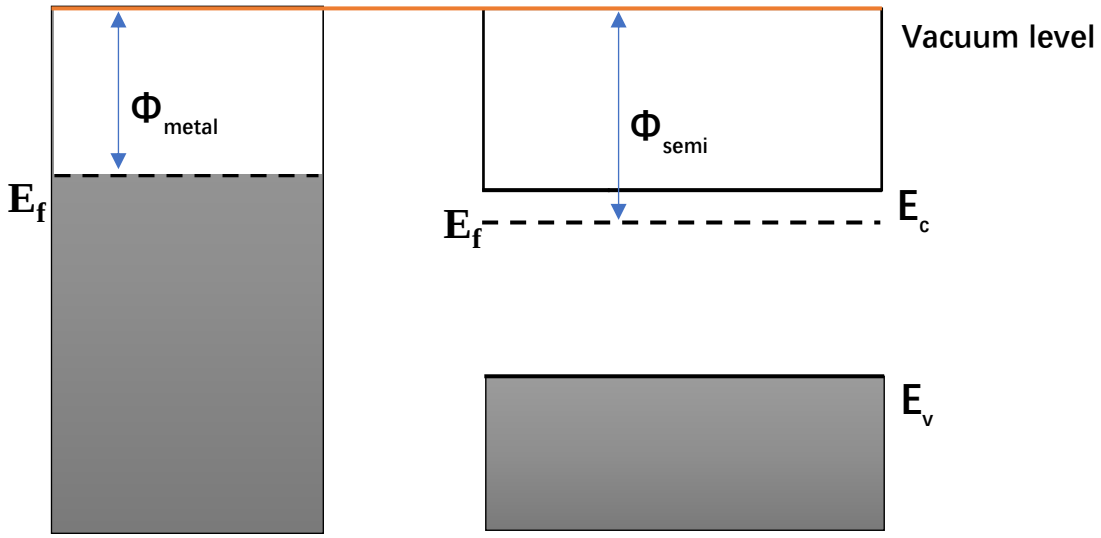
Figure 1.9. Two metals A and B in electrical contact at equilibrium condition, with Volta potential of $\Phi_{metal\ B} - \Phi_{metal\ A}$ (provided $\Phi_{metal\ B} > \Phi_{metal\ A}$), $\Phi_{metal\ A}$ and $\Phi_{metal\ B}$ are work functions of metal A and metal B respectively.

However, Volta potential cannot be measured using a voltmeter. Voltmeter measures difference in Fermi level between two materials, which is zero for electrically connected systems at equilibrium. The Volta potential of a metal surface can be mapped using a Kelvin probe force microscope (KPFM), which is based on the atomic force microscope (AFM).

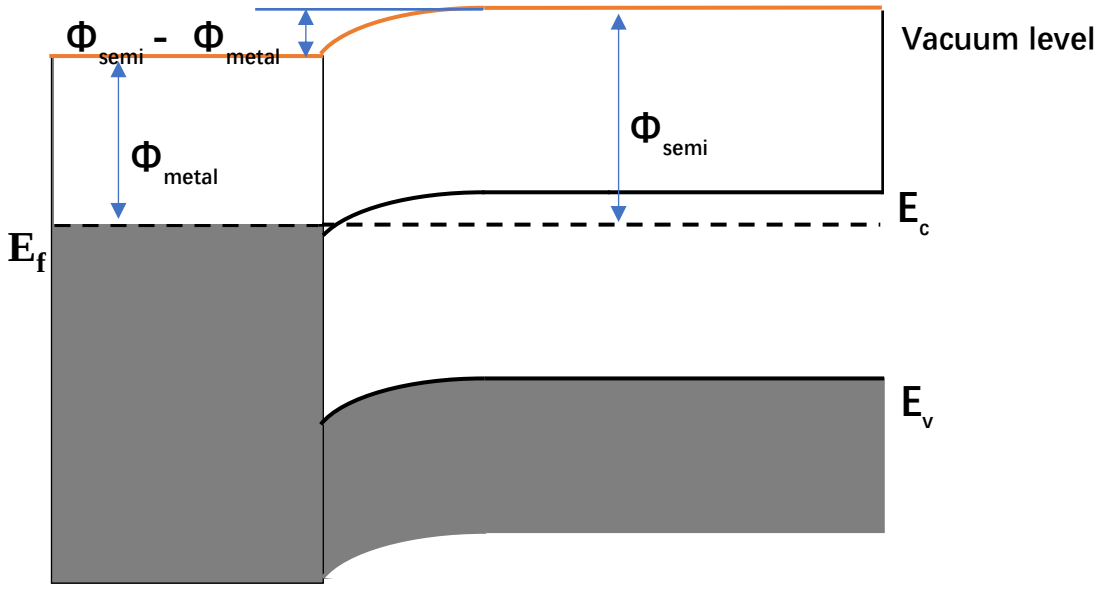
1.3.3 Semiconductor-metal interface

One of the oldest semiconductor devices is the Schottky diode. A Schottky diode is a metal-semiconductor junction with rectifying properties. In contrast, a non-rectifying metal-semiconductor junction is called an ohmic contact, which allows electric charges to pass freely across the interface. The formation of different junctions is dependant of the work function of the semiconductor relative to the work function of metal contact.

Take a n-type semiconductor for example, if the work function of the metal (Φ_{metal}) is less than the work function of semiconductor (Φ_{semi}), an ohmic contact is formed. (figure 1.10) Similar to a metal-metal junction discussed in section 1.3.2, when the metal-semiconductor junction is formed the Fermi levels must line up at equilibrium. However, the conductivity and charge carrier density of a semiconductor is several magnitudes lower than that of the metal. During equilibration, charges are transferred across the interface, and due to the low charge carrier density of the semiconductor, charges are moved not only from the surface but also from a certain depth of semiconductor and forming a space charge layer (SCL) in the form of an accumulation region. The accumulation region has a higher conductivity than the bulk of the semiconductor due to this higher concentration of electrons. The formation of SCL is shown as band bending in the band diagram, the amount of band bending amounts Φ_{semi} - Φ_{metal}. An ohmic junction behaves as a resistor conducting under forward and reverse bias. The overall resistivity is determined by the resistivity of the semiconductor.



Before contact

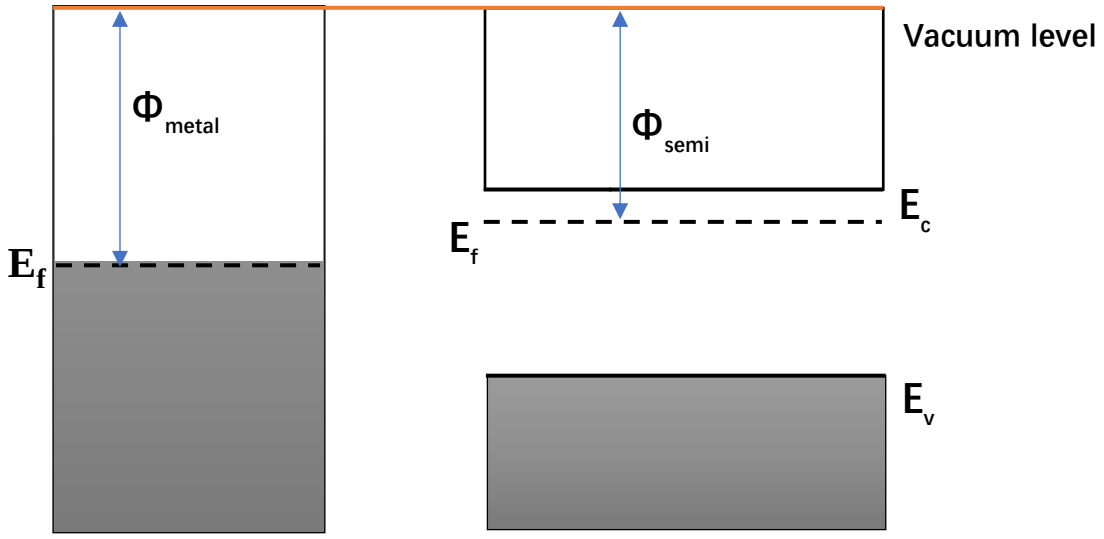


Ohmic contact

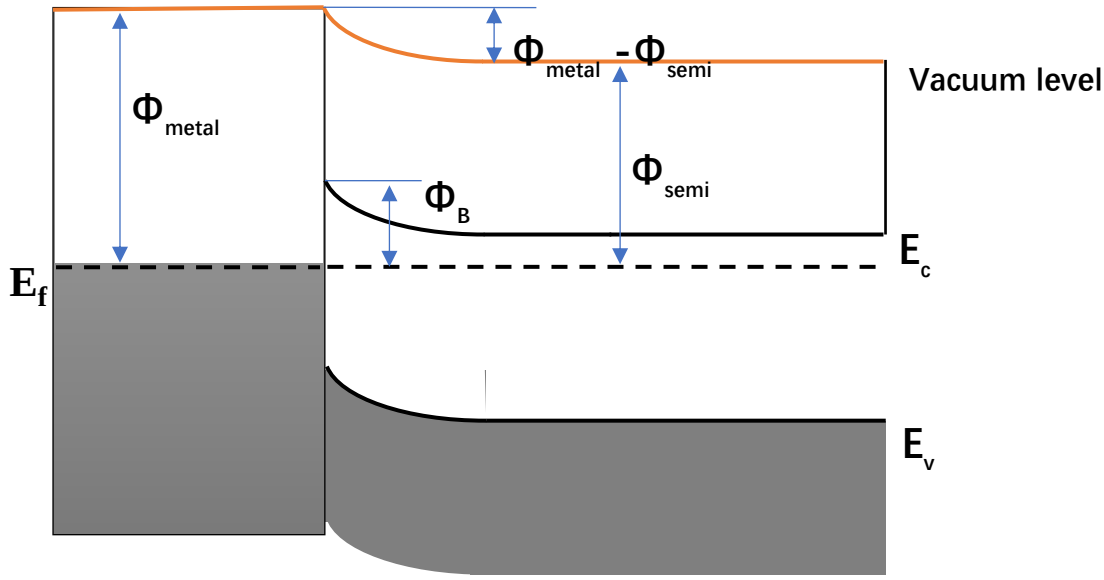
Figure 1.10. Energy diagram of formation of an ohmic contact between a metal and n-type semiconductor before and after contact ($\Phi_{semi} > \Phi_{metal}$). E_c and E_v are conduction band edge and valence band edge respectively.

If the work function of metal (Φ_{metal}) is larger than the work function of semiconductor (Φ_{semi}), a Schottky junction is formed. (figure 1.11) Once again, at equilibrium, the Fermi level must line up. Due to the low charge carrier density on the semiconductor side, electrons are depleted from certain depth within the semiconductor. This leads to the formation of a SCL in the form of a depletion region (different band bending direction compared to accumulation region). There is a built-in potential in the Schottky junction, given by the difference in work functions: $\Phi_{metal} - \Phi_{semi}$. The built-in potential acts as a barrier preventing electrons to move from n-type semiconductor to the metal. This is called the Schottky barrier,

with the Schottky barrier height Φ_B, defined as the difference between the interfacial conduction band edge E_C and Fermi level E_f which amounts to $\Phi_B = \Phi_{metal} - \Phi_{semi} + E_C - E_f$.



Before contact



Schottky junction

Figure 1.11. Energy diagram of formation of a Schottky junction between a metal and n-type semiconductor before and after contact ($\Phi_{semi} < \Phi_{metal}$). E_c and E_v are conduction band edge and valence band edge respectively, Φ_B is Schottky barrier height.

The ohmic contact has a linear current-voltage (I-V) curve (resistive characteristics) whereas the Schottky junction has a non-linear response. The Schottky barrier prevents electrons from moving across the junction. Under external bias the Fermi levels no longer line up but are shifted with respect to one another and the magnitude of the shift depends on the applied voltage.

If the metal is connected to positive terminal of the battery and the negative terminal of the battery is connected to the n-type semiconductor, the Schottky diode is said to be forward biased. In other words, forward bias is in the direction of easy charge transport. When forward bias is applied to the Schottky diode (n-type semiconductor), the Fermi level in the semiconductor side rises up and reduces the Schottky barrier height. If the applied voltage is continuously increased, the depletion region becomes thinner and ultimately disappears. Under large forward bias, Schottky diode behaves as a resistor.

If the n-type semiconductor is connected to a positive terminal of the battery and the negative terminal of the battery is connected to the metal, the Schottky diode is said to be reverse biased. Reverse bias is in the direction of little to no charge transport. When a reverse bias voltage is applied to the Schottky diode, the depletion width increases, thus undermines the flow of electrons. However, a small leakage current flows exists due to diffusion of minority carriers. This current is almost independent of the reverse voltage and varies with temperature. If the reverse bias voltage is further increased, a sudden increase in electric

current occurs. This sudden current increase is due to the structural breakdown of the depletion region.

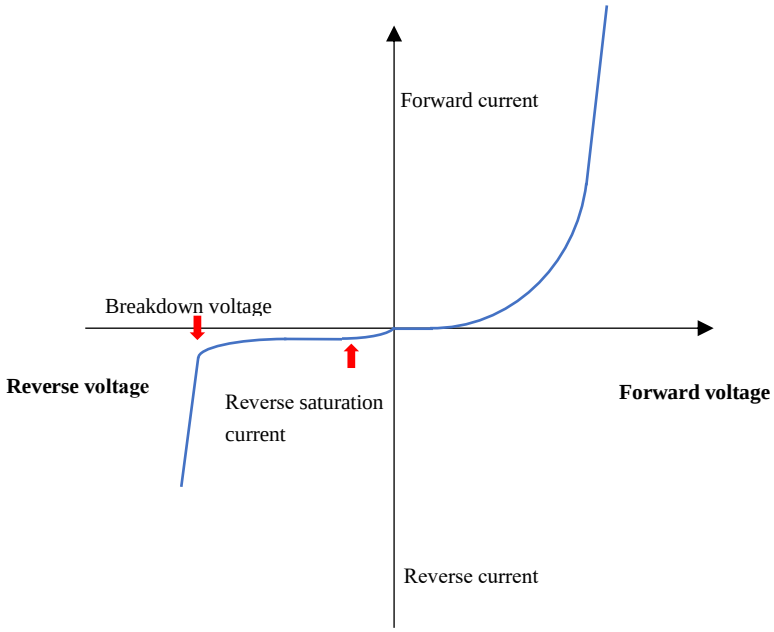


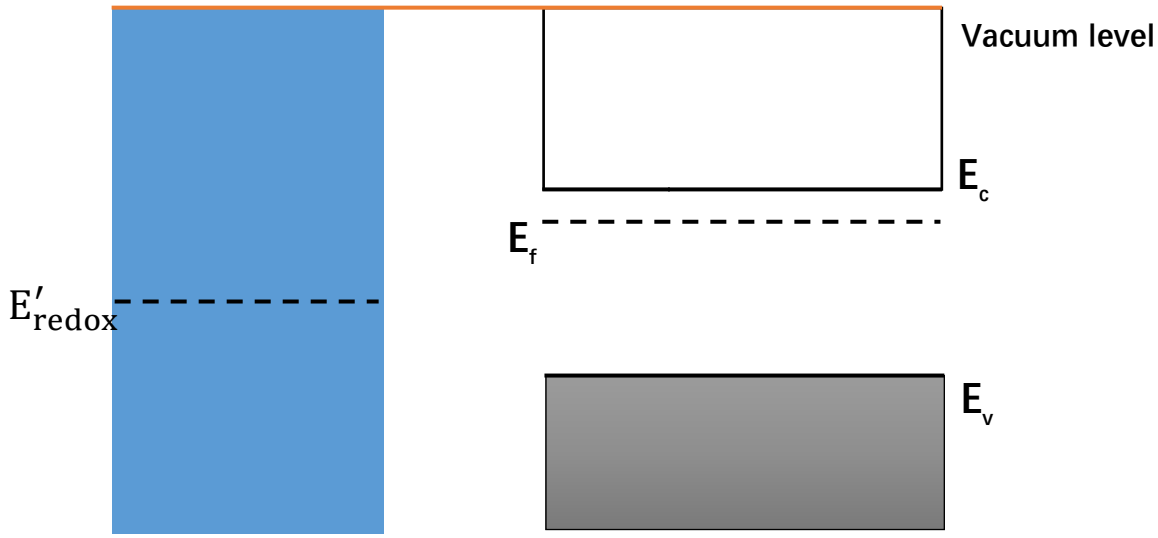
Figure 1.12. I-V characteristics of a Schottky diode showing rectifying properties.

1.3.4 Semiconductor-electrolyte interface

Similar to the above-mentioned interfaces, when semiconductor and electrolyte come into contact, the Fermi level must line up at equilibrium. In an electrolyte, the equivalent of the Fermi level is the electrochemical potential (reduction potential) discussed in section 1.2.3. Take a n-type semiconductor for example, during contact, charges are transferred across the interface until potential levels line up. It must be stressed that reduction potential and Fermi level could "line up", but they are a potential unit and energy unit respectively (discussed in section 1.2.3). Empirical estimates absolute electrode potential of SHE is 4.44 ± 0.02 V at 298 K [24]. Thus, the conversion between reduction potential E_{redox} in the electrolyte (electrode potential) and its equivalent energy level E'_{redox} is (derived from equation 1.2.7):

$$E'_{redox} = -e\psi_{redox} = -4.44\ eV - eE_{redox} \quad (1.3.1)$$

Where ψ_{redox} is the absolute electrode potential using vacuum as a reference, E_{redox} is the reduction potential measured using SHE as reference. The conductivity of a semiconductor is usually well below that of an electrolyte, thus most of the potential drop occurs on the semiconductor side and very little on the solution side of the interface. This situation is similar to the metal-semiconductor interface discussed in section 1.3.3.



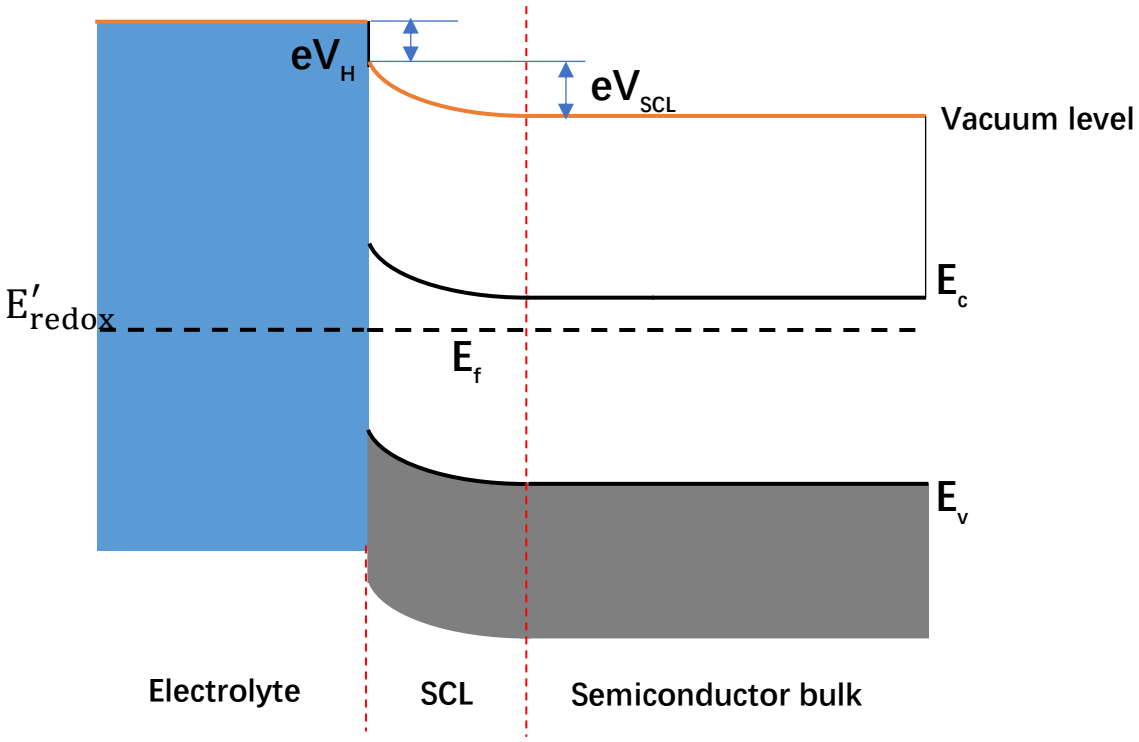


Figure 1.13. Energy diagram of formation of semiconductor-electrolyte interface between a metal and n-type semiconductor before and after contact. E_c and E_v are conduction band edge and valence band edge respectively, E'_{redox} is the equivalent energy level of redox potential in electrolyte, V_{SCL} is the potential drop in SCL and V_H is Helmholtz potential drop.

On the semiconductor side of the interface, electrons are depleted from the semiconductor surface until a certain depth. This leads to the formation of a SCL in the form of a depletion region. The SCL is represented as band bending in the band diagram, the amount is eV_{SCL}. Since the semiconductor electrode surface is positively charged, ions are chemically adsorbed on the surface (Stern layer) and drawn towards the surface via Coulombic force (Diffuse layer). This causes a potential drop in the form of a Helmholtz potential drop (V_H) and Gouy potential drop (V_G). For sufficiently concentrated electrolyte (> 0.1 M), the potential drop due to diffusion can be neglected. Thus, only V_H is shown at electrolyte interfaces (figure 1.13).

Within the SCL, an electric field appears as a result of charge density distribution. Using the Poisson–Boltzmann equation, the potential in the SCL can be correlated with the electric field strength and the charge density distribution:

$$\frac{d^2\psi}{dx^2} = -\frac{d\xi}{dx} = -\frac{\rho(x)}{\varepsilon_r \varepsilon_0} \tag{1.3.2}$$

Where ψ is the electric potential in the SCL, ξ is the electric field strength (avoiding confusion with symbol E), ρ is the charge density distribution, ε_0 is the permittivity of free space, and ε_r is the dielectric constant (relative permittivity) of the solvents.

The total charge density in the n-type semiconductor consists of the concentration of free electrons n(x) and the concentration of ionised donors N_D:

$$\rho(x) = -en(x) + eN_D \tag{1.3.3}$$

The concentration of free electrons can be derived from the energy difference between the conduction band minimum E_C and the Fermi level E_f using equation 1.1.6 (see section 1.1.3). Inside the SCL, the distance between E_f and E_C, is modified by the amount band bending $\psi(x)$ equation 1.1.6 becomes:

$$n(x) = N_C \, exp\left[-\left(E_C - E_f - e\psi(x)\right)/kT\right] \tag{1.3.4}$$

Inside the semiconductor bulk, where no band bending present, equation 1.16 becomes:

$$n_{bulk} = N_C \, exp\left[-\left(E_C - E_f\right)/kT\right] \tag{1.3.5}$$

In equation 1.3.3, replacing constant component with n_{bulk} simplifies to:

$$n(x) = n_{bulk} \, exp \, e\psi(x)/kT \tag{1.3.6}$$

Since the semiconductor bulk is electrically neutral, the electron concentration n_{bulk}, must equal to the ionized donor density N_D, equation 1.3.5 becomes:

$$n(x) = N_D \, exp \, e\psi(x)/kT \tag{1.3.7}$$

Combining the equations 1.3.2 and 1.3.6, the total charge density at point x in the SCL can be written as:

$$\rho(x) = -en(x) + eN_D = eN_D(1 - exp\,(\frac{-e\psi}{kT})) \tag{1.3.8}$$

Now total charge density in the SCL, $\rho(x)$, can be used to solve the Poisson–Boltzmann equation (equation 1.3.1). Using some elegant math techniques, Mott–Schottky equation can be derived:

$$\frac{1}{{C_{SCL}}^2} = \frac{2}{\varepsilon_r \varepsilon_0 A^2 e N_D}\left(\psi - V_{fb} - \frac{kT}{e}\right) \tag{1.3.9}$$

where C_{SCL} is the capacitance of SCL, A is the area of the semiconductor-electrolyte interface, N_D is the donor density, ψ is the applied electric potential on the semiconductor and V_{fb} is the flat band potential. The details of the derivation can be found here[33].

On the electrolyte side, an EDL is formed. As discussed in section 1.3.1, the EDL is consisted of capacitive Helmholtz layer and diffusive Gouy layer. For sufficiently concentrated electrolyte, the potential drop due to diffusion can be neglected. The potential drop across the Helmholtz layer is given by:

$$V_H = Ed = \frac{Q_{surface} d}{\varepsilon_0 \varepsilon_r A} \tag{1.3.10}$$

Where $Q_{surface}$ is the surface charge, d is the Helmholtz layer width, A is surface area, ε_0 is the permittivity of free space, and ε_r is the dielectric constant (relative permittivity) of the

solvents. The width of the Helmholtz layer is around 2-5 Å, the relative permittivity of water is estimated to be around 80, the potential drop across Helmholtz layer is typically in the order of 0.1–0.5 V.

During adsorption and desorption from the semiconductor surface, the ions gain or lose energy while crossing the Helmholtz layer as a result of Helmholtz layer potential. The equilibrium constants for surface hydroxylation reactions:

$$MOH \overset{k_a}{\leftrightarrow} MO^- + H^+ \tag{1.3.11}$$

$$MOH + H^+ \overset{k_b}{\leftrightarrow} MOH_2^+ \tag{1.3.12}$$

Are:

$$k_a = \frac{[MO^-][H^+]}{[MOH]} = exp\left(-\frac{\Delta G_a - eV_H}{kT}\right) \tag{1.3.13}$$

$$k_b = \frac{[MOH_2^+]}{[MOH][H^+]} = exp\left(-\frac{\Delta G_b + eV_H}{kT}\right) \tag{1.3.14}$$

Respectively. Dividing equation 1.3.12 and 1.3.14 lead to:

$$2.3log\left(\frac{[MO^-][H^+]^2}{[MOH_2^+]}\right) = \frac{\Delta G_b - \Delta G_a + 2eV_H}{kT} \tag{1.3.15}$$

At a certain pH, called point of zero charge (PZC), the net adsorbed charge is zero ($[MO^-] = [MOH_2^+]$), and the potential drop across the Helmholtz layer is zero ($V_H = 0$):

$$-2.3 \times 2PZC = \frac{\Delta G_b - \Delta G_a}{kT} \tag{1.3.16}$$

Using equation 1.3.15, the Gibbs free energy component in equation 1.3.14 can be eliminated leading to the following expression:

$$V_H = \frac{2.3kT}{e} log\ (\frac{[MO^-]}{[MOH_2^+]})^{0.5} + \frac{2.3kT}{e}(PZC - pH) \quad (1.3.17)$$

The excess charge at the surface is usually very small, in the order of 1% of a monolayer. Thus, $[MO^-] \approx [MOH_2^+]$, and above equation is simplified to:

$$V_H = \frac{2.3kT}{e}(PZC - pH) = 59\,mV \times (PZC - pH) \quad (1.3.18)$$

This shows that the Helmholtz potential changes by -59 mV per pH unit (298 K).

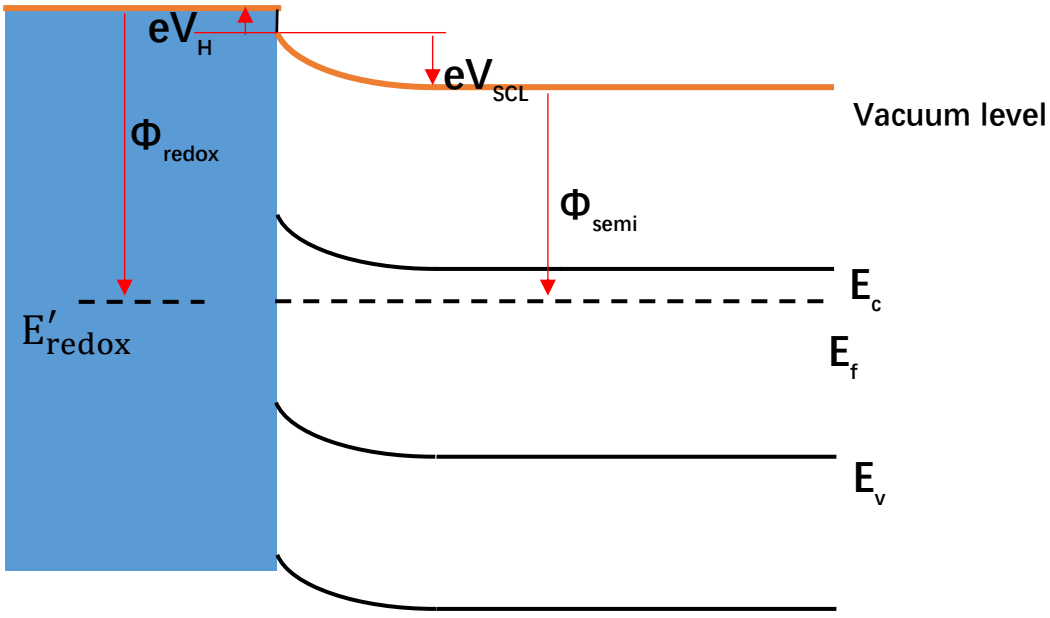


Figure 1.14. Energy band diagram of a n-type semiconductor- electrolyte interface at equilibrium. The vacuum energy level is used as reference zero. E_c and E_v are conduction band edge and valence band edge respectively, E'_{redox} is the equivalent energy level of reduction potential in electrolyte, V_{SCL} is the potential drop in SCL and V_H is Helmholtz potential drop. The semiconductor work function Φ_{semi} and the work function of a reduction potential Φ_{redox} in an electrolyte with respect to the vacuum level is shown.

Now we can draw a detailed band diagram for the semiconductor-electrolyte interface. An example is shown in figure 1.14 for an interface composed of a n-type semiconductor and an electrolyte. The y-axis represents the energy of an electron with vacuum as reference. It

is important to note that the vacuum level bends in the SCL due to the presence of an electric field, and a sharp drop at the interface due to potential drop in the Helmholtz layer (Gouy potential drop is neglected). It may seem odd to use vacuum as a reference energy level; it is a consequence of the convention in solid state physics that the electrochemical potential (Fermi energy) of the electrons is drawn as a constant value throughout the system at equilibrium.

Under most circumstances, the redox species is sufficiently concentrated that the potential drop across the Gouy (diffuse) layer in the solution can be neglected. From this energy alignment using vacuum as a reference energy level, we obtain the following energy relationship for a semiconductor-electrolyte interface under equilibrium:

$$\Phi_{redox} = eV_H + eV_{SCL} + \Phi_{semi} \tag{1.3.19}$$

Where Φ_{semi} is the work function of semiconductor, Φ_{redox} is the work function of an equivalent energy level E'_{redox}, V_{SCL} is the potential drop in SCL and V_H is Helmholtz potential drop. In potential terms, equation 1.3.19 is dived by -e leading to:

$$\psi_{redox} = \psi_{semi} - V_H - V_{SCL}$$

Where ψ_{redox} is the absolute electrode potential and ψ_{semi} is the potential in semiconductor bulk. How come under equilibrium when the Fermi level of the semiconductor and equivalent energy level of reduction potential line up, there is a potential drop in between? Misleading as it may seem, this is due to the distortion of the vacuum level by an electric field. The electric field exists inside the SCL and EDL region which causes the potential drop. The built-in potential is essential for photo-electrochemical reactions, it

acts as the driving force for photo-generated electron-hole pairs and contributes to the separation of electrons and holes which leads to improved charge carrier lifetime.

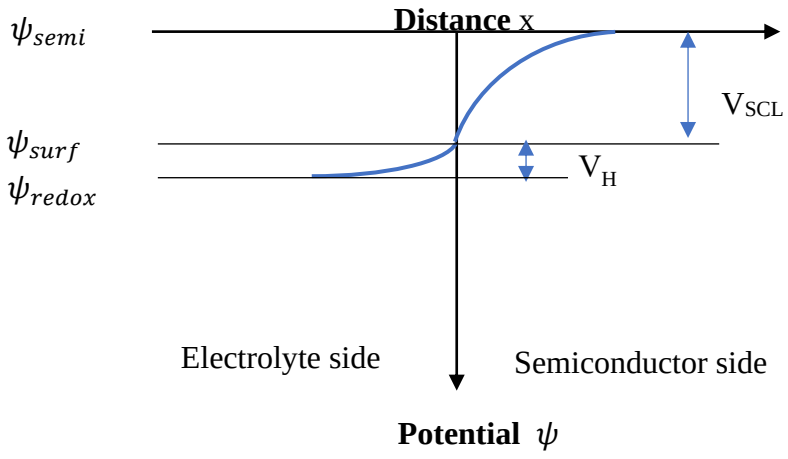


Figure 1.15. Electrostatics at a semiconductor–electrolyte interface. ψ_{redox} is the absolute electrode potential, ψ_{surf} is the potential at surface of the electrode, and ψ_{semi} is the potential in the semiconductor bulk. V_{SCL} is the potential drop in SCL and V_H is the Helmholtz potential drop. The Gouy potential drop is neglected.

1.4 Photoelectrochemical Cell

1.4.1 PEC basics

Figure 1.16 is a typical photoelectrochemical cell (PEC) consisting of a photoanode and metal cathode. This n-type semiconductor based PEC device originated from the discovery of the photolysis of water using TiO_2 semiconductor electrodes by Fujishima and Honda[34] in 1972. The key component of the PEC is the semiconductor photoanode, which converts photons to electron-hole pairs. The electron-hole pairs are separated due to the electric field in the semiconductor SCL which is discussed in section 1.3.4. The separated electrons are transported through an external circuit to the metal cathode. On the metal cathode, water is

reduced to hydrogen. Separated holes are swept towards the semiconductor-electrolyte interface where water is oxidised to oxygen.

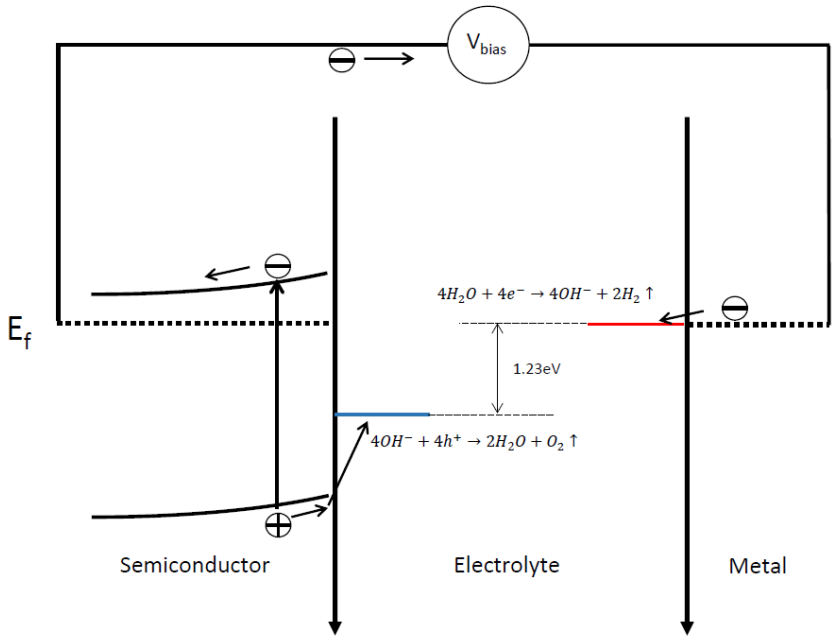


Figure 1.16. PEC consisted of n-type photoanode and metal cathode connected via a circuit. Fermi level (E_f) is shown as black dotted lines, water reduction and oxidation potential are shown as red and blue solid lines respectively (pH>7).

In an acidic environment (standard electrode potentials, H^+ effective concentration of 1 mol/L), the reduction and oxidation reactions can be written as:

$$4H^+ + 4e^- \rightleftarrows 2H_2, E_{red} = 0\,V\ vs.SHE \quad (1.4.1)$$

$$2H_2O + 4h^+ \rightleftarrows 4H^+ + O_2, E_{ox} = 1.23\,V\ vs.SHE \quad (1.4.2)$$

In an alkaline environment (standard electrode potentials, OH^- effective concentration of 1 mol/L), the reduction and oxidation reactions can be written as:

$$4H_2O + 4e^- \rightleftarrows 2H_2 + 4OH^-, E_{red} = -0.828\,V\ vs.SHE \quad (1.4.3)$$

$$4OH^- + 4h^+ \rightleftarrows 2H_2O + O_2, E_{ox} = 0.401\,V\ vs.SHE \quad (1.4.4)$$

The Gibbs free energy change for the overall water splitting at standard temperature (298 K) and conditions (1 mol/L, 1 bar), is 237 kJ per mol of hydrogen produced. The increase in Gibbs free energy means the reaction is thermodynamically uphill (non-spontaneous see section 1.2.5). Photolysis of water is very different from the photo-assisted degradation of organic pollutants, for which the Gibbs free energy change is negative (discussed in section 1.5.2).

1.4.2 Band diagram

Now we understand the structure of the semiconductor-electrolyte interface, a detailed energy diagram for a complete PEC device can be drawn. Figure 1.17 is a ideal energy diagram of a PEC composed of a n-type photoanode and a metal counter electrode connected via an external circuit.

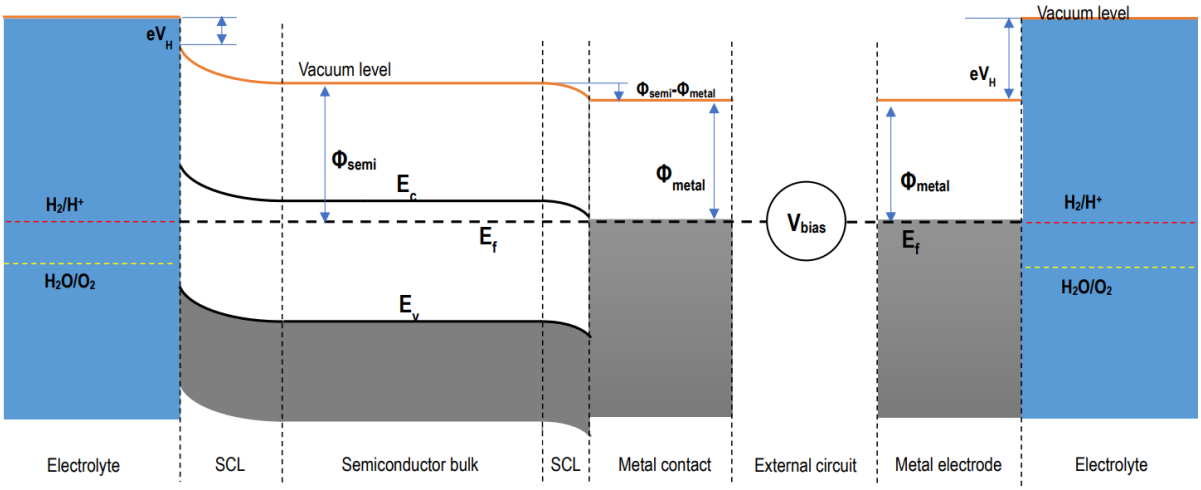


Figure 1.17. Energy diagram for an ideal PEC device based on a n-type semiconductor and a metal counter electrode. The vacuum energy level is used as reference (orange solid line). The semiconductor work function (Φ_{semi}), metal's work function (Φ_{metal}) are material constants. For simplicity, both metal contact and metal electrode are made of the same material.

The energy of an electron in vacuum is chosen as the reference (orange solid line). It is important to note that the vacuum level bends in the presence of electric field which exists in the EDL (section 1.3.1) and semiconductor SCL (section 1.3.3 and 1.3.4). Having such a "non-uniform" level as the reference energy may seem a bit odd, this is a consequence of the convention that the electrochemical potential (or Fermi energy) of the electrons is drawn as a constant value when the system is in equilibrium.

Taking a closer look at the electrolyte phase. The energy of a redox couple in the electrolyte with respect to the vacuum level is not accurately known. Empirical estimates absolute electrode potential of SHE to be 4.44 ± 0.02 V at 298 K [24]. As discussed in section 1.3.1, the EDL is consisted of capacitive Helmholtz layer and diffusive Gouy layer. For sufficiently concentrated electrolyte (> 0.1 M), the potential drop due to diffusion can be neglected. Thus, only the Helmholtz potential drop (V_H) is shown at electrolyte interface.

The key parameters for the semiconductor are the band edge positions, Fermi level and the amount of band bending. In Figure 1.17, photogenerated holes will be able to oxidise water if the H_2O/O_2 redox potential (yellow dash line) is above the valence band edge (E_V). Similarly, only electrons with an energy (E_f) above the H_2/H^+ redox potential (red dash line) can reduce the corresponding species in the electrolyte. If the Fermi level (E_f) of the semiconductor is below the H_2/H^+ redox potential (red dash line), introducing an adequate external bias (V_{bias}) with external circuit could allow the Fermi level (E_f) of the metal counter electrode to rise above the H_2/H^+ redox potential (red dash line) at the cost of reducing overall PEC efficiency. By measuring the potential (Fermi level) of the semiconductor with

respect to that of a reference electrode, the alignment of energy levels across the interface can be determined. The advantage of using a reference electrode for this is that the measured potential difference does not depend on the amount of current that flows through the cell. However, in non-ideal condition, quasi-Fermi level is needed to fully explain the alignment of energy levels on the semiconductor-electrolyte interface. This is discussed thoroughly in Chapter 4 in context of Sn-doped TiO_2 photoanode.

1.4.3 PEC configurations

When the conduction and valence bands of a photoanode/photocathode do not align with the water reduction and oxidation potentials, the available potential window is insufficient for water splitting, a combination of multiple semiconductors may be required. In such a device, single/multiple semiconductors act as a regular photoanode or photocathode complementing each other.

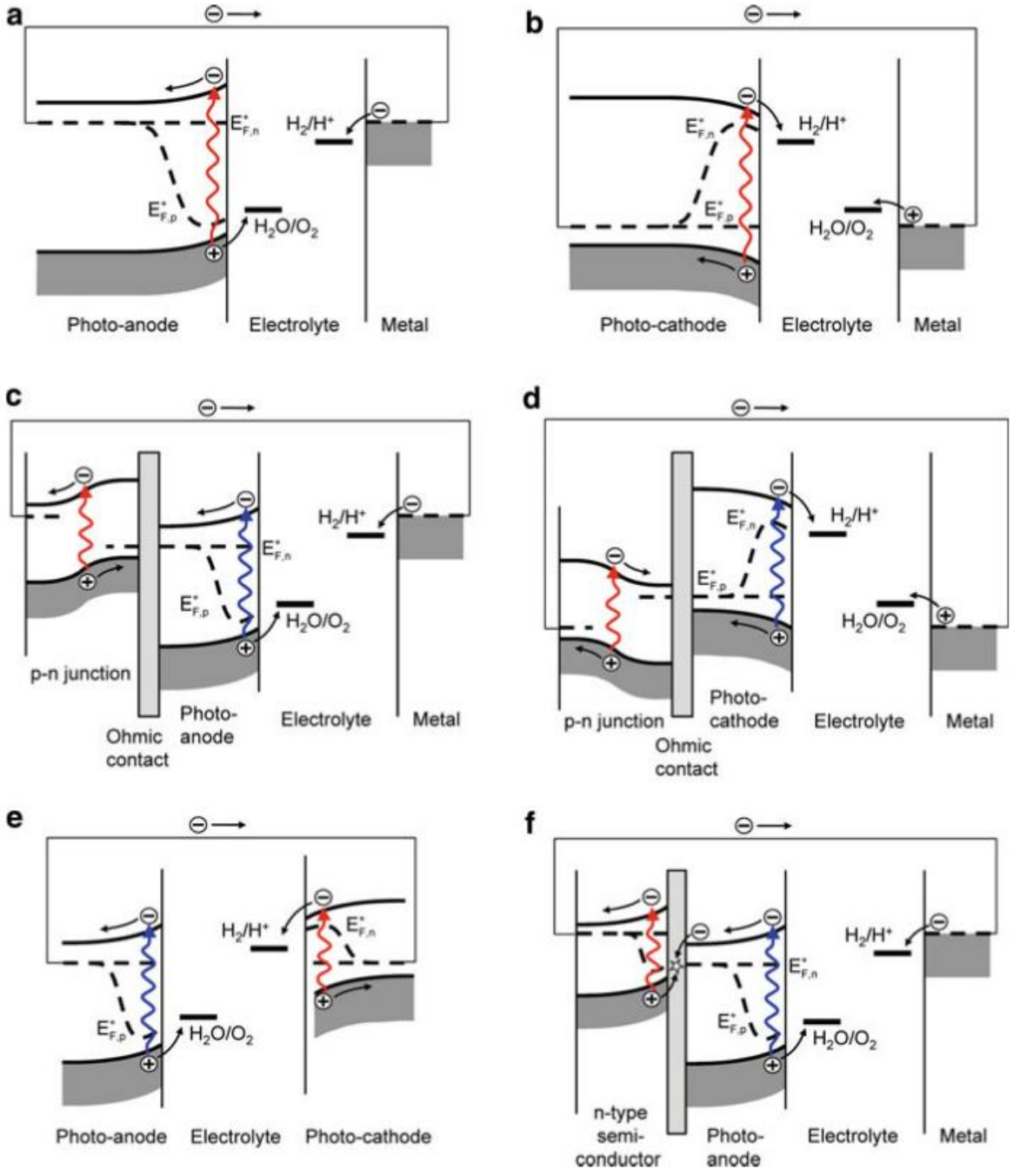


Figure 1.18. Examples of possible PEC configurations under illumination. Top row: Standard single-semiconductor devices based on a photoanode (a) or photocathode (b) with a metal counter electrode. Middle row: Monolithic devices based on a photoanode (c) or photocathode (d) biased with an integrated p–n junction. Bottom row: p–n junction photoelectrochemical device (e), and an n–n heterojunction PEC device based on a photoanode deposited on top of a second n-type semiconductor that "boosts" the energy of the electrons (f).[35]

The simplest PEC device made of a single photoanode or photocathode connected with a metal counter electrode shown in configuration A and configuration B respectively.

Configuration A is the one we have been using in this chapter to illustrate the key principles of PEC water splitting. $SrTiO_3$ is one of the few photoanode materials that could be used in this configuration.[36] P-type photocathode material such as SiC are candidates for configuration B.[37] In configurations (C) and (D) a bias voltage is added to the photoanode and photocathode, respectively, through an integrated p–n junction. A tandem device consisting of a p-type $GaInP_2$ photocathode and a GaAs p–n junction can achieve solar-to-hydrogen efficiency of 12.4%,[38] which is a good example of configuration C. In configurations E and F an additional bias potential is generated by a single semiconductor material instead of a p–n junction. A good example of configuration E is a device based on n-type TiO_2 photoanode and p-type GaP photocathode.[39] More complex devices can be achieved by combining configurations described above into multi-layered tandem devices.[40]

1.5 Doped TiO_2 for advanced oxidation processes

1.5.1 Rise of TiO_2

Commercially, TiO_2 has been widely used in sunscreens, paints and pigments.[41–43] In 1972, Fujishima and Honda discovered the phenomenon of photocatalytic splitting of water on a TiO_2 electrode under ultraviolet (UV) light which lead to an explosion of research on TiO_2 material. These applications can be roughly divided into two categories: environmental and energy.

Advanced oxidation processes (AOPs) have been proposed as an alternative method for the cleaning-up of many toxic organic compounds which accumulate in the environment. These

organic toxins are a results of the abusive use of pharmaceutical and personal care products (PPCPs), pesticides, industrial chemicals, and combustion by-products.[44] TiO_2 is environmentally benign, low cost, abundantly available and a highly stable metal oxide photocatalyst with the ability to efficiently degrade a spectrum of contaminants,[45] which makes it one of the top choices amongst metal oxide photocatalysts.

One of the most important research areas for the future is clean energy production. Photocatalysis is an emerging technology that enables the transformation of solar energy to solar fuel or electricity. Modified TiO_2 has been widely used in both applications. For example, an overall solar to current conversion efficiency of 10.6% has been reached by the group led by Gratzel using dye-sensitized solar cells (DSSCs) based on TiO_2 substrate;[46] efficient photocatalytic water splitting has been demonstrated by Chen et al. using black hydrogenated TiO_2.[47]

1.5.2 Advanced oxidation processes

Semiconductor band structure is key to a metal oxide photocatalyst. It is well established[48] that under suitable light irradiation conditions ($h\nu > E_{bandgap}$), conduction band electrons (e^-) and valence band holes (h^+) are generated. The photogenerated electrons could reduce the dye or react with electron acceptors such as O_2 adsorbed on the Ti (III)-surface or dissolved in water, reducing it to the superoxide radical anion $O_2^{\bullet-}$. The photogenerated holes can oxidise the organic molecule to form R^+ or react with OH^- or H_2O oxidizing them into hydroxyl radicals ($OH^\bullet$). These radical species are reported to be responsible for the heterogeneous TiO_2 photodecomposition of organic substrates as dyes. According to this,

the relevant reactions at the semiconductor surface causing the degradation of dyes can be expressed as follows[49]:

$$h^+ + H_2O \rightarrow H^+ + OH^\bullet$$

$$h^+ + OH^- \rightarrow OH^\bullet$$

$$e^- + O_2 \rightarrow O_2^{\bullet -}$$

$$O_2^{\bullet -} + H^+ \rightarrow HO_2^\bullet$$

$$Dye + OH^\bullet \rightarrow degradation\ products$$

$$Dye + h^+ \rightarrow oxidation\ products$$

$$Dye + e^- \rightarrow reduction\ products$$

The resulting hydroxyl radical, being a very strong oxidizing agent (standard reduction potential +2.8 V) can oxidize most of azo dyes to the mineral end products.

1.5.3 Modified TiO_2

The optical response of a material is largely defined by the electronic structure. The electronic structure is closely related to the material's chemical composition, structure of atomic arrangement and physical dimensions. The chemical composition of TiO_2 can be altered by doping by which the titanium and/or oxygen component is replaced. Doping alters the material's optical properties, but sometimes at the cost of undesirable consequences. It is favourable to maintain the crystal structure of the host material to produce desirable changes in the electronic structure that are beneficial to photocatalytic properties. It appears

easier to substitute the Ti (IV) cation in TiO_2 with other transition metals, and it is more difficult to replace the O^{2-} anion with other anions due to differences in charge states and ionic radii.[50]

TiO_2 doped with cations such as rare earth metals, noble metals, transition and post-transition metals have been widely investigated.[51] The metallic ion doping improves the light absorption range, increases the reduction potential of photogenerated radicals, and enhances the quantum efficiency by inhibiting the recombination of photogenerated electron-hole pairs.[52] For example, doping with rare earth elements having incompletely occupied 4f and empty 5d orbitals, could promote catalysis[53]; noble metal nanoparticle surfaces serve as visible light absorbing sensitizers and improves electron-hole pair charge separation[54]; charge-transfer transition between the d electrons of the transition metals and the conduction or the valence band of TiO_2 shifts the light absorption region from UV to visible light[55]. However, the width of the SCL, photo-corrosion, and surface chemical properties are altered through metal cation doping which may negatively impact overall photocatalytic activity.[56] Although many researches demonstrated improved visible light absorption of TiO_2 using metal ion dopants,[57] it should be mentioned that the increase in visible light absorption alone is not sufficient to improve the overall photocatalytic activity of doped TiO_2. Defects are introduced through doping which acts as recombination centres that ultimately decrease the photocatalytic activity. Doping TiO_2 with cations having higher or lower oxidation state increases electrical conductivity. For example doping with Fe^{3+}[58] and Nb^{5+}[59], electron-neutrality is achieved by adding holes into the valence band (p-type doping) and injecting

electrons into the conduction band (n-type doping) respectively, which increases the charge carrier concentration that leads to an increase in electrical conductivity.

TiO_2 doped with non-metal anions such as carbon[60–64], nitrogen[65–70], and sulphur[71,72] have received much attention. Compared to cation doping, anion doping minimizes the effects of charge carrier recombination. Non-metal anion doping of TiO_2 can narrow the band gap and shift the optical response to the visible light region. For example, carbon doping introduces new states (C 2p) close to the valence band edge of TiO_2 (O 2p)[73]; N 2p level could mix with O 2p which results in the narrowing of the band gap[65], and the S 3p band is above the valence band edge which also reduces the band gap[74]. Despite the advantages of non-metal anion doping, researchers have found that the content of dopant would decrease during the annealing process.[51] This drawback limits the doping level of non-metal anions, thus limiting the photoactivity under visible radiation.

1.6 Electrical double-layer capacitor

1.6.1 EDL Interface

The main energy storage mechanism in electrical double-layer capacitor (EDLC), also known as supercapacitors, arises from the reversible electrostatic accumulation of ions on the surface of porous carbon which was patented by Becker[75] in 1957. The Helmholtz model (section 1.3.1) describes the charge separation at the electrode-electrolyte interface under polarization. Under such condition, ions of opposite sign diffuse through the electrolyte to form a thin layer parallel to the electrode surface ensuring charge neutrality. This

accumulation of charges is called electrical double layer (EDL). The simplified Helmholtz double-layer capacitance C_H defined by:

$$C_H = \varepsilon_0 \varepsilon_r \frac{A}{d}$$

Where ε_0 is the vacuum permittivity, ε_r the relative permittivity of the dielectric electrolyte, A is the electrode surface area, and d is the effective thickness of the EDL (often approximated as the Debye length). Considering the very large surface of porous carbon (~1000 m^2/g) and a Debye length in the range of ~1 nm, the resulting Helmholtz capacitance is unrealistically higher than actual values. This is due to the Helmholtz model does not consider several factors such as the diffusion of ions and interactions between the dipole moment of solvents and electrode. Later this is addressed by Stern[29], combining the Helmholtz layer with the diffuse layer. These two layers are equivalent to two capacitors in series:

$$\frac{1}{C_{EDL}} = \frac{1}{C_H} + \frac{1}{C_D}$$

Where C_{EDL} is the total EDL capacitance, C_H and C_D are capacitance due to Helmholtz layer and diffuse layer respectively.

1.6.2 EDLC electrodes

An EDLC usually consists of two porous carbon electrodes in direct contact with the current collector and separated by a porous film immersed in an electrolyte solution. When a bias potential is applied between the electrodes, the negatively polarized electrode-electrolyte interface is electrically balanced by electrons/cations while the positively polarized

electrode-electrolyte interface is electrically balanced by holes/anions. Thus, a supercapacitor consisting of two electrodes is equivalent to two capacitors in series and the resulting capacitance C (in F) can then be expressed as:

$$\frac{1}{C} = \frac{1}{C_+} + \frac{1}{C_-}$$

Where C_+ and C_- are the capacitance (in F) of the positive electrode and negative electrode respectively. The maximum energy E stored in a supercapacitor is given by:

$$E = \frac{1}{2} C U^2$$

Where C is the specific capacitance in F, U is the maximum operating voltage in V. The maximum power P (in W) of a supercapacitor is given by:

$$P = \frac{U^2}{4ESR}$$

Where U is the maximum operating voltage in V, ESR is the equivalent series resistance (in Ω) of the system. The ESR corresponds to the sum of the resistances related to the ionic resistance of the electrolyte, the electronic resistance of electrodes, and interface resistances between electrodes and external circuit.

Electrolytes used in supercapacitors are aqueous, organic, or ionic liquids. The two main criteria for selection of an electrolyte are the electrochemical stability window and the ionic conductivity. A larger stability window of an electrolyte would mean higher maximum operating voltage thus increasing energy storage capability, and ionic conductivity has a major influence on maximum power by changing the capacitor ESR.

1.6.3 Carbon-based EDLC electrodes

The key in achieving high capacitance on EDLC is high material conductivity and high specific surface area (SSA). Carbon being one of the most abundantly available materials, happens to suit the needs of an EDLC material.[76] Activated porous carbon[77], templated carbon[78], and carbon nanostructures[79] have been intensely researched in recent years.

Activated carbons (ACs) are the most widely used materials today, due to high SSA and moderate cost.[80] ACs are generally produced from activation of various types of carbonaceous materials such as wood, coal, paper etc. Physical activation process such as high temperature oxidation of carbon precursors. Chemical activation is usually carried out at lower temperatures with activating agents like phosphoric acid and potassium hydroxide. Depending on the activation methods as well as the carbon precursors used, ACs could achieve surface areas as high as 3200 m^2g^{-1}.[81] However, as Endo and co-workers pointed out[82], there is a significant discrepancy between the capacitance and SSA of the ACs. Therefore, besides SSA, other aspects such as pore size distribution, pore dimension and surface functionality have a major influence on electrochemical performance of EDLC. The studies by the Beguin and co-workers concluded that the optimal pore size for EDL capacitance is 0.7 nm in aqueous media and 0.8 nm in organic electrolytes.[83] Recent studies by Largeot and co-workers have demonstrated ion size and pore size dependency in EDLC and concluded that the maximum EDL capacitance is achieved when the pore size matches with the ion size.[84] Apart from SSA, the surface functionalities also play important roles on capacitive performance, as they will affect the wettability of the carbon surface.[85]

Templating methods offer an effective way to produce nanostructured carbons with controlled pore size distributions and structures. There has been remarkable progress in the synthesis of ordered nanostructured carbons through templating techniques.[86] In general, the production of templated carbons consists of the deposition of a carbon precursor into the pores of the template, followed by a carbonization treatment and finally the removal of the template leaving behind a well-defined carbon structure. Various carbon structures with well-controlled pore sizes produced from different types of template and carbon precursors have been studied for supercapacitor applications.[87] Compared to ACs, which are made of disordered pore structures and broad pore-size distribution, templated carbons with a narrow pore size distribution and well-defined pore dimensions are superior for applications in high energy density EDLCs. However, the high cost of producing templated carbon nanostructures is limited to the commercial value significantly. Development of a simple, economical and environmentally friendly template method would be advantageous for future applications.

The discovery of CNTs has significantly advanced the research in carbon materials. CNTs can be categorized as single-walled carbon nanotubes (SWNTs) or multi-walled carbon nanotubes (MWNTs), both of which have been widely explored as energy storage electrode materials.[88] Having well defined physical dimension, unique pore structure, superior electrical properties and good mechanical stability, CNTs have attracted much attention for EDLC electrode applications.[89] However, compared to ACs, CNTs have relatively smaller specific surface area, which limits the maximum achievable energy density. Moreover,

retaining the intrinsic properties of individual CNTs on a macroscopic scale is very difficult.[90] Despite having excellent properties, the difficulty in purification and high cost of production still hinders practical applications of CNTs.

The ultimate carbon thin film system, of course, is mono-layer graphene. There has been tremendous excitement stimulated by the promising properties of graphene such as high surface area and high electron mobility. The first graphene EDLC electrode was reported several years ago.[91] However, using chemically modified graphene, a specific capacitance of 135 F/g in 5.5 M KOH and 99 F/g in 1 M TEA-BF 4 /AN was achieved which is not an improvement over ACs. This may be a result of not exploiting the in-plane electron mobility of graphene. A recent study by Feng and co-workers[92] showed that a calculated theoretical capacitance of 550 F/g is achieved using graphene-based in-plane micro-supercapacitors.

1.7 Thesis outline

This thesis aims to utilize the unique properties of liquid-solid interfaces for AOPs, PECs and EDLCs applications, and investigate the relevant underlying mechanism. This chapter covers some of the background information related to solid-liquid interfaces.

Chapter 2 introduces the relevant experimental techniques used in sample growth and characterisations. The basic concepts and methodologies involved in the characterisation process are explained.

In Chapter 3, a novel one-pot solvothermal evaporation process is introduced to grow N-doped TiO_2 nano-powder. The effects of annealing temperature and precursor concentration on

nitrogen doping level were investigated. The photocatalytic activity of as grown N-doped TiO_2 nano-powder were characterised using photo-degradation of methylene blue (MB) solution. An interesting hypsochromic shift in MB absorption spectra was observed which is analysed using an improved peak deconvolution technique.

In Chapter 4, Sn-doping is investigated to improve the PEC water splitting performance of anatase TiO_2 thin films. The effects of Sn-doping level on PEC enhancement were investigated using electrochemical method. More importantly, a comprehensive review on band structures at semiconductor-electrolyte interface under illumination was carried out to re-evaluate the interpretation of current-voltage data.

In Chapter 5, Sn-doping is investigated to improve the PEC water splitting performance of rutile TiO_2 thin films. The effects of Sn-doping level on PEC enhancement were investigated using electrochemical method. Additionally, PEC performance difference between Sn-doped rutile and anatase TiO_2 thin films were compared.

In Chapter 6, carbonised rice husks (cRHs) was investigated as a potential material for EDLC applications. The specific capacitance of cRHs was further enhanced with Mn and Co modification using carbonised metal-organic frameworks (MOFs).

In Chapter 7, summary, findings, and recommendations for future research are provided.

Reference

1. Strite, S. GaN, AlN, and InN: A review. J. Vac. Sci. Technol. B Microelectron. Nanom. Struct. 10, 1237 (1992).

2. Aberle, A. G. Surface passivation of crystalline silicon solar cells: a review. Prog. Photovoltaics Res. Appl. 8, 473–487 (2000).

3. Smith, D. A., Holmberg, V. C. & Korgel, B. A. Flexible germanium nanowires: Ideal strength, room temperature plasticity, and bendable semiconductor fabric. ACS Nano 4, 2356–2362 (2010).

4. Ni, M., Leung, M. K. H., Leung, D. Y. C. & Sumathy, K. A review and recent developments in photocatalytic water-splitting using TiO 2 for hydrogen production. Renewable and Sustainable Energy Reviews 11, 401–425 (2007).

5. Bueno, P. R., Varela, J. A. & Longo, E. SnO2, ZnO and related polycrystalline compound semiconductors: An overview and review on the voltage-dependent resistance (non-ohmic) feature. Journal of the European Ceramic Society 28, 505–529 (2008).

6. Xie, R. J. & Hirosaki, N. Silicon-based oxynitride and nitride phosphors for white LEDs-A review. Science and Technology of Advanced Materials 8, 588–600 (2007).

7. Green, M. A. et al. Solar cell efficiency tables (version 49). Prog. Photovoltaics Res. Appl. 25, 3–13 (2017).

8. Fortunato, E., Barquinha, P. & Martins, R. Oxide semiconductor thin-film transistors: A review of recent advances. Advanced Materials 24, 2945–2986 (2012).

9. Patil, S. J. et al. Semiconductor metal oxide compounds based gas sensors: A literature review. Frontiers of Materials Science 9, 14–37 (2015).

10. Chetvorno. Solid State Electronic Band Structure. Wikipedia (2017).

11. Vásquez, G. C. et al. Oxygen vacancy related distortions in rutile Ti O2 nanoparticles: A combined experimental and theoretical study. Phys. Rev. B (2016). doi:10.1103/PhysRevB.94.235209

12. Sorantin, P. I. & Schwarz, K. Chemical Bonding in Rutile-Type Compounds. Inorg. Chem. 31, 567–576 (1992).

13. Nanite. Band filling diagram. Wikipedia (2013).

14. Allen J. Bard, L. R. F. Electrochemical Methods: Fundamentals and Applications, 2nd Edition. John Wiley & Sons, 2000 (2001).

15. Madelung, O. (Otfried). Introduction to solid-state theory. (Springer-Verlag, 1978).

16. Ashcroft, N. W. & Mermin, N. D. Solid state physics. (Brooks/Cole Cengage Learning, 2003).

17. Stock, J. T. (John T. et al. Electrochemistry, past and present. (American Chemical Society, 1989).

18. Trasatti, S. The concept of absolute electrode potential an attempt at a calculation. J. Electroanal. Chem. Interfacial Electrochem. 52, 313–329 (1974).

19. Tti, S. T. The absolute electrode potential: an explanatory note (Recommendations 1986). J. Electroanal. Chem. 209, 417–428 (1986).

20. Reiss, H. The Fermi Level and the Redox Potential. J. Phys. Chem 89, 3783–3791 (1985).

21. Bockris, J. O. M. & Khan, S. U. M. Fermi levels in solution. Appl. Phys. Lett. 42, 124–125 (1983).

22. O', J., Bockris, M. & Khan, S. U. M. Comment on "Fermi levels in electrolytes and the absolute scale of redox potentials" (1984).

23. Khan, S. U. M., Kainthla, R. C. & Bockris, M. The Redox Potential and the Fermi Level in Solution. J. Phys. Chem 91, 5974–5977 (1987).

24. standard hydrogen electrode. in IUPAC Compendium of Chemical Terminology (IUPAC). doi:10.1351/goldbook.S05917

25. Tem5psu. PourbaixWater.png. Wikipedia (2017).

26. Gibbs energy (function), G. IUPAC Compend. Chem. Terminol. 957, 2629 (2014).

27. Matijević, E. Principles of colloid and surface chemistry. J. Colloid Interface Sci. 70, 399 (1979).

28. Sant, S. B. Physics and Chemistry of Interfaces. Mater. Manuf. Process. 28, 1379–1380 (2013).

29. Otto, S. Zur Theorie der Elektrolytischen Doppelschicht. Zeitschrift für Elektrochemie und Angew. Phys. Chemie 30, 508–516 (2014).

30. Grahame, D. C. The electrical double layer and the theory of electrocapillarity. Chem. Rev. 41, 441–501 (1947).

31. Zhang, L. L. & Zhao, X. S. Carbon-based materials as supercapacitor electrodes. Chemical Society Reviews 38, 2520–2531 (2009).

32. contact potential difference (Volta potential difference). in IUPAC Compendium of Chemical Terminology (IUPAC, 2008). doi:10.1351/goldbook.c01293

33. Hyde, F. J. The Physics of Semiconductors. Electron. Power 13, 176 (2010).

34. Fujishima, a & Honda, K. Electrochemical photolysis of water at a semiconductor electrode. Nature 238, 37–38 (1972).

35. Krol, R. & Gratzel, M. Photoelectrochemical Hydrogen Production. Hydrogen Energy System 102, (Springer US, 2012).

36. Mavroides, J. G., Kafalas, J. A. & Kolesar, D. F. Photoelectrolysis of water in cells with SrTiO3 anodes. Appl. Phys. Lett. 28, 241–243 (1976).

37. Ma, Q. B., Kaiser, B. & Jaegermann, W. Novel photoelectrochemical behaviors of p-SiC films on Si for solar water splitting. J. Power Sources 253, 41–47 (2014).

38. Khaselev, O. & Turner, J. A. A monolithic photovoltaic-photoelectrochemical device for hydrogen production via water splitting. Science (80-.). 280, 425–427 (1998).

39. Nozik, A. J. P-n photoelectrolysis cells. Appl. Phys. Lett. 29, 150–153 (1976).

40. Miller, E. L., Rocheleau, R. E. & Deng, X. M. Design considerations for a hybrid amorphous silicon/photoelectrochemical multijunction cell for hydrogen production. Int. J. Hydrogen Energy 28, 615–623 (2003).

41. Braun, J. H., Baidins, A. & Marganski, R. E. TiO2 pigment technology: a review. Prog. Org. Coatings 20, 105–138 (1992).

42. Bunhu, T., Kindness, A. & Martincigh, B. S. Determination of titanium dioxide in commercial sunscreens by inductively coupled plasma-optical emission spectrometry. South African J. Chem. 64, 139–143 (2011).

43. Pfaff, G. & Reynders, P. Angle-Dependent Optical Effects Deriving from Submicron Structures of Films and Pigments. Chem. Rev. 99, 1963–1982 (2002).

44. Daghrir, R., Drogui, P. & Robert, D. Modified TiO2 for environmental photocatalytic applications: A review. Industrial and Engineering Chemistry Research 52, 3581–3599 (2013).

45. Chong, M. N., Jin, B., Chow, C. W. K. & Saint, C. Recent developments in photocatalytic water treatment technology: A review. Water Research 44, 2997–3027 (2010).

46. Grätzel, M. Conversion of sunlight to electric power by nanocrystalline dye-sensitized solar cells. J. Photochem. Photobiol. A Chem. 164, 3–14 (2004).

47. Chen, X., Liu, L., Yu, P. Y. & Mao, S. S. Increasing solar absorption for photocatalysis with black hydrogenated titanium dioxide nanocrystals. Science (80-.). 331, 746–750 (2011).

48. Byrne, C., Subramanian, G. & Pillai, S. C. Recent advances in photocatalysis for environmental applications. J. Environ. Chem. Eng. 6, 3531–3555 (2018).

49. Konstantinou, I. K. & Albanis, T. A. TiO2-assisted photocatalytic degradation of azo dyes in aqueous solution: Kinetic and mechanistic investigations: A review. Appl. Catal. B Environ. 49, 1–14 (2004).

50. Chen, X. & Mao, S. S. Titanium dioxide nanomaterials: Synthesis, properties, modifications and applications. Chemical Reviews 107, 2891–2959 (2007).

51. Teh, C. M. & Mohamed, A. R. Roles of titanium dioxide and ion-doped titanium dioxide on photocatalytic degradation of organic pollutants (phenolic compounds and dyes) in aqueous solutions: A review. J. Alloys Compd. 509, 1648–1660 (2011).

52. Carp, O., Huisman, C. L. & Reller, A. Photoinduced reactivity of titanium dioxide. Progress in Solid State Chemistry 32, 33–177 (2004).

53. Štengl, V., Bakardjieva, S. & Murafa, N. Preparation and photocatalytic activity of rare earth doped TiO2 nanoparticles. Mater. Chem. Phys. 114, 217–226 (2009).

54. Yoon, J. W., Sasaki, T. & Koshizaki, N. Dispersion of nanosized noble metals in TiO2 matrix and their photoelectrode properties. Thin Solid Films 483, 276–282 (2005).

55. Kment, S. et al. Notes on the photo-induced characteristics of transition metal-doped and undoped titanium dioxide thin films. J. Colloid Interface Sci. 348, 198–205 (2010).

56. Karakitsou, K. E. & Verykios, X. E. Effects of altervalent cation doping of titania on its performance as a photocatalyst for water cleavage. J. Phys. Chem. 97, 1184–1189 (2005).

57. Diebold, U. The Surface Science of Titanium Dioxide. Appl. Surf. Sci. 48, 53–229 (2003).

58. Bally, A. R., Korobeinikova, E. N., Schmid, P. E., Lévy, F. & Bussy, F. Structural and electrical properties of Fe-doped TiO2 thin films. J. Phys. D. Appl. Phys. 31, 1149–1154 (1998).

59. Furubayashi, Y. et al. A transparent metal: Nb-doped anatase TiO2. Appl. Phys. Lett. 86, 1–3 (2005).

60. Park, J. H., Kim, S. & Bard, A. J. Novel carbon-doped TiO 2 nanotube arrays with high aspect ratios for efficient solar water splitting. Nano Lett. 6, 24–28 (2006).

61. Sakthivel, S. & Kisch, H. Daylight Photocatalysis by Carbon-Modified Titanium Dioxide. Angew. Chemie - Int. Ed. 42, 4908–4911 (2003).

62. Di Valentin, C., Pacchioni, G. & Selloni, A. Theory of carbon doping of titanium dioxide. Chem. Mater. 17, 6656–6665 (2005).

63. Khan, S. U. M., Al-Shahry, M. & Ingler, W. B. Efficient photochemical water splitting by a chemically modified n-TiO2. Science (80-.). 297, 2243–2245 (2002).

64. Choi, Y., Umebayashi, T. & Yoshikawa, M. Fabrication and characterization of C-doped anatase TiO2 photocatalysts. J. Mater. Sci. 39, 1837–1839 (2004).

65. Asahi, R., Morikawa, T., Ohwaki, T. & Taga, Y. Visible-Light Photocatalysis in Nitrogen-Doped Titanium Oxides. Science (80-.). 293, 269–271 (2001).

66. Oropeza, F. E., Harmer, J., Egdell, R. G. & Palgrave, R. G. A critical evaluation of the mode of incorporation of nitrogen in doped anatase photocatalysts. Phys. Chem. Chem. Phys. 12, 960–9 (2010).

67. Breault, T. & Bartlett, B. Composition Dependence of \cf{TiO2}:(Nb, N)-x Compounds on the Rate of Photocatalytic Methylene Blue Dye Degradation. J. Phys. Chem. C 117, 8611–8618 (2013).

68. Breault, T. M. & Bartlett, B. M. Lowering the band gap of anatase-structured TiO 2 by coalloying with Nb and N: Electronic structure and photocatalytic degradation of methylene blue dye. J. Phys. Chem. C 116, 5986–5994 (2012).

69. Jagadale, T. C. et al. N-doped TiO2 nanoparticle based visible light photocatalyst by modified peroxide sol-gel method. J. Phys. Chem. C 112, 14595–14602 (2008).

70. Li, F. T. et al. N-doped P25 TiO2-amorphous Al2O3 composites: One-step solution combustion preparation and enhanced visible-light photocatalytic activity. J. Hazard. Mater. 239–240, 118–127 (2012).

71. ZHOU, Z. Mechanochemical preparation of sulfur-doped nanosized TiO2 and its photocatalytic activity under visible light. Chinese Sci. Bull. 50, 2691 (2006).

72. Ohno, T., Mitsui, T. & Matsumura, M. Photocatalytic Activity of S-doped TiO 2 Photocatalyst under Visible Light. Chem. Lett. 32, 364–365 (2003).

73. Wong, M. S., Hsu, S. W., Rao, K. K. & Kumar, C. P. Influence of crystallinity and carbon content on visible light photocatalysis of carbon doped titania thin films. J. Mol. Catal. A Chem. 279, 20–26 (2008).

74. Rehman, S., Ullah, R., Butt, A. M. & Gohar, N. D. Strategies of making TiO 2 and ZnO visible light active. Journal of Hazardous Materials 170, 560–569 (2009).

75. Becker, H. I. Low voltage electrolytic capacitor. (1957).

76. Rufford, T. E., Hulicova-Jurcakova, D., Zhu, Z. & Lu, G. Q. Nanoporous carbon electrode from waste coffee beans for high performance supercapacitors. Electrochem. commun. 10, 1594–1597 (2008).

77. Morishita, T., Soneda, Y., Tsumura, T. & Inagaki, M. Preparation of porous carbons from thermoplastic precursors and their performance for electric double layer capacitors. Carbon N. Y. 44, 2360–2367 (2006).

78. Ania, C. O., Khomenko, V., Raymundo-Piñero, E., Parra, J. B. & Béguin, F. The large electrochemical capacitance of microporous doped carbon obtained by using a zeolite template. Adv. Funct. Mater. 17, 1828–1836 (2007).

79. Jurewicz, K., Babeł, K., Pietrzak, R., Delpeux, S. & Wachowska, H. Capacitance properties of multi-walled carbon nanotubes modified by activation and ammoxidation. Carbon N. Y. 44, 2368–2375 (2006).

80. Qu, D. & Shi, H. Studies of the activated carbons used in double-layer supercapacitors. J. Power Sources 74, 99–107 (1998).

81. Kierzek, K., Frackowiak, E., Lota, G., Gryglewicz, G. & Machnikowski, J. Electrochemical capacitors based on highly porous carbons prepared by KOH activation. Electrochim. Acta 49, 515–523 (2004).

82. Endo, M. et al. Capacitance and Pore-Size Distribution in Aqueous and Nonaqueous Electrolytes Using Various Activated Carbon Electrodes. J. Electrochem. Soc. 148, A910 (2002).

83. Raymundo-Piñero, E., Kierzek, K., Machnikowski, J. & Béguin, F. Relationship between the nanoporous texture of activated carbons and their capacitance properties in different electrolytes. Carbon N. Y. 44, 2498–2507 (2006).

84. Largeot, C. et al. Relation between the ion size and pore size for an electric double-layer capacitor. J. Am. Chem. Soc. 130, 2730–2731 (2008).

85. Hulicova-Jurcakova, D. et al. Effect of surface phosphorus functionalities of activated carbons containing oxygen and nitrogen on electrochemical capacitance. Carbon N. Y. 47, 1576–1584 (2009).

86. Zhao, X. S. et al. Templating methods for preparation of porous structures. in Journal of Materials Chemistry 16, 637–648 (2006).

87. Fuertes, A. B., Lota, G., Centeno, T. A. & Frackowiak, E. Templated mesoporous carbons for supercapacitor application. Electrochim. Acta 50, 2799–2805 (2005).

88. Béguin, F., Presser, V., Balducci, A. & Frackowiak, E. Carbons and electrolytes for advanced supercapacitors. Adv. Mater. 26, 2219–2251 (2014).

89. Zhang, H. et al. Growth of manganese oxide nanoflowers on vertically-aligned carbon nanotube arrays for high-rate electrochemical capacitive energy storage. Nano Lett. 8, 2664–2668 (2008).

90. Futaba, D. N. et al. Shape-engineerable and highly densely packed single-walled carbon nanotubes and their application as super-capacitor electrodes. Nat. Mater. 5, 987–994 (2006).

91. Stoller, M. D., Park, S., Yanwu, Z., An, J. & Ruoff, R. S. Graphene-Based ultracapacitors. Nano Lett. 8, 3498–3502 (2008).

92. Wu, Z. S., Parvez, K., Feng, X. & Müllen, K. Graphene-based in-plane micro-supercapacitors with high power and energy densities. Nat. Commun. 4, (2013).

Chapter 2 Experimental Techniques

2.1 Introduction

This chapter gives a brief overview of the experimental techniques used in sample growth and preparation as well as giving some background information on the analytical methods used for characterisation.

Electrochemistry is employed to characterise the electrochemical properties of electrode materials that are used in photoelectrochemical cells (PEC) and electrical double layer capacitor (EDLC) application. Particular interest will be on cyclic voltammetry (CV) and electrochemical impedance spectroscopy (EIS).

The morphological characterisations were conducted using scanning electron microscopy (SEM). Chemical, structural and elemental analysis was examined via techniques including but not limited to X-ray diffraction (XRD) and X-ray photoelectron spectroscopy (XPS).

Photocatalytic properties of N-doped TiO_2 was investigated with photodegradation of methylene blue (MB) solution. The MB degradation setup and background knowledge on MB peak deconvolution are presented. Based on these knowledge, a novel MB peak deconvolution technique was developed which is applied in Chapter 3.

2.2 Material synthesis

2.2.1 Dip-coating

The sol-gel dip-coating method[1] was used to grow a thin film sample on a substrate, this process requires a metal alkoxide precursor solution. For TiO_2 based material, Titanium (IV)

isopropoxide was used with 2-propanol to achieve a suitable solution. As for Sn dopant, Tin (IV) tert-butoxide is a suitable choice. Both Titanium (IV) isopropoxide and Tin (IV) tert-butoxide are easily hydrolysed in air, a glove box is required to handle the preparation of sol-gel solution. Nitric acid was added to prevent hydrolysis of the precursor. Sonication was used to improve homogeneity of sol-gel solution. The concentrations of precursor solutions are outlined in the relevant chapters individually.

In this study, the 5% Nb-doped $SrTiO_3$ (001) single crystalline substrate was provided by PI-KEM, cut to 10*10*1 mm with single side epitaxial polished surface. FTO glass was provided by Visiontek Systems (TCO-VIS 15, CNC cut to 20*20*2.2 mm, <15 Ω/sq), cut in half to 10*20*2.2cm using a Bohle carbide cutter.

For pristine surfaces such as $SrTiO_3$, nitrogen flow was used to rid the surface of dust. The FTO glass substrate was covered in oil and dirt due to CNC processes, a more extensive surface cleaning is therefore required. First, a sonication bath using Fairy washing-up liquid solution for 5 min removes the majority of contaminants; followed by a sonication bath using DI water for 5 min to remove residual Fairy surfactants. Then, a sonication bath using a mixture of ethanol, 2-propanol, DI water with 1:1:1 volumetric ratio for 5 min; followed by sonication bath with HPLC grade 2-propanol for 5 min. The cleaned substrate was blow-dried using nitrogen flow and attached to the dip coater. Using this cleaning method, watermark or similar reflection can be fully removed, the substrate should show a mirror-like finish when examined against the light.

For a typical dip-coating cycle, the substrate was dipped into the precursor solution and rested for 5 min before slowly pulled out at a speed of 3.5 mm/min. The coated substrate was then hydrolysed with wet nitrogen flow for 5 min before dipped back into the precursor solution.

The coated substrate was placed in a clean alumina boat with the coated side facing up. The boat was transferred into an alumina/quartz tube and sealed off. The sample was annealed at 600- 800°C for up to 10 h in argon gas or air and cooled down to room temperature.

2.2.2 Thermal evaporation

Powder samples were produced by evaporation of aqueous or alcohol solutions. For the aqueous solutions, deionised water was mixed with concentrated HCl to suppress hydrolysis of the precursor. Titanium (IV) tetrachloride with an appropriate amount of dopant precursor chloride was added to the acidic mixture to achieve a suitable solution. For the alcohol solutions, the same precursor was used with 2-propanol as a solvent. The prepared solution was sealed in a round bottom flask and ultrasonicated for 10 min to improve the homogeneity of the sol-gel solution. The concentrations of precursor solutions are outlined in the experimental section of chapter 3.

The evaporation process was carried out using an oil bath with an oil temperature of 125°C. 100 mL beakers with a 1/2-inch magnetic stirring bar were preheated in an oil bath for 15 min to equilibrate before evaporation.

For the aqueous solutions, the evaporation process takes about one hour, and a fine powder was obtained at the end of the evaporation. The product was transferred into an alumina boat annealed 600°C in a muffle furnace for 10 h.

For alkoxide solutions, the evaporation process takes about 30 min to complete. After the rapid evaporation process, the solidified sample was kept roasting using the same oil bath. During the roasting procedure, the sample breaks into coarse grains while releasing a white fume. The product was ground with a pestle and mortar and transferred into an alumina boat annealed at 250 °C to 600 °C in a muffle furnace for 10 h.

2.2.3 Mn/Co bi-metallic MOFs

The MOFs are synthesised by collaborators at Korea institute of energy research (KIER). The synthesis procedure is described as follows. $Mn(CH_3CO_2)_2$ (0.040 g, 0.227 mmol) / $Co(NO_3)_2 \cdot 6H_2O$ (0.066 g, 0.227 mmol) for acetate prepared MOFs (**ACT**) or $MnCl_2$ (0.030 g, 0.227 mmol) / $Co(NO_3)_2 \cdot 6H_2O$ (0.066 g, 0.227 mmol) for chloride prepared MOFs (**Cl**) with H_4DOBDC (0.030 g, 0.15 mmol) were placed in a 20 mL vial and dissolved in a solution mixture of DMF (10 mL), ethanol (0.6 mL) and water (0.6 mL). The solution was heated at 130 °C for 16 h. After reaction, the solution was cooled to room temperature, and the product was collected on filter paper. Finally, the product was washed with DMF and methanol, and then dried under vacuum.

2.3 Electrochemical characterisation

Electrochemistry is the study of chemical processes at interfaces associated with the transfer of electrons. Most commonly this is done at an electrode-electrolyte interface, which accompanies a chemical reduction/oxidation reaction, thus being a 'heterogeneous' process. Here, the basic principles of electrochemistry will be explained and discussed with reference to their utility for understanding electrochemical reactions.

2.3.1 Overview of electrode processes

When a potential is applied, two types of processes occur at the electrode surface: faradaic and non-faradaic processes. In the faradaic process, charges are transferred across the electrode-electrolyte interface. The transfer of electrons causes oxidation or reduction at the electrode surface, and the amount of chemical reactions due to the flow of current is proportional to the amount of electricity passed. According to Faraday's laws of electrolysis[2]:

$$Q = \frac{zFm}{M} = zFN \tag{2.3.1}$$

Where Q is the charge passed through the interface in coulombs, C, z is the number of electrons transferred in the electrochemical redox reaction, F is the Faraday constant 96485 C/mol, m is the mass of species participating redox reaction in unit g, M is the molar mass of substance in unit g/mol and N is the number of moles of the species participating redox reaction. Thus, the current of electrochemical reaction:

$$I = \frac{dQ}{dt} = \frac{d(zFN)}{dt} = zF\frac{dN}{dt} \tag{2.3.2}$$

where I is the current in unit A, Q is the charge passed through the interface in unit C, t is the time in unit s, z is the number of electrons transferred involved in the oxidation or reduction of the chemical species, F is the Faraday constant in C/mol and N is the number of mols of the species participating redox reaction.

At equilibrium, where no net current flows, the potential established at the electrode is described by the Nernst equation[3]. For example, for a general charge transfer reaction:

$$Ox + ze^{-} \rightarrow Red \tag{2.3.3}$$

the potential is

$$E = E^{0} - \frac{RT}{zF} lnQ = E^{0} - \frac{RT}{zF} ln\left(\frac{a_{Red}}{a_{Ox}}\right) \tag{2.3.4}$$

Where a_{Red} and a_{Ox} are activities of species Red and Ox respectively, which can be regarded as concentrations in ideal conditions. (Chapter 1, section 1.2)

The electrochemical cells with Faradaic process can be classified as either galvanic or electrolytic. In galvanic cells the reactions occur spontaneously at the electrode-electrolyte interface when a load is connected via an external circuit. Typical galvanic cells include the commonly used rechargeable/single-use batteries (lithium, alkaline, lead batteries) and fuel cells in discharge. In electrolytic cells, the reactions are driven by external potential such as a battery during charging, electrometallurgy production of aluminium, industrial chlorine production and anodising; in this process the reaction is non-spontaneous. (Chapter 1, section 1.2.5) This thesis focus is on electrolytic cells. In electrochemical cells the cathode is defined as the electrode where reduction occurs, and the anode is defined as the electrode

where oxidation occurs. In an electrolytic cell, the cathode is negative with respect to the anode, but the opposite is true in a galvanic cell.

Electrodes at which charge transfer can occur freely at the electrode-electrolyte interface at an applied voltage is called an idealised non-polarizable electrode. On an idealised non-polarizable electrode, the electrode-electrolyte interface is generally modelled as an electrical double layer (EDL, see section 1.3.1). When the applied potential is more negative than reduction potential in the electrolyte ($\Delta\phi$), reduction of oxidized species (Ox) to reduced species (Red) occurs, and the concentration of O near the electrode surface decreases. Assuming a one-electron transfer process, the cathodic (forward reaction) current can be expressed as:

$$i_f = AFk_f[Ox] \tag{2.3.5}$$

Where k_f is the rate constant of the reduction (forward) reaction, A is the electrode reaction area, F is the Faraday constant, and $[Ox]$ is the concentration of oxidized species at the electrode surface. Conversely if anodic (backward) reaction occurs:

$$i_b = -AFk_b[Red] \tag{2.3.6}$$

Where k_b is the rate constant of oxidation (backward) reaction, A is the electrode reaction area, F is the Faraday constant, and $[Red]$ is the concentration of reduced species at the electrode surface. The net current of the redox reaction is, therefore:

$$i = AF(k_f[Ox] - k_b[Red]) \tag{2.3.7}$$

In transition state theory, it is assumed that rate constants k_f and k_b have an Arrhenius form[4] that can be expressed as:

$$k_f = \mathcal{A}_f exp(-\frac{\Delta G_{red}^{\neq}}{RT}) \tag{2.3.8}$$

$$k_b = \mathcal{A}_b exp(-\frac{\Delta G_{ox}^{\neq}}{RT}) \tag{2.3.9}$$

Where $\Delta G^{\neq}$ is the activation Gibbs free energy, and $\mathcal{A}_f$ and $\mathcal{A}_b$ are frequency factors with the same dimensions as rate constant k in unit cm/s. The electrode kinetics can be described by the Butler-Volmer model. An overpotential $\eta = E - E^0$ is used to drive the free energy of a reactant over an energy barrier, which corresponds to a transition state, to the product. The Gibbs energy of the reactant, transition state and product are influenced by the interfacial potential:

$$\Delta G_{red}^{\neq} = \Delta G_{red}^{\neq}(0) + \alpha F\eta \tag{2.3.10}$$

$$\Delta G_{ox}^{\neq} = \Delta G_{ox}^{\neq}(0) - (1-\alpha)F\eta \tag{2.3.11}$$

where α is called cathodic or anodic transfer coefficient which reflects the sensitivity of the transition state to the drop in potential between the electrode and the solution. Experimentally α is found to be about 0.5 in most cases. These relationships can simplify the rate constant of reduction and oxidation (Eq 2.3.8 and Eq 2.3.9):

$$k_f = \mathcal{A}_f exp(-\frac{\Delta G_{red}^{\neq}(0)}{RT}) exp(\frac{-\alpha F\eta}{RT}) \tag{2.3.12}$$

$$k_b = \mathcal{A}_b exp(-\frac{\Delta G_{ox}^{\neq}(0)}{RT}) exp(\frac{(1-\alpha)F\eta}{RT}) \tag{2.3.13}$$

Now consider the special case in which the interface is at equilibrium which has a solution of $[Red]^* = [Ox]^*$ (bulk concentrations). Under such conditions, $\eta = E - E^0 = 0$ and

$k_f[Red]^* = k_b[Ox]^*$, so that $k_f = k_b$. Thus E^0 is the potential where the forward and reverse rate constants have the same value. That value is called the standard rate constant k^0. The rate constants at other potentials can then be expressed in terms of k^0:

$$k_f = k^0 exp(\frac{-\alpha F\eta}{RT}) \tag{2.3.14}$$

$$k_b = k^0 exp(\frac{(1-\alpha)F\eta}{RT}) \tag{2.3.15}$$

Combining these equations into Eq 2.3.7, the complete current-potential characteristic can be obtained:

$$i = AFk^0\{[Ox]exp\left(\frac{-\alpha F\eta}{RT}\right) - [Red]exp(\frac{(1-\alpha)F\eta}{RT})\} \tag{2.3.16}$$

This is the Butler-Volmer equation[5], which is a fundamental equation for electrode kinetics. i_0 is the standard exchange current density which has two limiting cases. One is when i_0 is large, a small overpotential is required to drive a reaction, essentially a reversible process. By contrast a small value of i_0 results in the necessity of a high overpotential and hence such a process is described as irreversible. The Butler-Volmer equation provides good qualitative prediction. However, this macroscopic model does not permit any other rationalisation of the molecular nature of the electrochemical reactions than a possible indication of the position of the transition state. Therefore, the alternative Marcus theory[6] has been increasingly employed to acquire more physical insights of various electrochemical reactions, particularly for surface-bound redox couples. However, this is beyond the scope of this thesis.

Under some conditions, the interface shows a range of potentials with no charge-transfer reactions occur because such reactions are thermodynamically or kinetically unfavourable. This type of electrode is called the ideal polarizable electrode. Also processes such as adsorption or desorption can occur when the structure of electrode-electrolyte interface can change with varying applied potentials or solution composition. These processes are named non-faradaic processes. This behaviour of the electrode-electrolyte interface is analogous to the main principle governing the charge storing mechanism of dielectric capacitors and EDLC. Charges gradually accumulate at the metallic plates separated by an insulating dielectric layer. This then causes the excess and deficiency of electrons on the two plates, leading to the flow of charging current. The amount of electrical charge stored per unit voltage between the plates is capacitance and can be calculated by:

$$C = \frac{dQ}{dV} \tag{2.3.17}$$

where C is the capacitance in unit F, Q is the charge stored in unit C and V is the potential change it in unit V.

2.3.2 PEC setup and photoelectrode preparation

There were various drawbacks with the previous lamp configuration. Uniformity of the illumination condition was undesirable, and unfixed PEC cell position creates challenges on maintaining optical path consistently. The xenon arc lamp is an old model made in 1983, the temporal stability is questionable. The excessive UV component from xenon arc lamp may lead to inaccurate conclusions.

The new testbench is designed addressing these issues. The setup is based on a Newport LCS-100 solar simulator mounted on a 300*450*12.7 mm solid aluminium optical breadboard (MB3045/M, Thorlabs). A mini lab jack (L200, Thorlabs) is attached to the breadboard to adjust the vertical position of PEC while maintaining the horizontal position. A homemade PTFE holder is firmly screwed onto the mini lab-jack with a slot to hold the PEC in position. Various filters can be placed in front of the PEC to adjust the illumination spectrum. A Ø1" stainless steel diaphragm optical beam shutter (SHB1, Thorlabs) with TTL controller is used to chop the incoming beam. Rubber feet were attached to aluminium breadboard to absorb ambient vibration.

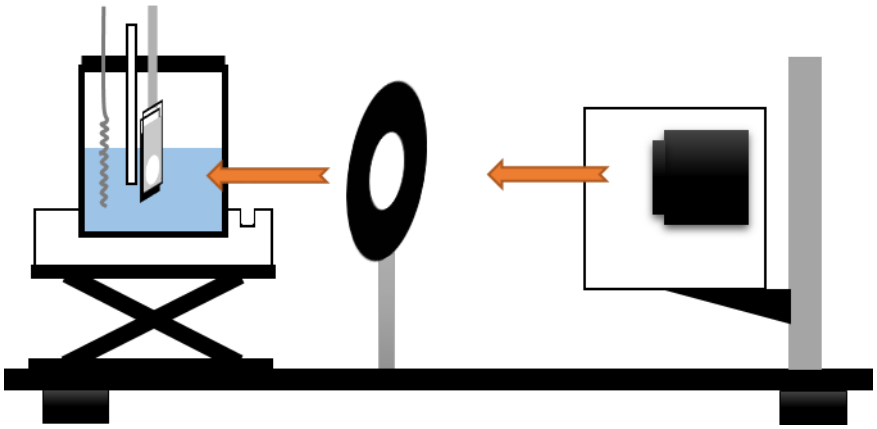


Figure 2.1. Diagram of solar simulator bench setup showing the solar simulator (right), optical beam shutter (middle) and PEC cell mounted on mini lab jack via a PTFE holder (left).

The PEC cell is a homemade Ø30 mm quartz beaker with a PTFE cap. The cap has three openings for the platinum wire counter electrode, 1 M silver chloride reference electrode and the sample clip that fix the sample in the middle of the beaker.

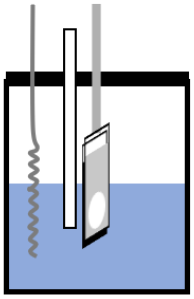


Figure 2.2. Diagram of homemade PEC cell showing the positioning of the platinum wire counter electrode, 1 M silver chloride reference electrode (middle white) and the sample attached to the holder in the middle of the beaker.

For photoelectrochemical cell (PEC) in electrolytic water splitting setup, a three-electrode method was used with the sample substrate as the working electrode, platinum wire as the counter electrode and 1M silver chloride electrode as the reference electrode. The reaction area of all the samples was fixed at 113.1 mm^2. To achieve this, a perforator was used to fabricate disc of Parafilm M with a diameter of 6 mm. The Parafilm M disc was applied to the thin film sample surface for protection. Water-resistant coating (OPI® Top Coat) was used to cover the entire sample (a small area on the top end of the sample was left out for electrical contact). The coating was left to dry for 10 min before removing the Parafilm M with sharp tweezers. Thus, the sample surface of 113.1 mm^2 was exposed while other parts were covered with a water-resistant coating.

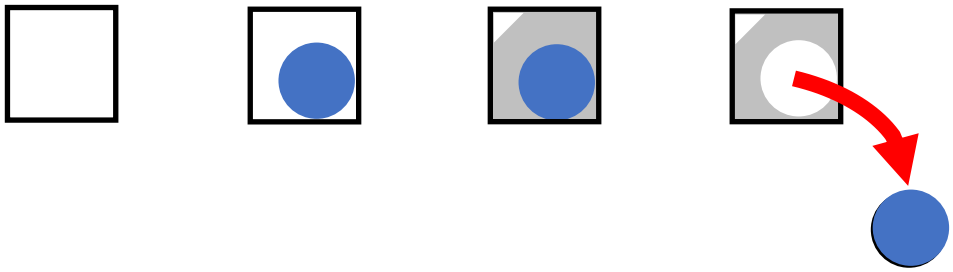


Figure 2.3. A typical procedure for fixing the reaction area. Parafilm M disc (blue) covering the sample surface, apply water-resisting OPI Top Coat (grey) while leaving a corner of the sample intact for electrical contact, and peel-off Parafilm M to expose electrode surface.

2.3.3 EDLC electrode preparation

We devised a simple drop-coating technique to examine the electrochemical properties of powder-form samples conveniently. This approach uses a GC working electrode as a sample holder which is convenient to use. The shortcomings of losing sample material during electrochemical measurement were solved by covering the sample with Nafion® 117 film. Nafion® was discovered in the late 1960s by Walther Grot of DuPont. Nafion has received a considerable amount of attention as a proton conductor for proton exchange membrane (PEM) fuel cells because of its excellent thermal and mechanical stability. The equivalent weight and material thickness are used to describe most commercially available membranes. For example, Nafion® 117 indicates a material with 1100 g equivalent weight and 0.007 inches in thickness.

The drop coating solution is prepared by mixing the appropriate amount of DI water with sample powder to generate a 2 g/L mixture. The mixture was extensively sonicated and

cooled to room temperature. Before each drop coating session, the water/sample mixture was physically agitated using a PV-1 vortex mixer (Grant Instruments). 9 μL of the mixture was extracted with a pipette and drop coated onto the GC electrode which forms a half-spherical droplet within the GC area. The mixture was slowly evaporated at room temperature. Nafion® 117 film was tested as a protective measure. 9 μL of Nafion® 117 solution (Sigma-Aldrich) was drop coated on bare GC electrode and dried in ambient condition.

2.3.4 Electrochemical method

A basic experimental set up for electrochemistry consists of a potentiostat, and three electrodes including a working electrode, a counter electrode and a reference electrode. The potentiostat controls the voltage across the working electrode-counter electrode pair while keeping the potential of the working electrode at a constant level with respect to the reference electrode with a very small current through a high impedance feedback loop. As the current is mainly passed between the working electrode and the counter electrode (platinum wire), and the current between the working electrode and the reference electrode is very weak, this arrangement eliminates the effect of the potential drop in resistive media.

A reference electrode has a stable and known electrode potential by using a redox system with constant concentrations of each participant of the redox reaction. The internationally recognised primary reference electrode is the standard hydrogen electrode (SHE), which has all components at unit activity:

$$Pt/H_2\ (a\ =\ 1)/H^+\ (a\ =\ 1, aqueous)$$

Other reference electrodes which are more convenient for experiments are also developed, such as silver-silver chloride electrode:

$$Ag/AgCl/KCl\ (1\ M\ KCl)$$

with a potential of 0.23 V vs SHE. A more relevant reference scale for PEC is the reversible hydrogen electrode (RHE). The RHE scale is explained in detail with context in Chapter 4.

The kinetics of electrode processes can be studied by voltammetry. The potential is swept linearly with time and the current is recorded as a function of potential. If the potential sweep is reversed and repeated, it is called cyclic voltammetry (CV). CV has become a very popular technique for electrochemistry studies. The current observed from the voltammogram is contributed from both electrochemical reaction and double layer capacitance referring back to the Faradaic (i_F) and non-Faradaic (i_C) currents:

$$i = i_F + i_C = i_F + vC_{EDL} \tag{2.3.18}$$

Where υ is the sweep rate and C_{EDL} is the double layer capacitance. Therefore, the charging current i_C is proportional to scan rate.

In real circuits, there are both resistive and capacitive elements hence it is not viable to just consider the resistance to acquire all the information about a circuit. Impedance measurement has nowadays replaced the measurement of resistance alone. Impedance is a measurement of the ability of a circuit to resist the flow of electrical current without being limited to only the resistance.

In electrochemical impedance spectroscopy (EIS), the frequency response of an electrochemical system to an external voltage perturbation at certain AC frequencies is measured. An expression analogous to Ohm's law can be used to describe impedance as:

$$Z = \frac{V(t)}{I(t)} = Z_{re} + jZ_{im} \tag{2.3.19}$$

where it is presented as the sum of the real (Z_{re}) and imaginary components (jZ_{im}) using real and imaginary complex numbers. The ability of the circuit to resist the flow of electrical current contributes to the real part of the impedance while the imaginary part reflects the capacitive property of the circuit considering any phase difference between current and voltage.

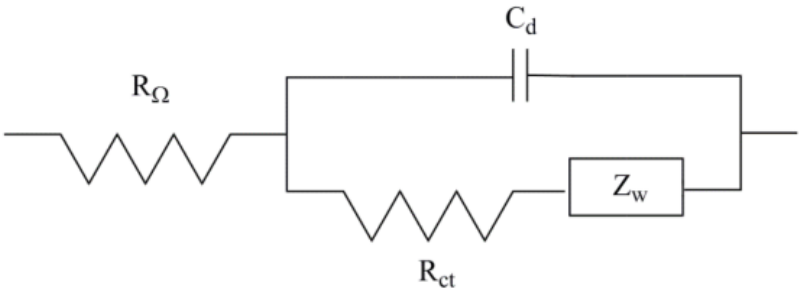


Figure 2.4 Randles circuit, an equivalent circuit of an electrochemical cell.

An equivalent circuit called a 'Randles circuit' can be drawn as shown above in Figure 2.4. This is an equivalent circuit to an electrochemical cell. The Randles circuit consists of series resistance (R_Ω), double layer capacitance (C_d) which models the electrical double layer that is in parallel with a charge transfer resistance (R_{ct}) and Warburg impedance (Z_w) which represents resistance to mass transfer in electrochemical systems. The R_{ct} and Z_w model the resistance to faradaic current while C_d is associated with double layer charging current.

2.4 Physical characterisation

2.4.1 X-ray diffraction

X-ray diffraction (XRD) is a common technique for structure characterisation to identify a specific phase or compound from an unknown sample. X-rays are produced when outer shell electron drops in to fill the vacancy that is created by high energy electrons bombarding on the metal. The X-rays interact with matter and are scattered in different directions which are then collected by a detector to produce a characteristic X-ray pattern. The brighter the radiation the more intense the peaks are on the pattern which is a result of constructive interference. This was explained by W. L. Bragg in 1912 when he found that some X-rays diffract from the atoms at the surface whereas others penetrate through the crystal. The penetrating X-ray travels to the next layer of atoms and diffracts and then travels back the same distance before reaching the surface again; hence this X-ray travels further than that diffracted off the surface. The difference in crystal plane distance, d, depends on the spacing between the two planes and the angle, θ, of incidence. Constructive interference of the two rays requires that they must be in-phase with each other. This principle is shown in Bragg's law:

$$n\lambda = 2dsin\theta \tag{2.4.1}$$

Where θ is the glancing angle, d is the distance between the two planes, and λ is the wavelength of incident X-rays. Reflections with n=1, 2, … are called first order, second order, … reflection respectively. Bragg's equation correctly predicts that a diffracted X-ray

will be observed only at certain angles of incidence. X-rays that do not satisfy Bragg's Law will be partly or completely out of phase (destructive interference) and hence will show faint/broad peaks or be completely absent from the X-ray diffraction pattern respectively. From equation 2.4.1, it can be derived that when the distance between the two planes, d, expands due to lattice stress, the corresponding reflection will shift to lower angles. This effect was used to determine that Sn doping in anatase TiO_2 lead to expansion of lattice structure in Chapter 4 of the thesis.

The mean crystallite size in a crystal in the form of a powder can be calculated using the Scherrer equation:

$$D = \frac{k\lambda}{\beta \cos\theta} \tag{2.4.2}$$

where D is the crystallite size; λ is the wavelength of radiation used; k is a constant that varies with the shape of the crystallite but usually taken as 0.9; β is the peak broadening at half the maximum intensity (FWHM), in radians; and θ is the Bragg angle in radians. The equation is limited to nano-sized particles.

2.4.2 X-ray photoelectron spectroscopy

X-ray Photoelectron Spectroscopy (XPS), is one of the most common methods used for the chemical analysis of surfaces. It was first developed in the mid-1960s by Kai Siegbahn and his research group at the University of Uppsala in Sweden. The advanced development in vacuum and other technologies enabled its commercial production. Siegbahn was awarded the Noble Prize in physics for his contribution to XPS in 1981.

The operation of XPS involves irradiating the sample in ultra-high vacuum with soft monochromatic X-rays and analysing the energy of photoelectrons. Usually, Al Kα (1486.6 eV) or Mg Kα (1253.6 eV) X-rays are used. These photons can penetrate up to 10 μm into the sample and create photoelectrons in this region. Most of the photoelectrons cannot escape the surface due to inelastic scattering and the consequent loss in kinetic energy. Only electrons from the top several layers (1~10 nm) can leave the surface and be detected by XPS, so XPS is very surface sensitive. An XPS spectrum is obtained by plotting the number of electrons per energy interval versus their kinetic energy or the corresponding binding energy. Because each element has a unique binding energy, the XPS spectrum can be used to identify the element and determine the relative concentration of each element. The chemical shift of binding energy also reflects the chemical state of the material.

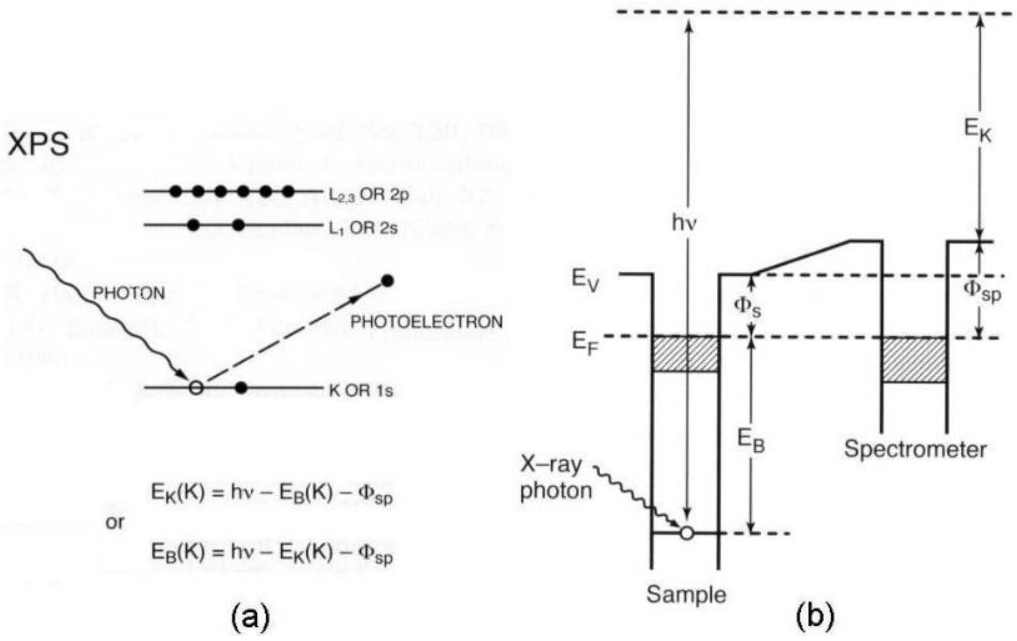


Figure 2.5 (a) The X-ray photoemission emission process for an atom. (b) The energy

levels involved in the XPS process.[7]

The process of photoelectron emission is schematically illustrated in Figure 2.5. When an electron is ejected by a photon, the system energy must be conserved such that:

$$h\nu = E_B + E_K + \phi_{sp} \tag{2.4.3}$$

where $h\nu$ is the energy of incident X-ray, E_B is the binding energy of the atomic orbital from which the electron originates, E_K is the kinetic energy of an electron in the spectrometer, and ϕ_{sp} is the spectrometer work function. As can be seen from the equation, the work function of the material in question is not relevant. Since the work function of the spectrometer is a known constant, the binding energy of the sample material thus can be derived by measuring the kinetic energy of the photoelectron.

Binding energy is a measure of energy required to free electrons from the atomic orbitals to above the Fermi level. It can be regarded as the energy difference between the initial and final states after the photoelectron has left the atom. The photoelectron spectrum will reproduce the electronic structure of an element quite accurately since all electrons with binding energy less than the X-ray photon energy will feature in the spectrum. Those electrons which are excited and freed without energy loss produce the characteristic peaks in the spectrum; those which undergo inelastic scattering and suffer energy loss contribute to the background of the spectrum.

XPS spectrum provides an elemental analysis of material surface since the binding energy of each characteristic peak is associated with an elemental core level. Chemical shift of

elements can be observed in XPS as a small change in the core level binding energy, which is related to the chemical bonds with electronegative atoms. It can be caused by either initial chemical bonding before the photoelectron ejection or post photoemission processes e.g. relaxation of photoionisation, core hole screening, and polarisation of surrounding ions.

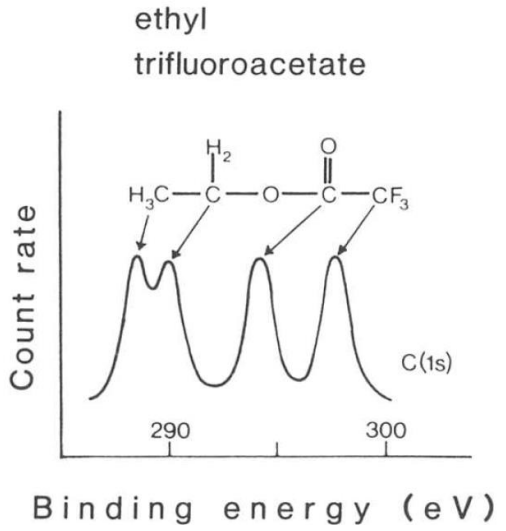


Figure 2.6. Chemical shifts of C 1s electrons for ethyl trifluoroacetate. The different chemical shifts can be roughly attributed to the varied electronegative values.[8]

Figure 2.6 depicts the chemical shifts of the C 1s peak in ethyl trifuoroacetate. There are 4 types of carbon atoms in this molecule structure. The one in the $-CF_3$ group is adjacent to three highly electronegative fluorine atoms which deplete the electron density around the carbon atom. The bonding between the nuclei and 1s electrons is enhanced significantly for this carbon, resulting in the largest shift to higher binding energy. Comparatively, the carbon atom in C=O group, electron density is affected by the two adjacent electronegative oxygen atoms, leading to a second largest chemical shift. Similarly, carbon atoms in CH_2 and CH_3 groups have one and no neighbouring oxygen atoms, leading to a smaller and the smallest chemical shift respectively.

The intensity (I) of a photoelectron peak can be determined by equation:

$$I = J\rho\sigma \mathrm{K}\lambda \tag{2.4.4}$$

Where J is the photon flux, ρ is the concentration of atoms or ions on the surface, σ is the photonionisation cross-section for photoelectron emission, K includes the instrumental factors influencing the measurement, such as transmission function of the spectrometer, the efficiency of the detector, and λ is the electron attenuation length. Quantitative analysis of XPS data can be achieved by determining the peak area (*i.e.* intensity I_i of a given peak after the subtraction of the background). According to equation 2.4.4, the elemental concentration in a given sample will be equal to the peak intensity divided by a set of factors which should be constant from sample to sample. These factors are well known and are tabulated as atomic sensitivity factors (ASF) or relative sensitivity factors (RSF) S_i. The relative elemental proportion N_i is represented as:

$$N_i = \frac{I_i/S_i}{\sum I_i/S_i} \tag{2.4.5}$$

Use of this formula assumes uniform composition over the XPS sampling depth (5 to10 nm) and that the spectrometer in use performs in a similar way to the spectrometer which was used to determine the sensitivity factors.

2.4.3 Scanning Electron Microscopy

This technique is widely used to obtain information about the surface topography of a sample. Due to its large depth of field, SEM images are 3D in appearance. The technique employs the use of electron beams to create images instead of light used in optical microscopes, which

has a much shorter wavelength. This allows much higher magnification (>100,000x). Incident electrons are produced from a heated metallic filament or field emission source. The electron beam is rastered across the surface and the secondary electrons, which are produced from the interaction of the primary beam with the solid, are detected a to form the image. Therefore, there is a spot by spot correlation between the signal level of an object point and the brightness of the corresponding display spot. Backscattered electrons are due to elastic scattering. The intensity of backscattered electrons increases with atomic number and thus this is useful for examining chemical compositions. As the backscattered electrons are more energetic than secondary electrons, they may escape from a greater depth within the sample. Therefore the backscattered electrons signal carries less information about the topography and bears poor spatial resolution compared to that of secondary electrons. If the high energetic incident electron beam excites an electron in the inner shell and creates a core hole, the excess energy can be released in the form of X-rays during relaxation. The X-rays are characteristic of the element of the specimen and can be used for chemical analysis which is referred to as Energy Dispersive X-ray spectroscopy (EDX).

2.5 Methylene blue degradation

2.5.1 Photocatalytic degradation of methylene blue

The custom-made setup uses Heraeus mercury lamp with gallium iodide additive. Metal halide dopant modifies the spectral by enhancing UV output at 415 nm. The spectrum was adjusted using various UV cut-off filters (λ>420 nm or λ>400 nm long pass) to remove undesired UV component.

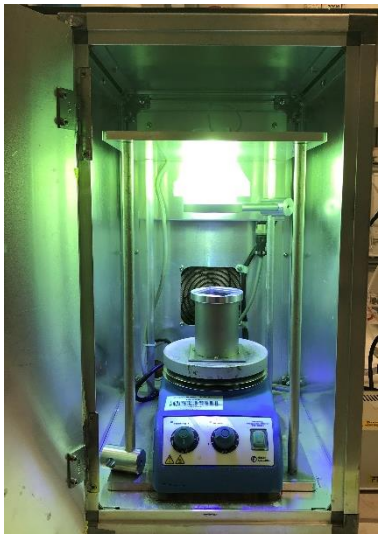


Figure 2.7 custom-made methylene blue degradation setup.

In a typical experiment, 0.05 g of sample was added to 50 mL of 10 ppm MB solution and stirred in dark condition for 10 min for adsorption/desorption equilibrium. The beaker containing the MB solution is housed in an aluminium container to maintain fixed amount of illumination from above. (Figure 2.7) The degradation process was monitored by taking a 1 mL sample solution every 10 min. These sample solutions were filtered with Advantec syringe filters before obtaining absorption spectra with a portable visible region spectrometer (Biochrome Libra S6).

2.5.2 Methylene blue spectrum deconvolution

Methylene blue (MB) photodegradation is widely used to determine photocatalytic activity of materials. To analyse the concentration of MB during photodegradation experiments, most works used the absorbance at the maximum absorption wavelength, typically around 664 nm, which corresponds to the maximum absorption wavelength for unreacted MB monomer.[9–13] However, in some cases, using only the MB monomer absorption maximum

at 664 nm wrongly estimates concentration of MB. In order to distinguish different spieces present, deconvolution of the MB spectrum is required. At the moment, only one paper on MB spectrum deconvolution can be found.[14] Thus, based on this novel approach, an improved spectrum deconvolution technic is introduced in our study which lead to many interesting findings presented in Chapter 3 of this thesis. In this section, the background knowledge on MB spectrum deconvolution are explained.

Intermediate compounds generated during MB photodegradation contributes to the total absorption spectrum. In rare cases, the maximum absorption wavelength shifts to lower values (hypsochromic/blue shift) during the degradation process. It is believed that this shift is produced by the formation of intermediates that have absorption maxima at lower wavelengths than MB. According to some authors, the photocatalytic degradation of methylene blue by TiO_2 takes place via the sequential decomposition of methyl groups, through the formation of azure A and azure B (also azure C, thionine and phenothiazine).[15–17]

It is shown from literature that spectrum of MB monomer exhibits an absorption maximum at 664 nm and a shoulder maximum at 620 nm; MB dimer has an absorption maximum at 607 nm with a second minor band at 685 nm; MB trimer consists of three peaks: 577 nm, 630 nm and 687 nm (Figure 2.8a).[18] Thus, three signiture peaks were selected to represent MB monomer, dimer and trimer composition: 664 nm for monomer (**MB1**), 615 nm for dimer (**MB2**) and 580 nm for trimer (**MB3**). However, due to the influence of minor absorption peaks, these reference peak maxima will be shifted.

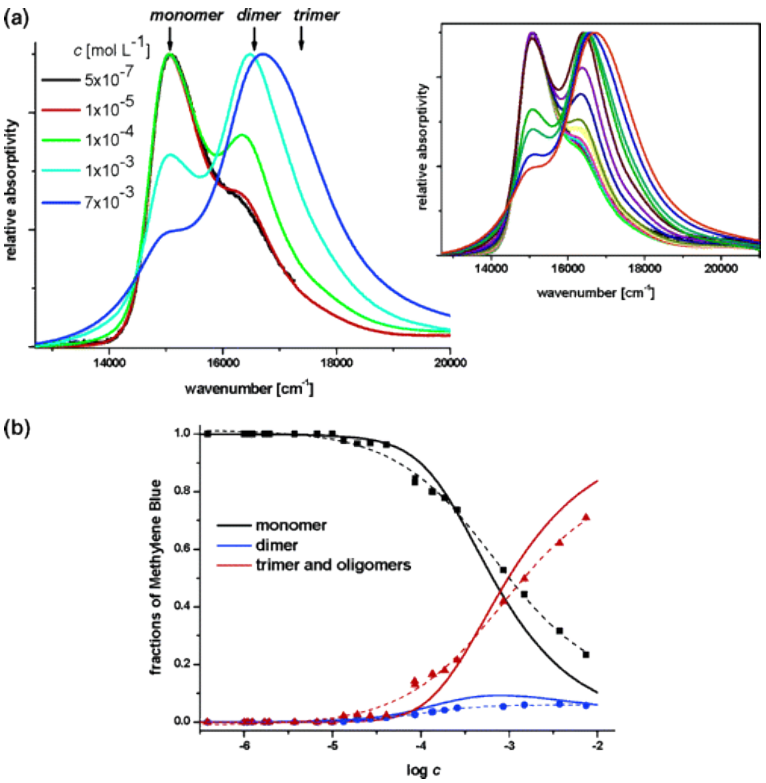
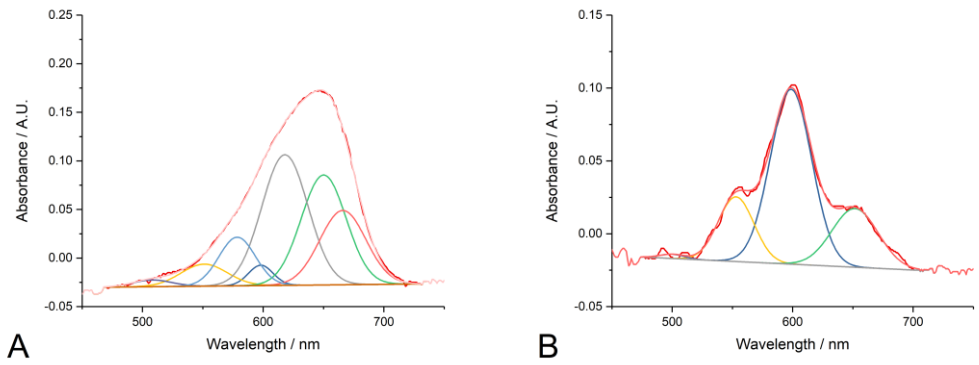


Figure 2.8. (a) Normalized representative spectra of MB in liquid aqueous solutions at 293 K. The arrows show the known wavenumber values corresponding to the absorption maxima of individual species. The insert displays the spectra of all samples at concentrations in the interval of 5.0×10^{-7}–7.5×10^{-2} mol L^{-1}. (b) The concentration-dependent abundances obtained by the Gaussian fitting analysis (solid points; monomer, black; dimer, blue; trimer and oligomers, red; the dotted lines are nonlinear regression fits) in samples at 293 K as a function of the MB concentration c. The solid lines represent the calculated concentration profiles obtained from the estimated equilibrium constants.[18]

The Figure 2.9 is the photodegraded MB absorption spectrum using three different samples (**05N**, **10N** and **20N,** see Chapter 3, section 3.3.3) at the final stage of the degradation process.



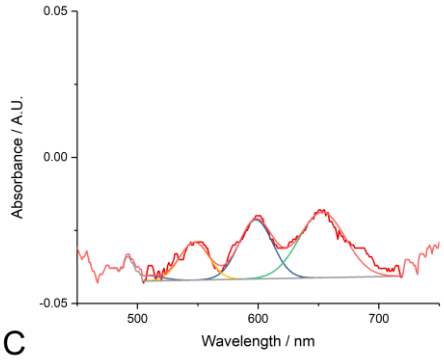


Figure 2.9. Deconvoluted UV/Vis absorption curves of degraded methylene blue of N-doped samples (A) **05N** after 40 mins, **(**B) **10N** after 110 mins and (C) **20N** after 110 mins.

There are three distinct peaks in Figure 26 B/C: 550 nm, 600 nm and 650 nm. According to the decomposition mechanism of methyl groups, at the final stage of degradation, the intermediaries should be azure A, B, C and thionine. These three peaks should be related to azure A, B and C.

Figure 2.9 shows the deconvolution[14] of visible spectra of aqueous solutions of azure A, B and C taken from the literature[19].

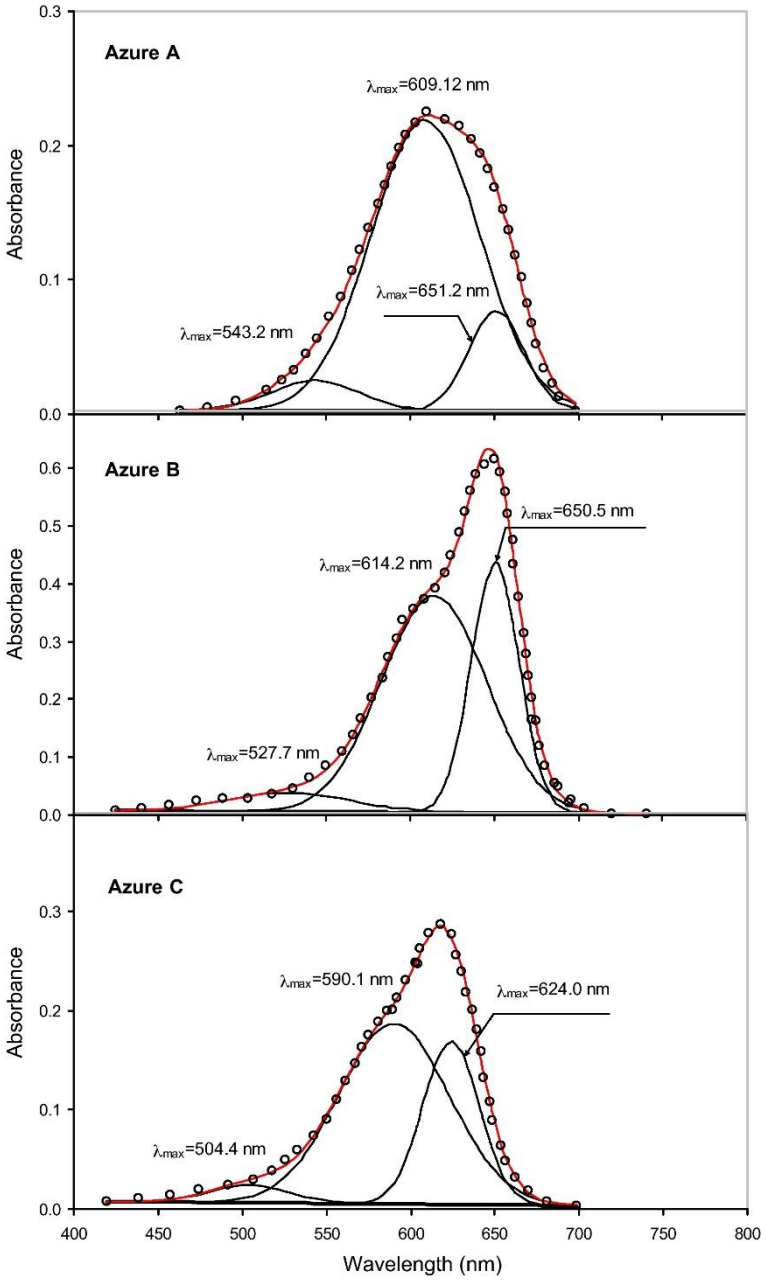


Figure 2.10. Visible spectra of azure A, azure B and azure C (10 μM aqueous solutions); original data were taken from[19]. Curve deconvolutions performed by[14].

As can be seen, the azure A and B spectra contain three peaks near 540 nm, 600 nm and 650 nm whose Gaussian parameters are very similar to Figure 2.9 B/C. During the peak deconvolution process, a peak at 500 nm is required for effective fitting (Figure 2.9 A). As can be seen spectra in Figure 2.10, azure C have a minor peak at 504.4 nm and 624 nm. However, the quality of deconvolution used by previous work is far from optimal. An

obvious drawback can be seen that the FWHM of main peak is close to 100 nm while FWHM of shoulder peaks are around 500 nm. For physically meaningful results, only four characteristic peaks (**AZ 500 nm**, **AZ 550 nm**, **AZ 600 nm** and **AZ 650 nm**) are used to represent the total mixed species of azure A, B and C.

In conclusion, three peaks were selected to represent MB monomer, dimer and trimer: 664 nm for monomer (**MB1**), 615 nm for dimer (**MB2**) and 580 nm for trimer (**MB3**). Four characteristic peaks (**AZ 500 nm**, **AZ 550 nm**, **AZ 600 nm** and **AZ 650 nm**) are used to represent the total mixed species of azure A, B and C. The procedure on MB peak deconvolution and peak constrains are discussed in detailed in Chapter 3, section 3.3.4.

Reference

1. Oropeza, F. E. *et al.* Growth of epitaxial anatase nano islands on SrTiO3(001) by dip coating. *Cryst. Growth Des.* **13**, 1438–1444 (2013).

2. Walsh, F. C. Faraday and his laws of electrolysis: an appreciation. *Bull. Electrochem.* **7**, 481–484 (2017).

3. Zoski, C. G. *Handbook of electrochemistry*. *Handbook of Electrochemistry* (Elsevier, 2007). doi:10.1016/B978-0-444-51958-0.X5000-9

4. P., A. A Dictionary of Chemistry. *Nature* **6**, 42–43 (1872).

5. Guidelli, R. *et al.* Defining the transfer coefficient in electrochemistry: An assessment (IUPAC Technical Report). *Pure Appl. Chem.* **86**, 245–258 (2014).

6. Rudolph, A. M. Electron Transfer Reactions in Chemistry: Theory and Experiment (Nobel Lecture). *Angew. Chemie Int. Ed. English* **32**, 1111–1121 (1993).

7. Fultz, B. & Howe, J. M. *Transmission electron microscopy and diffractometry of materials*. *Transmission Electron Microscopy and Diffractometry of Materials* (2008). doi:10.1007/978-3-540-73886-2

8. Kumar, J. Photoelectron spectroscopy: Fundamental principles and applications. in *Handbook of Materials Characterization* 435–495 (Springer Berlin Heidelberg, 2018). doi:10.1007/978-3-319-92955-2_12

9. Breault, T. M. & Bartlett, B. M. Lowering the band gap of anatase-structured TiO 2 by coalloying with Nb and N: Electronic structure and photocatalytic degradation of methylene blue dye. *J. Phys. Chem. C* **116**, 5986–5994 (2012).

10. Breault, T. & Bartlett, B. Composition Dependence of \cf{TiO2}:(Nb, N)-x Compounds on the Rate of Photocatalytic Methylene Blue Dye Degradation. *J. Phys. Chem. C* **117**, 8611–8618 (2013).

11. Zhao, Y. *et al.* Shape-dependent acidity and photocatalytic activity of Nb 2O 5 nanocrystals with an active TT (001) surface. *Angew. Chemie - Int. Ed.* **51**, 3846–3849 (2012).

12. An, H.-R. *et al.* Advanced nanoporous TiO 2 photocatalysts by hydrogen plasma for efficient solar-light photocatalytic application. *Nat. Publ. Gr.* (2016). doi:10.1038/srep29683

13. Oropeza, F. E., Harmer, J., Egdell, R. G. & Palgrave, R. G. A critical evaluation of the mode of incorporation of nitrogen in doped anatase photocatalysts. *Phys. Chem. Chem. Phys.* **12**, 960–9 (2010).

14. Marbán, G., Vu, T. T. & Valdés-Solís, T. A simple visible spectrum deconvolution technique to prevent the artefact induced by the hypsochromic shift from masking the

concentration of methylene blue in photodegradation experiments. *Appl. Catal. A Gen.* **402**, 218–223 (2011).

15. Rauf, M. A., Meetani, M. A., Khaleel, A. & Ahmed, A. Photocatalytic degradation of Methylene Blue using a mixed catalyst and product analysis by LC/MS. *Chem. Eng. J.* **157**, 373–378 (2010).

16. Zhang, T. *et al.* Photooxidative N-demethylation of methylene blue in aqueous TiO2dispersions under UV irradiation. *J. Photochem. Photobiol. A Chem.* **140**, 163–172 (2001).

17. Yogi, C. *et al.* Photocatalytic degradation of methylene blue by TiO2film and Au particles-TiO2composite film. *Thin Solid Films* **516**, 5881–5884 (2008).

18. Heger, D., Jirkovský, J. & Klán, P. Aggregation of methylene blue in frozen aqueous solutions studied by absorption spectroscopy. *J. Phys. Chem. A* **109**, 6702–6709 (2005).

19. Narband, N. Nanoparticles and photosensitisers; their interactions and antibacterial properties. (2009).

Chapter 3 Nitrogen-Doped TiO_2 Powder: A Methylene Blue Degradation Study

3.1 Introduction

In the past decades, TiO_2 has been extensively studied for environmental and energy applications due to its low cost, low toxicity, chemical inertness and photo-stability and high photocatalytic activity under UV.[1–8] Narrowing the band gap is advantageous for enhancing light-harvesting capability of TiO_2, and the most common approach is to modify with dopants. Non-metal dopants such as boron,[9] fluorine,[10] nitrogen,[11] carbon,[12] and sulfur[13] are used to raise the valence band maximum. Alternatively, by the incorporation of transition metal dopants, such as iron,[14] cobalt,[15] nickel,[16] niobium[17] and vanadium,[18] distortions on the TiO_2 lattice structure results in overall band gap reduction and improvements in charge carrier lifetime.

Among all dopants, nitrogen doping seems to be attractive due to its comparable atomic size with oxygen, small ionisation energy and stability. Yin et al. find that (N, N) homo doping results in the formation of filled impurity bands lying above the valence band of TiO_2, leading to an efficient band gap reduction to 2 eV.[19] To achieve appropriate nitrogen doping, there are several well-established approaches: physical treatments such as sputtering,[20,21] and ion implantation;[22,23] chemical treatments such as high-temperature annealing in a nitrogen-containing atmosphere,[24,25] sol-gel,[26,27] or oxidation of titanium nitride[28] etc.

In physical treatments, TiO_2 films are exposed to energetic ions. In the chemical annealing and titanium nitride oxidation processes, TiO_2 is exposed to high-temperature conditions. In the chemical sol-gel process, nitrogen incorporation is achieved by hydrolysis of titanium alcohol precursors and a nitrogen source such as aliphatic amines, ammonia etc which can be carried out in a low-temperature condition. The sol-gel process is the preferred method for producing doped TiO_2 powders due to easier control over doping levels, short preparation process and low energy. Several groups have already demonstrated successful incorporation of nitrogen in TiO_2 using the sol-gel process.[26,27,29–31] Traditional sol-gel solvent extraction process requires the use of hydrolysis which is a complicated process involving many steps such as refluxing and pH control. Also, it involves the use of acids, bases, or other reagents such as sulphides and amines which need further washing to remove excess ions after nanoparticle formation. These approaches are generally time-consuming.

In this chapter, a simple and swift one-pot solvothermal evaporation process was developed to prepare N-doped anatase TiO_2 powder. The novel aspect of the 2-propanol/HNO_3 solvothermal evaporation method is the ability to synthesise highly N-doped TiO_2 nanoparticles with doping level up to 4.1 atomic % at low annealing temperature of 250°C. The influence of annealing temperature, nitric acid precursor concentration and pre-annealing preparation details on the doping level nitrogen were studied using XPS. It has been confirmed that increase in annealing temperature leads to a decrease in nitrogen doping level, and annealing temperature beyond 400 °C lead to a complete loss of nitrogen.

The photodegradation of 10 ppm MB solution using N-doped TiO_2 under UV irradiation was investigated. A new hypsochromic shift (blueshift) in photodegraded MB spectra was identified. A deconvolution procedure that permits a detailed evaluation of the MB monomer, dimer, trimer, and intermediate product concentrations during photodegradation experiments was introduced. The hypsochromic effect was identified as a result of dimerization and trimerization during degradation. This reaffirms that the MB degradation process occurs on the surface of photocatalyst by direct hole oxidation rather than the traditional hydroxyl/ superoxide radical oxidation. It has been demonstrated that the total area of MB absorption spectra followed pseudo-first-order kinetics, which is a much better indicator than the 664 nm MB monomer absorption maximum.

3.2 Experimental

Powder samples were produced by evaporation of aqueous or alcohol solutions. For the aqueous solutions, 10 mL of deionised water was mixed with 10 mL of concentrated HCl (Fisher Scientific, 37%). 1.37 cm^3 of Titanium (IV) tetrachloride (Sigma-Aldrich, 99.9%) with an appropriate amount of Antimony(V) chloride (Sigma-Aldrich, ≥99.99%) were added to give a titanium precursor concentration of 0.625 M.

For the alcohol solutions, Titanium(IV) tetrachloride (Sigma-Aldrich, 99.9%) with an appropriate amount of Antimony(V) chloride (Sigma-Aldrich, ≥99.99%) were added to 2-propanol (Fisher Scientific, analytical grade) to give 25 mL of solution with 0.5 M titanium concentration, then acidified using appropriate amount of HNO_3 (Fisher Scientific, 70%).

The evaporation process was carried out using an oil bath with an oil temperature of 125 °C. For the aqueous solutions, the evaporation process takes about one-hour, fine power was obtained at the end of the evaporation. The product was transferred into an alumina boat annealed 600 °C in a muffle furnace for 10 h,

For alcohol solutions, the evaporation process takes about 30 min to complete. After the rapid evaporation process, the solidified sample was roasted by keeping in the same oil bath (125 °C). During the roasting procedure, the sample breaks into coarse grains while releasing a white fume. The product was ground with an agate mortar and pestle (Cole-Parmer 75 mL) and transferred into an alumina boat (Fisher Scientific) annealed at 250 °C to 600 °C in a muffle furnace for 10 h.

3.3 Results and discussion

3.3.1 Process optimisation

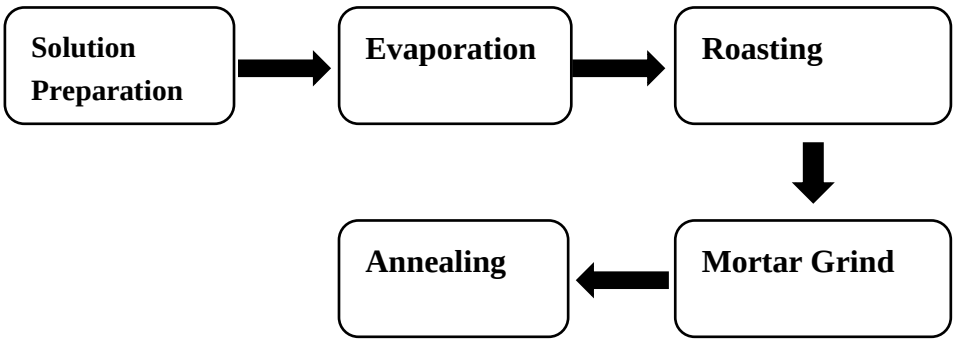
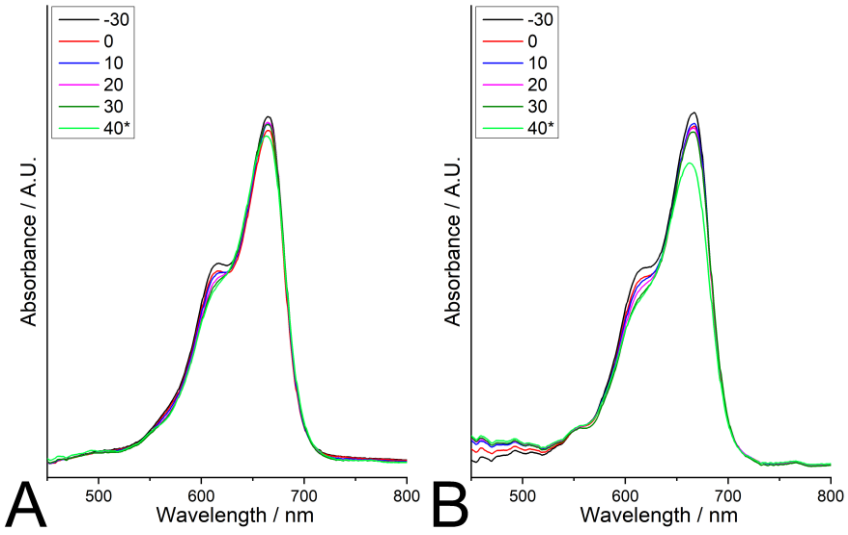


Figure 3.1. Flowchart of a typical solution evaporation process

As seen in Figure 3.1, after evaporation of the sample precursor solution, there are two steps leading to the annealing of the sample. To establish a robust and reproducible process, variables of roasting time and the need for mortar grinding were investigated.

First, the necessity of mortar grinding was investigated. Four samples are prepared with varying roasting time of 0, 10, 20, and 30 mins without mortar grinding. The typical preparation procedure as follows: after a rapid evaporation process that takes around 30 mins, the solidified samples were kept on roasting in the same oil bath for an extended period up to 30 mins. Mortar grinding of the coarse products was avoided. The products were annealed at 250 °C for 10 h in a muffle furnace.

A shortened MB degradation test was used to investigate the optimisation process. Before degradation process starts, MB spectrum is measured (-30 spectrum), then sample is mixed with10 ppm MB solution and stirred in the dark for 30 min (0 spectrum). After turning on the lamp, degraded solutions were checked every 10 min up to 40 min (10, 20, 30 and 40 spectrum). The irradiation spectrum was adjusted using a 400 nm long pass filter to remove UV contribution from 0 to 30 min. From 30 min to 40 min, the 400 nm long pass filter was removed so that the solution was exposed to full-spectrum irradiation. The absorption spectra of the degraded MB using these samples are shown in Figure 3.2.



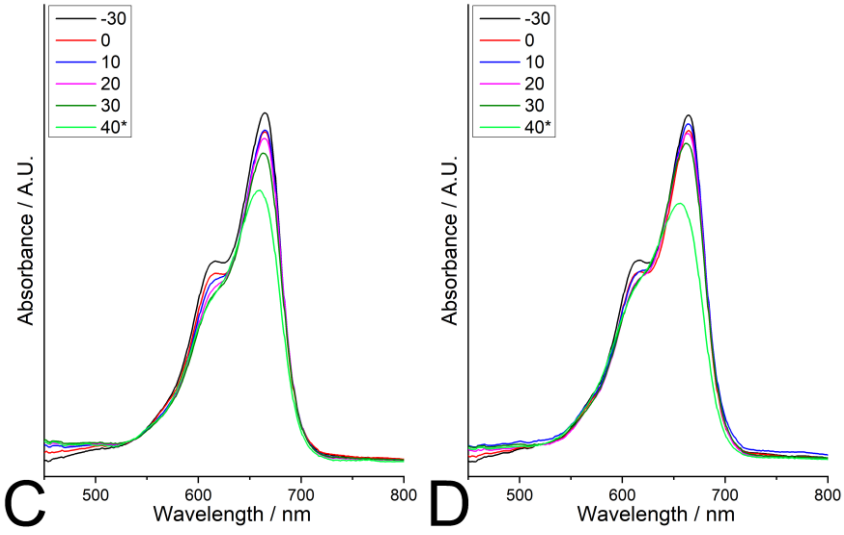


Figure 3.2. Absorption spectra of 10 ppm MB solution degraded with alcohol prepared N-doped TiO_2 with a roasting time of (A) 0 min, (B) 10 min, (C) 20 min and (D) 30 min without mortar grinding.

As mentioned in the experimental chapter, the MB absorption spectrum is composed of MB monomer/ dimer/ trimer peaks at 664 nm / 615 nm / 580 nm respectively. In radical oxidation mechanism, MB monomer/ dimer/ trimer peak decreases uniformly.[32] The temporal evolution of MB monomer absorption maximum at 664 nm is presented in Figure 3.3

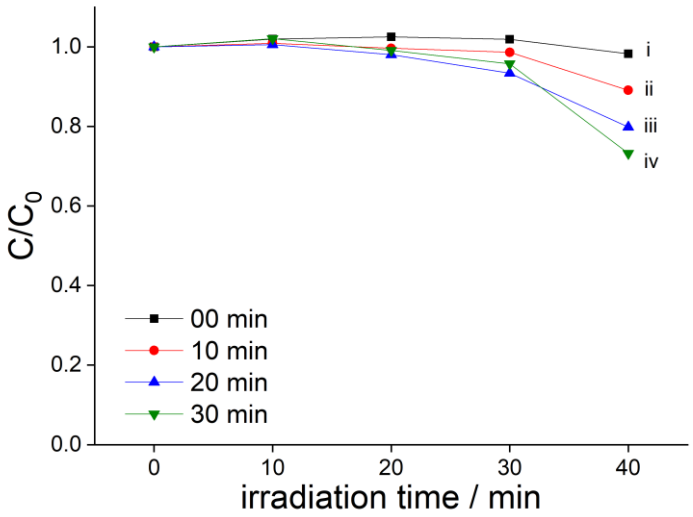
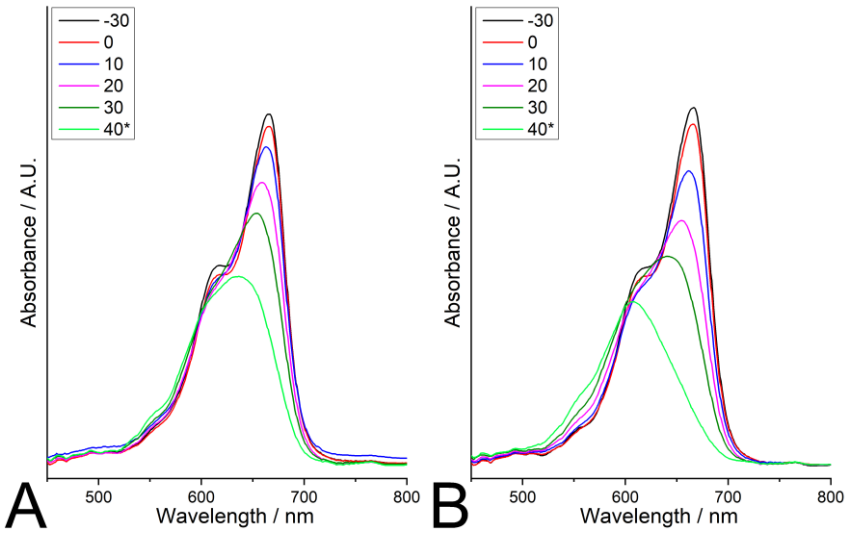


Figure 3.3. Temporal evolution of the concentration of 10 ppm MB indicated by C/C_0 for 664nm absorption maximum degraded with alcohol prepared N-doped TiO_2 with roasting time (i) 0 min, (ii) 10 min, (iii) 20 min and (iv) 30 min without mortar grinding.

It is obvious that there is little change in MB absorption spectra under filtered (>400 nm) irradiation in the first half-hour of MB degradation. Moreover, in the final 10 mins under full-spectrum irradiation insignificant change in MB absorption spectra is observed. This result shows without mortar grinding process the N-doped TiO_2 samples have almost no photocatalytic activity under both UV and visible irradiation. Thus, in the following experiments, mortar grinding process is applied.

Next, the effects of roasting time were investigated. Four samples are prepared with a varying roasting time of 0, 10, 20, and 30 mins with mortar grinding. The typical preparation procedure as follows: after a rapid evaporation process, the solidified samples were kept in the same oil bath for 0, 10, 20, and 30 mins for the roasting process. The brittle brown product was mortared to a fine powder and annealed at 250 °C for 10 h using muffle furnace.

The absorption spectra of the degraded MB using these samples are shown in Figure 3.4.



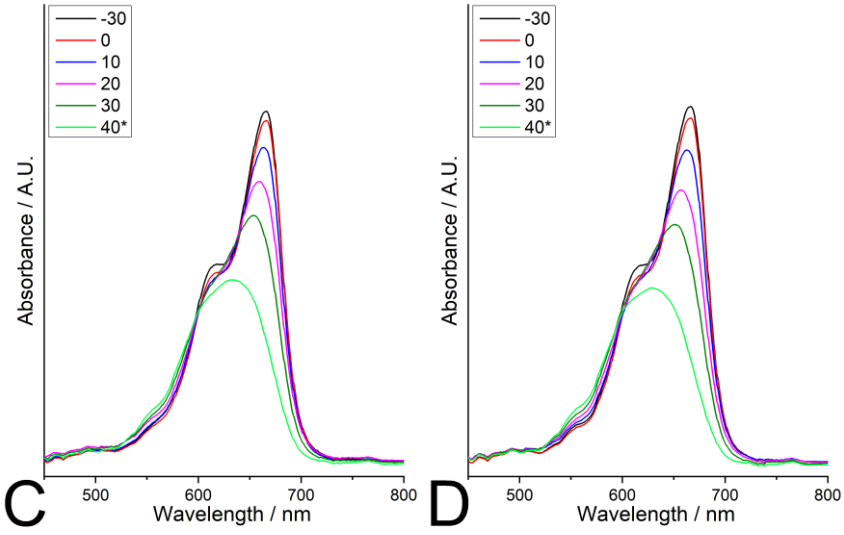


Figure 3.4. Absorption spectra of 10 ppm MB solution degraded with alcohol prepared N-doped TiO_2 with a roasting time of (A) 0 min, (B) 10 min, (C) 20 min and (D) 30 min.

It has been demonstrated that in direct surface decomposition of MB using Nb_2O_5 nanocrystals, MB monomer degradation rate is higher than MB dimer,[32] which lead to a similar hypsochromic shift in MB absorption spectra. (Figure 3.4) The temporal evolution of MB monomer absorption maximum at 664 nm is presented in Figure 3.5.

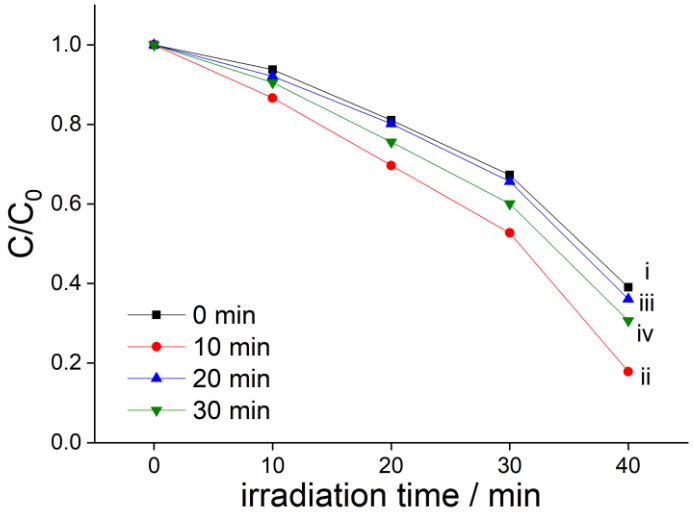


Figure 3.5. Temporal evolution of the concentration of 10 ppm MB indicated by C/C_0 for 664nm absorption maximum degraded with alcohol prepared N-doped TiO_2 with roasting time (i) 0 min, (ii) 10 min, (iii) 20 min and (iv) 30 min.

The 10 min roasted sample displays a lead in photocatalytic activity albeit small. At longer roasting time of 20 and 30 min, the photocatalytic activity drops back to unroasted level with insignificant difference. The release of white fume occurs around 5-10 min into the roasting process, it is possible this is a key turning point for material preparation, which is associated with the small increase in photocatalytic activity for 10 min roasted sample. Since there is no merit extending the roasting period beyond this turning point, in the following experiments, the roasting process is stopped as soon as release of white fume occurs.

Finally, the reproducibility and consistency of the solvothermal procedure were investigated. Samples I, II and III were made using identical preparation procedure. The typical preparation procedure as follows: after a rapid evaporation process that takes around 30 mins, the mud-like product solidifies around the magnetic stirrer bar. Samples were roasted in the same oil bath (125 °C) until disintegrating into coarse grains while releasing a white fume (typically 5-10 mins into the roasting process). Samples were taken out of the oil bath immediately, mortared to a fine powder and annealed at 250 °C for 10 h using a muffle furnace in an alumina boat container.

The absorption spectrum of the degraded MB using these samples are shown in Figure 3.6, and the temporal evolution of absorption maximum at 664 nm is presented in Figure 3.7.

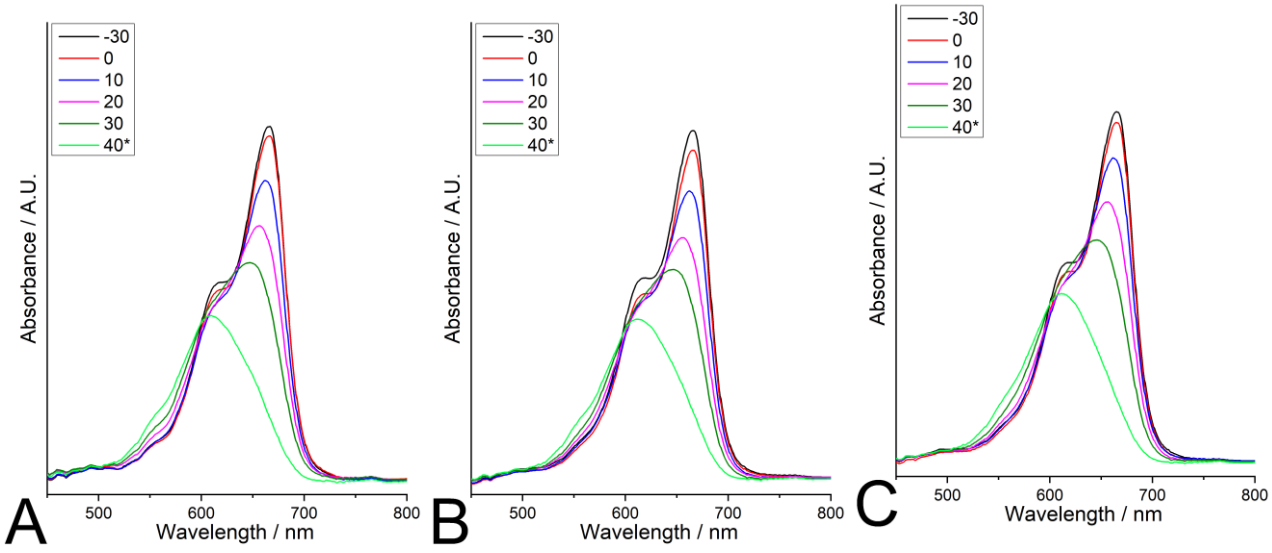


Figure 3.6. Absorption spectra of 10 ppm MB solution degraded with alcohol prepared N-doped TiO_2 (A) sample I, (B) sample II and (C) sample III using the same condition.

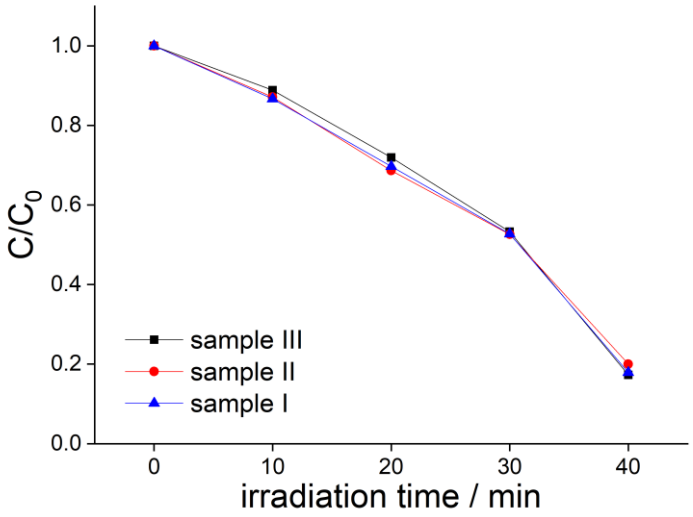


Figure 3.7. Temporal evolution of the concentration of 10 ppm MB indicated by C/C_0 for 664 nm absorption maximum degraded with alcohol prepared N-doped TiO_2 samples using the same condition.

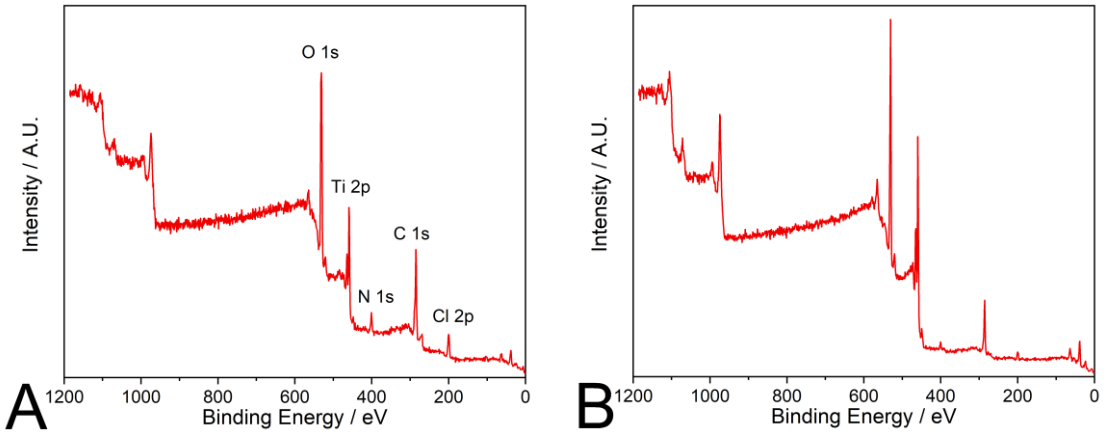
There is almost no difference between the evolution of degraded MB absorption spectra. MB degradation performance is reasonably consistent. This optimized one-pot solvothermal evaporation process can reliably reproduce powder samples with consistent photocatalytic activity.

3.3.2 Effect of annealing temperature

The effects on nitrogen doping and other surface chemical changes due to annealing temperature were studied with XPS. The photocatalytic activity changes due to annealing temperature were studied with MB degradation experiments.

Samples **T250**, **T300**, **T350** and **T400** were annealed at temperatures of 250 °C, 300 °C, 350 °C and 400 °C respectively for 10 hours in a muffle furnace with an alumina boat as a container. Sample **PRE** is the just mortared sample that did not go through the above-mentioned annealing process. All samples were acidified by adding 1 mL concentrated nitric acid to alcohol precursor solution (25 mL).

To investigate the chemical states and proportion of the species present in the N-doped TiO_2 powder surfaces, X-ray photoelectron spectra (XPS) of the C 1s and N 1s core levels were measured.



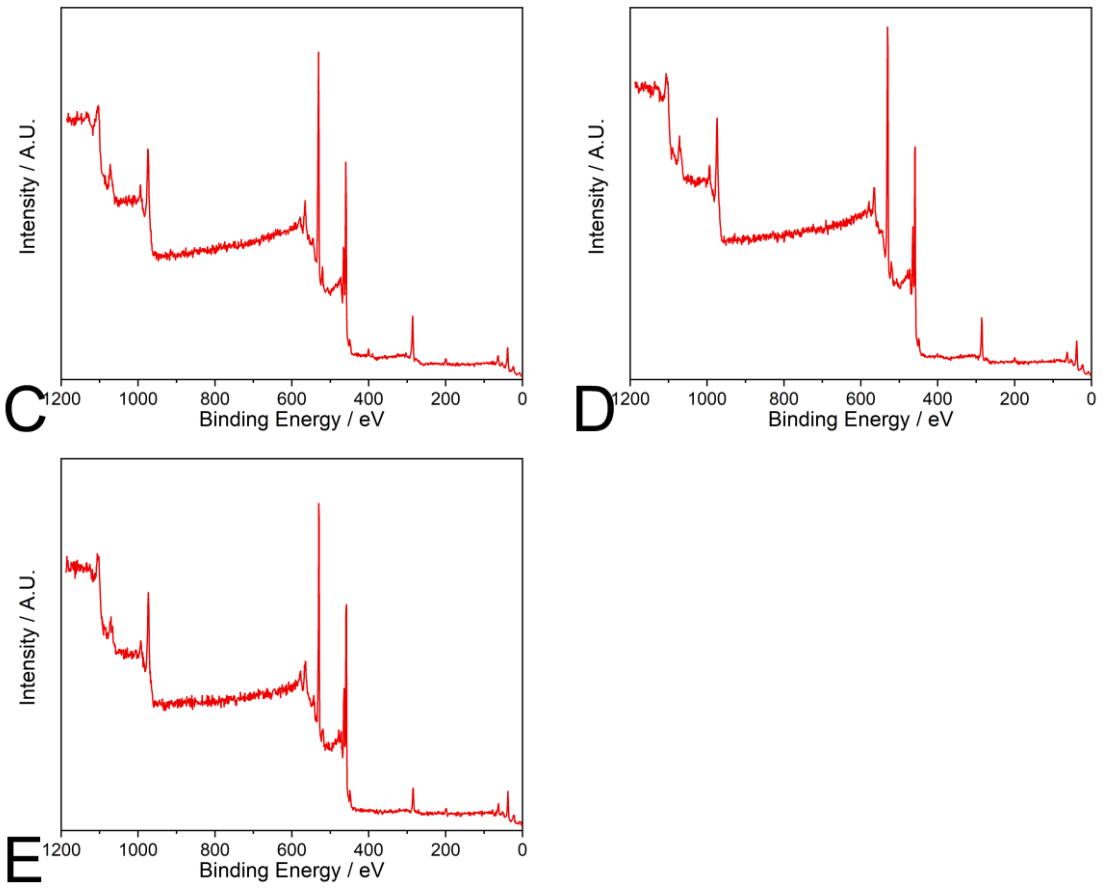


Figure 3.8. XPS survey spectra of for the N-doped samples: (A) pre annealed (**PRE**) and annealed at temperatures of (B) 250 °C (**T250**), (C) 300 °C (**T300**), (D) 350 °C (**T350**) and (E) 400 °C (**T400**).

The survey spectra in Figure 3.8 show an obvious carbon 1s peak at 284.5 eV, a nitrogen 1s peak at 399.8 eV, titanium 2p peaks at 458.6 eV and 464.3 eV, an oxygen 1s peak at 529.8 eV, and overlapped chlorine 2p peaks at 200 eV. The presence of the N 1s peak at 399.8 eV and C 1s at 284.5 eV reduces with the increase in annealing temperature.

To calculate the percentage value of each element, CasaXPS software was used. Peak fitting GL(30) (Gaussian (70%)–Lorentzian (30%)) was applied to all peaks beside Ti 2p peak which uses a GL(70) fitting.[33] Normalised atomic percentages were determined from peak areas of the main elemental peaks applying Thermo's relative sensitivity factors (RSF). RSF

of 6.471, 2.881, 1.676 and 2.741 were used for Ti 2p, O 1s, N 1s and Cl 2p respectively. The results are presented in Table 3.1 below in atomic %.

Table 3.1. Surface element concentrations results from XPS analysis in atomic %.

Atomic % / ***Sample ID***	***Ti***	***O***	***C***	***Cl***	***N***
PRE	8.5	36.3	44.8	5.2	5.2
T250	19.4	45.5	30.6	1.9	2.6
T300	19.5	47.1	28.8	1.5	3.1
T350	21.3	49.7	27.1	1.1	0.7
T400	25.9	53.2	19.4	1.6	0.0

From the data in Table 3.1, it is obvious that the ratio of Ti and O is not in stoichiometric 1:2 but with an excess amount of oxygen. Especially in the case of the pre-annealed sample (**PRE**), the atomic ratio of Ti and O is as high as 1:4.27 and with a significant presence of carbon. This is probably due to surface organic residue generated by the solvothermal process.

By examining the XPS C 1s core level structure, besides the C-C peak at 284.5 eV, there are clear shoulder components at higher energies which indicates the presence of oxidised carbon spicies.[34] The fitted peaks are presented in Figure 3.9, and composition analysis is presented in Table 3.2.

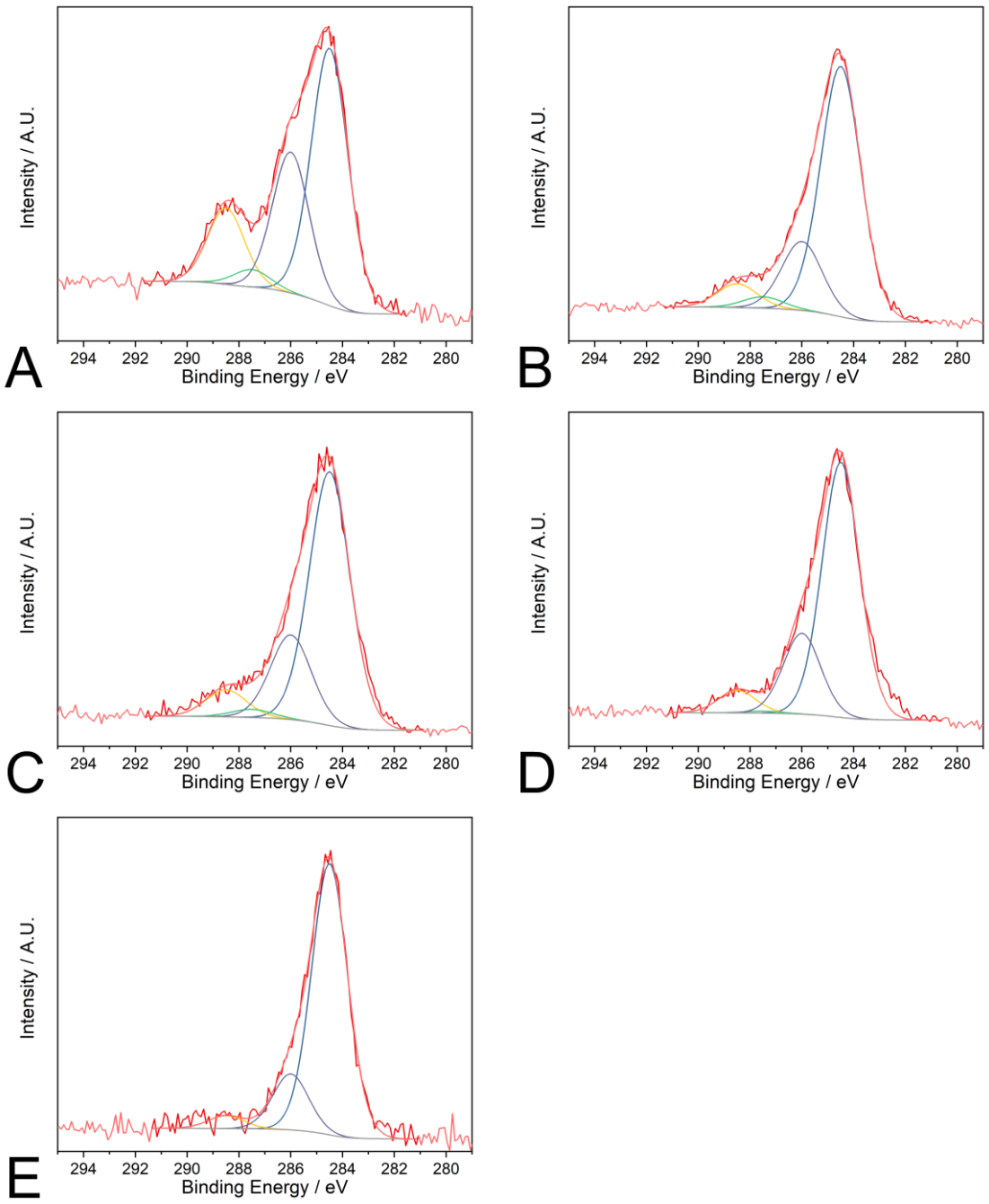


Figure 3.9. XPS C 1s core level spectra of samples (A) pre-annealed (**PRE**) and annealed at temperatures of (B) 250 °C (**T250**), (C) 300 °C (**T300**), (D) 350 °C (**T350**) and (E) 400 °C (**T400**).

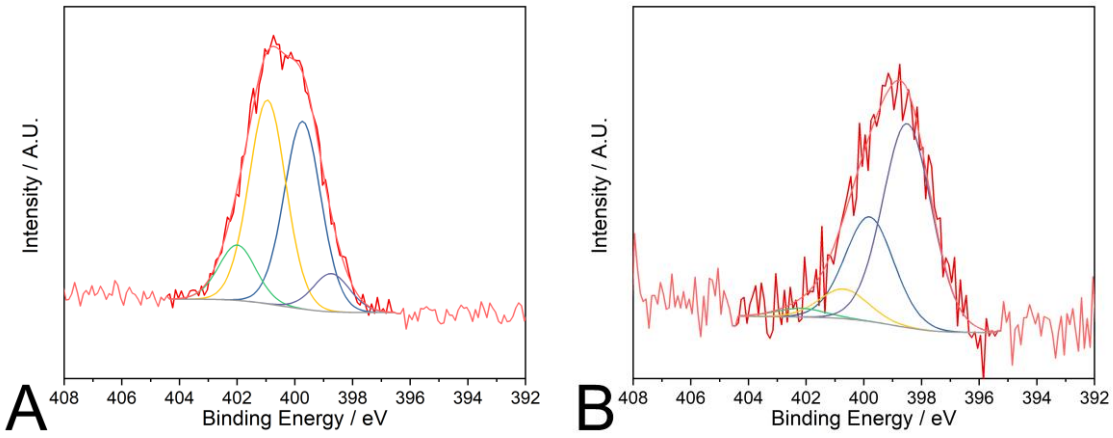
A peak at 1.5 eV above the main peak ascribed to alcohol (C–OH) and/or ether (C–O–C) functionality is observed. A third peak at 3 eV above the main peak ascribed to carbonyl (C=O) is also seen. A fourth peak 4 eV above the main peak ascribed to carboxylate functional groups (O-C=O) is also detected.

Table 3.2. Deconvolution of carbon 1s XPS peak: binding energy (eV) and peak area (%).

	C	*C-O*	*C=O*	*O-C=O*
Binding Energy (eV)	*284.5*	*286*	*287.5*	*288.5*
PRE (Area%)	52.3	28.7	3.5	15.5
T250 (Area%)	70.6	19.4	3.3	6.7
T300 (Area%)	67.9	22.6	2.2	7.2
T350 (Area%)	70.8	22.4	0.6	6.3
T400 (Area%)	79.7	16.5	0.0	3.8

It is shown that the carboxylate functional groups (O-C=O) component decreases dramatically with annealing. Carbonyl (C=O) disappears above 350 °C. However, the alcohol (C–OH) and/or ester (C–O–C) component is very stable up to 400 °C.

By examining the XPS N 1s core level structure, the FWHM of a single peak fitting would amount to 4 eV which is too large, given the energy resolution of the Thermo Fisher K alpha XPS employed. This large separation suggest more than one chemical species is present.



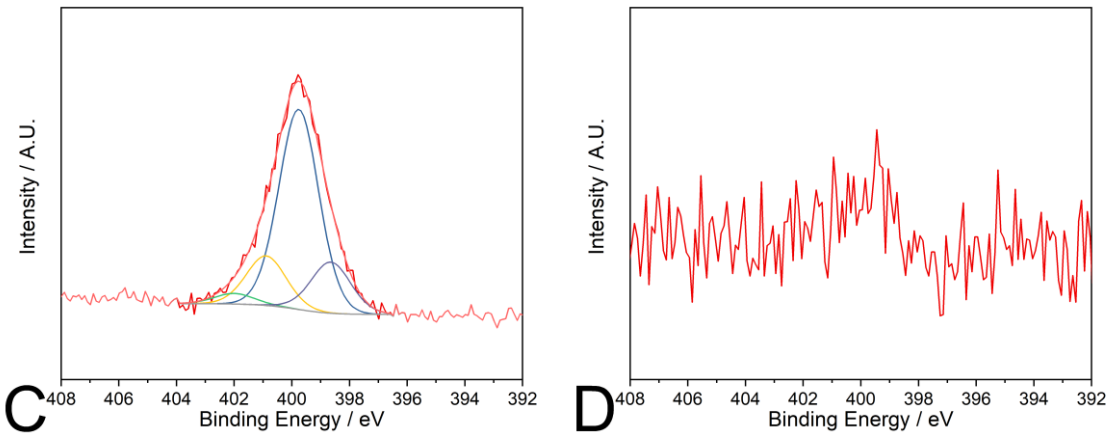


Figure 3.10. XPS N 1s core level structure for the samples (A) pre-annealed (**PRE**) and annealed at temperatures of (B) 250 °C (**T250**), (C) 300 °C (**T300**) and (D) 350 °C (**T350**).

Deconvolution of this peak yields an imine nitrogen peak at 398.7 eV, an amine/amide nitrogen peak at 399.7 eV, an imide nitrogen peak at 400.9 eV and an alkyl ammonium peak at 402 eV.[35] It is understood that nitrate peaks occur around 407 eV and titanium nitride peak positions at around 397 eV[36] which are absent from this scan. This suggests the surface of TiO_2 is coated with a continuous layer of a nitrogen-containing organic compound.

Table 3.3. Deconvolution of N 1s XPS peak: binding energy (eV) and peak area (%).

	NH=C (imine)	***NH_2-C (amine)***	***(C=O)-NR-(C=O) (imide)***	***NR_4^+ (alkyl ammonium)***
Binding Energy (eV)	*398.7*	*399.7*	*400.9*	*402*
PRE (Area%)	7.9	38.7	42.0	11.4
T250 (Area%)	58.8	30.1	8.5	2.6
T300 (Area%)	17.1	61.3	16.1	5.6

As seen in Table 3.3 and Figure 3.10, imide and alkyl ammonium were reduced with an annealing process. On increasing the annealing temperature from 250 °C to 300 °C, imine is removed leaving amine as the major source of nitrogen. It is possible that alkyl ammonium

decomposes to ammonia at high temperature. At 350 °C nitrogen-containing surface organics are removed.

MB degradation experiments were performed to determine the photocatalytic activity of powder samples subject to differing annealing temperatures. The degradation experiments were conducted using a 420 nm long pass filter to remove certain UV component. Samples were irradiated up to 120 min.

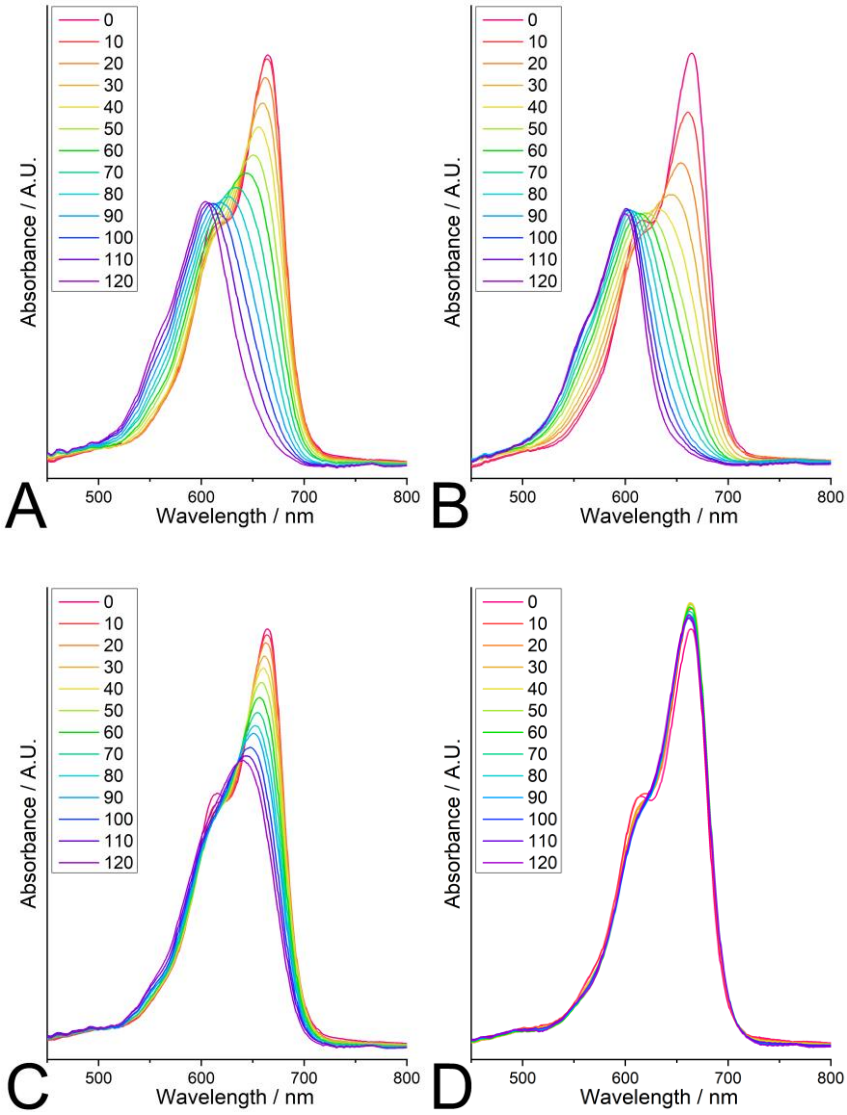


Figure 3.11. Absorption spectra of 10 ppm MB solution degraded with alcohol prepared N-doped TiO_2 annealed at temperatures of (A) 250 °C (**T250**), (B) 300 °C (**T300**), (C) 350 °C (**T350**) and (D) 400 °C (**T400**) using 420 nm long pass filtered irradiation.

From Figure 3.11, it is evident that 250 °C and 300 °C annealing yields visible degradation results, but above 350 °C annealing temperature degradation speed reduces dramatically.

The 664 nm MB monomer absorption maximum is shown in C/C_0 evolution in Figure 3.12 A. It is obvious the MB concentration remained constant for **T400** sample. Without nitrogen doping, TiO_2 is unable to harness the visible spectrum energy for photocatalytic activity. MB concentration decreases most rapidly using **T300** sample. 300 °C appears to be the most suitable annealing temperature for N-doped TiO_2 preparation.

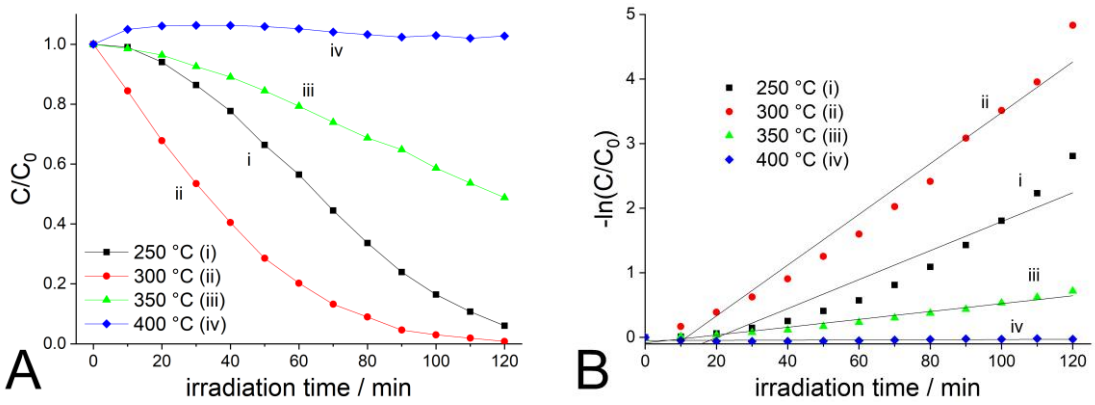


Figure 3.12. Photocatalytic activity of N-doped sample as indicated by MB absorption maximum at 664 nm versus filtered irradiation (>420 nm) time: N-doped samples annealed at temperatures of (i) 250 °C (**T250**), (ii) 300 °C (**T300**), (iii) 350 °C (**T350**) and (iv) 400 °C (**T400**). Temporal concentration change indicated by (A) C/C_0 for 664 nm absorption maximum and (B) pseudo-first-order reaction plot.

Applying pseudo-first-order reaction kinetics model on data, **T250** and **T300** results does not match accurately. Looking closer at the MB absorption curve, the decrease of MB dimer and monomer peak is uneven at 664 nm and 615 nm respectively. From the uneven decrease in absorption peaks, it suggests the degradation process is far more complicated. This is further investigated in section 3.3.4 and section 3.3.5.

In conclusion, an increase in annealing temperature from 250 °C to 400 °C reduces the nitrogen doping level. Annealing temperature at/above 350 °C lead to a complete loss of surface nitrogen which significantly reduced the photocatalytic MB degradation capability under visible (420 nm long pass) illumination. 300 °C annealing temperature yields the best MB degradation results out of temperature range from 250 °C to 400 °C, which is used as the annealing temperature for the following study.

3.3.3 Effect of HNO_3 concentration

The effects on nitrogen doping and other surface chemical changes due to the nitric acid concentration in the preparation process were studied with XPS. The photocatalytic activity changes due to nitric acid concentration were studied with MB degradation experiments.

It seems likely that by changing the concentration of HNO_3, the nitrogen doping content could be adjusted accordingly. **05N**, **10N** and **20N** correspond to samples adding 0.5 mL, 1 mL and 2 mL of concentrated nitric acid to alcohol precursor solution (25 mL). All samples were annealed at 300 °C for 10 h in a muffle furnace with an alumina boat as a container.

To calculate the percentage value of each element, normalised atomic percentages were determined from peak areas of the main elemental peaks applying Thermo's RSF as described previously. The results are presented in Table 3.4 below in atomic %.

Table 3.4. Surface element concentrations results from XPS analysis in atomic %.

Atomic % / ***Sample ID***	***Ti***	***O***	***C***	***Cl***	***N***

05N	19.4	46.5	30.4	1.6	2.2
10N	20.0	44.6	30.3	2.1	3.0
20N	18.7	42.1	33.1	2.0	4.1

Table 3.4 shows the presence of the nitrogen increased from 2.2 to 4.1 atomic % with the increased amount of HNO_3 in the precursor solution, while Ti, O and C composition remained the same. The atomic ratio of Ti and O is close to 1:2.

XPS N 1s core level structure is presented in Figure 3.13. Deconvolution of this peak yields an imine nitrogen peak at 398.7 eV, an amine/amide nitrogen peak at 399.7 eV, an imide nitrogen peak at 400.9 eV and an alkyl ammonium peak at 402 eV.[35]

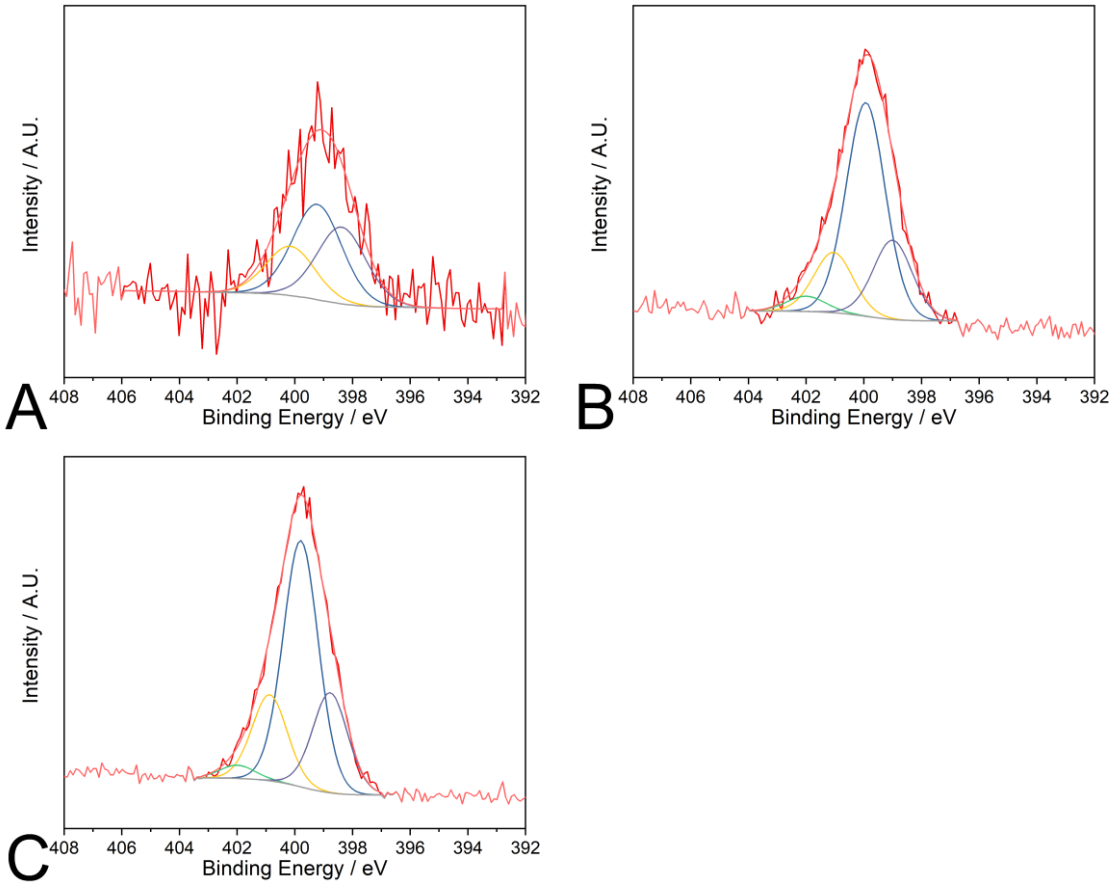


Figure 3.13. N 1s core level XPS spectra for the N-doped samples with (A) 0.5 ml (**05N**), (B) 1 ml (**10N**) and (C) 2 ml (**20N**) concentrated nitric acid added in the alcohol precursor solution.

The two new samples (**05N** and **20N**) show somewhat similar behaviour to the reference sample **10N** which is the **T300** sample discussed in the previous section. It is understood that nitrate peaks occur around 407 eV and titanium nitride peak positions at around 397 eV which are absent from this scan.[36] This suggests the surface of TiO_2 is coated with a continuous layer of a nitrogen-containing organic compound. The majority contribution of nitrogen signal is due to amine which is consistent across different samples.

Table 3.5. Deconvolution of N 1s XPS peak: binding energy (eV) and peak area (%).

	NH=C (imine)	***NH_2-C (amine)***	***(C=O)-NR-(C=O) (imide)***	***NR_4^+ (alkyl ammonium)***
Binding Energy (eV)	*398.7*	*399.7*	*400.9*	*402*
05N (Area%)	34.6	43.1	22.3	0.0
10N (Area%)	21.5	58.0	16.4	4.2
20N (Area%)	22.4	55.3	19.3	3.0

The consistent distribution of nitrogen containing species with different samples (**05N**, **10N**, **20N**) indicates change in nitric acid concentration does not change surface chemical species, only the nitrogen doping level.

The alcohol prepared N-doped TiO_2 powder samples **05N**, **10N** and **20N** appears to be have an anatase structure. A typical XRD result of **20N** sample is shown in Figure 3.14.

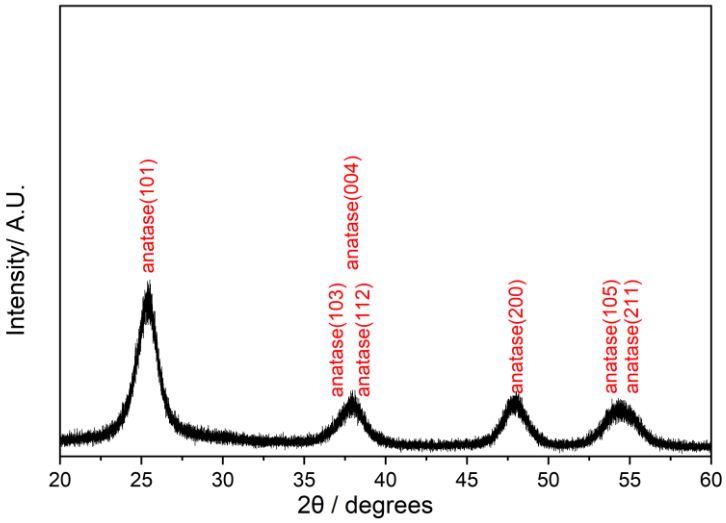


Figure 3.14. θ-2θ X-ray diffraction profiles for N-doped TiO_2 powder prepared with adding 2 mL of concentrated nitric acid to alcohol precursor solution (25 mL), then annealed at 300 °C for 10 h.

Only anatase TiO_2 reflections are found in the N-doped rutile TiO_2 thin film diffraction result, with all anatase reflections present. The (110), (101), and (111) rutile reflections are absent at 27.5°, 36.1°, and 41.2° respectively. This indicates the N-doped TiO_2 powder is in pure anatase phase. The broad diffraction peaks suggest crystal size is very small. Using Scherrer equation, the calculated mean particle size for N-doped TiO_2 sample is ~5.3 nm.

MB degradation experiments were performed to determine the photocatalytic activity of powder samples subject to varying amount of nitric acid precursor. The spectrum was adjusted using a 420 nm long pass filter to remove specific UV component. Samples were irradiated up to 120 min.

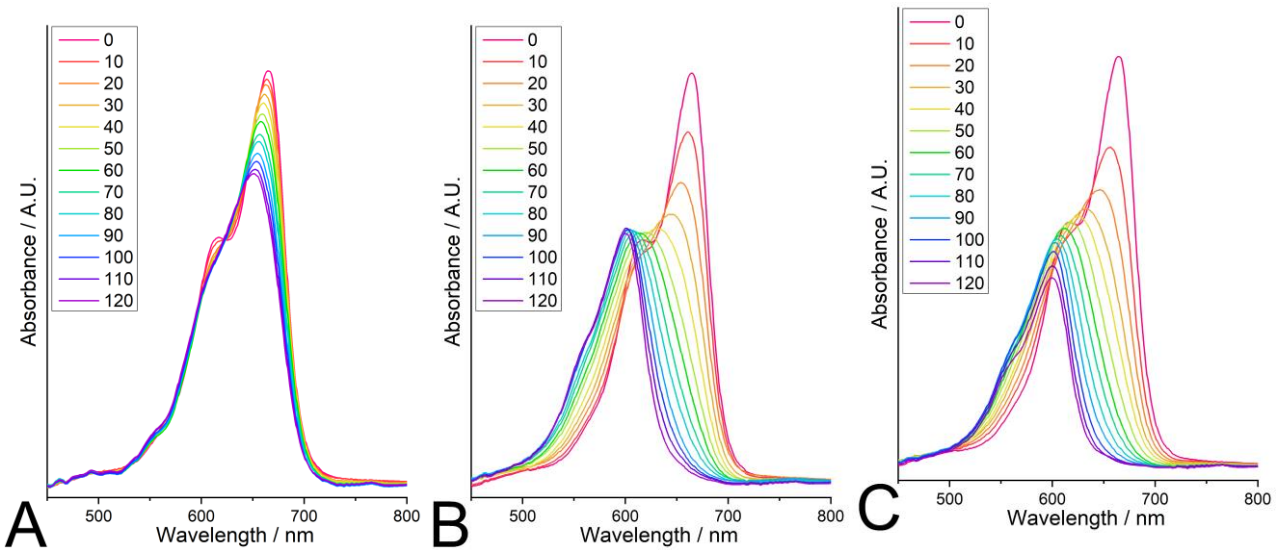


Figure 3.15. Absorption spectra change of 10 ppm MB solution degraded with N-doped samples with (A) 0.5 ml (**05N**), (B) 1 ml (**10N**) and (C) 2 ml (**20N**) concentrated nitric acid added in alcohol precursor solution under 420 nm long pass filtered irradiation.

From Figure 3.15, hypsochromic shift of 615 nm absorption peak in photodegraded MB spectra is more pronounced with increased nitrogen doping level. The MB dimer peak at 615 nm shown a much faster decrease with sample **20N** compared to **10N**. With increase in nitrogen doping, MB dimer degradation is observed. The kinetics of MB dimer degradation is explained in the section 3.3.5.

The 664 nm MB monomer absorption maximum is shown in C/C_0 evolution in Figure 3.16 A. It is evident that with an increase in nitrogen doping level from 2.2 to 4.1 atomic %, the MB degradation rate increases (**05N**, **10N**, **20N**). By increasing the nitrogen doping level, photocatalytic performance under visible irradiation was enhanced.

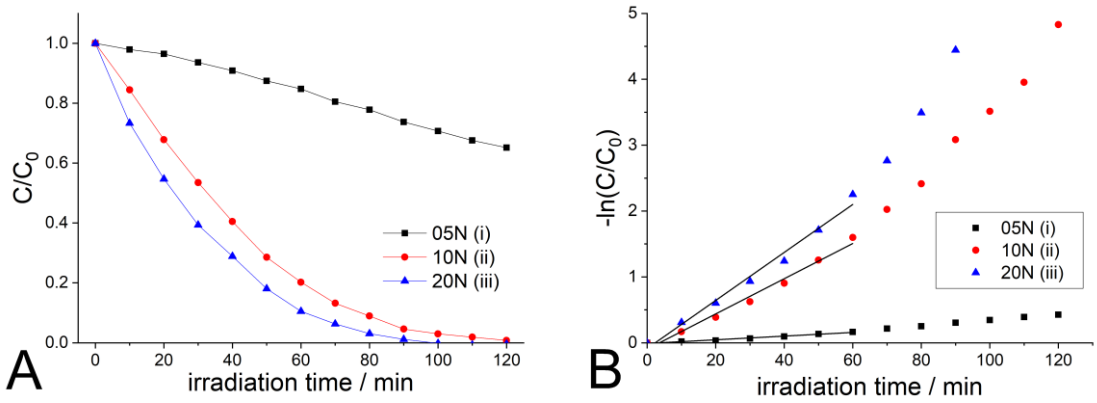


Figure 3.16. Photocatalytic activity of N-doped sample versus filtered irradiation (>420 nm) time: N-doped samples with (i) 0.5 ml (**05N**), (ii) 1 ml (**10N**) and (iii) 2 ml (**20N**) concentrated nitric acid added in the alcohol precursor solution. Temporal concentration change indicated by (A) C/C_0 for 664 nm absorption maximum and (B) pseudo-first-order reaction plot.

Applying the pseudo-first-order reaction kinetics model to the data, **10N** and **20N** results show inadequate linearity. (Figure 3.16 B) Looking closer at the linear fitted curve before and after 60 min, there appears to be a change in degradation rate at around 60 mins. This is addressed in section 3.3.5.

MB degradation experiments conducted with unfiltered irradiation were recorded in Figure 3.17. The degradation rate is generally faster under full-spectrum irradiation compared to 420 nm long pass filtered irradiation.

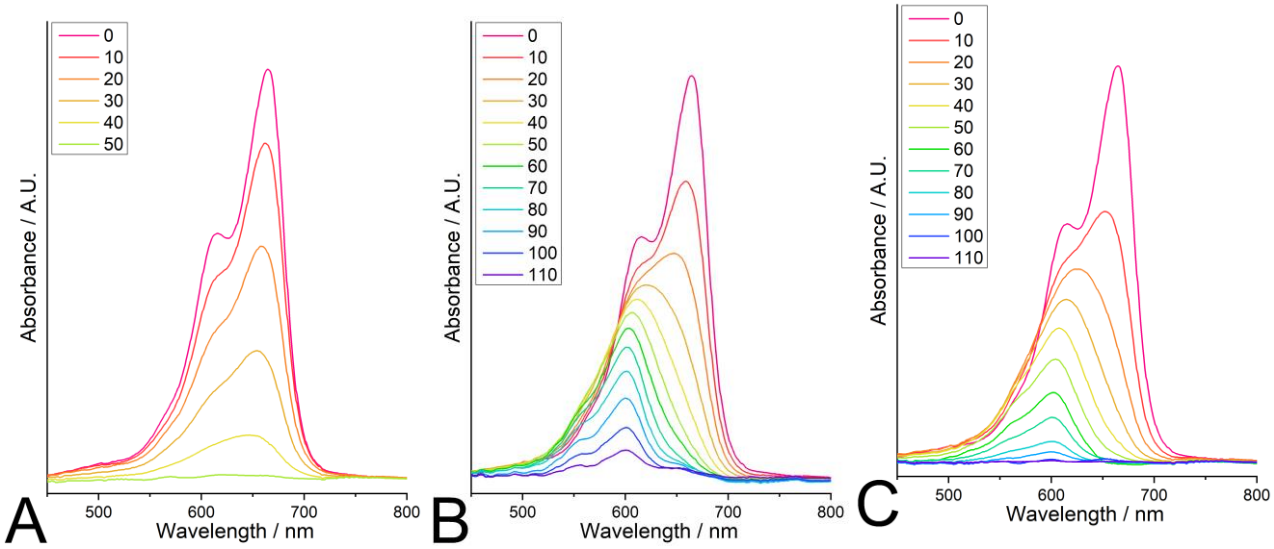


Figure 3.17. Absorption spectra change of 10 ppm MB solution degraded with N-doped samples with (A) 0.5 ml (**05N**), (B) 1 ml (**10N**) and (C) 2 ml (**20N**) concentrated nitric acid added in alcohol precursor solution under unfiltered irradiation.

Sample **05N** shows a similar MB degradation profile to undoped TiO_2 where all peaks in the MB spectrum reduce uniformly.[37] This is similar to radical oxidation mechanism using ZnO that presents an uniform decrease in MB monomer/ dimer peaks.[32] **10N** and **20N** show hypsochromic shift with a faster rate at 664 nm absorption maximum relative to 600 nm peak. This type of hypsochromic shift in MB absorption was identified in direct surface decomposition of MB on Nb_2O_5 nanocrystals surfaces.[32] This presence/absence of hypsochromic effect is discussed in detail in the following section.

Under unfiltered irradiation, the 664 nm MB monomer absorption maximum is shown in C/C_0 evolution in Figure 3.18 A. Applying the pseudo-first-order reaction kinetics model to the data, **05N** and **20N** results show inadequate linearity.

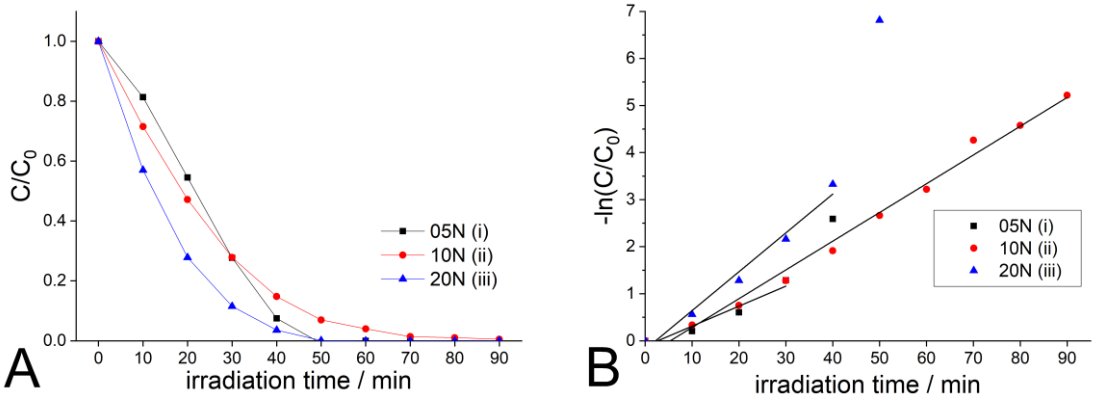


Figure 3.18. Photocatalytic activity of N-doped sample versus unfiltered irradiation time: N-doped samples with (i) 0.5 ml (**05N**), (ii) 1 ml (**10N**) and (iii) 2 ml (**20N**) concentrated nitric acid added in the alcohol precursor solution. Temporal concentration change indicated by (A) C/C_0 for 664 nm absorption maximum and (B) pseudo-first-order reaction plot.

In Figure 3.18, **05N** show worse degradation rate than **20N**. However, in Figure 3.17, **05N** completes MB degradation within 50 min which is faster than 110 min using **20N**. The

photocatalytic performance under unfiltered spectrum is different when interpreting using the 664 nm MB monomer absorption maximum compared to total absorption spectrum. This suggests that MB degradation using N-doped TiO_2 is much more complex and only taking MB monomer peak as the indicator does not fully reflect the total photocatalytic reactions. The detailed study is discussed in the following sections.

In conclusion, the increase in nitric acid concentration increases nitrogen doping level. The increase in nitrogen doping level results in improved photocatalytic degradation of MB under visible (420 nm long pass) irradiation. The N-doped TiO_2 samples display a hypsochromic effect during MB degradation, which cause complications in determining photocatalytic degradation of MB under full spectrum irradiation. This hypsochromic effect requires further investigation.

3.3.4 Deconvolution of methylene blue absorption spectra

The hypsochromic effects during MB degradation have caused inconsistencies in the interpretation of degradation data using only the MB monomer absorption maximum at 664 nm compared to full spectrum. Thus, deconvolution of MB absorption spectrum is required to distinguish individual chemical species for comprehensive investigation. In this section, a novel peak deconvolution technique is shown that identifies MB monomer/ dimer/ trimer and azure A/B/C components in the MB absorption spectra.

The common software for spectra peak deconvolution is OriginPro and MATLAB. However, these software are highly inflexible which creates unnecessary impediments for fine-tuning

multiple peaks. CasaXPS is a very effective software used in fitting XPS spectra. In this study, CasaXPS software was adapted for UV/Vis peak deconvolution. To perform a Gaussian deconvolution of the spectrum a linear baseline between the lowest point around 500 nm of the spectrum and the point around 720 nm was set. Peak fitting GL (0) (Gaussian (100%)–Lorentzian (0%)) was applied to all peaks. The FWHM of individual peaks remained relatively constant throughout the entire degradation process.

To achieve a trustworthy fitting, there are a few key points to keep in mind. The position and FWHM of individual components should remain constant throughout the degradation process. The deconvoluted data should be supported by the underlying physical chemistry model.

The MB reference absorption spectrum is measured at the start of MB degradation experiment before subjected to irradiation. Using just three fixed position peaks from MB monomer/ dimer/ trimer (**MB1/MB2/MB3**) for reference spectrum deconvolution, the mismatch between the convoluted envelope and the actual spectrum is visible. (Figure 3.19 A)

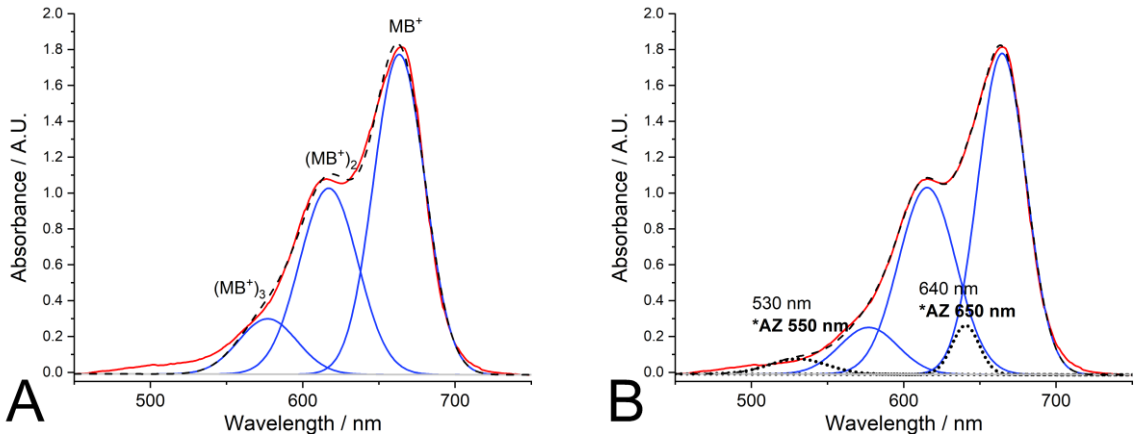


Figure 3.19. MB reference absorption spectrum deconvolution with A) using fixed position MB

monomer/ dimer/ trimer peaks, and B) using two flexible positioned peaks and the fixed position MB monomer/ dimer/ trimer peaks.

In Figure 3.19 B, when two additional peaks with a flexible position are added, the deconvolution results improve considerably. The two additional peaks (black dotted lines) sit at 640 nm and 530 nm respectively which coincides with **AZ 650 nm** and **AZ 550 nm** component peaks from azure A/B/C.[38,39] This result suggests azure A/B/C co-exists with MB species from the start, thus the need to incorporate azure A/B/C peaks together with MB peaks.

For the MB absorption spectrum at terminal stage of degradation (110 to 120 min), only using four component peaks from mixed azure A/B/C species (**AZ 500 nm**, **AZ 550 nm**, **AZ 600 nm** and **AZ 650 nm**) yields a good match for the full spectrum irradiated results (Figure 3.20A), but significant mismatch for 420 nm long pass filtered spectrum irradiated results (Figure 3.20B).

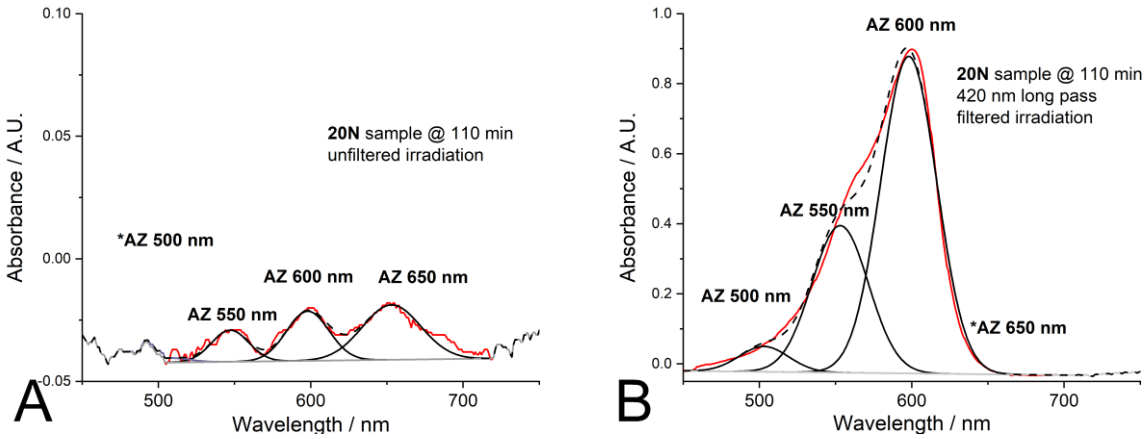


Figure 3.20. Deconvolution with only four azure A/B/C component peaks (**AZ 500 nm**, **AZ 550 nm**, **AZ 600 nm** and **AZ 650 nm**), for MB absorption spectrum obtained at terminal stage (110 min) of degradation, under A) full spectrum irradiated and B) 420 nm long pass filtered spectrum irradiated results. Asterisk means absence of certain component peaks.

Adding the MB monomer/ dimer/ trimer peaks (**MB1/MB2/MB3**) together with azure A/B/C component peaks (**AZ 500 nm**, **AZ 550 nm**, **AZ 600 nm** and **AZ 650 nm**) would significantly improve deconvolution result (Figure 3.21). Similar findings are observed with samples **05N** and **10N** during deconvolution of degraded MB spectra. This suggests without UV contribution, the photocatalytic activity of N-doped TiO_2 is reduced that at 110 min into degradation, MB species are not completely degraded to azure A/B/C species. Thus, deconvolution of MB absorption spectra requires at least all seven peaks mentioned above. The peak position constraints are given in Table 3.6 below.

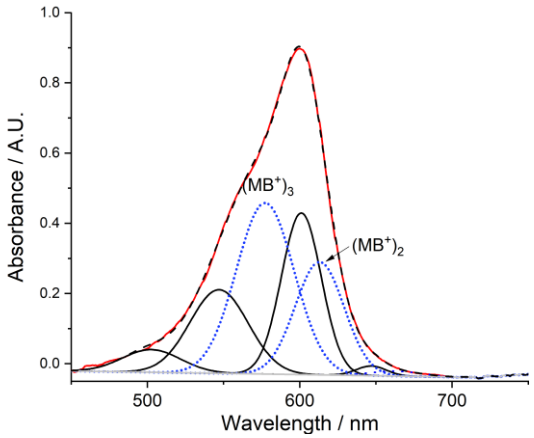


Figure 3.21. Deconvolution with four azure A/B/C component peaks (**AZ 500 nm**, **AZ 550 nm**, **AZ 600 nm** and **AZ 650 nm**) and three MB component peaks (**MB1/MB2/MB3**). Azure component peaks in solid black lines, MB component peaks in dotted blue lines. MB absorption spectrum obtained at terminal stage (110 min) of degradation under 420 nm long pass filtered irradiation using sample **20N**.

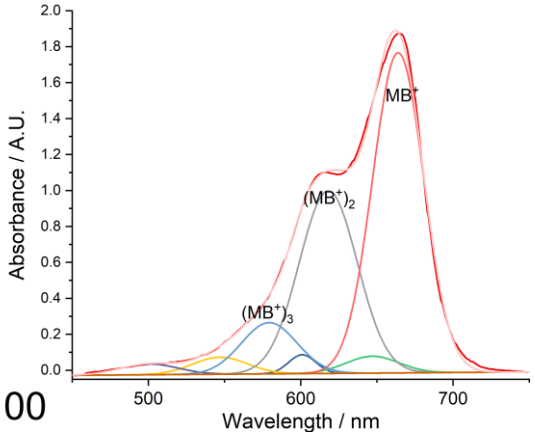
Table 3.6. Peak fitting parameters for MB and intermediate species: peak position (nm) and FWHM (nm) values and constraints.

peak	***position ideal (nm)***	***position constraint (nm)***	***FWHM typical (nm)***	***FWHM constraint (nm)***
MB1	664	663-673	39	20-45
MB2	615	607-620	45	20-45
MB3	580	577-587	40	20-45

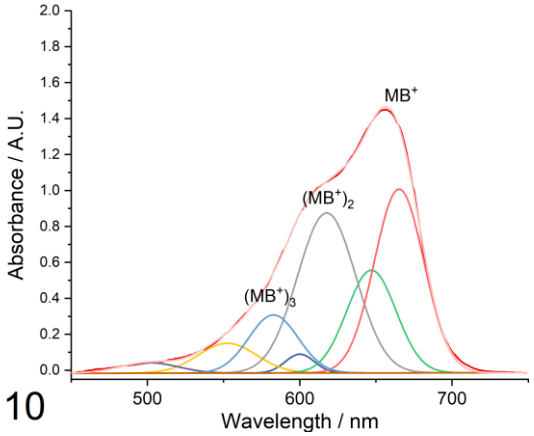
AZ 600 nm	600	598-601	29	20-45
AZ 650 nm	650	647-653	37	20-45
AZ 550 nm	550	547-553	45	20-45
AZ 500 nm	500	500-508	45	20-45

It is possible to add all the relevant component peaks, but that would mean adding nine peaks from azure A/B/C and an additional seven from MB monomer/ dimer/ trimer. With such a large number of variables, it would generate less physically meaningful results. Peak deconvolution should be performed with fewer variables when possible. After extensive testing, having four peaks to represent mixed azure A/B/C species is the minimum requirement to achieve reasonable peak deconvolution.

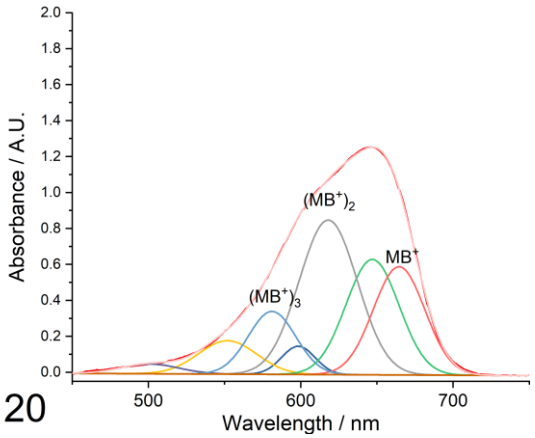
A typical deconvolution result using sample **20N** with 420 nm long pass filtered irradiation is shown in Figure 3.22.



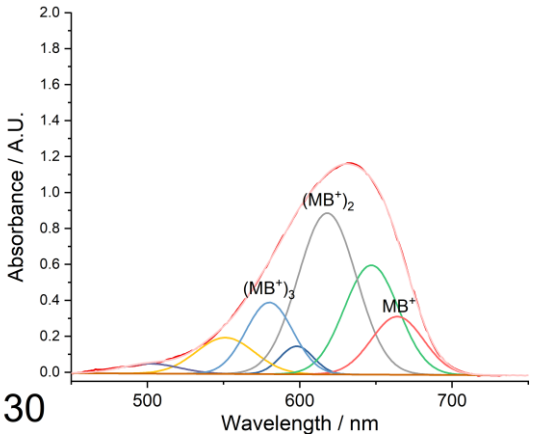
00



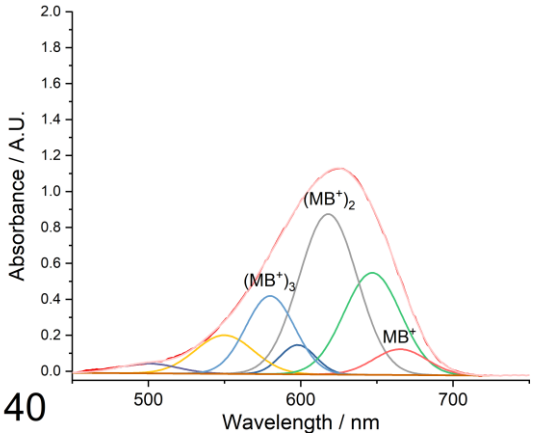
10



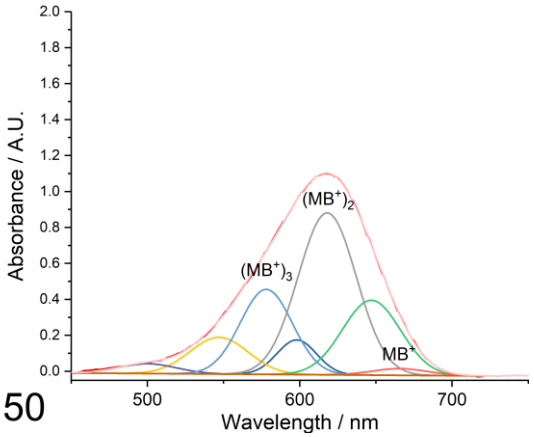
20



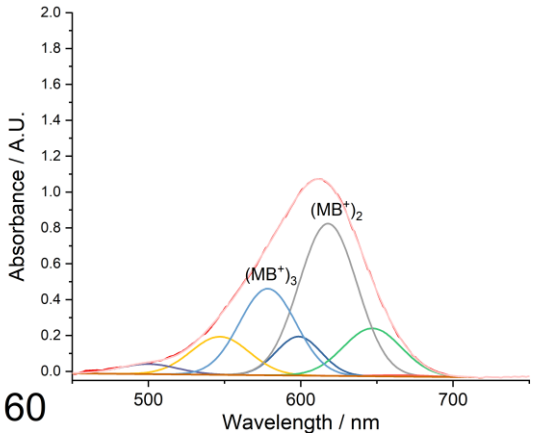
30



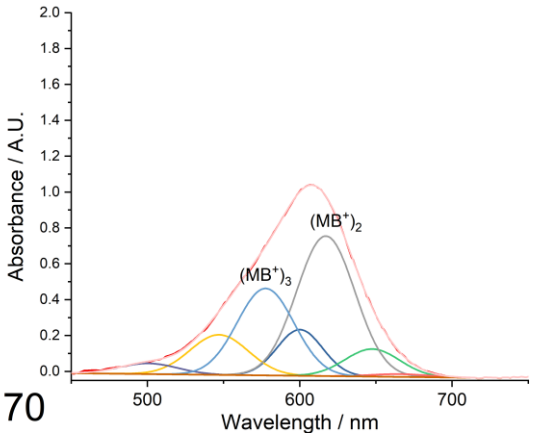
40



50



60



70

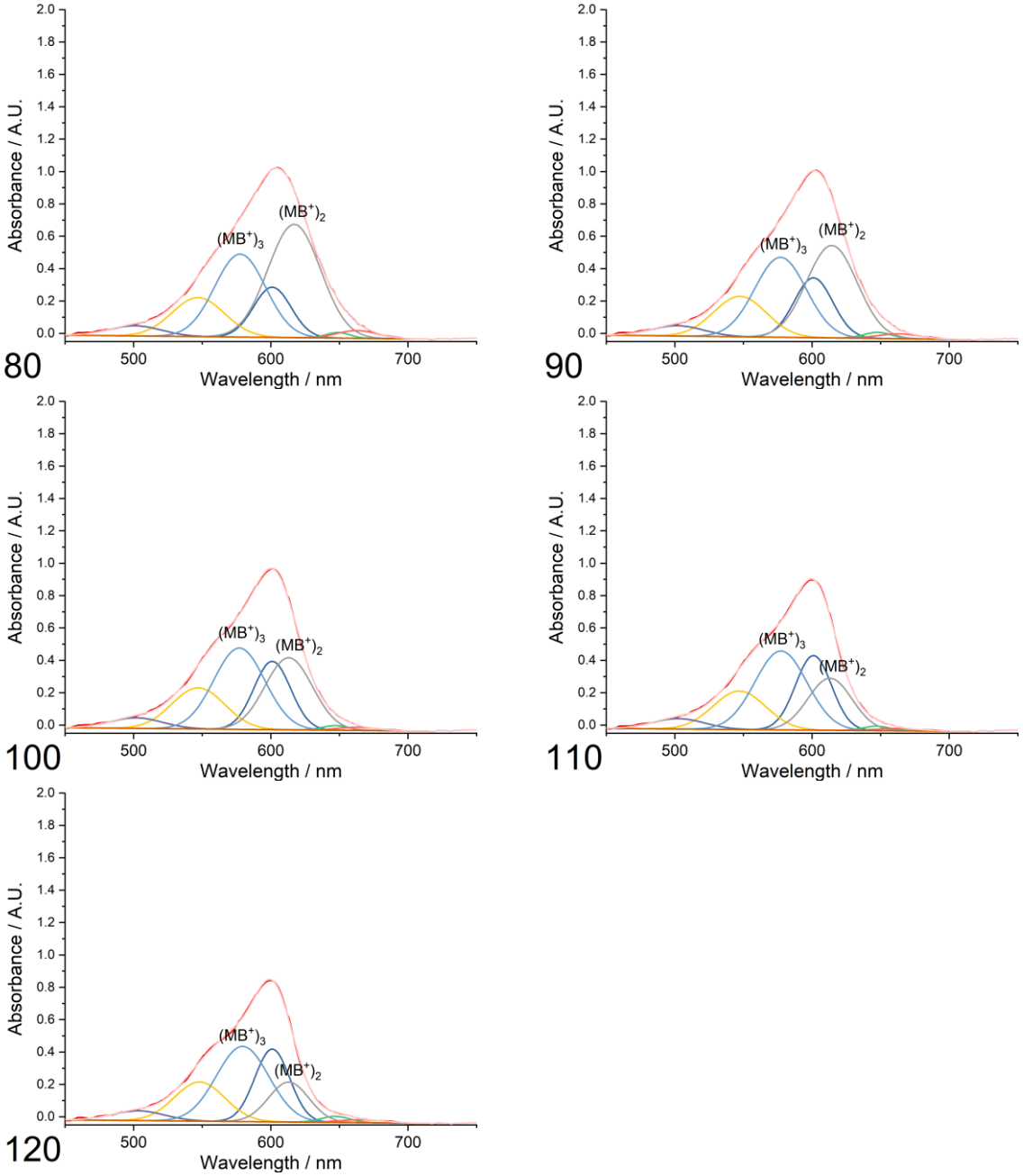
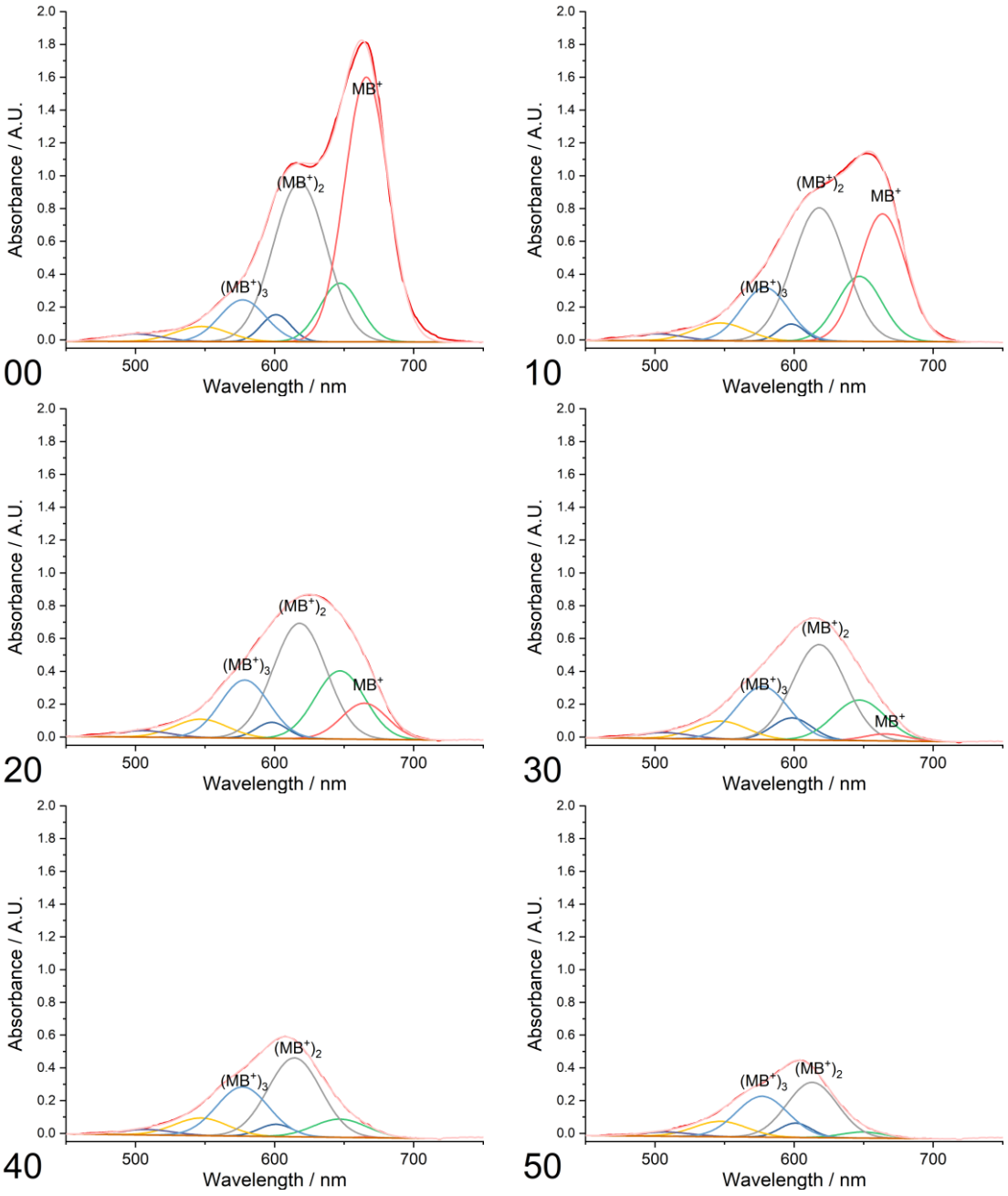


Figure 3.22. Deconvoluted MB absorption spectra under filtered irradiation (>420 nm) using N-doped samples **20N** with an increase in irradiation time from 00 min to 120 mins.

Under visible irradiation (420 nm long pass filtered), deconvoluted MB monomer peak disappeared around 50-60 mins during degradation. But simply using 664 nm MB monomer absorption maximum as the indicator, the value does not reach zero until 120 min. If photocatalytic performance is probed using MB monomer degradation rate, this significant difference between deconvoluted peak height and absorption maximum at 664 nm will result

in the wrong determination of reaction rate. Azure A/B/C peaks exist throughout the entire degradation process. At the end of degradation (120 mins), MB dimer and trimer peaks are still present while MB monomer is absent. This is the main cause of the hypsochromic shift in MB absorption spectra. A typical deconvolution result using sample **20N** with unfiltered irradiation is shown in Figure 3.23.



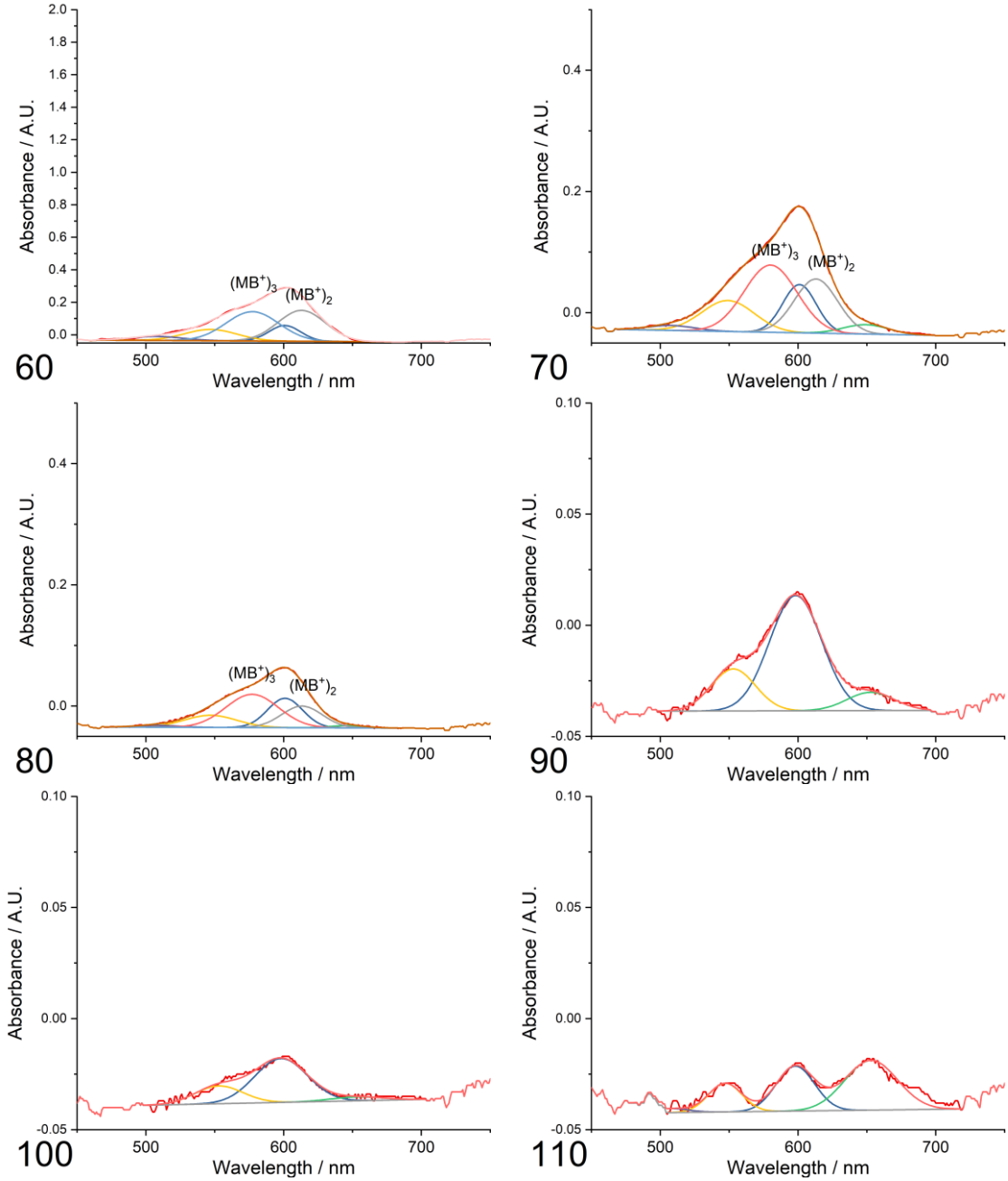


Figure 3.23. Deconvoluted MB absorption spectra under unfiltered irradiation using N-doped samples 20N with an increase in irradiation time from 00 min to 110 mins.

Under unfiltered irradiation, MB monomer peak disappears around 30-40 mins into the degradation process which is earlier than 420 nm long pass filtered irradiation results (50-60 mins). After the disappearance of MB monomer peak, MB dimer and trimer peaks persisted until 80-90 mins during the degradation process. This suggests MB is the preferred substance for degradation. At the end of the degradation process (90-110 mins) only **AZ 550**

nm, **AZ 600 nm** and **AZ 650 nm** component peaks of the azure A/B/C exists. This suggests azure A/B/C are intermediary degradation products of MB, which agrees with findings using liquid chromatography–mass spectrometry (LC-MS) analysis.[40]

In conclusion, the deconvolution of MB absorption spectrum requires a total of seven peaks: a MB monomer peak (**MB1**) at 664 nm, a MB dimer peak (**MB2**) at 615 nm, a MB trimer peak (**MB3**) at 580 nm, and four peaks (**AZ 500 nm**, **AZ 550 nm**, **AZ 600 nm** and **AZ 650 nm**) to represent the total mixed species of azure A, B and C. The azure A/B/C was identified as the intermediary degradation product of MB.

3.3.5 Direct hole oxidation of methylene blue on N-doped TiO_2 surface

In this section, based on deconvolution results, a direct hole oxidation model for MB degradation is proposed to explain the hypsochromic effect in the degradation spectra. This demonstrated that using N-doped TiO_2, the MB degradation process occur on the surface of photocatalyst rather than in the solution.

Traditional AOP uses photochemically produced hydroxyl or superoxide radicals to oxidise MB monomer/ dimer/ trimer at the same rate, which leads to an even decrease of MB absorption spectra.[41,42] However, AOP that uses direct surface oxidation, selective absorption of MB monomer/ dimer lead to uneven degradation of MB monomer/ dimer which yields an hypsochromic shifted degradation spectra.[32] Moreover, N-demethylation of MB at TiO_2 surface was proposed by Zhang and co-workers that MB is sequentially degraded to azure B, azure A, azure C, thionine and eventual mineralisation using surface

radicals, which yields a similar hypsochromic effect.[43] Thus, based on previous models, a direct hole oxidation model is proposed. In this model, MB monomer is oxidised to azure A/B/C and eventual mineralisation on the surface of N-doped TiO_2 using photogenerated holes. This degradation model is presented in Figure 3.24.

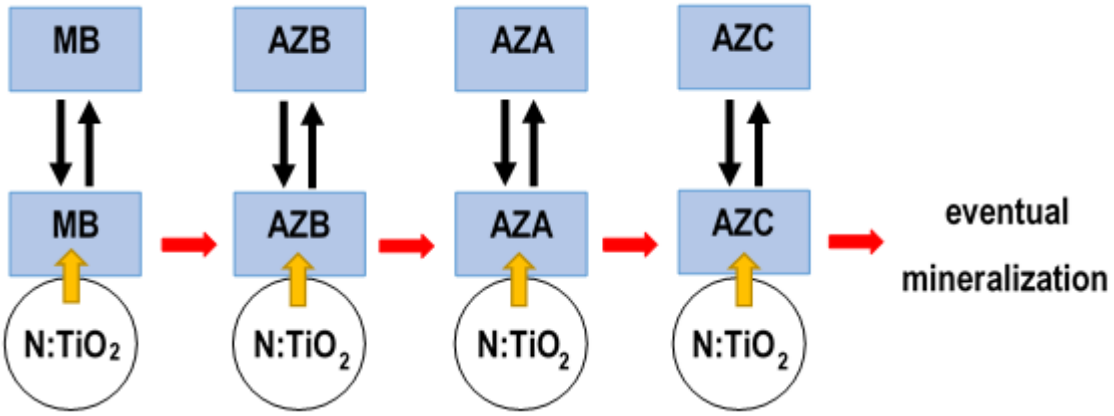


Figure 3.24. Scheme depicting degradation of MB through direct hole oxidation on the N-doped TiO_2 particle surface during the photodegradation of MB. The chemisorption/desorption of MB monomer (MB) and N-demethylated species of azure A/ B/ C (AZA/AZB/AZC) are shown with black arrows, the direction of photocatalytic degradation is shown with red arrow, and photogenerated hole oxidation on the photocatalyst surface is shown with yellow arrow.

Previously it is identified that azure A/ B/ C are intermediary degradation product of MB. The **AZ 650 nm** peak at 650 nm is the major component peak for both azure A and azure B.[39] Plotting the evolution of deconvoluted peak area for MB monomer (**MB1**) and azure A/B (**AZ 650 nm**) yields the data in Figure 3.25.

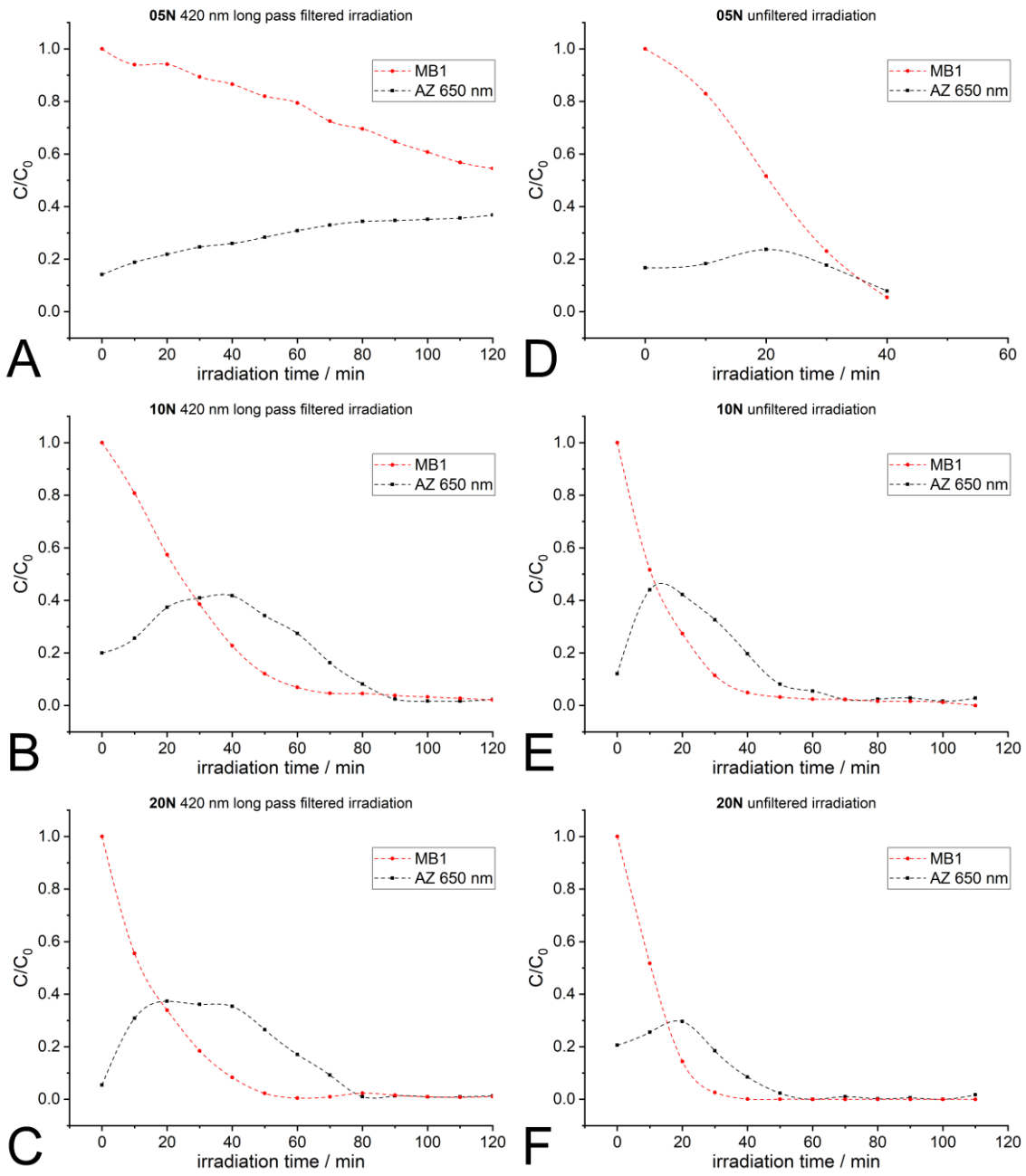
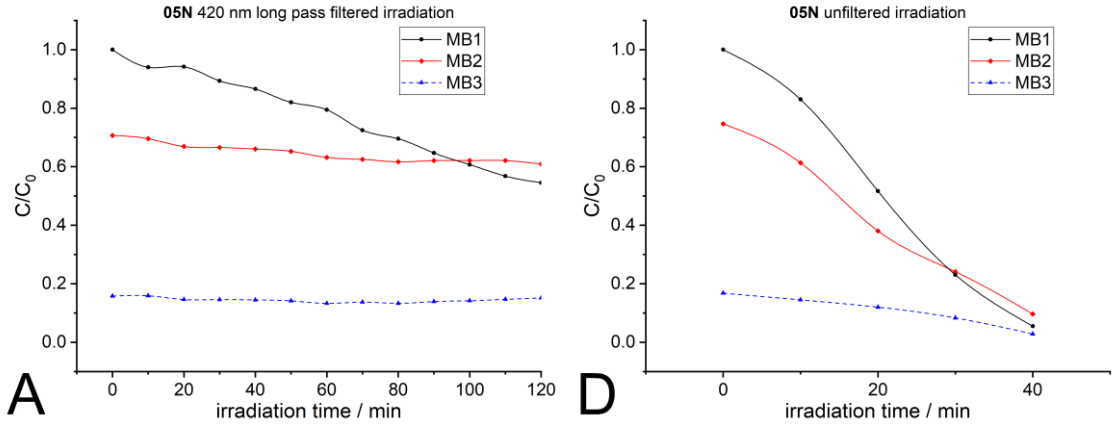


Figure 3.25. Temporal evolution of the deconvoluted peak area for methylene blue monomer (**MB1**) and azure A/B (**AZ 650**) using filtered irradiation (>420 nm) with N-doped TiO_2 samples (A) 0.5 mL (**05N**), (B)1 mL (**10N**) and (C) 2 mL (**20N**) concentrated nitric acid added in alcohol precursor solution; and using unfiltered irradiation with the same N-doped TiO_2 samples (D) **05N**, (E) **10N** and (F) **20N**.

It is obvious that the increase in azure A/B concentration is associated with the rapid decrease in MB monomer concentration with all N-doped TiO_2 samples (**05N**, **10N** and **20N**) under different irradiation conditions (unfiltered and 420 nm long pass filtered). This

reaffirms the fact that azure A/B are intermediary degradation product of MB. There is a clear trend of increased degradation rate when irradiation is switched from filtered (>420 nm) to unfiltered. The higher-energy photons from UV spectrum can be converted to higher energy holes that enhances the oxidative rate using N-doped TiO_2.

According to the proposed direct hole oxidation model, MB monomer is degraded on the surface with photogenerated holes. However, the percentage of absorbed MB species is small compared to MB species in the solution. (see experimental chapter) Thus the MB monomer/ dimer/ trimer equilibrium is maintained in the solution. Moreover, due to the low energy of photogenerated hole, the rate of MB dimer and trimer oxidation is significantly reduced under visible spectrum irradiation. The uneven degradation rate of MB monomer and dimer leads to a hypsochromic shift of MB absorption spectra. Plotting the evolution of deconvoluted peak area for MB monomer (**MB1**) dimer (**MB2**) and trimer (**MB3**) in Figure 3.26.



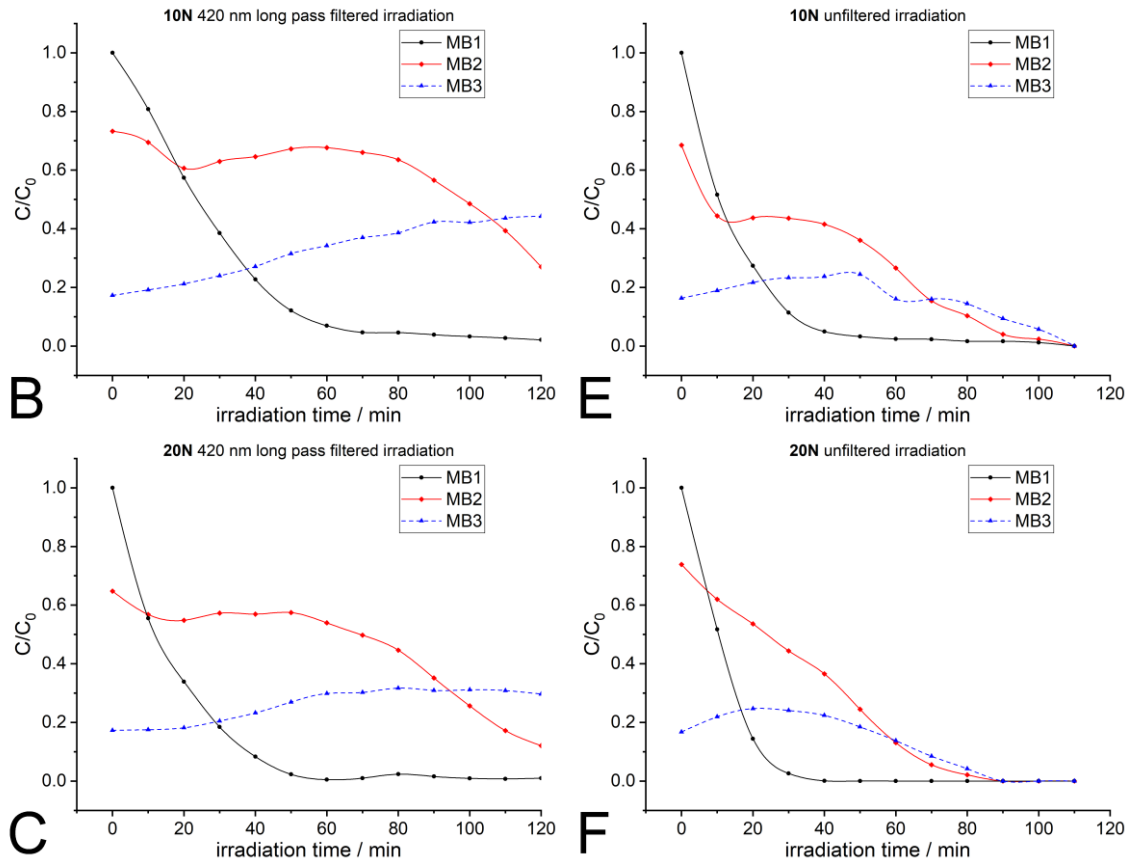


Figure 3.26. Temporal evolution of the deconvoluted peak area for MB monomer (**MB1**) dimer (**MB2**) and trimer (**MB3**) using filtered irradiation (>420 nm) with N-doped TiO_2 samples (A) 0.5 mL (**05N**), (B)1 mL (**10N**) and (C) 2 mL (**20N**) concentrated nitric acid added in alcohol precursor solution; and using unfiltered irradiation with the same N-doped TiO_2 samples (D) **05N**, (E) **10N** and (F) **20N**.

It is obvious that MB monomer concentration (**MB1**) constantly decreases throughout its existence in every scenario. The MB dimer and trimer concentration behaviour, however, is quite interesting. For low nitrogen doping level, sample **05N** (2.2% N-doped), the MB dimer/trimer concentration decreased uniformly with MB monomer concentration under unfiltered irradiation. (Figure 3.26 D) This kind of kinetics is consistent with undoped TiO_2 results, which MB monomer/ dimer/ trimer are reduced on the TiO_2 surface without changing the monomer/ dimer/ trimer equilibrium.[37] Under filtered irradiation the MB dimer/trimer concentration remained constant. (Figure 3.26 A) This is due to reduced energy

of photogenerated electron which lead to reduced MB dimer/ trimer oxidation rate. With higher N-doping levels, for sample **10N** (3.0% N-doped) and **20N** (4.1% N-doped), the dimer/trimer concentration had a temporal increase before eventual decreasing. It is believed this is a result of two factors: 1) decreased photogenerated electron energy due to either reduced photon energy or decreased band gap, 2) shift of MB monomer/ dimer/ trimer equilibrium due to MB monomer detachment.

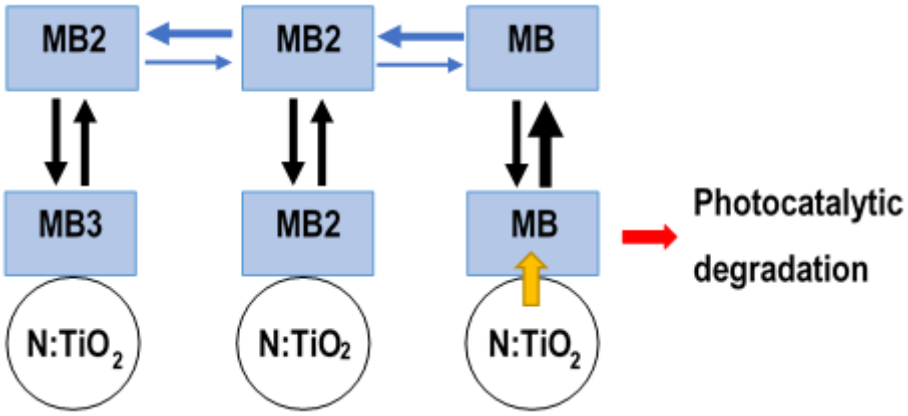


Figure 3.27. Scheme depicting dynamic equilibrium of MB monomer/ dimer/ trimer (MB1/MB2/MB3) under irradiation. The dynamic equilibrium of MB species in solution are shown in blue arrows, the chemisorption/desorption of MB species are shown with black arrows, the direction of photocatalytic degradation is shown with red arrow, and photogenerated hole oxidation on the photocatalyst surface is shown with yellow arrow.

Under dark conditions, MB species are attracted to the N-doped TiO_2 surface through electrostatic interactions between N-methyl groups (positively charged) and Ti-OH (negatively charged).[37] Then the N-methyl groups of MB species form hydrogen bonds with amine groups of N-doped TiO_2 which firmly binds MB species on the surface of photocatalyst. Under irradiation, the N-doped TiO_2 surface becomes positively charged which can repel MB species by electrostatic repulsion. However due to increased N-doping, (more amine groups on the material surface) the amount of hydrogen bonds increases with

MB dimer/ trimer compared to monomer, thus harder to detach. The increase in MB concentration in the solution disrupts the monomer/ dimer/ trimer equilibrium. Equilibrium constants for dimerization and trimerization are large at 282×10^3 and 9.1×10^3 L mol^{-1} respectively.[44] This lead to increase in MB dimer/ trimer concentration in the solution, and since photogenerated charge carrier energy is slower in degrading MB dimer/trimer, an overall temporal increase in MB dimer/trimer occurs.

Plotting the evolution of deconvoluted peak area for MB monomer (**MB1**) dimer (**MB2**) and trimer (**MB3**) and azure A/B (**AZ 650 nm**) of sample **20N** under unfiltered irradiation in Figure 3.28.

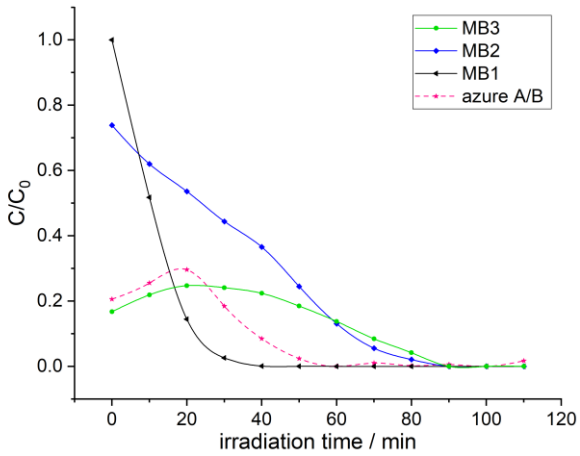


Figure 3.28 Temporal evolution of the deconvoluted peak area for MB monomer (**MB1**) dimer (**MB2**), trimer (**MB3**), and azure A/B (**AZ 650 nm**) using unfiltered irradiation with N-doped TiO_2 samples 2 mL (**20N**) concentrated nitric acid added in alcohol precursor solution.

At the early stage of MB photodegradation, MB monomer is photo-catalytically degraded to azure A/B causing an increase in concentration in the solution. At the same time, MB is desorbed from the photocatalyst surface and converted to MB dimer and trimer in the solution. At the end of the degradation process, MB dimer/trimer coexists with azure A/B/C

while MB monomer is absent. This suggests as soon as MB dimer/trimer breaks into MB monomer, MB monomer is immediately reduced to azure A/B/C. The driving force of MB dimer/trimer to monomer should be due to lack of MB monomer for further photocatalytic N-demethylation. This reaffirms the significantly reduced rate of MB dimer/trimer degradation using photocatalyst.

In conclusion, using peak deconvolution technique, hypsochromic shift is found as a result of reduced degradation rate of MB dimer/ trimer. This is due to reduced energy of photogenerated holes under visible spectrum irradiation. It is reaffirmed that azure A/B/C are intermediary degradation products of MB. Based on the N-demethylation model proposed by Zhang and co-workers,[43] a direct hole oxidation model is proposed. It is demonstrated that the MB degradation process occur on the surface of photocatalyst by direct hole oxidation rather than in the solution by traditional hydroxyl or superoxide radical oxidation.

3.3.6 Interpretation of methylene blue degradation results with hypsochromic shift

In this section, the choice of indicator for MB degradation rate analysis is investigated. It is demonstrated that the 664 nm absorption maximum is no longer a reliable indicator when pronounced hypsochromic shift in MB absorption spectra is present. Alternatively, using deconvoluted MB monomer peak area yields an overestimation of degradation rate at the early stage of degradation. The total spectrum area is an effective indicator that is efficient in determination of MB degradation rate when hypsochromic shift is present.

Traditional AOP uses photochemically produced hydroxyl or superoxide radicals to oxidise MB monomer/ dimer/ trimer at the same rate, which lead to an even decrease of MB absorption spectra. However, AOP that uses photogenerated holes for MB oxidation is limited by the photon energy. Under the visible spectrum, the photogenerated hole energy is at disadvantage in oxidising MB dimer and trimer compared to monomer thus give rise to a hypsochromic shift of MB spectra. Since the degradation rates for MB monomer/ dimer/ trimer are no longer uniform, simply using the absorption maximum at 664 nm as an indicator leads to inaccurate interpretation. This issue was observed previously. (Figure 3.16B and Figure 3.19B) For comparison, the pseudo-first-order reaction kinetics model on temporal change of 664 nm absorption maximum under filtered and unfiltered irradiation are reproduced in Figure 3.29.

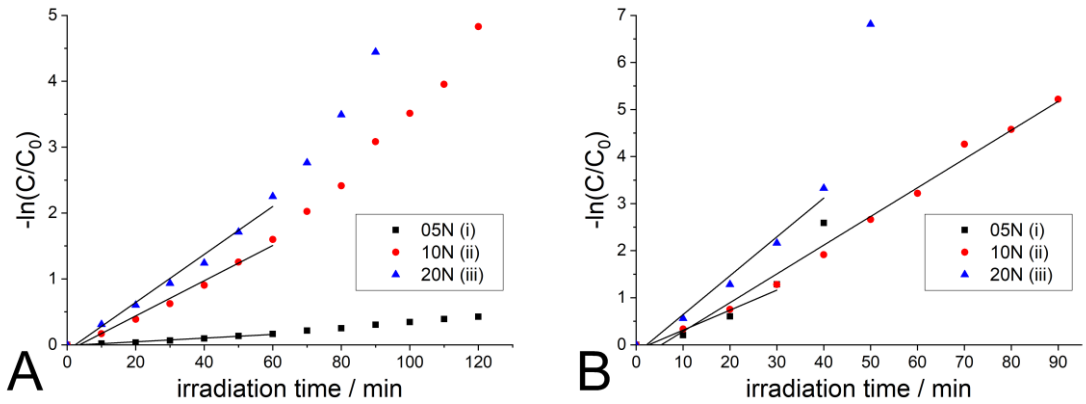


Figure 3.29. Degradation of 10 ppm MB solution using N-doped samples 0.5 mL (**05N**), 1 mL (**10N**) and 2 mL (**20N**) concentrated nitric acid added in alcohol precursor solution under (A) filtered irradiation (>420 nm) and (B) full spectrum irradiation. Temporal concentration change indicated by 664 nm absorption maximum pseudo-first-order reaction plot.

For filtered results (Figure 3.29A), **10N** and **20N** fittings show inadequate linearity, there appears to be a change in degradation rate at around 60 mins. For unfiltered results (Figure 3.29B), **05N** show worse degradation rate than **20N**. However, **05N** fully degrades MB

within 50 min which is significantly faster than 110 min using **20N**. The hypsochromic shift lead to a faster reduction

If only MB monomer is used as an indicator for photocatalytic performance. Applying the pseudo-first-order reaction kinetics model on temporal change of deconvoluted MB monomer peak area. Results from filtered and unfiltered irradiation are shown in Figure 3.30.

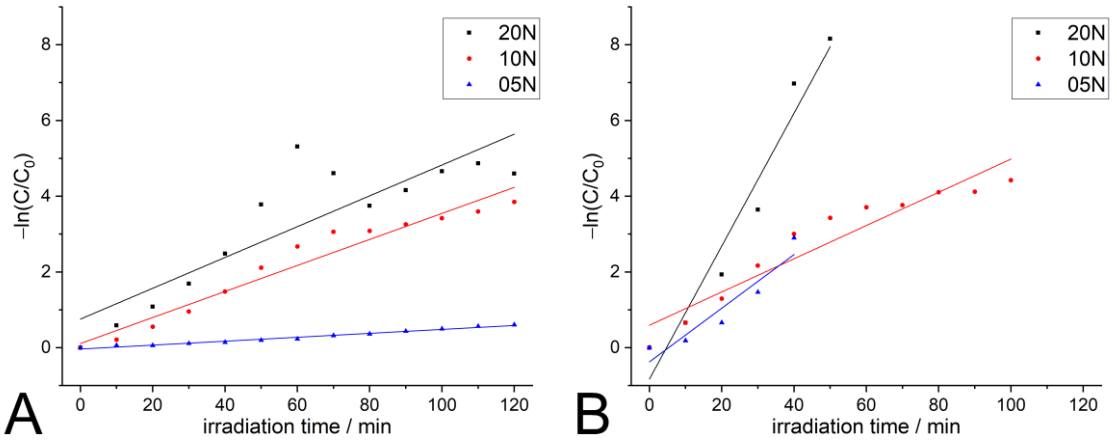


Figure 3.30. Degradation of 10 ppm MB solution using with N-doped samples 0.5 mL (**05N**), 1 mL (**10N**) and 2 mL (**20N**) concentrated nitric acid added in alcohol precursor solution under (A) filtered irradiation (>420 nm) and (B) full spectrum irradiation. Temporal concentration change indicated by deconvoluted MB monomer peak area pseudo-first-order reaction plot.

The linearity of using deconvoluted MB monomer peak area has improved compared to using 664 nm absorption maximum in Figure 3.16B and 3.18B. But for higher nitrogen doping level samples (**20N**), the fittings are unsatisfactory. Since MB monomer undergoes photocatalytic degradation and dimerization simultaneously. Just using MB monomer as an indicator will overestimate degradation rate initially which is observed in the Figure 3.30 A.

Instead of only using a single peak as degradation indicator, why not use the entire spectrum? Using the total spectrum can alleviate issues caused by the hypsochromic effect of non-

degrading chemical reactions (dimerization/ trimerization). Dimerization and trimerization lead to peak shifts, which have a significant impact on the MB monomer peak area while having very little impact on the combined peak area. Applying the pseudo-first-order reaction kinetics model on the temporal evolution of the total absorption spectrum area. Results from filtered and unfiltered irradiation are shown in Figure 3.31.

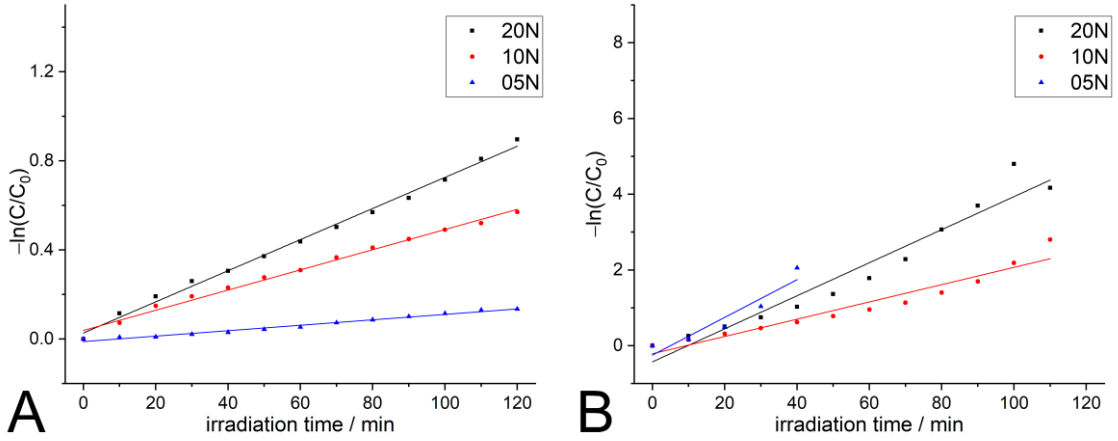


Figure 3.31. Degradation of 10 ppm MB solution using with N-doped samples 0.5 mL (**05N**), 1 mL (**10N**) and 2 mL (**20N**) concentrated nitric acid added in alcohol precursor solution under (A) filtered irradiation (>420 nm) and (B) full spectrum irradiation. Temporal concentration change indicated by total absorption peak area pseudo-first-order reaction plot.

The pseudo-first-order reaction plot using the absorption spectrum area in Figure 3.31 shows much improved linear correlation for both filtered and unfiltered results. Comparing Figure 3.31A to Figure 3.29A. It is reaffirmed that an increase in nitrogen doping increases photocatalytic properties under the visible spectrum. Comparing Figure 3.31B to Figure 3.29B. It is corrected that **05N** is the better photocatalyst under unfiltered irradiation which agrees with degraded MB absorption spectra overlay shown in the previous section. (Figure 3.16) Using temporal evolution of the total absorption spectrum area (Figure 3.31B) yields a correct interpretation of photocatalytic activity compared to using the MB monomer 664 nm absorption maximum (Figure 3.29B).

In conclusion, using the total spectrum area is an effective yet efficient way of characterising MB degradation results with a hypsochromic shift. The 664 nm absorption maximum is no longer a reliable indicator for MB degradation rate determination.

3.3.7 Sb/N co-doped TiO_2

The Sb-doped TiO_2 and SnO_2 were studied intensely in the past decades showing promising prospects of narrowing the band gap of TiO_2 and SnO_2.[45–47] So far, only Sb-doped SnO_2 reports yields good photocatalytic performance.[48] The lack of exciting reports on photocatalytic performance increase using Sb-doped TiO_2 suggests antimony may be an unfavourable trapping site reducing the charge carrier lifetime, which overshadowed the improvements in band gap reduction. Based on previous findings that alcohol prepared N-doped TiO_2 increases photocatalytic activity under the visible spectrum irradiation. In this section, Sb/N co-doping approach is investigated to mitigate the adverse effect of Sb trapping sites.

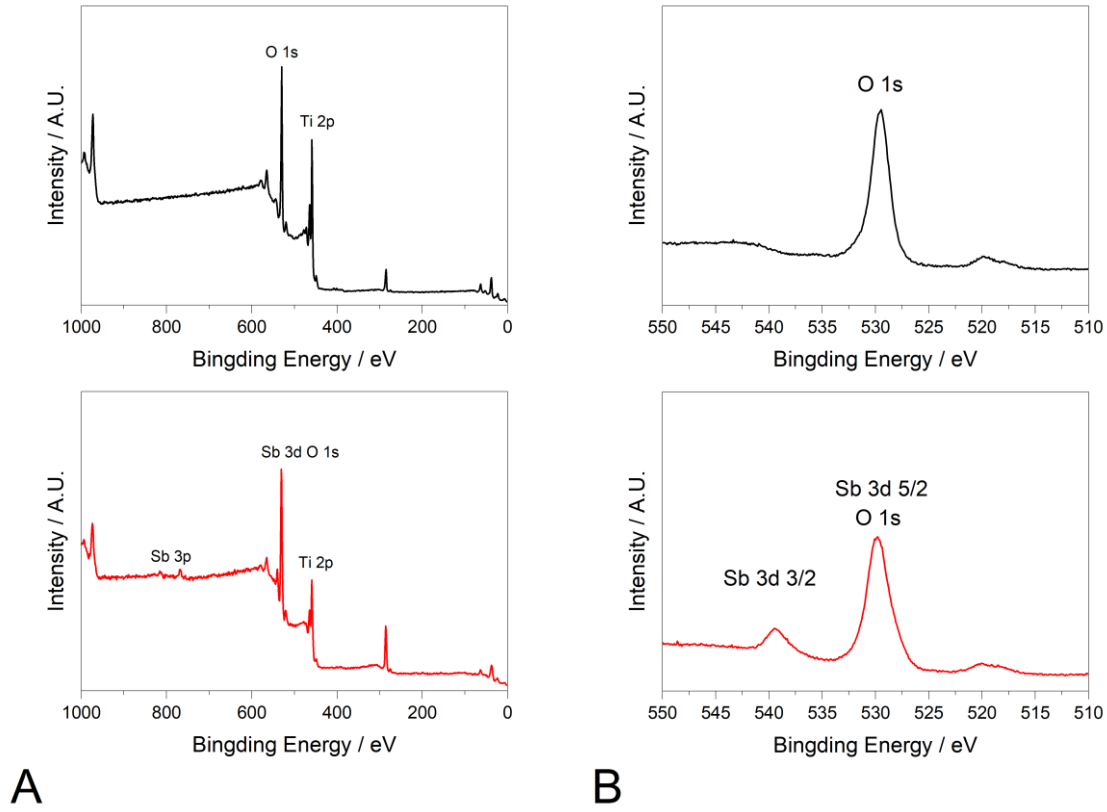


Figure 3.32. XPS (A) survey spectra and (B) Sb 3d core level spectra for the Sb-doped (red line) and undoped (black line) TiO_2.

The 10 % Sb-doped TiO_2 and undoped TiO_2 were synthesised using the aqueous approach. The products were annealed at 600 °C for 10 h. XPS data confirms the incorporation of antimony (Figure 3.32).

The results of MB degradation with 400 nm long pass filtered irradiation is presented in Figure 3.33, and the temporal evolution with filtered (>400 nm) irradiation is shown in Figure 3.34.

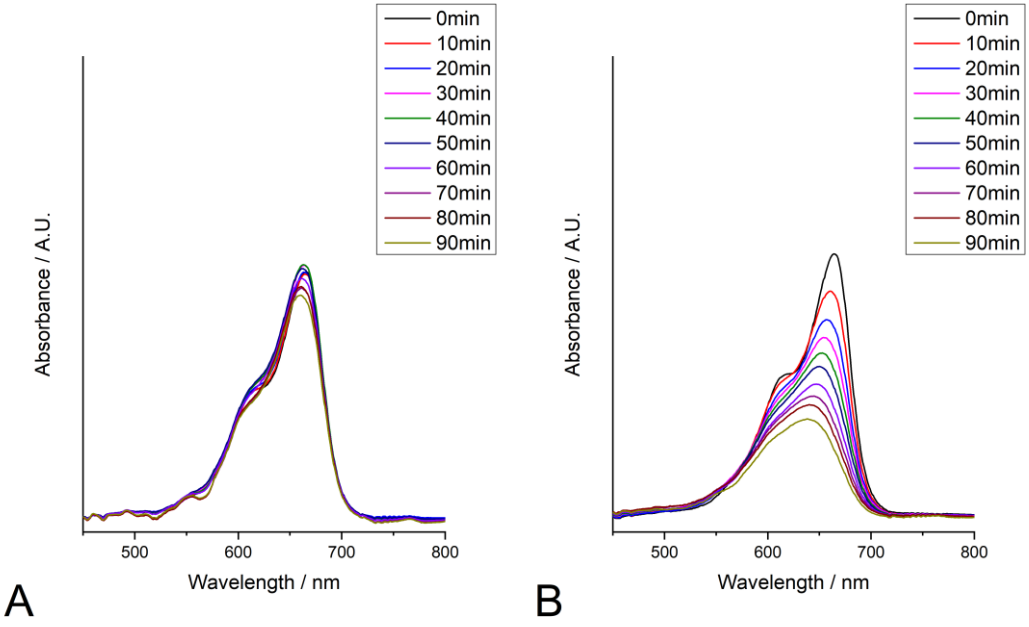


Figure 3.33. Absorption spectra change of 10 ppm MB solution degraded with aqueously prepared (A) 10% Sb-doped TiO_2 and (B) undoped TiO_2 under 400 nm long pass filtered irradiation.

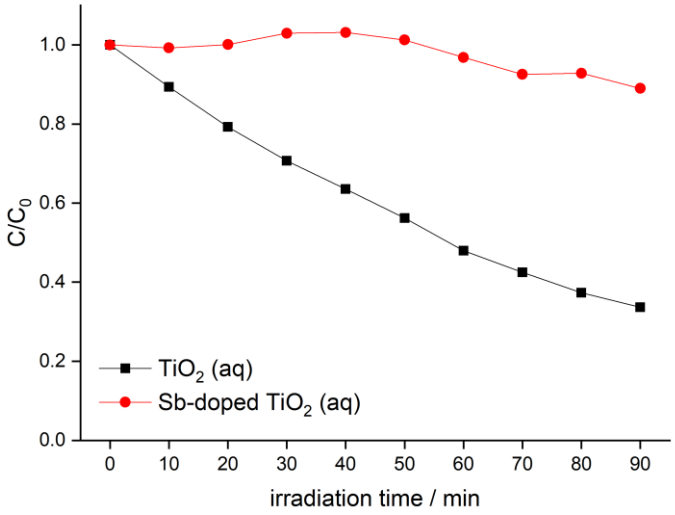


Figure 3.34. Temporal evolution of the concentration of 10 ppm MB indicated by C/C_0 for 664nm absorption maximum using aqueous prepared: 10% Sb-doped TiO_2 (red dot) and undoped TiO_2 (black square) under 400 nm long pass filtered irradiation.

The absorbance change at the 664 nm absorption maximum was used as an indicator for photocatalytic activity. The Sb-doped TiO_2 sample was found to be less active compared to

the undoped TiO_2 sample. This could be due to the large number of trapping sites created by heavy Sb doping which leads to the reduction in charge carrier lifetime.

The Sb/N co-doping improvements were investigated by synthesizing 10 % Sb-doped TiO_2 using the alcohol approach (described in the experimental section) with 1 mL and 2 mL of concentrated nitric acid in alcohol precursor solution (25 mL). All samples were annealed at 300 °C for 10 h in a muffle furnace with an alumina boat as a container. The results of MB degradation with 400 nm long pass filtered irradiation is presented in Figure 3.35, and the temporal evolution of 664 nm absorption maximum with filtered (>400 nm) irradiation is shown in Figure 3.36.

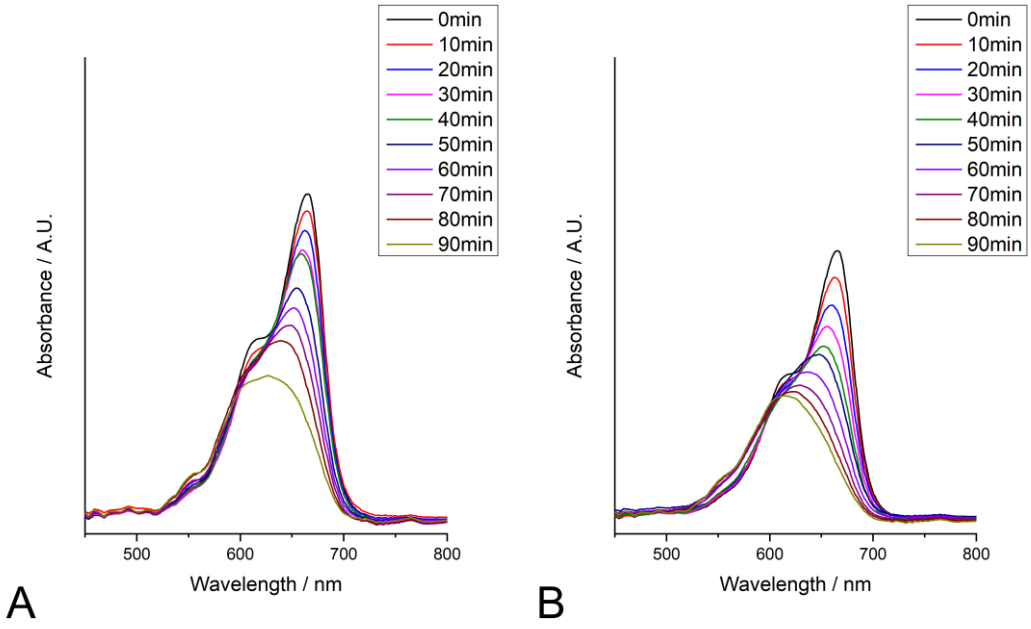


Figure 3.35. Absorption spectra change of 10 ppm MB solution degraded with 10% Sb-doped TiO_2 prepared with (A) 1 mL and (B) 2 mL HNO_3 in precursor solution using alcohol approach. Irradiation spectrum was filtered with 400 nm long pass UV filter.

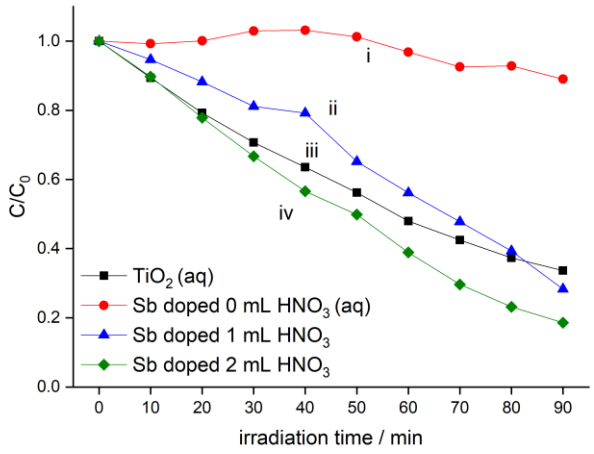


Figure 3.36. Temporal concentration change of 10 ppm MB solution indicated by C/C_0 for 664 nm absorption peak using samples (i) aqueous prepared 10% Sb-doped TiO_2, (ii) alcohol prepared 10% Sb-doped TiO_2 adding 1 ml HNO_3 in precursor solution, (iii) aqueous prepared undoped TiO_2 and (iv) alcohol prepared 10% Sb-doped TiO_2 adding 2 ml HNO_3 in precursor solution.

The photocatalytic performance of alcohol prepared Sb/N co-doped TiO_2 exceeds that of previous aqueously prepared undoped TiO_2. This improvement should be due to nitrogen doping by adding HNO_3 in the alcohol precursor solution, which is thoroughly investigated in the previous sections. It appears that nitrogen incorporation using the alcohol approach can somewhat mitigate the adverse effect of Sb doping. However, due to limited time, the details of Sb/N co-doped TiO_2 are not further investigated. This could be of interest in the future regarding a range of co-doping studies with group 5 elements.

3.4 Conclusion

This chapter can be divided into two parts: material synthesis and MB degradation. In the material synthesis part, an efficient one-pot solvothermal evaporation process was developed to efficiently produce N-doped anatase TiO_2 powder with varying doping level nitrogen up to 4.1%. In the photocatalytic degradation of MB part, a novel MB absorption

spectrum peak deconvolution technique is proposed using an adaptation of a peak fitting software (Casa XPS). This deconvolution procedure that permits a detailed evaluation of the MB monomer, dimer, trimer, and intermediary product concentrations during photodegradation experiments which facilitates the explanation MB degradation kinetics.

In the first section, the solvothermal preparation process was optimized regarding roasting time and mortar grinding. It is identified that mortar grinding is essential in obtaining a high performing N-doped TiO_2 powder and roasting time has little impact on photocatalytic performance.

In the second section, the influence on the nitrogen doping level due to annealing temperature was studied. Increase in annealing temperature from 250 °C to 400 °C leads to a drop in nitrogen doping level. Annealing temperature beyond 350 °C lead to complete loss of nitrogen incorporation supported with XPS data. 300 °C annealing temperature was identified to be the optimum annealing temperature for N-doped TiO_2 powder. In the third section, influence on nitrogen doping level due to nitric acid precursor was studied. The increase in concentrated nitric acid precursor from 0.5 mL to 2 mL per 25 mL precursor solution leads to a higher nitrogen doping level and increase in photocatalytic performance under visible spectrum irradiation.

In the fourth section, the peak deconvolution method for MB absorption spectra was presented for sample **20N** (2 mL concentrated nitric acid per 25 mL precursor solution). Three peaks were selected to represent MB monomer, dimer and trimer composition: 664 nm for monomer (**MB1**), 615 nm for dimer (**MB2**) and 580 nm for trimer (**MB3**). Four

component peaks (**AZ 500 nm**, **AZ 550 nm**, **AZ 600 nm** and **AZ 650 nm**) are used to represent the total mixed species of azure A, B and C. Peak deconvolution yields good fitting for results under full-spectrum and 420 nm long pass filtered irradiation.

In the fifth section, peak deconvolution results for samples **05N**, **10N** and **20N**, correspond to adding 0.5 mL, 1 mL and 2 mL of concentrated nitric acid to alcohol precursor solution (25 mL), were investigated. Based on the N-demethylation model proposed by Zhang and co-workers,[43] a direct hole oxidation model is proposed. The photocatalytic degradation of MB takes place via the sequential decomposition of methyl groups from MB to azure A/B/C and further mineralisation on the surface of N-doped TiO_2 through direct hole oxidation rather than traditional hydroxyl or superoxide radical oxidation. The energy of photogenerated holes is at a disadvantage in oxidising MB dimer/ trimer reducing the degradation rate. The uneven degradation rate of MB monomer/ dimer/ trimer leads to the hypsochromic shift in the MB degradation spectra.

In the sixth section, The total MB absorption spectrum area was found to be a better indicator of MB degradation compared to traditional absorption maximum at MB monomer peak position (664 nm), which is well suited for absorption spectra with uneven peak reduction rate (such as hypsochromic shift). Temporal evolution of total absorption area agrees with pseudo-first-order reaction kinetics.

Finally, the effect of Sb doping was briefly investigated showing a negative impact on photocatalytic activity. Sb/N co-doping approach is investigated which somewhat mitigated the adverse effect of Sb doping.

In conclusion, nitrogen doping enables photocatalytic response of anatase TiO_2 under visible spectrum (>420 nm) irradiation. The novel aspect of the 2-propanol/HNO_3 based one-pot sol-gel evaporation method is the ability to synthesise highly N-doped TiO_2 nanoparticles with doping level up to 4.1 atomic % at low temperature. 4.1% N-doped TiO_2 sample prepared using 2 mL concentrated nitric acid in 25 mL 2-propanol solution (0.5 M Ti concentration) and annealed at 300 °C for 10 h yield best MB degradation results under visible spectrum irradiation. This process could potentially be used other metal oxide semiconductor materials such as ZnO and SnO_2. It is possible that increasing concentrated nitric acid beyond 2 mL per 25 mL precursor solution could further increase nitrogen doping level and improve MB degradation efficiency, which may be of interest for future study.

Reference

1. Carp, O., Huisman, C. L. & Reller, A. Photoinduced reactivity of titanium dioxide. *Prog. Solid State Chem.* **32**, 33–177 (2004).

2. Antonelli, D. M. & Ying, J. Y. Synthesis of Hexagonally Packed Mesoporous TiO2 by a Modified Sol-Gel Method. *Angew. Chemie Int. Ed. English* **34**, 2014–2017 (1995).

3. Crepaldi, E. L. *et al.* Controlled formation of highly organized mesoporous titania thin films: From mesostructured hybrids to mesoporous nanoanatase TiO2. *J. Am. Chem. Soc.* **125**, 9770–9786 (2003).

4. Ye, J. *et al.* Nanoporous anatase TiO2 mesocrystals: Additive-free synthesis, remarkable crystalline-phase stability, and improved lithium insertion behavior. *J. Am. Chem. Soc.* **133**, 933–940 (2011).

5. Liu, B. *et al.* Doping high-surface-area mesoporous TiO 2 microspheres with carbonate for visible light hydrogen production. *Energy Environ. Sci.* **7**, 2592 (2014).

6. Chen, X. & Mao, S. S. Titanium dioxide nanomaterials: Synthesis, properties, modifications and applications. *Chemical Reviews* **107**, 2891–2959 (2007).

7. Thompson, T. L. & Yates, J. T. Surface science studies of the photoactivation of TIO2 - New photochemical processes. *Chemical Reviews* **106**, 4428–4453 (2006).

8. Fujishima, a & Honda, K. Electrochemical photolysis of water at a semiconductor electrode. *Nature* **238**, 37–38 (1972).

9. In, S. *et al.* Effective visible light-activated B-doped and B,N-codoped TiO2 photocatalysts. *J. Am. Chem. Soc.* **129**, 13790–13791 (2007).

10. Ho, W., Yu, J. C. & Lee, S. Synthesis of hierarchical nanoporous F-doped TiO2 spheres with visible light photocatalytic activity. *Chem. Commun. (Camb).* 1115–1117 (2006). doi:10.1039/b515513d

11. Asahi, R., Morikawa, T., Ohwaki, T. & Taga, Y. Visible-Light Photocatalysis in Nitrogen-Doped Titanium Oxides. *Science (80-.).* **293**, 269–271 (2001).

12. Sakthivel, S. & Kisch, H. Daylight Photocatalysis by Carbon-Modified Titanium Dioxide. *Angew. Chemie - Int. Ed.* **42**, 4908–4911 (2003).

13. Ohno, T. *et al.* Preparation of S-doped TiO2 photocatalysts and their photocatalytic activities under visible light. *Appl. Catal. A Gen.* **265**, 115–121 (2004).

14. Li, Y., Yue, Y., Que, Z.-Q., Zhang, M. & Guo, M. Preparation and visible-light photocatalytic property of nanostructu- red Fe-doped TiO 2 from titanium containing electric furnace molten slag. *Int. J. Miner.* (2013). doi:10.1007/s12613-013-0828-y

15. Weng, H. *et al.* Electronic structure and optical properties of the Co-doped anatase TiO_{2} studied from first principles. *Phys. Rev. B* **69**, 125219 (2004).

16. Park, M. S., Kwon, S. K. & Min, B. I. Electronic structures of doped anatase TiO_2: Ti_1-xM_xO_2 (M=Co, Mn, Fe, Ni). *Phys. Rev. B* **65**, 161201 (2002).

17. Gan, L. *et al.* Oxygen sensing performance of Nb-doped TiO2 thin film with porous structure. *J. Alloys Compd.* **585**, 729–733 (2014).

18. Du, X. S., Li, Q. X., Su, H. B. & Yang, J. L. Electronic and magnetic properties of V-doped anatase TiO2 from first principles. *Phys. Rev. B* **74**, (2006).

19. Yin, W. J., Wei, S. H., Al-Jassim, M. M. & Yan, Y. Double-hole-mediated coupling of dopants and its impact on band gap engineering in TiO2. *Phys. Rev. Lett.* **106**, 066801 (2011).

20. Mwabora, J. M. *et al.* Structure, Composition, and Morphology of Photoelectrochemically Active TiO 2 - x N x Thin Films Deposited by Reactive DC Magnetron Sputtering. *J. Phys. Chem. B* **108**, 20193–20198 (2004).

21. Asahi, R., Morikawa, T., Ohwaki, T. & Taga, Y. Visible-Light Photocatalysis in Nitrogen-Doped Titanium Oxides. *Science (80-.).* **293**, 269–271 (2001).

22. Diwald, O. & Thompson, T. The effect of nitrogen ion implantation on the photoactivity of TiO2 rutile single crystals. *J. …* **108**, 52–57 (2004).

23. Ghicov, A. *et al.* Ion implantation and annealing for an efficient N-doping of TiO2 nanotubes. *Nano Lett.* **6**, 1080–1082 (2006).

24. Irie, H., Watanabe, Y. & Hashimoto, K. Nitrogen-Concentration Dependence on Photocatalytic Activity of TiO2-xNx Powders. *J. Phys. Chem. B* **107**, 5483–5486 (2003).

25. Diwald, O., Thompson, T. L., Zubkov, T., Walck, S. D. & Yates, J. T. Photochemical Activity of Nitrogen-Doped Rutile TiO 2 (110) in Visible Light. *J. Phys. Chem. B* **108**, 6004–6008 (2004).

26. Prokes, S. M., Gole, J. L., Chen, X., Burda, C. & Carlos, W. E. Defect-related optical behavior in surface-modified TiO2 nanostructures. *Adv. Funct. Mater.* **15**, 161–167 (2005).

27. Gole, J. L., Stout, J. D., Burda, C., Lou, Y. & Chen, X. Highly Efficient Formation of Visible Light Tunable TiO 2 - x N x Photocatalysts and Their Transformation at the Nanoscale. *J. Phys. Chem. B* **108**, 1230–1240 (2004).

28. Morikawa, T., Asahi, R., Ohwaki, T., Aoki, K. & Taga, Y. Band-Gap Narrowing of Titanium Dioxide by Nitrogen Doping. *Jpn. J. Appl. Phys.* **40**, L561–L563 (2001).

29. Burda, C. *et al.* Enhanced nitrogen doping in TiO2 nanoparticles. *Nano Lett.* **3**, 1049–1051 (2003).

30. Lin, Z., Orlov, A., Lambert, R. M. & Payne, M. C. New insights into the origin of visible light photocatalytic activity of nitrogen-doped and oxygen-deficient anatase TiO2. *J. Phys. Chem. B* **109**, 20948–20952 (2005).

31. Sakthivel, S., Janczarek, M. & Kisch, H. Visible light activity and photoelectrochemical properties of nitrogen-doped TiO2. *J. Phys. Chem. B* **108**, 19384–19387 (2004).

32. Zhao, Y. *et al.* Shape-dependent acidity and photocatalytic activity of Nb 2O 5 nanocrystals with an active TT (001) surface. *Angew. Chemie - Int. Ed.* **51**, 3846–3849 (2012).

33. Biesinger, M. C., Lau, L. W. M., Gerson, A. R. & Smart, R. S. C. Resolving surface chemical states in XPS analysis of first row transition metals, oxides and hydroxides: Sc, Ti, V, Cu and Zn. *Appl. Surf. Sci.* **257**, 887–898 (2010).

34. Miller, D. J., Biesinger, M. C. & McIntyre, N. S. Interactions of CO2and CO at fractional atmosphere pressures with iron and iron oxide surfaces: One possible mechanism for surface contamination? *Surf. Interface Anal.* **33**, 299–305 (2002).

35. Mohtasebi, A., Chowdhury, T., Hsu, L. H. H., Biesinger, M. C. & Kruse, P. Interfacial Charge Transfer between Phenyl-Capped Aniline Tetramer Films and Iron Oxide Surfaces. *J. Phys. Chem. C* **120**, 29248–29263 (2016).

36. Parra, E. R., Jose, P., Arango, A. & Benavides, V. J. XPS STRUCTURE ANALYSIS OF TiN / TiC BILAYERS PRODUCED BY PULSED VACUUM ARC DISCHARGE ANÁLISIS ESTRUCTURAL DE BICAPAS DE TiN / TiC. 64–74 (2010).

37. Liu, B. *et al.* Polymeric adsorption of methylene blue in TiO 2 colloids-Highly sensitive thermochromism and selective photocatalysis. *Chem. - A Eur. J.* **18**, 12705–12711 (2012).

38. Narband, N. Nanoparticles and photosensitisers; their interactions and antibacterial properties. (2009).

39. Marbán, G., Vu, T. T. & Valdés-Solís, T. A simple visible spectrum deconvolution technique to prevent the artefact induced by the hypsochromic shift from masking the concentration of methylene blue in photodegradation experiments. *Appl. Catal. A Gen.* **402**, 218–223 (2011).

40. Rauf, M. A., Meetani, M. A., Khaleel, A. & Ahmed, A. Photocatalytic degradation of Methylene Blue using a mixed catalyst and product analysis by LC/MS. *Chem. Eng. J.* **157**, 373–378 (2010).

41. Teh, C. M. & Mohamed, A. R. Roles of titanium dioxide and ion-doped titanium dioxide on photocatalytic degradation of organic pollutants (phenolic compounds and dyes) in aqueous solutions: A review. *J. Alloys Compd.* **509**, 1648–1660 (2011).

42. Konstantinou, I. K. & Albanis, T. A. TiO2-assisted photocatalytic degradation of azo dyes in aqueous solution: Kinetic and mechanistic investigations: A review. *Appl. Catal. B Environ.* **49**, 1–14 (2004).

43. Zhang, T. *et al.* Photooxidative N-demethylation of methylene blue in aqueous TiO2dispersions under UV irradiation. *J. Photochem. Photobiol. A Chem.* **140**, 163–172 (2001).

44. Heger, D., Jirkovský, J. & Klán, P. Aggregation of methylene blue in frozen aqueous solutions studied by absorption spectroscopy. *J. Phys. Chem. A* **109**, 6702–6709 (2005).

45. Terrier, C., Chatelon, J. P. & Roger, J. A. Electrical and optical properties of Sb:SnO2 thin films obtained by the sol-gel method. *Thin Solid Films* **295**, 95–100 (1997).

46. Taverner, A. E., Gulino, A., Egdell, R. G. & Tate, T. J. A photoemission study of electron states in Sb-ion implanted TiO2(110). *Appl. Surf. Sci.* **90**, 383–387 (1995).

47. Gulino, A., Taverner, A. E., Warren, S., Harris, P. & Egdell, R. G. A photoemission study of Sb-doped TiO2. *Surf. Sci.* **315**, 351–361 (1994).

48. Peng, Q. *et al.* Solution-processed, antimony-doped tin oxide colloid films enable high-performance TiO2 photoanodes for water splitting. *Nano Lett.* **13**, 1481–1488 (2013).

Chapter 4 Sn-Doped Anatase TiO_2 Thin Film

4.1 Introduction

As mentioned in the introduction chapter of this thesis, titanium dioxide (TiO_2) is a popular photocatalyst in solar energy conversion and environmental applications. There is a growing interest in modifying TiO_2 to improve its performance in photocatalytic reactions such as degradation of organic pollutants, production of hydrogen from water and photovoltaic applications.[1–5]

Both anatase and rutile polymorphs of TiO_2 have limited ability to bring about photo-catalytic reactions under visible light irradiation, because of the large band gap (rutile 3.06 eV, anatase 3.20 eV at room temperature[6]). However, under UV irradiation catalytic activity is observed. Despite its wider bandgap anatase is generally found to be the better photocatalyst.[7] This is probably due to the efficient separation of the photoexcited electron-hole pairs enabled by improved charge carrier lifetime in the anatase phase.[8] The longer lifetime of photoexcited electrons and holes in anatase is because it has an indirect band gap (rutile has a direct band gap), thus, direct transitions of photogenerated electrons from the conduction band (CB) to valence band (VB) in anatase TiO_2 is impossible.[9]

Extensive research has been conducted to modify TiO_2 in order to enhance performance in the visible region. Previous group members discovered that Sn-doped anatase and rutile TiO_2 exhibits improved photocatalytic activity in methylene blue degradation.[10,11] However,

whether this superior advanced oxidation processes (AOPs) capability with Sn doping can be translated into enhanced PEC water splitting remains a question.

In this chapter, Sn-doped anatase TiO_2 thin films were grown on a 5%Nb:$SrTiO_3$ (001) conductive single crystalline substrate. Sn-doping was investigated as a potential method in improving PEC water splitting performance of anatase TiO_2 thin films. The PEC performance of Sn-doped anatase TiO_2 thin film was investigated with a three-electrode setup using CV under simulated solar irradiation. A 54% increase in photocurrent at 1.23 V vs RHE was achieved using 10% Sn doping under simulated one sun illumination. A comprehensive review on band structures at semiconductor-electrolyte interface under illumination was carried out to revaluate the interpretation of current-voltage data.

4.2 Experimental

Sn-doped anatase TiO_2 thin film was grown using the sol-gel dip-coating method discussed in the experimental chapter. This process is composed of 3 parts: a) preparation of metal alkoxide solution, b) dip-coating process and c) furnace annealing.

25 mL of 2-propanol (CHROMASOLV® Plus, for HPLC, 99.9% Sigma-Aldrich) was used as solvent. An appropriate amount of Titanium (IV) isopropoxide (97% Sigma-Aldrich) was then added to achieve a 0.33 M Ti concentration mixture. Various amounts of Tin (IV) tert-butoxide (≥99.99% Sigma-Aldrich) were added to create Ti^{4+}: Sn^{4+} ratio ranging from 95: 5 to 85: 15. 150 µL of Nitric acid (ACS reagent, 70% Sigma-Aldrich) was added to prevent hydrolysis of the precursor.

The 5% Nb-doped $SrTiO_3$ (001) single crystalline substrate was provided by PI-KEM. The substrate was cut to 10×10×1 mm with a single side epitaxial polished surface. For a typical dip-coating cycle, the substrate was dipped into the precursor solution and held for 5 min and slowly pulled out at a speed of 3.5 mm/min, then hydrolysed with wet nitrogen flow for 5 min. Up to 5 dip-coating cycles were used for each sample.

The coated substrate was placed in a clean alumina boat with the coated side facing up. The sample was annealed at 800°C for 10 h in argon gas and cooled down to room temperature.

4.3 Results and discussion

4.3.1 Feasibility of using Sn-doped anatase TiO_2 photoanode in PEC characterisation

There are a range of techniques to epitaxially grow thin films of pure and transition-metal-doped anatase including magnetron sputtering,[12] pulsed laser deposition,[13] and magnetron and oxygen plasma-assisted molecular beam epitaxy.[14] However, dip-coating process is both cheap and straightforward without the need for expensive vacuum equipment, and was chosen as the primary way of growing Sn-doped anatase thin film in this chapter.

Anatase phase cannot be maintained at high annealing temperatures (such as 800°C used in this chapter). Although anatase phase is usually obtained when TiO_2 is precipitated from solution in sol-gel related preparation processes.[10] Anatase phase is metastable at room temperature and converts exothermically and irreversibly to rutile at elevated temperatures, with an activation barrier of around 20 kJ/mol.[15,16] Thus, an epitaxial substrate template is required to stabilize the anatase structure during annealing.

Moreover, in order to carry out PEC measurements, a conductive substrate is required. 5% Nb-doped $SrTiO_3$ (001) crystalline substrates (PI-KEM) were used for this study due to the good epitaxy relationship with anatase and good conductivity.

The samples were prepared using 5 dip−hydrolysis cycles with alkoxide precursor solution. The as-prepared sample was then annealed at 800 °C for 10 h in argon to prevent oxidation of niobium dopant in the substrate. Four sets of samples were made: **undoped** (TiO_2) and doping level of **5** ($Sn_{0.05}Ti_{0.95}O_2$), **10** ($Sn_{0.1}Ti_{0.9}O_2$) and **15** ($Sn_{0.15}Ti_{0.85}O_2$) atomic % Sn anatase thin films. θ-2θ XRD results of these thin films are shown in Figure 4.1.

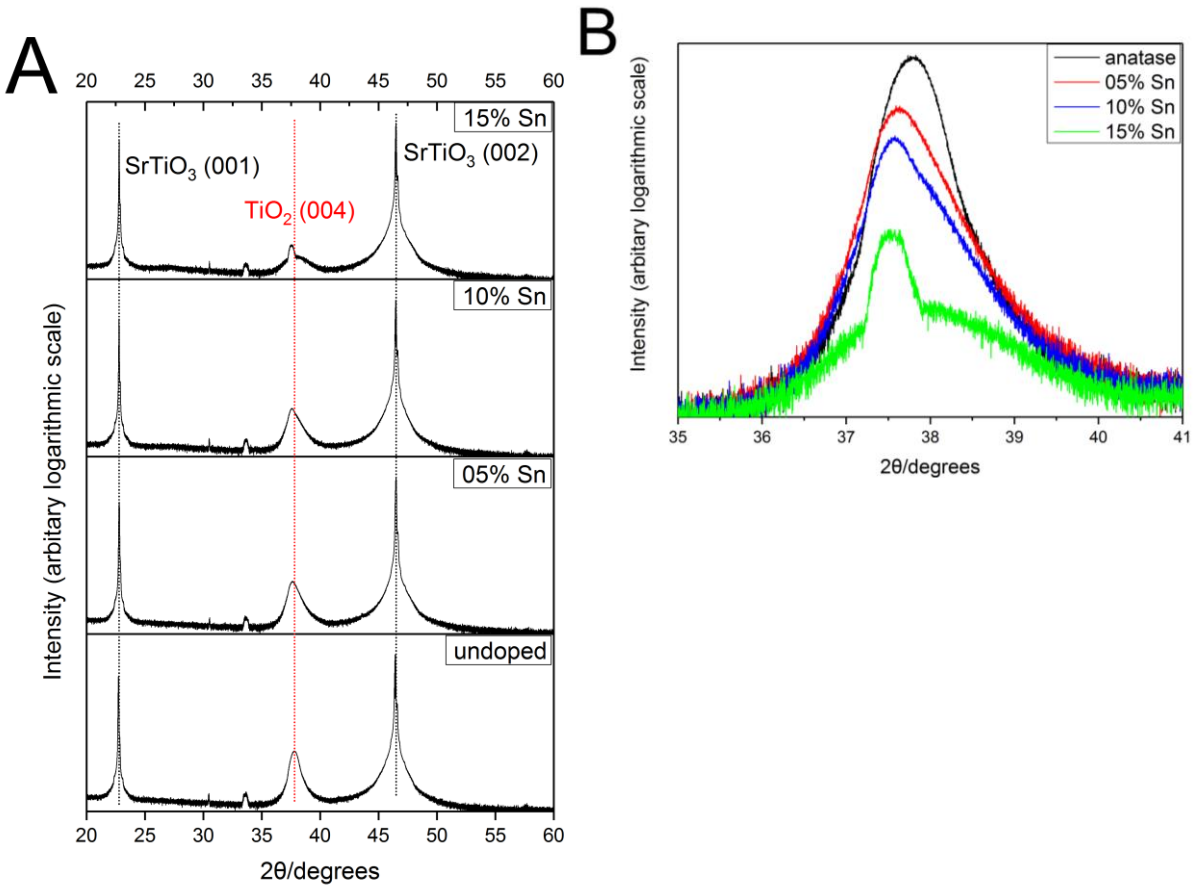


Figure 4.1. θ-2θ X-ray diffraction profiles for (A) undoped and 5%, 10%, 15% Sn-doped anatase thin films grown on 5%Nb: $SrTiO_3$(001) by 5 dip-hydrolysis cycles, followed by annealing at 800 °C for 10 h; (B) anatase (004) peaks shown in detail. The intensity scale is logarithmic to enhance the thin film reflections from the strong substrate reflections.

Since the substrate is cut along the (001) planes of the 5%Nb: $SrTiO_3$ single crystal. Only the (001) and (002) $SrTiO_3$ substrate reflections can be identified at 22.7° and 46.4° respectively. The (110), (111) and (112) $SrTiO_3$ reflections are absent at 32.4°, 40° and 57.8° respectively. The only thin-film peak found in the diffraction patterns is the (004) reflection of anatase TiO_2 at 37.8°. The (110) anatase reflection is absent at 25.3°. This indicates crystal growth with the anatase c axis normal to the substrate surface, so that film and substrate have the epitaxial relationship: $SrTiO_3$ (001) || TiO_2 (001).

The anatase (004) diffraction peaks shifted toward lower 2θ angles with increasing Sn content was observed. This is a consequence of the expansion of the TiO_2 unit cell due to substitutional incorporation of Sn onto Ti sites which is also observed in other publication.[17]

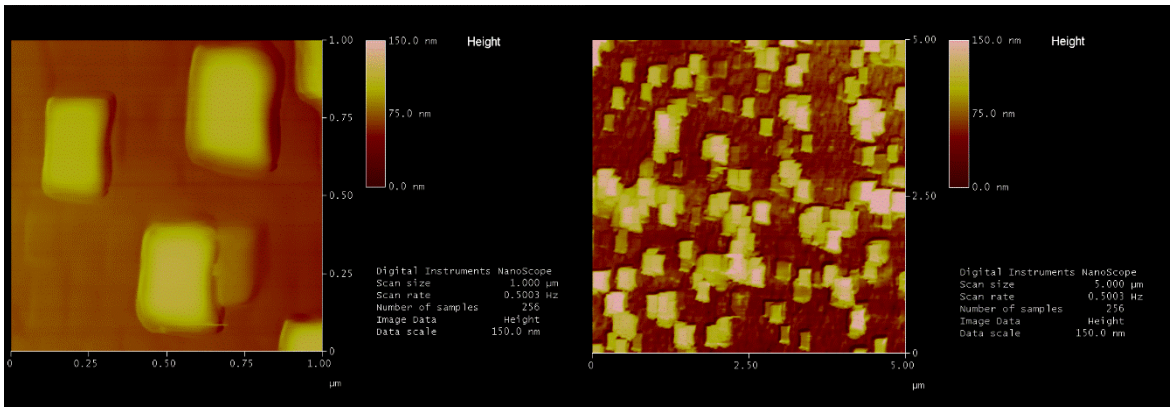


Figure 4.2 AFM image of 10% Sn-doped anatase thin film.

Atomic force microscopy images (AFM) images of 10% Sn-doped anatase thin film annealed at 800 °C is shown in Figure 4.2. The film morphology is seen to present an array of interlinked rectangular islands, confirming good oriented growth of Sn-doped anatase thin film.

To investigate the chemical states and proportion of the species present in the Sn-doped TiO_2 thin film surface, X-ray photoelectron spectra (XPS) of Sn 3d core levels were measured.

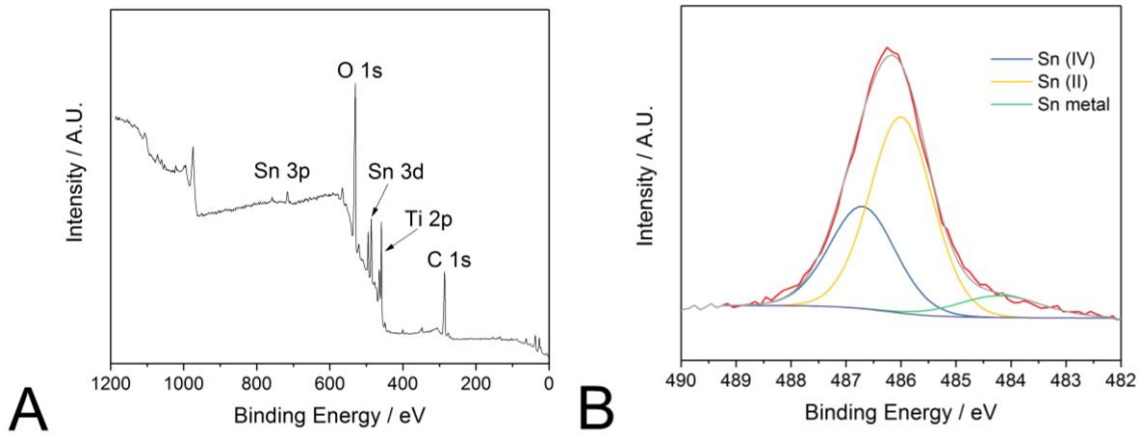


Figure 4.3. XPS (A) survey spectrum and (B) Sn $3d_{5/2}$ core level spectrum of 10% Sn-doped anatase thin film.

The survey spectrum in Figure 4.3A show the carbon 1s peak at 285 eV, titanium 2p peaks at 458.4 eV and 464.3 eV, tin 3d peaks at 486.7 eV and 494.6 eV, and an oxygen 1s peak at 529.8 eV. To calculate the percentage value of each element, CasaXPS software was used. Peak fitting GL(30) (Gaussian (70%)–Lorentzian (30%)) was applied to all peaks beside Ti 2p peak which uses a GL(70) fitting.[18] Normalised atomic percentages were determined from peak areas of the main elemental peaks applying CasaXPS's relative sensitivity factors (RSF). RSF of 7.81 and 25.05 were used for Ti 2p and Sn 3d respectively. The calculated ratio of Ti to Sn amounts to 1: 0.23. Sn surface concentration was higher than the nominal bulk value (10% doping). Dopant surface enrichment has been seen in other systems where a post transition metal ion dopant is introduced into an oxide host lattice.[19–21] The enrichment of Sn on the surface has been attributed to the fact that Sn (II) are more easily accommodated in surface sites than in bulk sites, thus providing a driving force for surface segregation.[22]

The Sn $3d_{5/2}$ core level spectrum in Figure 4.3B show a significant amount of Sn (II) presence reaffirming the surface enrichment of Sn due to Sn (II) cation. Deconvolution of this peak yields an Sn (IV) peak at 486.7 eV, an Sn (II) peak at 486.0 eV and a Sn metal peak at 484.2 eV which agrees well with another finding.[23] The main parameters used in the applied fitting procedure as well as the best fitting parameters are summarized in Table 4.1.

Table 4.1 The binding energy, full width at half maximum (FWHM) and relative peak area of main components of XPS $Sn3d_{5/2}$ peak from 10% Sn-doped anatase thin film.

XPS peak parameters	Sn $3d_{5/2}$		
Components	Sn (IV)	Sn (II)	Sn Metal
Binding energy / eV	486.7	486.0	484.2
FWHM / eV	1.41	1.33	1.79
Relative peak area / %	32.37	58.88	8.75

The electron required to reduce Sn (IV) to Sn (II) derive from oxygen vacancies in host lattice (anatase TiO_{2-y}) as each vacancy generates two electrons. Sn-doping will partially eliminate the formation of undesirable Ti (III) traps in anatase bulk, which improves charge carrier lifetime. Moreover, Sn (II) 5s electrons hybridise strongly with O 2p states to give antibonding states of mixed Sn 5s–O 2p character at the top of the valence band.[24] Since holes tend to migrate to the highest possible occupied states, which is the hybridized Sn 5s-O 2p states illustrated in Figure 4.4, Sn (II) enrichment at the surface makes good hole traps which are optimally placed to facilitate redox reactions for the photogenerated holes.

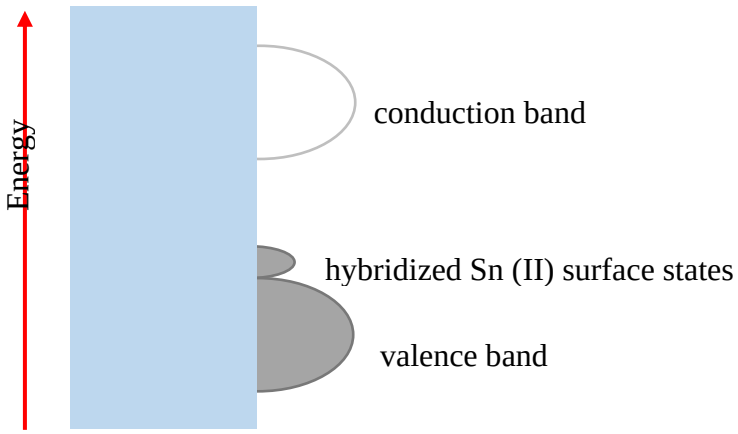


Figure 4.4 Density of states diagrams for Sn-doped anatase TiO_2 surface.

Initial PEC investigation with the thin film sample as the working electrode was conducted by carefully lowering half of the substrate into the 0.1 M NaOH electrolyte (50 mm^2). Continuous CV result (Figure 4.5) show an increase in photocurrent with increasing scan cycle number indicating activation of electrode surface.

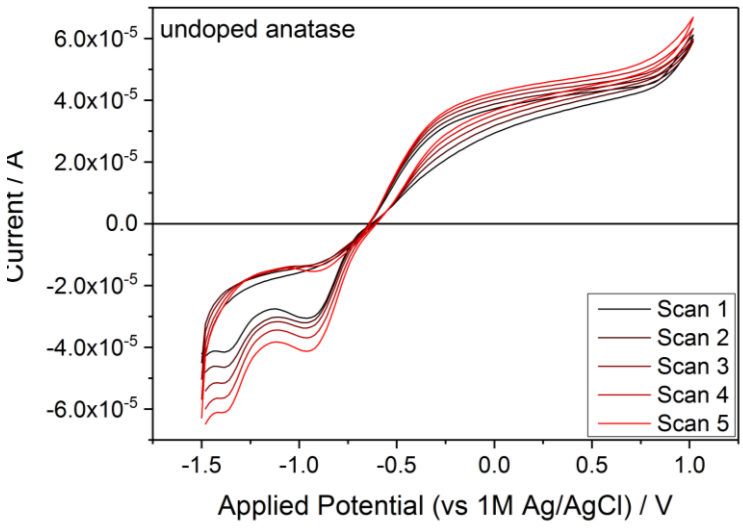


Figure 4.5 20 mV/s cyclic voltammetry plots of anatase TiO_2 thin film under one sun illumination in 0.1 M NaOH solution.

In order to improve consistency across different samples, the reaction area of all the samples was fixed at 28.26 mm^2 using a special approach explained in the experimental chapter of

this thesis. The thin film samples are activated using multiple sets of five CV scans from -1.5 V to +1.0 V with a scan rate of 20 mV/s. The activation process is repeated until no photocurrent increase is observed. As can be seen in Figure 4.6 the discrepancy between scans are negligible, indicating a fully activated electrode surface.

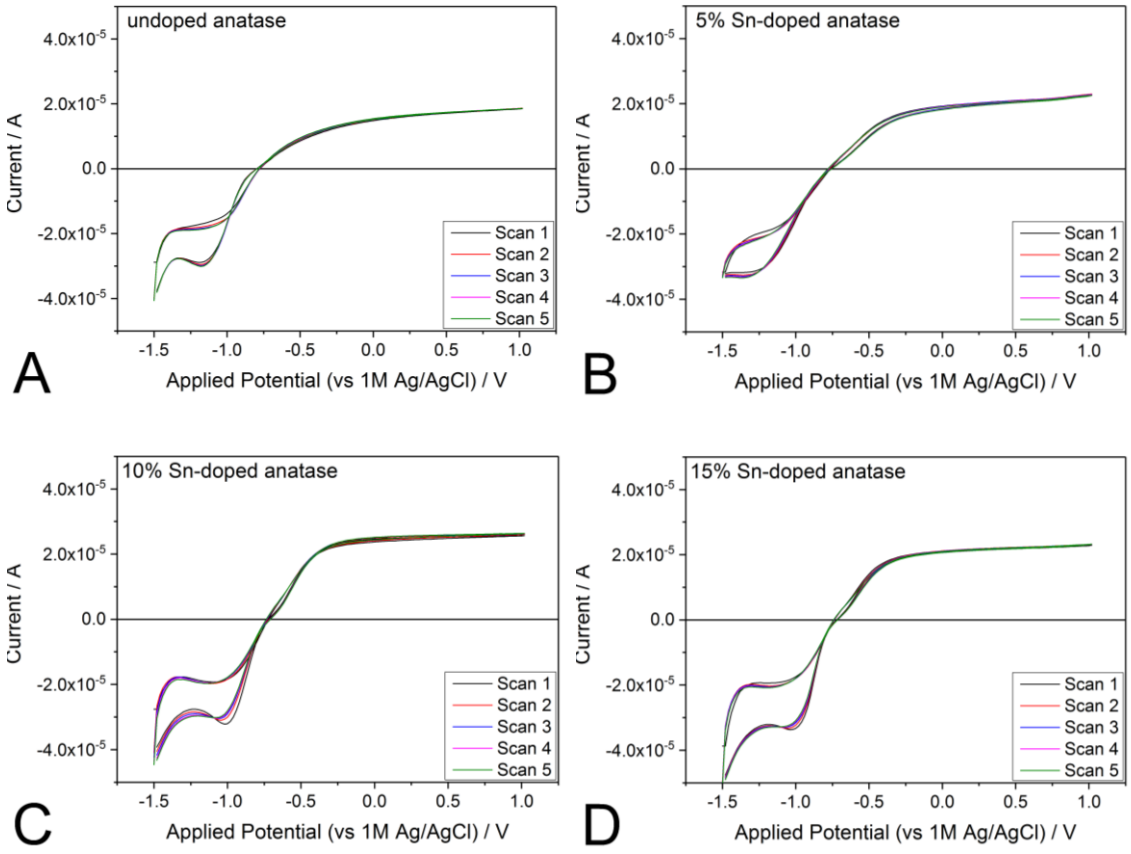


Figure 4.6. 20 mV/s cyclic voltammetry plots of anatase TiO_2 thin films with various level of Sn doping (A 0%, B 5%, C 10%, D 15%) grown on 5%Nb:$SrTiO_3$ (5 dip-hydrolysis cycles, followed by annealing at 800 °C for 10 h) under one sun illumination in 0.1 M NaOH solution.

Overlaying the fifth CV scan for **undoped** (TiO_2) and doping level of **5** ($Sn_{0.05}Ti_{0.95}O_2$), **10** ($Sn_{0.1}Ti_{0.9}O_2$) and **15** ($Sn_{0.15}Ti_{0.85}O_2$) atomic % Sn thin films in the same graph yield the data shown in Figure 4.7.

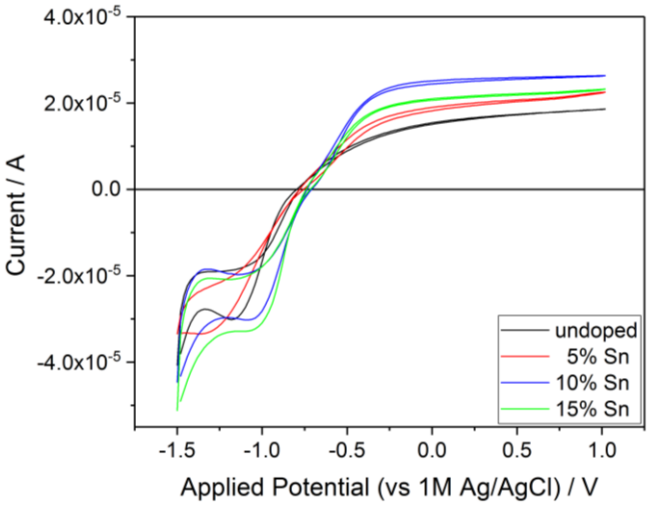


Figure 4.7. Overlapped Scan No. 5 of 20 mV/s cyclic voltammetry plots of anatase TiO_2 with various level of Sn doping (red 5%, blue 10%, green 15%, black 0%) thin films under one sun illumination in 0.1 M NaOH solution.

It is somewhat obvious that Sn-doped sample have increased anodic current response over the potential window from -0.75 V to 1 V vs 1 M silver chloride electrode. Taking a closer look at the anodic current potential region, there is an observable difference between the forward and backward scan. And in the cathodic current region, this issue becomes more pronounced. This capacitive response issue is discussed in the following sections and addressed accordingly.

In conclusion, the 5%Nb: $SrTiO_3$ substrate has proven to be suitable for growth of Sn-doped anatase thin film as a photoelectrode material for PEC investigation. How Sn-doping improves PEC performance is further investigated in the following sections.

4.3.2 Light on/off experiment

Light on/off experiments were used to identify photocurrent responses from the electrochemical response in dark. Linear CV scans were performed while an electronic optical shutter was used to chop the incoming light at a frequency of 0.5 Hz. Coupled with

a scan rate of 0.02 V/s and step voltage of 0.02 V, data points of photocurrent and dark current alternate throughout the potential window. This approach provides an intuitive view of the photo-responsive potential regions.

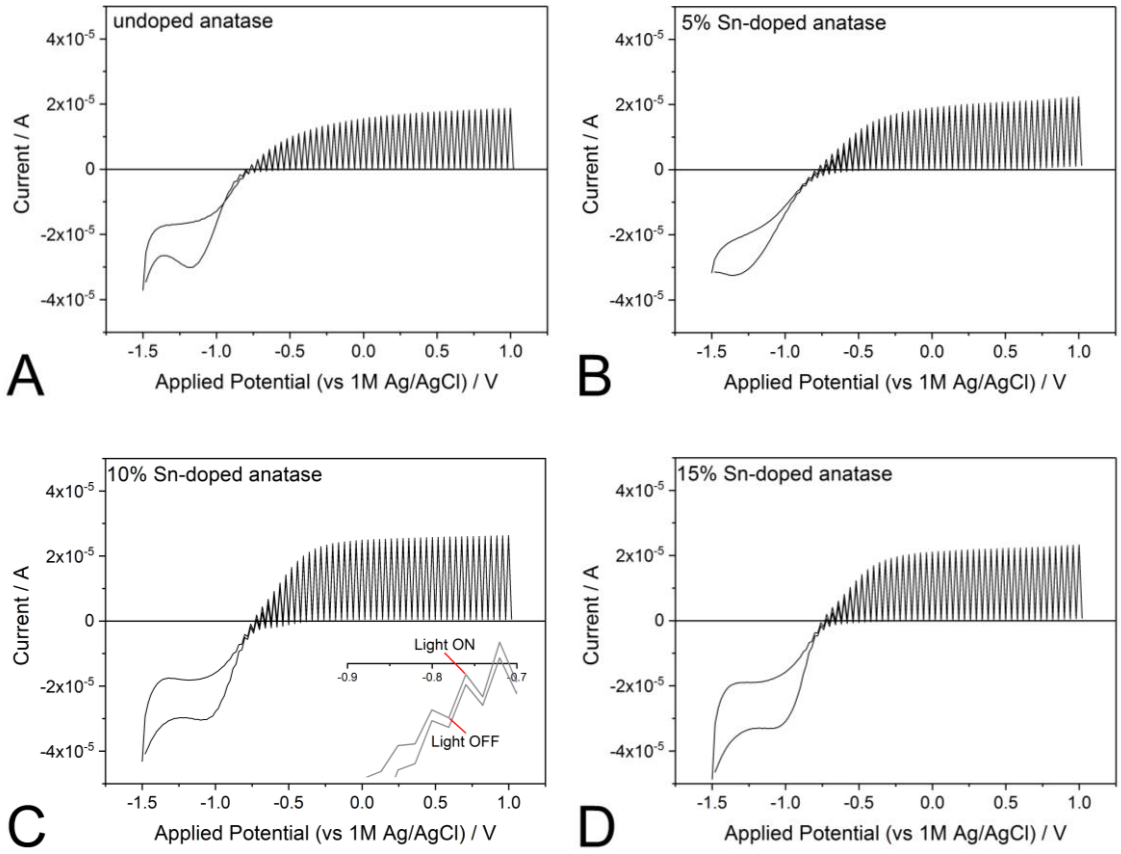


Figure 4.8. 20 mV/s cyclic voltammetry plots of anatase TiO_2 thin films with various level of Sn doping (A 0%, B 5%, C 10%, D 15%) under one sun illumination in 0.1 M NaOH solution with a light-on-light-off frequency of 0.5 Hz. The detailed cathodic photocurrent region of 10 % Sn-doped anatase thin film is shown in bottom right corner of caption C.

In the -0.75 to 1.0 V region, anodic photocurrent is present for all samples. Sn doped TiO_2 is an n-type semiconductor, holes are a minority charge carrier. At this potential region the semiconductor should have an upward band bending with a built-in electric field pointing outwards into the electrolyte. Photogenerated holes in the space charge layer (SCL) are forced to the electrode surface by the electric field to participate in water oxidation, thus the

anodic photocurrent makes sense. In the -0.8 to -0.75 V region, cathodic photocurrent is present for all samples. This potential region is equivalent to 0.2 to 0.25 V vs RHE which is insufficient for photocatalytic water reduction which needs further explanation. Moreover, the significant capacitive response in the cathodic current region requires further clarification. Thus, it warrants a comprehensive review on energy structures at semiconductor-electrolyte interface under illumination.

4.3.3 Semiconductor-electrolyte interface under illumination

The understanding of semiconductor-electrolyte (S-E) interface has stemmed from both electrochemistry and solid-state physics perspectives, and both have proven to be very fruitful. However, there is some lack of clarity between the two approaches in the literature.

Electrochemists have restricted interest understanding towards photo-electrochemical response under illumination, and electrochemical behaviour in the dark has been their focus.[25,26] For example in "Photo-electrochemistry and Electrogenerated Chemiluminescence" chapter of A.J. Bard's book[27], the discussion on S-E interface under irradiation only shows a misalignment between semiconductor Fermi level and the electrolyte redox potential; the examples of different types of PECs only presents a qualitative band diagram without showing specific energy level alignment.

Material scientists have a limited interest of the overall photo-electrochemical response at different potentials, and photocurrent has been their focus. For example, multiple reviews[28,29] on S-E interface demonstrated the flat-band potential using Mott-Schottky

equation and steady state photocurrent under bias. The interface band structure at other potentials were not investigated, which limits understanding of I-V behaviour at these potentials.

Recently, work done by Lewis and Krol[30,31] used the concept of quasi-Fermi level to explain the alignment of water oxidation potential (1.23 V vs RHE) with quasi-Fermi level of holes for a n-type semiconductor photoanode under illumination. This concept has provided the opportunity to relate specific potentials to specific energy level alignments in the S-E interface structure. Thus, a better understanding of important data points such as photocurrent onset potential, photocurrent inversion potential, and water oxidation potential at 1.23 V vs RHE scale etc is achieved.

In this section, the CV data of 10% Sn-doped anatase thin film is analysed in close relationship with S-E interfacial energy diagrams. For a typical CV plot using a photoanode working electrode, the CV data is composed of 3 parts: 1) cathodic capacitive forward/reverse (red/light-red), 2) cathodic photocurrent forward/reverse (green/light-green), and 3) anodic photocurrent forward/reverse (blue/light-blue). And three important potential points are present: A) electrolytic water reduction potential (V_{wr}), B) photocurrent onset potential (V_{onset}), and C) photocurrent inversion potential (V_{inv}). (Figure 4.9 A)

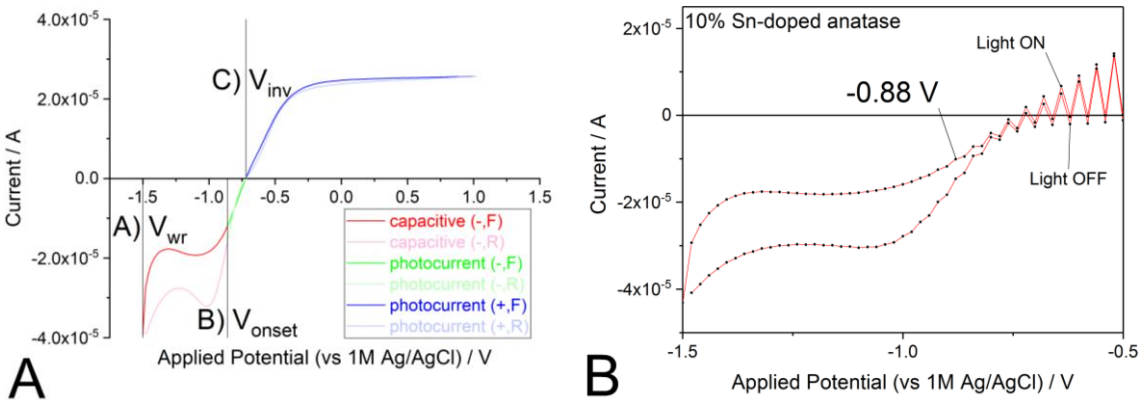


Figure 4.9. 20 mV/s cyclic voltammetry plots of 10% Sn-doped anatase TiO_2 thin film grown on 5%Nb: $SrTiO_3$ (5 dip-hydrolysis cycles, followed by annealing at 800°C for 10 h) A) under continuous one sun illumination, B) under 0.5 Hz light on/off one sun illumination, in 0.1 M NaOH solution.

The photocurrent onset potential (V_{onset}) is defined as the potential at which photocurrent emerges, which can be identified in the light on/off experiment showing a visible change in current when light is switched on (-0.88 V, Figure 4.9 B). The photocurrent inversion potential (V_{inv}) is the photocurrent intersect with the X-axis (-0.74 V, Figure 4.9 A), this is sometimes confused as the photocurrent onset. The electrolytic water reduction potential (V_{wr}) is the potential at which an abrupt increase of cathodic current in dark (-1.5 V, Figure 4.9 A), which indicates electrolytic water reduction to hydrogen.

It must be stressed beforehand that in the following S-E energy diagrams (Figure 4.10, 4.11 and 4.12), the absolute energy scale (electron potential energy, vacuum as reference 0 eV) is used in the energy diagram for both semiconductor side and electrolyte side of the interface. The corresponding electric potential distribution in the S-E interface is shown separately with the matching x-axis (distance from the S-E interface). Although in some cases, electrode potential (potential term in unit V) is used on the electrolyte side,[32,33] this additional layer of absolute electrode potential to absolute energy scale conversion

(discussed in the introduction chapter) complicates presentation of the S-E interface energy diagram, especially when the two scales are increasing in the opposite directions. Thus, in this chapter, any reference of equivalent energy of electrode potential, such as water oxidation potential at 1.23 V vs RHE, the corresponding equivalent energy level is shown in the S-E energy diagram.

4.3.3.1 Photocurrent inversion potential and anodic photocurrent region

In this section, the S-E interface structure at photocurrent inversion potential (V_{inv}) under steady state conditions is investigated. Then, the changes when potential is shifted to more positive regions are considered. Finally, the quasi-Fermi levels are explained, and calculation of the quasi-Fermi level splitting is provided.

In the introduction chapter of this thesis the two key conclusions of the S-E interface in the dark are: 1) the alignment of semiconductor Fermi level (energy term in unit eV) and electrolyte redox potential (potential term in unit V) is required at steady state conditions; 2) due to the depletion of charge carriers in the SCL, an electric field is present which influence current flow across the interface. So, alignment of energy/potential levels dictates whether an electrochemical reaction can spontaneously happen (electrochemical or photo-electrochemical), while electric field in the SCL dictate the allowed direction of photocurrent.

Under illumination, the energy level alignments at the S-E interface is slightly different. Electric field in the SCL promotes current flow from semiconductor to the electrolyte which manifests as an anodic photocurrent. Since anodic photocurrent is a result of photogenerated

holes participating in water oxidation reaction, the relevant energy levels are quasi-Fermi level of holes (E_h) and water oxidation level (E_{ox}). At emergence of PEC water oxidation, the quasi-Fermi level of holes (E_h, dashed red line, Figure 4.10) aligns with equivalent energy level of water oxidation potential (E_{ox}, solid red line, Figure 4.10).

At this potential, the S-E interface is under reverse bias. The electric field in the SCL is pointing outwards into the electrolyte, which drives the separation of photogenerated electron-hole pairs in the SCL. This is shown as continuous drop in potential from to the bulk (ψ_h) to the S-E interface. The positively charged holes are swept across the S-E interface and participate in water oxidation reaction, while the electrons are transported to the counter electrode to participate in water reduction reaction. However, the quasi-Fermi level of electrons (E_e) is lower than the water reduction level (E_{red}), external bias is required to give photogenerated electrons a "boost-up" in energy (higher electron potential energy) to satisfy energy level alignment of metal-electrolyte interface at the counter electrode (metal Fermi-level, water reduction level).

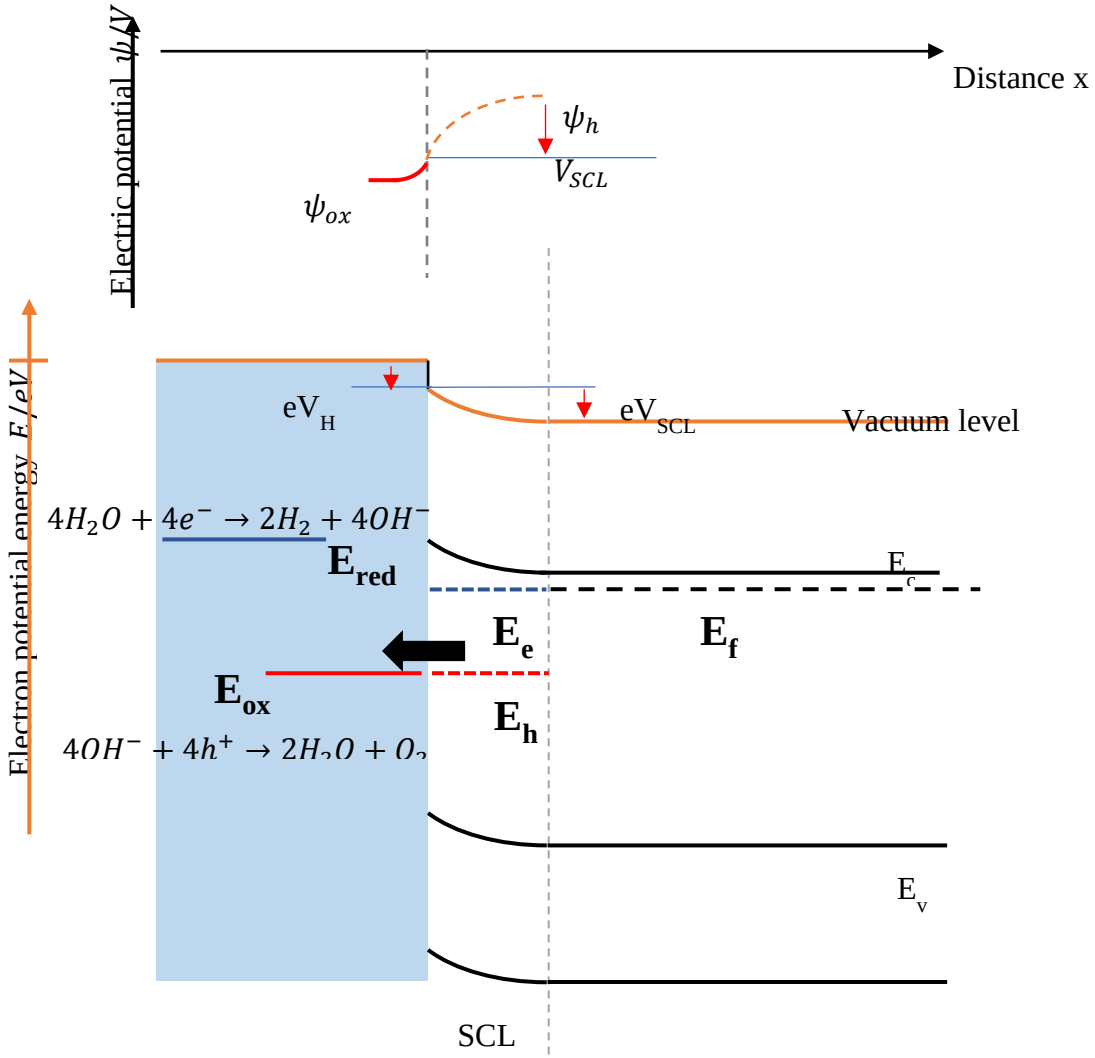


Figure 4.10. Energy diagram of an n-type S-E interface at photocurrent inversion potential (V_{inv}) under illumination. The equivalent energy level of water oxidation (E_{ox}) and reduction (E_{red}) are shown as solid red and blue lines respectively. Quasi-Fermi level of holes (E_h) and electrons (E_e) are shown as dashed red and blue lines respectively. The relevant potential distribution across S-E interface is on top of the band diagram with matching x-axis, current flow direction is shown in black arrow.

When the bias on the semiconductor electrode is shifted to more positive potentials (increasing reverse bias), the majority carrier (electrons) are further depleted from SCL, increasing the SCL width. An increase in the SCL region means more photogenerated charges are under the influence of the built-in electric field, thus the increase in photocurrent. When the SCL width extended beyond the mean free path of charge carriers, a saturation in

photocurrent occur, which is seen in the -0.2 to 1 V (vs 1 M silver chloride electrode) region of the CV data.

With increasing reverse bias, the semiconductor bulk Fermi level shifts downwards. Simultaneously, quasi-Fermi level of holes (E_h) is shifted to lower electron potential energy (higher hole potential energy) than water oxidation level (E_{ox}). This increase in overpotential reduces the PEC efficiency. When the bulk Fermi level reaches 1.23 V vs RHE, the alignment of water oxidation level (E_{ox}) and bulk Fermi level (E_f) occurs. At this potential, electrolytic water oxidation can happen, and the PEC efficiency is reduced to zero.

The quasi-Fermi levels are a direct measure of the concentrations of electrons and holes at a certain point in the semiconductor, which can be defined as:

$$n = n_0 + \Delta n = N_C e^{-(E_C - E_e)/kT} \qquad \text{Eq 4.1}$$

$$p = p_0 + \Delta p = N_V e^{-(E_h - E_V)/kT} \qquad \text{Eq 4.2}$$

Where n_0 and p_0 are the equilibrium carrier concentrations in the dark, Δn and Δp are concentrations of photogenerated electrons and holes, N_C and N_V are effective DOS in the conduction band and valence band, E_C and E_V are energy of conduction band and valence band edges, and E_e and E_h are quasi-Fermi level of electrons and holes respectively. For a n-type semiconductor, electron is the majority charge carrier. Thus, $n = n_0 + \Delta n \approx n_0$ and $p = p_0 + \Delta p \approx \Delta p$. This means quasi-Fermi level of electrons (E_e) remain in the same level as bulk Fermi level (E_f) while quasi-Fermi level of holes (E_h) drops down moving closer to the valence band edge.

At photocurrent inversion potential (V_{inv}), quasi-Fermi level of hole (E_h) align with water oxidation level (E_{ox}). When electrode is biased to 1.23 V vs RHE, bulk Fermi level (E_f) align with water oxidation level (E_{ox}). And for a n-type semiconductor, quasi-Fermi level of electrons (E_e) is the same level as bulk Fermi level (E_f). The energy separation between quasi-Fermi level of electrons and holes can be calculated by:

$$\frac{E_e - E_h}{e} = 1.23\ V - V_{inv}^{RHE} \qquad \text{Eq 4.3}$$

Where E_e and E_h are quasi-Fermi level of electrons and holes respectively (in unit eV), and V_{inv}^{RHE} is the photocurrent inversion potential measured in vs RHE scale (in unit V).

4.3.3.2 Photocurrent onset potential and cathodic photocurrent region

In this section, the photocurrent onset potential (V_{onset}) is identified to be the flat band potential (V_{fb}). The S-E interface structure at this potential is investigated. The photocurrent and electrolytic leakage current are discussed. The underlying causes for cathodic photocurrent response are explained.

When the bias on the semiconductor electrode is shifted to more negative potentials than the photocurrent inversion potential (V_{inv}), the majority carrier (electrons) accumulates in the SCL. This process fills the depleted holes in the SCL, thus reducing the SCL width and band bending. When all the depleted sites are filled, the SCL vanishes and the semiconductor band become flat, this potential point is called the flat band potential (V_{fb}). Having a flat band means there is no electric field near the S-E interface to separate photogenerated electron-holes, which lead to zero photocurrent flow across the interface. Thus, this flat band

potential (V_{fb}) is also the photocurrent onset potential (V_{onset}). The S-E interface structure at this potential point is presented in Figure 4.11.

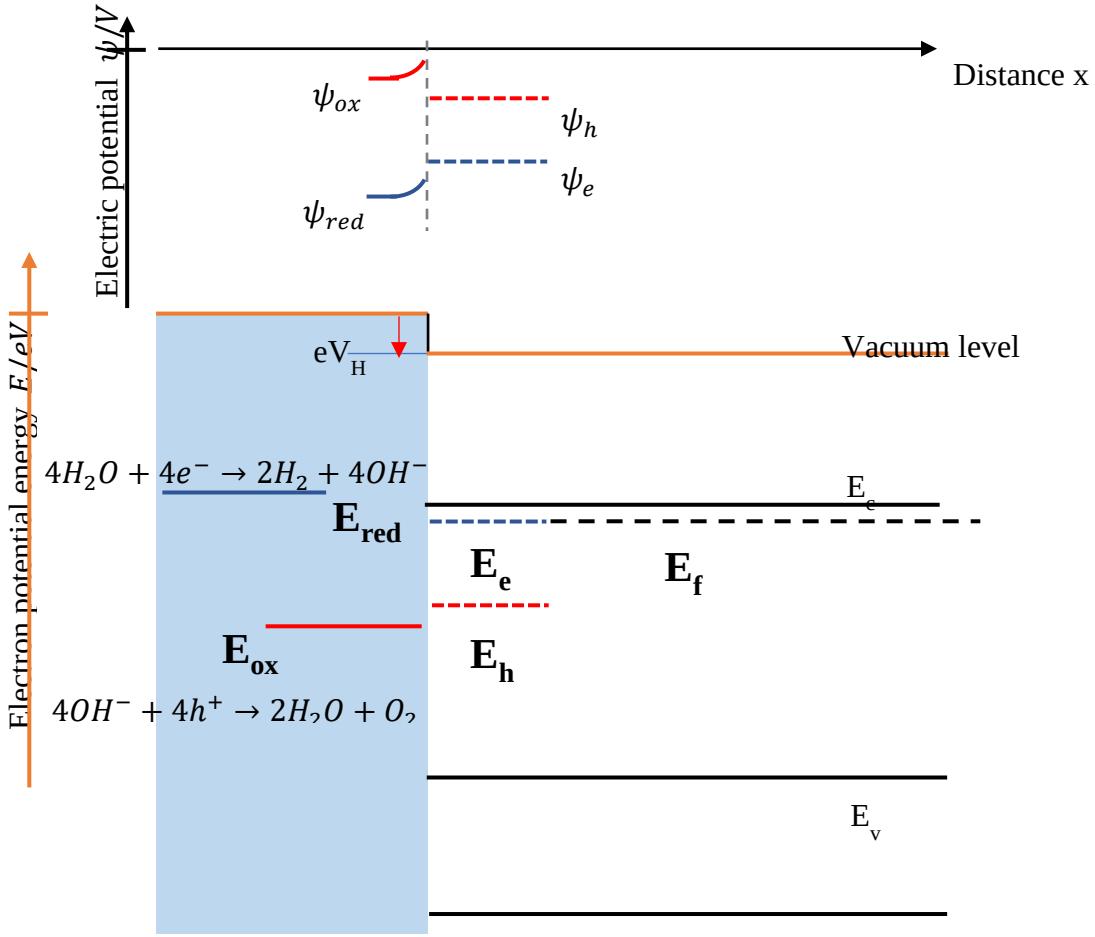


Figure 4.11. Energy diagram of an n-type S-E interface at photocurrent onset potential (V_{onset}) under illumination. The equivalent energy level of water oxidation (E_{ox}) and reduction (E_{red}) are shown as solid red and blue lines respectively. Quasi-Fermi level of holes (E_h) and electrons (E_e) are shown as dashed red and blue lines respectively. The relevant potential distribution across S-E interface is on top of the band diagram with matching x-axis.

The quasi-Fermi level of electron (E_e) and holes (E_h) in the SCL sits in between the water oxidation level (E_{ox}) and water reduction level (E_{red}). In this case, energy of photogenerated hole is insufficient for water oxidation and energy of pure-electrical-electron is insufficient for water reduction. Furthermore, there is no electric field in the SCL to separate

photogenerated electron-hole pairs, and electron-holes ultimately recombine, and no photocurrent flow across the S-E interface. However, the flat band condition is maintained by accumulation of electrons due to external electrical source, and electrons are constantly leaking into the electrolyte. Thus, a non-photo-related leakage of electron is present as a pure electrical cathodic current.

In between the photocurrent onset potential (V_{onset}) and photocurrent inversion potential (V_{inv}), a cathodic photocurrent response is present. This does not mean photocatalytic water reduction to hydrogen is occurring on the S-E interface, but the reduction in electron leakage due to electron-hole recombination. The quasi-Fermi level of holes (E_h) has shifted to higher electron potential energy (lower hole potential energy) than water oxidation level, thus photogenerated holes are no longer capable of water oxidation. Since electric field in the SCL still forces the transport of photogenerated holes to the S-E interface. The photogenerated holes accumulates at the S-E interface which recombine with the leaking electrons. This is identified as reduction in cathodic current when light is on.

4.3.3.3 Electrolytic water reduction potential and cathodic capacitive region

In this section the lack of photocatalytic water reduction and significant capacitive response in the cathodic region are explained.

At electrolytic water reduction potential (V_{wr}), the CV data is the same under dark and illumination. This means the photogenerated charges and the corresponding quasi-Fermi levels are not relevant. At electrolytic water reduction potential (V_{wr} = -1.5 V vs 1 M silver

chloride electrode), the bulk Fermi level (E_f, dashed black line, figure 4.12) aligns with water reduction level (E_{red}, solid blue line, figure 4.12).

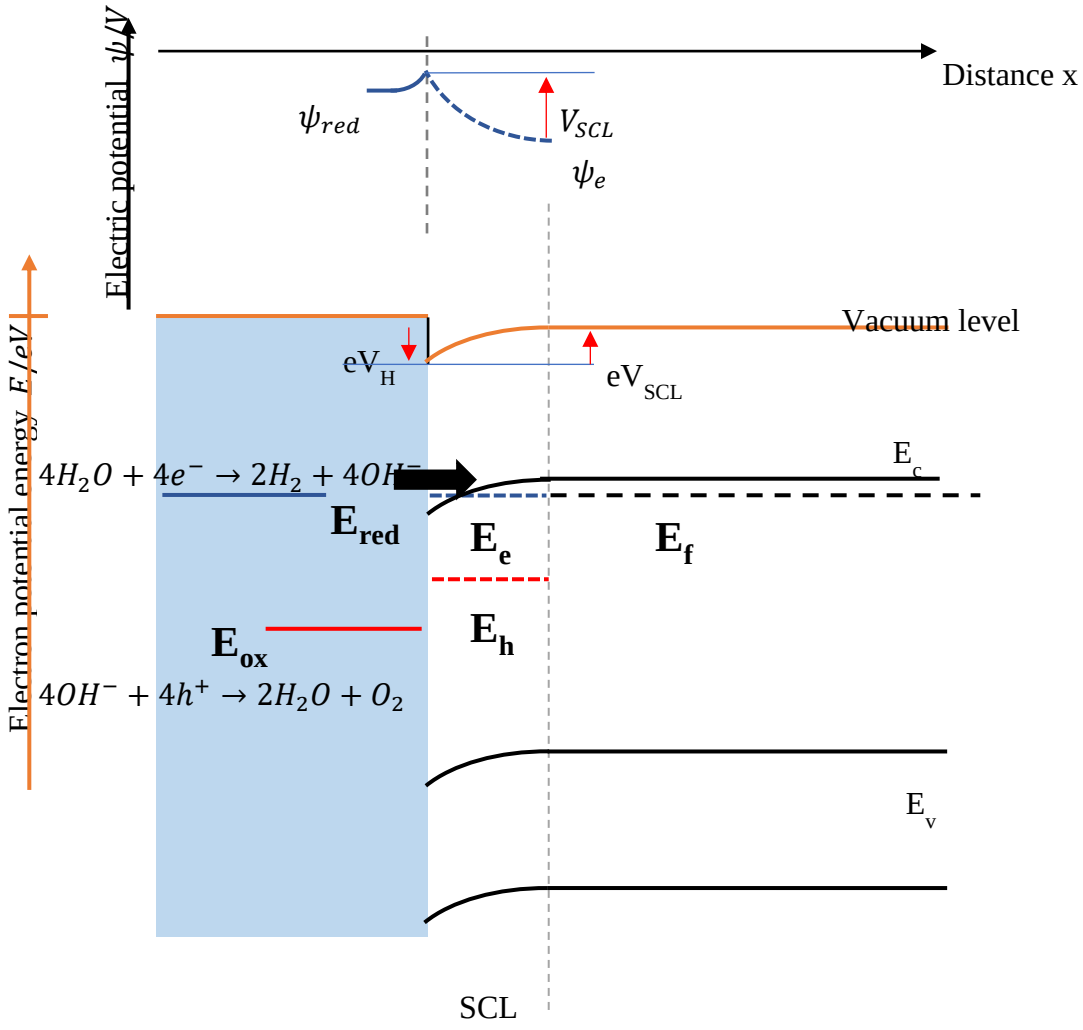


Figure 4.12. Energy diagram of an n-type S-E interface at electrolytic water reduction potential (V_{wr}) under illumination. The equivalent energy level of water oxidation (E_{ox}) and reduction (E_{red}) are shown as solid red and blue lines respectively. Quasi-Fermi level of holes (E_h) and electrons (E_e) are shown as dashed red and blue lines respectively. The relevant potential distribution across S-E interface is on top of the band diagram with matching x-axis, current flow direction is shown in black arrow.

The electrolytic water reduction potential (V_{wr}) is at much lower potential than the photocurrent onset potential (V_{onset}). Under such extreme forward bias, the accumulation of

charges results in a downward band bending. The electric field in the SCL is pointing inwards into the semiconductor bulk, which separates the photogenerated electron-hole pairs. However, accumulation of majority charge carriers in the SCL leads to severe thermal recombination. As soon as photogenerated electron-hole pairs occur in the SCL, the accumulated electrons will recombine with the photogenerated hole. Thus, no net increase in electron transfer across the S-E interface, which is why the absence of cathodic photocurrent.

In previous sections, significant capacitive feature in the cathodic current region (-1.5 to -0.75 V vs 1 M silver chloride electrode) and unpronounced capacitive feature in the photocurrent region (-0.75 to 1 V vs 1 M silver chloride electrode) was observed. In the cathodic capacitive region, the electric field in the SCL is pointing inwards into the semiconductor bulk, electrons are stored in the SCL. In the anodic photocurrent region, the electric field in the SCL is pointing outwards into the electrolyte, holes are stored in the SCL. Electrons are majority charge carriers in a n-type semiconductor, the density of which is a few orders of magnitudes higher than minority charge carriers (holes). It is reasonable that the number of stored electrons is higher than the holes in the SCL, thus the higher capacitance in the cathodic region. Since this current separation between forward and reverse scan is due to capacitive charging-discharging, this non-Faradaic current must be excluded from the CV data in order to obtain the real photocurrent.

4.3.3.4 Conclusions

It has been demonstrated that the photocurrent onset potential (V_{onset}) is different from photocurrent inversion potential (V_{inv}) which is sometimes misused.[34,35] The differentiation of these two potentials enabled the calculation of quasi-Fermi level splitting using photocurrent inversion potential (V_{inv}) and reaffirmed that photocurrent onset potential (V_{onset}) to be the flat band potential (V_{fb}).

The charge storage properties of SCL were discussed which explains the pronounced capacitive response in the cathodic CV data. The nature of cathodic photocurrent response and the absence of photocatalytic water reduction using a n-type photoanode was explained. Thus, by reviewing the S-E interface structure and energy level alignments we have provided more clarity on the interpretation of photoelectrode I-V data.

4.3.4 PEC performance comparison

In Figure 4.13 the two consecutive scans of the anodic photocurrent regions are shown with perfect overlap, indicating well activated electrode surfaces. The small capacitive response is visible as by separation between forward and backward scan currents. The SCL at the S-E interface has the ability to store charges similar to a capacitor plate, and the capacitance can be detected with CV, which was duely explained in the previous section.

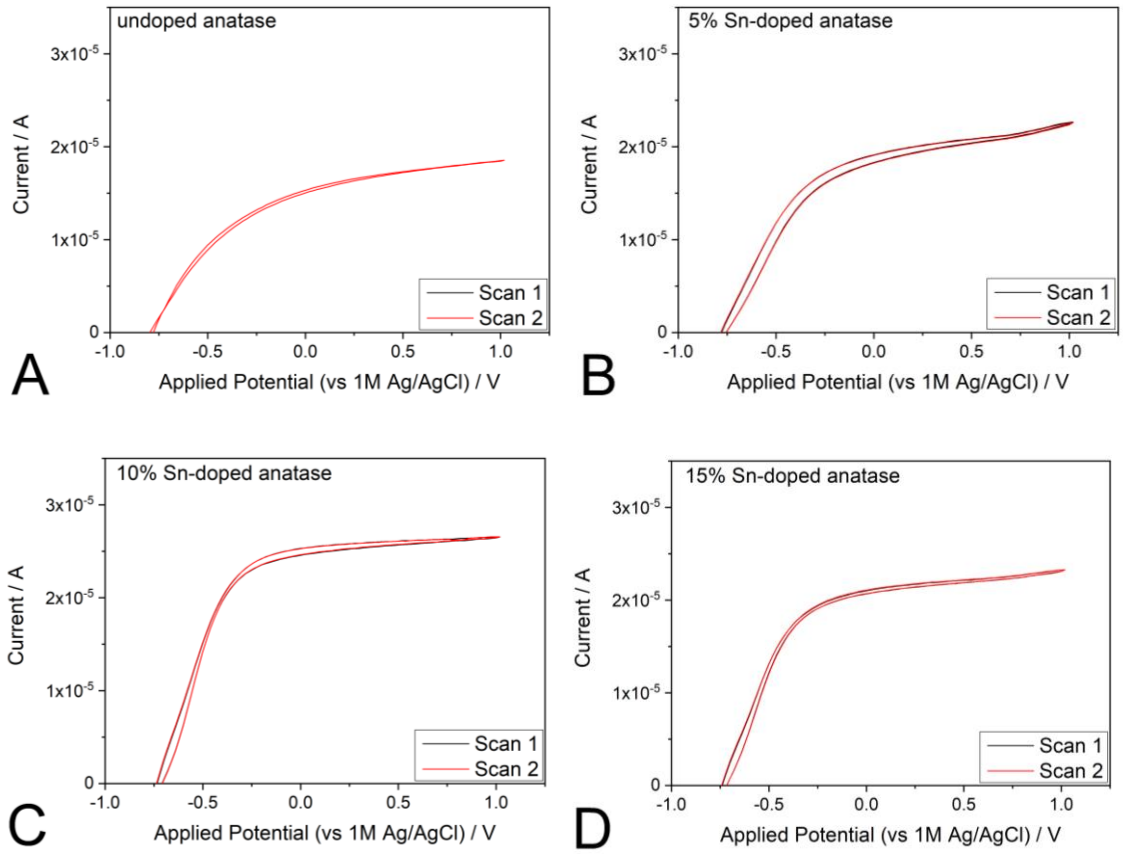


Figure 4.13. 20 mV/s cyclic voltammetry plots of anatase TiO_2 thin films with various level of Sn doping (A 5%, B 10%, C 15%, D 0%) grown on 5%Nb:$SrTiO_3$ (5 dip-hydrolysis cycles, followed by annealing at 800 °C for 10 h) under one sun illumination in 0.1 M NaOH solution. Only the photocurrent region of the data is shown.

The capacitive feature of Sn-doped samples are more pronouced than un-doped anatase. Under reverse bias (photocurrent region), holes are stored in the SCL. Sn (II) surface sites acts as hole traps increasing hole density in the SCL, which increases SCL capacitance. Capacitor charging/discharging current is non-Faradaic. Assuming charging and discharging current are of the same intensity, they are eliminated by averaging the forward and reverse current. The averaged photocurrent data is shown in Figure 4.14, which is the pure Faradaic current due to photogeneration.

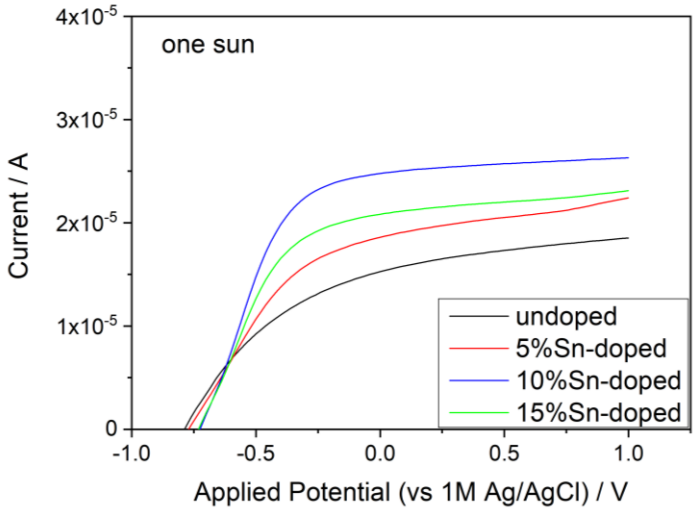


Figure 4.14. Photocurrent plot of anatase TiO_2 thin films with various level of Sn doping (red 5%, blue 10%, green 15%, black 0%) grown on 5%Nb:$SrTiO_3$ (5 dip-hydrolysis cycles, followed by annealing at 800 °C for 10 h) under one sun illumination in 0.1 M NaOH solution.

The applied potential on a working photo-electrode is a key parameter in understanding the the properties. RHE scale has become the preferred reference scale for reporting photo-electrode working potentials.[31] Zero volt on the RHE scale reflects the water reduction potential in the actual electrolyte, irrespective of the pH. This is more convenient than SHE scale which requires the H^+ ion at unit activity. A potential measured with respect to 1 M silver chloride electrode ($E_{Ag/AgCl}$) can be converted to the RHE scale (E_{RHE}) with the following expression at 298 K:

$$E_{RHE} = E_{Ag/AgCl} + 59\ mV \times pH + E^0_{Ag/AgCl} \qquad \text{Eq 4.4}$$

Where $E^0_{Ag/AgCl}$ is the standard potential of silver chloride electrode referenced against SHE, which is +0.2303 V for 1 M silver chloride electrode. At pH=13 (0.1 M NaOH electrolyte), the potential vs RHE is converted using $E_{RHE} = E_{Ag/AgCl} + 0.997\ V$. The

photocurrent plot in Figure 4.14 measured vs 1 M silver chloride reference electrode is converted to vs RHE scale in Figure 4.15.

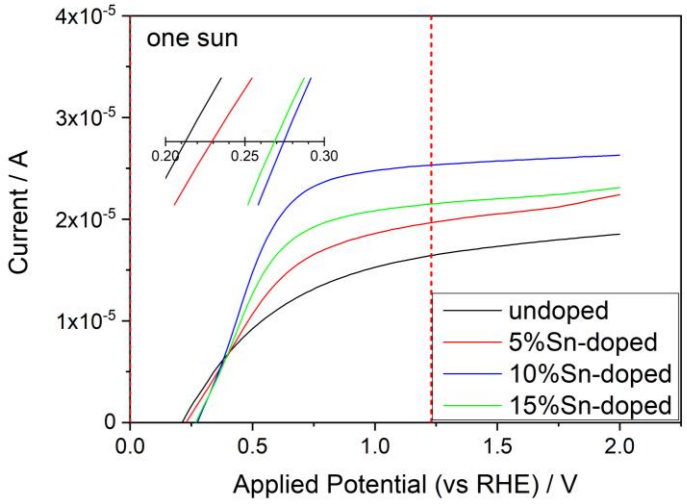


Figure 4.15. Photocurrent data of anatase TiO_2 thin films with various level of Sn doping (red 5%, blue 10%, green 15%, black 0%) grown on 5%Nb:$SrTiO_3$ (5 dip-hydrolysis cycles, followed by annealing at 800 °C for 10 h) under one sun illumination in 0.1 M NaOH solution. Photocurrent inversion region is enlarged at top left corner. 1 M silver chloride electrode is used as reference, potential converted to vs RHE scale. Water oxidation (1.23 V vs RHE) and reduction (0 V vs RHE) potentials are shown in red dotted lines.

Like many other doped TiO_2 photocurrent results,[36,37] the anodic photocurrent is not seen at 0 V vs RHE, which means modified TiO_2 is incapable of sustaining a self-driven PEC water splitting process without external bias. Sn-doping increases overall photocurrent in the external bias assisted PEC region (0.4 V to 1.23 V vs RHE) with 10% Sn-doped anatase showing best results.

In addition to the full solar spectrum, visible contribution towards PEC water splitting was investigated using a 400 nm long-pass filtered one sun spectrum. From the results in figure 4.16, we can see that doping improves photocurrent response under visible spectrum with 10% Sn-doped anatase showing best results.

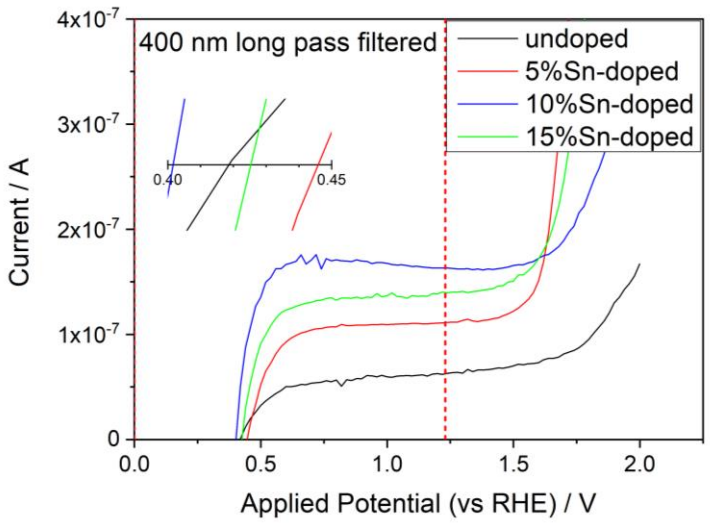


Figure 4.16. Photocurrent data of anatase TiO_2 thin films with various level of Sn doping (red 5%, blue 10%, green 15%, black 0%) grown on 5%Nb:$SrTiO_3$ (5 dip-hydrolysis cycles, followed by annealing at 800 °C for 10 h) under 400nm long pass filtered one sun illumination in 0.1 M NaOH solution. Photocurrent inversion region is enlarged at top left corner. 1 M silver chloride electrode is used as reference, potential converted to vs RHE scale. Water oxidation (1.23 V vs RHE) and reduction (0 V vs RHE) potentials are shown in red dotted lines.

Finally, UV contributions towards PEC water splitting were investigated using a 240-395 nm band-pass filtered one sun spectrum. (Figure 4.17) The photocurrent response is two orders of magnitude lower under visible spectrum (> 400nm) compared to UV spectrum (240-395 nm).

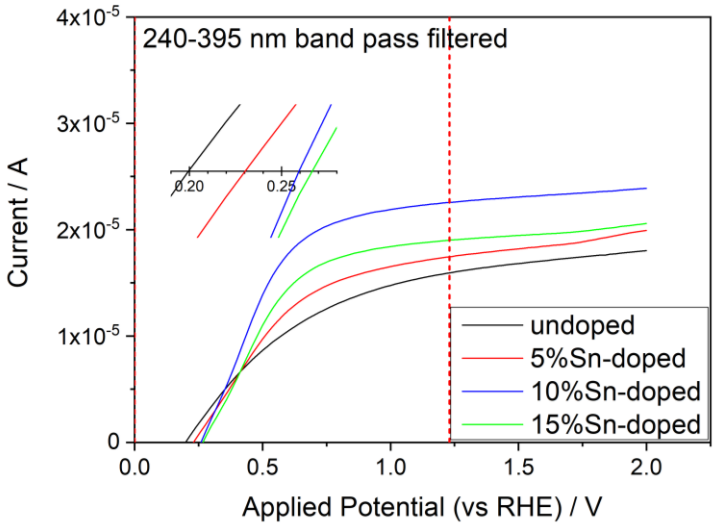


Figure 4.17. Photocurrent data of anatase TiO_2 thin films with various level of Sn doping (red 5%, blue 10%, green 15%, black 0%) grown on 5%Nb:$SrTiO_3$ (5 dip-hydrolysis cycles, followed by annealing at 800 °C for 10 h) under 240-395 nm band pass filtered one sun illumination in 0.1 M NaOH solution. Photocurrent inversion region is enlarged at top left corner. 1 M silver chloride electrode is used as reference, potential converted to vs RHE scale. Water oxidation (1.23 V vs RHE) and reduction (0 V vs RHE) potential are shown in red dotted lines.

The photocurrent of Sn-doped samples reaches plateau faster under visible illumination (0.2 V, Figure 4.16) than under UV illumination (0.5 V, Figure 4.17). Increase in reverse bias widens SCL width which provides additional photoactive sites in the photoanode bulk. Band narrowing is due to surface Sn (II), not a bulk property. Thus, under visible spectrum illumination, increasing SCL width beyond surface region provides no increase in photocurrent.

Although the band gap of anatase TiO_2 is significantly larger than 1.23 V (the minimum potential difference to drive water oxidation and reduction simultaneously), the separation between the quasi-Fermi level of electrons and holes is less than this amount. The calculated quasi-Fermi level splitting using Equation 4.3 under different illuminations are presented in Table 4.2.

Table 4.2 Calculated quasi-Fermi level splitting of undoped, 5%, 10% and 15% Sn-doped anatase thin films under different illumination conditions.

Samples	*quasi-Fermi level splitting / eV*		
Illumination	Full spectrum	240- 395 nm	> 400 nm
Undoped anatase	1.018	1.03	0.812

5% Sn-doped	1	1	0.784
10% Sn-doped	0.955	0.97	0.828
15% Sn-doped	0.962	0.95	0.804

Sn-doping reduces quasi-Fermi level splitting under full spectrum and UV spectrum, suggesting reduced concentration of photogenerated holes. But this conflicts with observation of photocurrent increase in the potential regions of 0 to 1.23 V vs RHE, which indicates increase in concentration of photogenerated holes. It has been shown in previous sections that Sn (II) species on the semiconductor surface introduces a Sn 5s- O 2p state just above the valence band. This narrows the band gap while facilitating electrochemical reactions by trapping holes at the surface where they are optimally placed to undergo water oxidation reaction. Thus, the "upward shift" of quasi-Fermi level of holes due to band gap narrowing on the surface is greater than the "downward shift" of quasi-Fermi level of holes due to increase in photoactive sites. Sn (II) surface doping improves charge transfer across the S-E interface while slightly reducing band gap on the semiconductor surface.

The 10% Sn-doped sample yields the highest photocurrent in the 0.4 to 2 V vs RHE potential region. At 1.23 V vs RHE the photocurrent density of 10% Sn-doped anatase thin film amounts to 0.895 A/m^2 which is a 54% increase compared to undoped anatase thin film. Although bandgap reduction at semiconductor surface is present, the photocurrent improvement is mainly due to increase in bulk photoactive sites through Sn-doping.

4.3.5 Potential PEC setups

In previous section, Sn-doped anatase photoanode was shown to be incapable of sustaining self-driven PEC water splitting without external bias. Although countless efforts have been made in search for a self-driven single photoanode/photocathode PEC solution, an effective water splitting PEC still requires heterogeneous structure.[30,38–42] In this section, pure photo-driven water splitting PECs using single ideal photoanode-metal-cathode structure and heterogeneous non-ideal photoanode-photocathode structure are illustrated with energy diagrams and photocurrents.

4.3.5.1 PEC with single ideal photoanode

First, let us consider an ideal n-type photoanode with noble metal cathode integration for self-driven PEC water splitting. Assuming no overpotential required on the metal cathode, the energy diagram for such a system is presented in Figure 4.18.

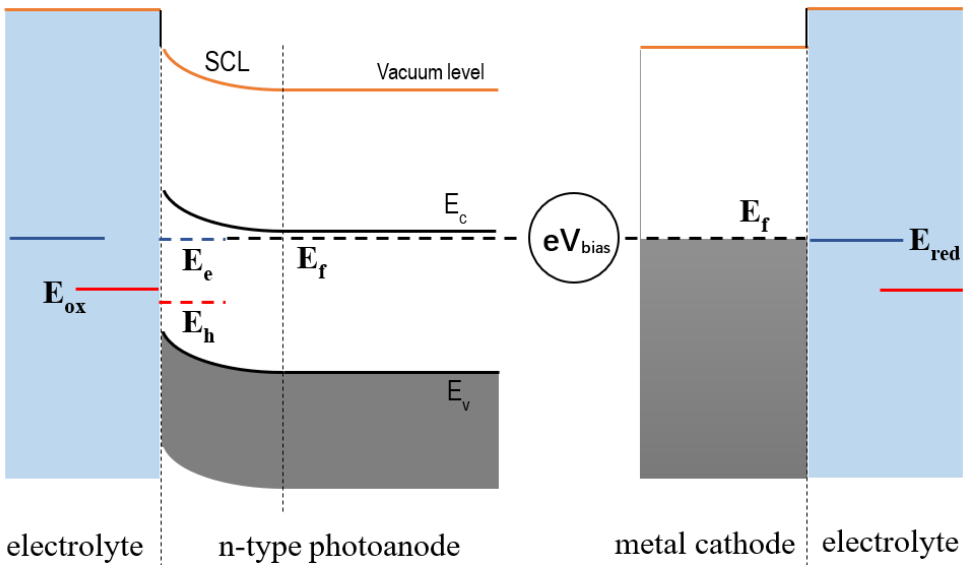


Figure 4.18. Energy diagram of an water splitting PEC device consists of an ideal n-type semiconductor photoanode and metal cathode under illumination. The equivalent energy levels of

water oxidation and reduction are shown as solid red and blue lines respectively. Quasi-Fermi levels of electron and holes are shown as dashed blue and red line respectively.

The quasi-Fermi level splitting on the photoanode surface needs to be greater than overall water splitting energy (1.23 eV) to satisfy self-driven requirement. Since the noble metal cathode works like an RHE. When the n-type semiconductor is subject to appropriate illumination, electrons are excited into the conduction band and collected at metal contact on the rear end of the semiconductor electrode. The electrons are transported to the metal counter electrode surface where water is reduced to hydrogen. The holes that remained in the valence band migrate towards the S-E interface under the influence of electric field in the SCL and oxidize water to oxygen. An illustrated photocurrent data vs RHE scale is shown in Figure 4.19; at 0 V vs RHE, anodic photocurrent should be present.

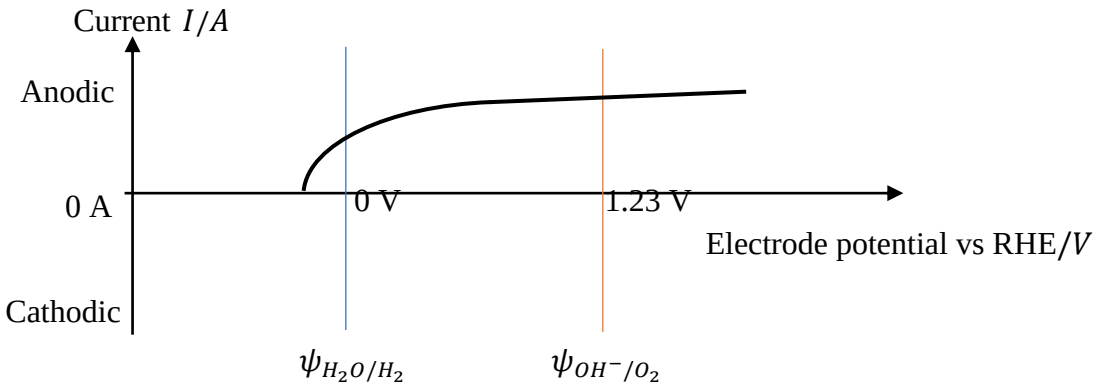


Figure 4.19. An illustrated photocurrent data of an ideal n-type semiconductor photoanode working electrode in vs RHE scale, only the anodic photocurrent region is shown.

4.3.5.2 PEC with heterogeneous non-ideal photoanode-photocathode

Consider a non-ideal p-type photocathode that cannot sustain self-driven PEC water splitting without external bias. Assuming no overpotential required on the metal anode, the energy diagram of such a device is shown in figure 4.20.

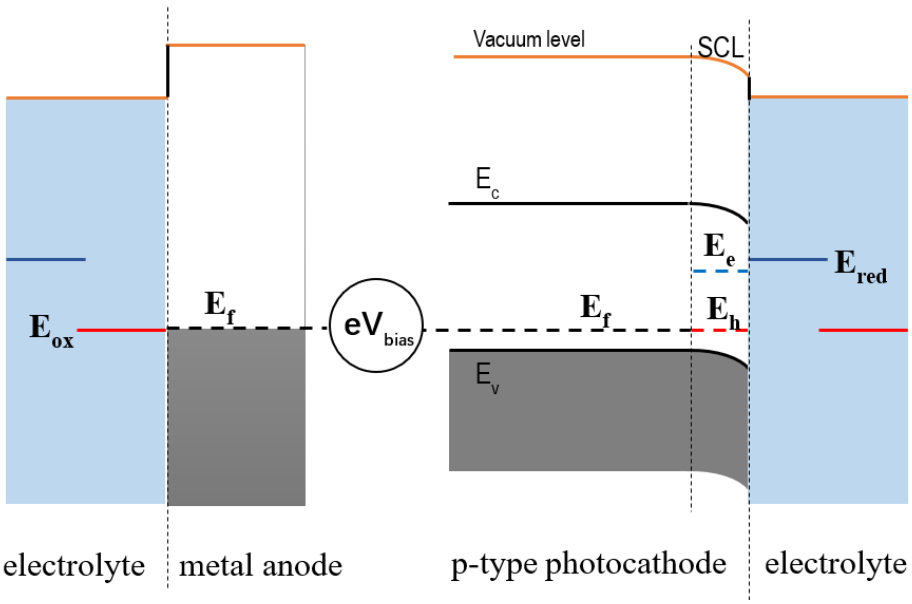


Figure 4.20. Energy diagram of a water splitting PEC device consists of a non-ideal p-type semiconductor photocathode and metal anode under illumination. The equivalent energy levels of water oxidation and reduction are shown as solid red and blue lines respectively. Quasi-Fermi levels of electron and holes are shown as dashed blue and red line respectively.

In figure 4.20, the energy separation between the quasi-Fermi level of electron and holes is not enough for overall water splitting. Thus, an illustrated photocurrent data vs RHE should look like Figure 4.21. At 1.23 V vs RHE, cathodic photocurrent should be absent, and photocurrent onset should be in between 0 V and 1.23 V vs RHE.

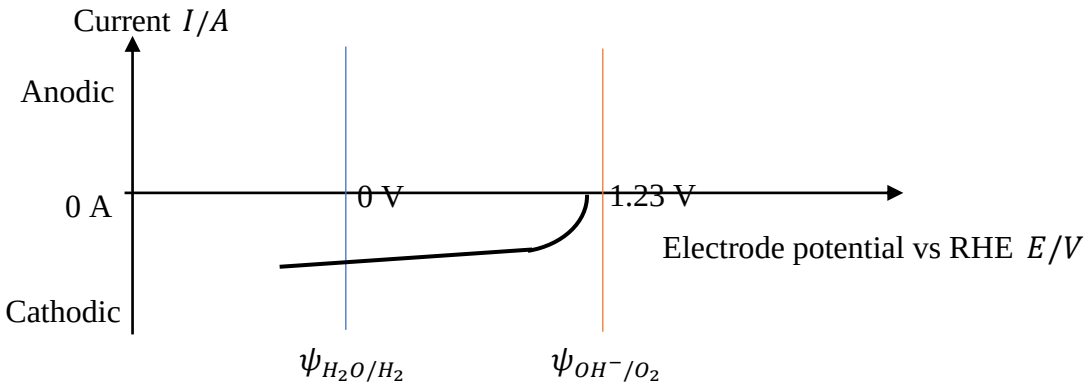


Figure 4.21. An illustrated photocurrent data of a non-ideal p-type semiconductor photocathode working electrode in vs RHE scale, only the cathodic photocurrent region is shown.

A PEC device consisted of this non-ideal p-type photocathode and a n-type non-ideal photoanode in direct electrical connection. The operating parameter of such a PEC device can be mathematically predicted. By taking an inverse of cathodic photocurrent and overlaying the two sets of data, the intersect point is the maximum current (I_{max}) for PEC water splitting. (Figure 4.22) The energy diagram of such a water splitting PEC under suitable illumination is shown in Figure 4.23.

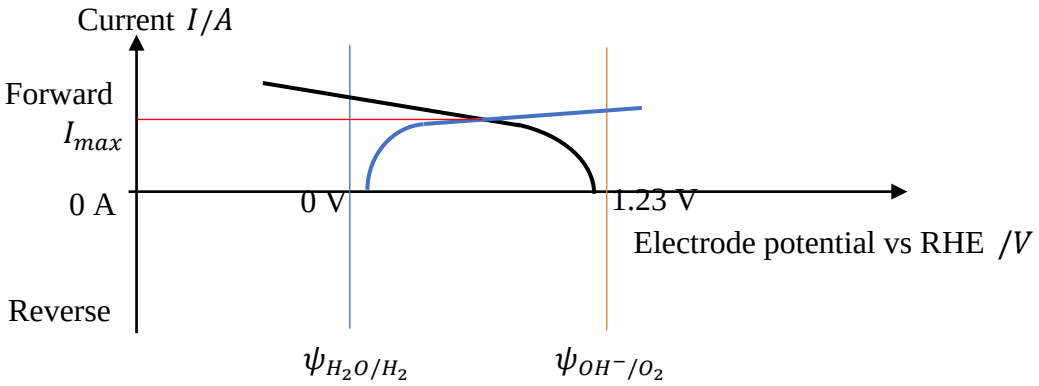


Figure 4.22. An illustrated photocurrent data form a non-ideal n-type semiconductor photoanode overlaid with a non-ideal p-type semiconductor photocathode.

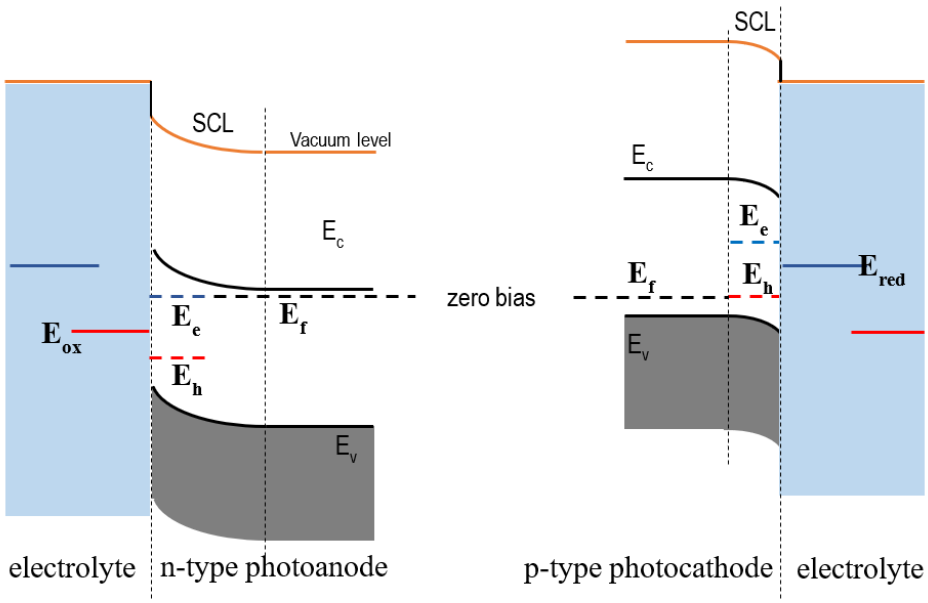


Figure 4.23. Energy diagram of a water splitting PEC device consists of a non-ideal p-type semiconductor photocathode and non-ideal n-type semiconductor photoanode under illumination. The equivalent energy levels of water oxidation and reduction are shown as solid red and blue lines respectively. Quasi-Fermi levels of electron and holes are shown as dashed blue and red line respectively.

Using quasi-Fermi level alignments from previous sections, more clarity on translation from I-V data to S-E interface structure can be achieved. In this section, we have demonstrated the energy level alignments for self-driven water splitting PEC and the corresponding I-V data.

4.4 Conclusions

In this chapter, Sn doping was investigated as a potential method for improving PEC water splitting capability of anatase TiO_2 thin film. A conductive 5% Nb-doped $SrTiO_3$ (001) single crystalline substrate was used to grow required Sn-doped anatase thin film material for PEC study. The PEC performance was investigated with a three-electrode setup using CV. S-E interface energy diagrams were presented to support the CV data.

In the first section, XRD results show that ordered Sn-doped anatase TiO_2 thin films were successfully grown on 5%Nb:$SrTiO_3$ (001) conductive substrate epitaxially using dip-coating method. Incorporating Sn into anatase TiO_2 lattice lead to an expansion of the unit cell, while the crystalline structure is maintained. The enrichment of Sn (II) species on the surface was identified using XPS. In the second section, Sn-doped anatase TiO_2 thin film was shown be to a n-type photoanode capable of photocatalytic oxidation of water using light on/off experiment. The irregular cathodic photocurrent response lead to the review of S-E interface in the third section. This review section explored the various details in CV data

and identified three important potential points: electrolytic water reduction potential (V_{wr}), photocurrent onset potential (V_{onset}), and photocurrent inversion potential (V_{inv}). The energy level alignments were demonstrated using S-E energy diagram at these three potentials.

In the fourth section, PEC improvements due to Sn-doping was investigated with various spectrum of illumination. The photocurrent increased up to 54% (at 1.23 V vs RHE) using 10 atomic % Sn doping, compared to undoped anatase TiO_2, achieving current density of 0.895 A/m^2 with just 5 dip-coating cycles. It is concluded that surface band gap reduction contribution is insignificant. The main contribution to PEC performance is due to bulk Sn doping which increases photoactive sites. In the final section, potential self-driven water splitting PEC configurations are discussed.

References

1. Chen, X. & Mao, S. S. Titanium dioxide nanomaterials: Synthesis, properties, modifications and applications. *Chemical Reviews* **107**, 2891–2959 (2007).

2. Diebold, U. The Surface Science of Titanium Dioxide. *Appl. Surf. Sci.* **48**, 53–229 (2003).

3. Daghrir, R., Drogui, P. & Robert, D. Modified TiO2 for environmental photocatalytic applications: A review. *Industrial and Engineering Chemistry Research* **52**, 3581–3599 (2013).

4. Anitha, V. C., Banerjee, A. N. & Joo, S. W. Recent developments in TiO2 as n- and p-type transparent semiconductors: synthesis, modification, properties, and energy-related applications. *J. Mater. Sci.* **50**, 7495–7536 (2015).

5. Zhang, J., Zhou, P., Liu, J. & Yu, J. New understanding of the difference of photocatalytic activity among anatase, rutile and brookite TiO 2. *Phys. Chem. Chem. Phys. Phys. Chem. Chem. Phys* **16**, 20382–20386 (2038).

6. RAO, K. V. K., NAIDU, S. V. N. & IYENGAR, L. Thermal Expansion of Rutile and Anatase. *J. Am. Ceram. Soc.* **53**, 124–126 (1970).

7. Luttrell, T. *et al.* Why is anatase a better photocatalyst than rutile? - Model studies on epitaxial TiO2 films. *Sci. Rep.* **4**, 4043 (2015).

8. Mo, S. Di & Ching, W. Y. Electronic and optical properties of three phases of titanium dioxide: Rutile, anatase, and brookite. *Phys. Rev. B* **51**, 13023–13032 (1995).

9. Zhang, J., Zhou, P., Liu, J. & Yu, J. New understanding of the difference of photocatalytic activity among anatase, rutile and brookite TiO2. *Phys. Chem. Chem. Phys.* **16**, 20382–20386 (2014).

10. Oropeza, F. E., Davies, B., Palgrave, R. G. & Egdell, R. G. Electronic basis of visible region activity in high area Sn-doped rutile TiO2 photocatalysts. *Phys. Chem. Chem. Phys.* **13**, 7882 (2011).

11. Oropeza, F. E. *et al.* Electronic structure of epitaxial sn-doped anatase grown on SrTiO 3(001) by dip coating. *J. Phys. Chem. C* **117**, 15221–15228 (2013).

12. Jellison, G. E., Boatner, L. A., Budai, J. D., Jeong, B. S. & Norton, D. P. Spectroscopic ellipsometry of thin film and bulk anatase (TiO2). *J. Appl. Phys.* **93**, 9537–9541 (2003).

13. Murakami, M. *et al.* Anatase TiO2 thin films grown on lattice-matched LaAiO3 substrate by laser molecular-beam epitaxy. *Appl. Phys. Lett.* **78**, 2664–2666 (2001).

14. Weng, X., Fisher, P., Skowronski, M., Salvador, P. A. & Maksimov, O. Structural characterization of TiO2 films grown on LaAlO3 and SrTiO3 substrates using reactive molecular beam epitaxy. *J. Cryst. Growth* **310**, 545–550 (2008).

15. Czanderna, A. W., Ramachandra Rao, C. N. & Honig, J. M. The anatase-rutile transition: Part 1. - Kinetics of the transformation of pure anatase. *Trans. Faraday Soc.* **54**, 1069–1073 (1958).

16. Yoganarasimhan, S. R. & Rao, C. N. R. Mechanism of crystal structure transformations. Part 3. - Factors affecting the anatase-rutile transformation. *Trans. Faraday Soc.* **58**, 1579–1589 (1962).

17. Hirata, T., Ishioka, K., Kitajima, M. & Doi, H. Concentration dependence of optical phonons in the system. *Phys. Rev. B - Condens. Matter Mater. Phys.* **53**, 8442–8448 (1996).

18. Biesinger, M. C., Lau, L. W. M., Gerson, A. R. & Smart, R. S. C. Resolving surface chemical states in XPS analysis of first row transition metals, oxides and hydroxides: Sc, Ti, V, Cu and Zn. *Appl. Surf. Sci.* **257**, 887–898 (2010).

19. Egdell, R. G., Flavell, W. R. & Tavener, P. Antimony-doped tin(IV) oxide: Surface composition and electronic structure. *J. Solid State Chem.* **51**, 345–354 (1984).

20. Cox, P. A. *et al.* Free-electron behaviour of carriers in antimony-doped tin(IV) oxide: A study by electron spectroscopy. *Solid State Commun.* **44**, 837–839 (1982).

21. Gulino, A., Condorelli, G. G., Fragalà, I. & Egdell, R. G. Surface segregation of Sb in doped TiO2 rutile. *Appl. Surf. Sci.* **90**, 289–295 (1995).

22. Cox, P. A., Egdell, R. G., Harding, C., Patterson, W. R. & Tavener, P. J. Surface properties of antimony doped tin(IV) oxide: A study by electron spectroscopy. *Surf. Sci.* **123**, 179–203 (1982).

23. Kwoka, M. *et al.* XPS study of the surface chemistry of L-CVD SnO2 thin films after oxidation. *Thin Solid Films* **490**, 36–42 (2005).

24. Walsh, A. & Watson, G. W. Electronic structures of rocksalt, litharge, and herzenbergite SnO by density functional theory. *Phys. Rev. B - Condens. Matter Mater. Phys.* **70**, 1–7 (2004).

25. Koval, C. A. & Howard, J. N. Electron Transfer at Semiconductor Electrode-Liquid Electrolyte Interfaces. *Chem. Rev.* **92**, 411–433 (1992).

26. Lewis, N. S. Progress in understanding electron-transfer reactions at semiconductor/liquid interfaces. *J. Phys. Chem. B* **102**, (1998).

27. Bard, A. J. & Faulkner, L. R. *ELECTROCHEMICAL METHODS Fundamentals and Applications*. **2**, (2012).

28. Kumar, A., Wilisch, W. C. & Lewis, N. S. The Electrical Properties of Semiconductor/Metal, Semiconductor/Liquid, and Semiconductor/Conducting Polymer Contacts. *Crit. Rev. Solid State Mater. Sci.* **18**, 327–353 (1993).

29. Peter, L. M. Dynamic Aspects of Semiconductor Photoelectrochemistry. *Chem. Rev.* **90**, 753–769 (1990).

30. Walter, M. G. *et al.* Solar water splitting cells. *Chem. Rev.* **110**, 6446–6473 (2010).

31. Krol, R. & Gratzel, M. *Photoelectrochemical Hydrogen Production*. *Hydrogen Energy System* **102**, (Springer US, 2012).

32. Li, L., Salvador, P. A. & Rohrer, G. S. Photocatalysts with internal electric fields. *Nanoscale* **6**, 24–42 (2014).

33. Bisquert, J., Cendula, P., Bertoluzzi, L. & Gimenez, S. Energy diagram of semiconductor/electrolyte junctions. *J. Phys. Chem. Lett.* **5**, 205–207 (2014).

34. Liu, C. *et al.* Ti-treatment and Co–Pi modification of hematite-based photoanodes for improved photoelectrochemical water oxidation. *J. Mater. Sci. Mater. Electron.* 17447–17458 (2019). doi:10.1007/s10854-019-02095-1

35. Matsuo, H. *et al.* Impact of lattice defects on water oxidation properties in SnNb 2 O 6 photoanode prepared by pulsed-laser deposition method . *J. Appl. Phys.* **126**, 094901 (2019).

36. Digdaya, I. A., Adhyaksa, G. W. P., Trześniewski, B. J., Garnett, E. C. & Smith, W. A. Interfacial engineering of metal-insulator-semiconductor junctions for efficient and stable photoelectrochemical water oxidation. *Nat. Commun.* **8**, 1–8 (2017).

37. Chen, X., Liu, L. & Huang, F. Black titanium dioxide (TiO 2) nanomaterials. *Chem. Soc. Rev. Chem. Soc. Rev* **44**, 1861–1885 (2015).

38. Kudo, A. & Miseki, Y. Heterogeneous photocatalyst materials for water splitting. *Chem. Soc. Rev.* **38**, 253–278 (2009).

39. Li, X. *et al.* Engineering heterogeneous semiconductors for solar water splitting. *J. Mater. Chem. A* **3**, 2485–2534 (2015).

40. Jiang, C., Moniz, S. J. A., Wang, A., Zhang, T. & Tang, J. Photoelectrochemical devices for solar water splitting-materials and challenges. *Chem. Soc. Rev.* **46**, 4645–4660 (2017).

41. Ni, M., Leung, M. K. H., Leung, D. Y. C. & Sumathy, K. A review and recent developments in photocatalytic water-splitting using TiO 2 for hydrogen production. *Renewable and Sustainable Energy Reviews* **11**, 401–425 (2007).

42. Ni, M., Leung, M. K. H., Leung, D. Y. C. & Sumathy, K. A review and recent developments in photocatalytic water-splitting using TiO2 for hydrogen production. *Renewable and Sustainable Energy Reviews* **11**, 401–425 (2007).

Chapter 5 Sn-Doped Rutile TiO_2 Thin Film

5.1 Introduction

In the previous chapter, we have investigated the Sn-doping improvements in PEC water splitting for TiO_2 in the anatase phase. Compared to undoped anatase, Sn-doped anatase thin films increased water oxidation photocurrent up to 54% (at 1.23 V vs RHE, pH 13) with 10 atomic % Sn doping, achieving current density of 0.895 A/m^2 with just 5 dip-coating cycles. Sn-doping improves anatase PEC water splitting performance in two ways: i) surface Sn (II) creates O 2p-Sn 5s character at the top of the valence band[1] narrowing band gap and traps photogenerated holes which are optimally placed to participate in water oxidation reaction; ii) bulk Sn increases photoactive sites which enhances maximum photocurrent.

It has been demonstrated that charge carrier lifetime in anatase is higher compared to rutile, which results in a higher surface activity for CO photo-oxidation to CO_2.[2] Also, anatase has a higher surface adsorption capacity to hydroxyl groups[3] and smaller grain size,[4] which increases photocatalytic activity compared to rutile. However, with Sn-doping, the drawbacks of low charge carrier lifetime and worse surface activity could be mitigated. Moreover, rutile has a narrower band gap (3.06 eV) than that of anatase (3.2 eV),[5] which increases absorbance ability towards solar light. It would be interesting to investigate how Sn-doped rutile compares to Sn-doped anatase in PEC water splitting.

Rutile structured TiO_2 can be easily obtained with high-temperature annealing, since anatase phase is metastable at room temperature and converts exothermically and irreversibly to

rutile at elevated temperatures, with an activation barrier of around 20 kJ/mol.[6,7] As for rutile thin films, common industrial substrates such as fluorine-doped tin oxide (FTO) is readily available and inexpensive for growth of rutile structured nanomaterials.[8] In this chapter, the dip-coating method was adapted to grow Sn-doped rutile TiO_2 thin films on FTO conductive glass substrates. PEC performance of Sn-doped rutile TiO_2 thin films were investigated using a three-electrode setup using CV under simulated solar irradiation. The photocurrent increased up to 23% (at 1.23 V vs RHE) using 1 atomic % Sn doping, compared to undoped rutile TiO_2, achieving current density of 1.036 A/m^2 with just 5 dip-coating cycles. PEC performance difference between Sn-doped rutile and anatase TiO_2 thin films were also investigated.

5.2 Experimental

Rutile TiO_2 thin film was grown using the sol-gel dip-coating method. This process is composed of 3 parts: a) preparation of metal alkoxide solution, b) dip-coating process and c) furnace annealing.

25mL of 2-propanol (CHROMASOLV® Plus, for HPLC, 99.9% Sigma-Aldrich) was used as solvent. An appropriate amount of Titanium (IV) isopropoxide (97% Sigma-Aldrich) was then added to achieve a 0.33 M Ti concentration mixture. Various amounts of Tin (IV) tert-butoxide (≥99.99% Sigma-Aldrich) was added to create Ti^{4+}: Sn^{4+} ratio ranging from 95: 5 to 85: 15. 150 µL of Nitric acid (ACS reagent, 70% Sigma-Aldrich) was added to prevent hydrolysis of the precursor.

The FTO glass was provided by Visiontek Systems (TCO-VIS 15, CNC cut to 20*20*2.2 mm, <15 Ω/sq). The substrate was cut in half to 10*20*2.2cm using a Bohle carbide cutter. The substrate was then cleaned using a special process explained in Chapter 2 to remove foreign substances introduced through CNC processes. For a typical dip-coating cycle, the substrate was dipped into the precursor solution and held for 5 min and slowly pulled out at a speed of 3.5 mm/min, then hydrolysed with wet nitrogen flow for 5 min. 5 dip-coating cycles were used for each sample.

The coated substrate was placed in a clean alumina boat with the conductive side facing up. The sample was annealed at 600°C for one hour and cooled down to room temperature.

5.3 Results and discussion

5.3.1 Physical characterisation of Sn-doped TiO_2 thin film

It has been demonstrated in Chapter 4 that sol-gel dip-coating is suitable for epitaxial thin film growth. Compared to anatase substrates, rutile substrates are much more available, such as ITO and FTO, which are widely used in touchscreen panels. Anatase phase is usually obtained when TiO_2 is precipitated from solution in sol-gel related preparation processes.[9] However, anatase irreversibly converts to rutile at elevated temperatures.[10] Moreover, rutile structure of FTO layer promotes the rutile phase growth on the surface.[11] Thus using FTO coated glass substrate and high-temperature annealing, pure rutile phase thin films could be obtained straightforwardly. Moreover, in order to carry out PEC measurements, a conductive substrate is required. FTO coated glass substrate (Visiontek Systems) were used

for this study due to the good epitaxy relationship with rutile and good conductivity. The reason for choosing FTO over ITO is because indium can be easily oxidised in the presence of oxygen at higher temperatures, which lead to degradation in electrical property of ITO.

The samples were prepared using 5 dip−hydrolysis cycles with alkoxide precursor solution. The as-prepared samples were then annealed at 600 °C for 1 h in air. Four sets of samples were made: **undoped** (TiO_2) and doping level of **0.5** ($Sn_{0.005}Ti_{0.995}O_2$), **1** ($Sn_{0.01}Ti_{0.99}O_2$) and **1.5** ($Sn_{0.015}Ti_{0.985}O_2$) atomic % Sn rutile thin films. θ-2θ XRD results for bare FTO substrate and 1% Sn-doped rutile TiO_2 ($Sn_{0.01}Ti_{0.99}O_2$) thin film are shown in Figure 5.1.

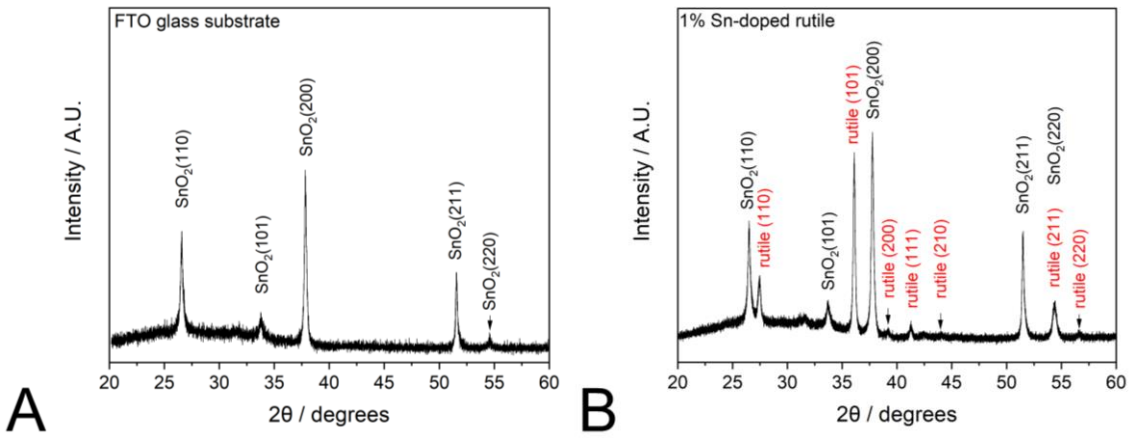


Figure 5.1. θ-2θ X-ray diffraction profiles for A) bare FTO glass substrate and B) 1 atomic % Sn-doped rutile ($Sn_{0.01}Ti_{0.99}O_2$) thin film grown on FTO glass substrate by 5 dip-hydrolysis cycles, followed by annealing at 600 °C for 1 h. The intensity scale is linear.

Since the substrate is polycrystalline, all SnO_2 reflections are present. The intensity distribution of different reflections in FTO glass result is similar to that of powder diffraction patterns, indicating no preferred crystal orientation. The broad hump in the 20 to 40 degrees region is indicative of amorphous glass.[12]

Only rutile TiO_2 and SnO_2 reflections are found in the Sn-doped rutile TiO_2 thin film diffraction result, with all rutile reflections present. The (101), (004), and (020) anatase

reflections are absent at 25.3°, 37.8°, and 48.1° respectively. This indicates the thin film is in pure rutile phase. The intensity distribution of different rutile reflections suggests no preferred orientation of thin film growth and the as-grown thin film should be polycrystalline.

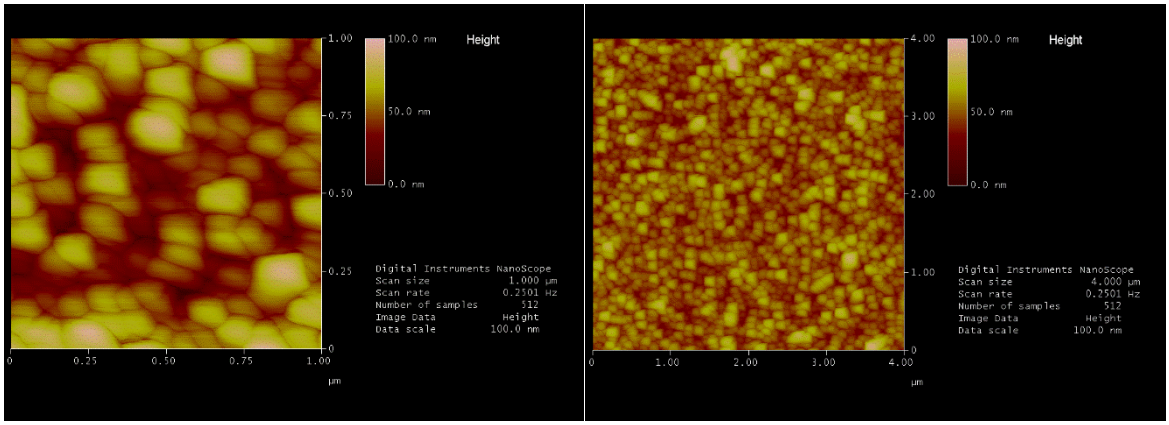


Figure 5.2 AFM image of 1% Sn-doped rutile thin film.

Atomic force microscopy images (AFM) images of 1 % Sn-doped rutile thin film annealed at 600 °C is shown in Figure 5.2. The film morphology is seen to present an array of interlinked quadrangle islands, with variation in size and orientation confirming polycrystalline structure.

To investigate the chemical states and proportion of the species present in the Sn-doped TiO_2 thin film surfaces, X-ray photoelectron spectra (XPS) of Sn 3d core levels were measured.

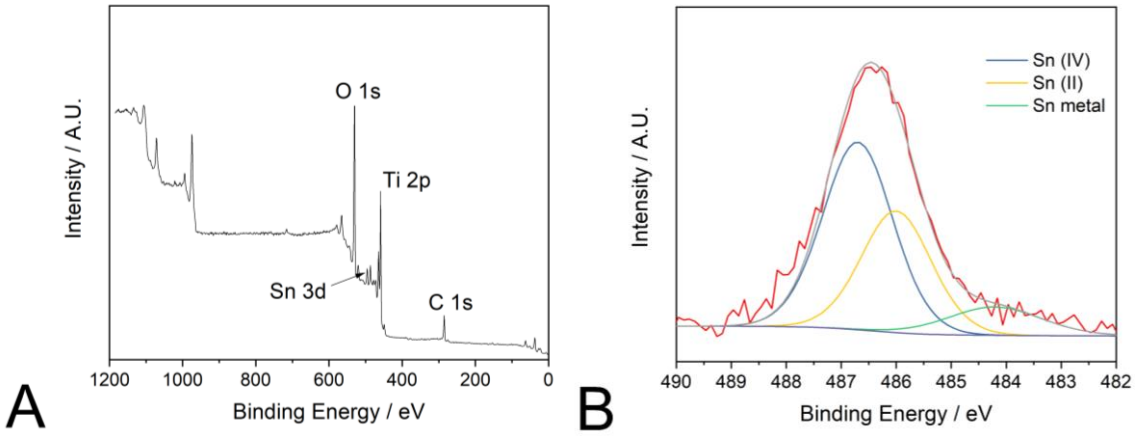


Figure 5.3. XPS (A) survey spectrum and (B) Sn $3d_{5/2}$ core level spectrum of 1% Sn-doped rutile thin film.

The survey spectrum in Figure 5.3A shows the carbon 1s peak at 284.8 eV, titanium 2p peaks at 458.4 eV and 464.3 eV, tin 3d peaks at 486.7 eV and 494.6 eV, and an oxygen 1s peak at 529.8 eV. To calculate the percentage value of each element, CasaXPS software was used. Peak fitting GL(30) (Gaussian (70%)–Lorentzian (30%)) was applied to all peaks beside Ti 2p peak which uses a GL(70) fitting.[13] Normalised atomic percentages were determined from peak areas of the main elemental peaks applying CasaXPS's relative sensitivity factors (RSF). RSF of 7.81 and 25.05 were used for Ti 2p and Sn 3d respectively. The calculated Sn to Ti percentage using XPS survey spectrum amounts to 3.6%, 6.5%, and 8.1% for 0.5, 1, and 1.5 atomic % Sn-doped rutile samples. Dopant surface enrichment has been seen in other systems where a post-transition metal ion dopant is introduced into an oxide host lattice.[14–16] The enrichment of Sn on the surface has been attributed to the fact that Sn (II) is more easily accommodated in surface sites than in bulk sites, thus providing a driving force for surface segregation.[17]

Similar to results in the previous chapter, the Sn $3d_{5/2}$ core level spectrum in Figure 5.3B show a significant amount of Sn (II) presence reaffirming the surface enrichment of Sn due

to Sn (II) cation. Deconvolution of this peak yields an Sn (IV) peak at 486.7 eV, an Sn (II) peak at 486.0 eV and a Sn metal peak at 484.2 eV which agrees well with another finding.[18] The main parameters used in the applied fitting procedure, as well as the best fitting parameters, are summarized in Table 5.1.

Table 5.1 The binding energy, full width at half maximum (FWHM) and relative peak area of main components of XPS $Sn3d_{5/2}$ peak from 1% Sn-doped rutile thin film.

XPS peak parameters	Sn $3d_{5/2}$		
Components	Sn (IV)	Sn (II)	Sn Metal
Binding energy / eV	486.7	486.0	484.2
FWHM / eV	1.5	1.5	2.0
Relative peak area / %	54.1	35.0	10.9

The electrons required to reduce Sn (IV) to Sn (II) derives from oxygen vacancies in host lattice (rutile TiO_{2-y}) as each vacancy generates two electrons. Sn-doping will partially eliminate the formation of undesirable Ti (III) traps in rutile bulk, which improves charge carrier lifetime. Moreover, Sn (II) 5s electrons hybridise strongly with O 2p states to give antibonding states of mixed Sn 5s–O 2p character at the top of the valence band.[1] Sn (II) enrichment at the surface makes good hole traps which are optimally placed to facilitate redox reactions for the photogenerated holes.

5.3.2 Light on/off experiment

The entire potential region was investigated using the light on/light off experiments to distinguish photocurrent response from the electrochemical response. Linear CV scans were performed while an electronic optical shutter is used to chop the incoming light at a frequency of 0.5 Hz. Coupled with a scan rate of 0.02 V/s and step voltage of 0.02 V, data points of photocurrent and dark current alternate throughout the potential window. This approach provides an intuitive view of the photo-responsive potential regions.

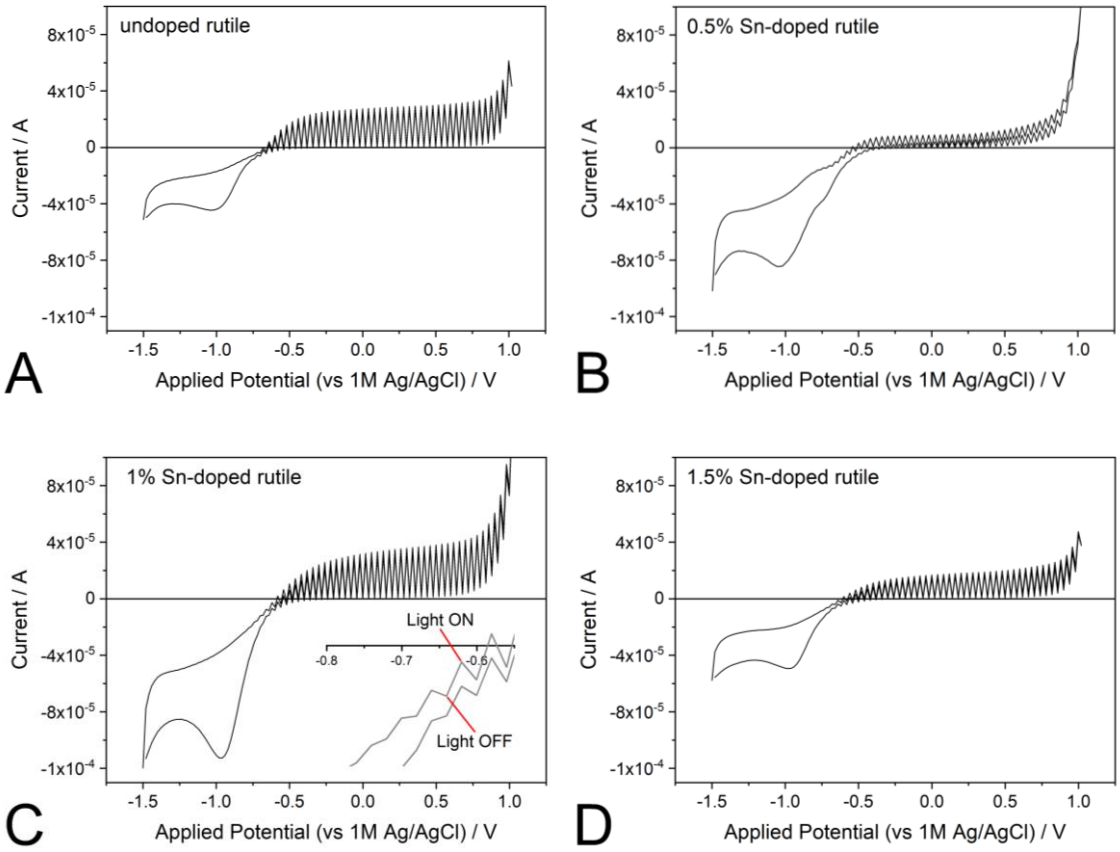


Figure 5.4. 20 mV/s cyclic voltammetry plots of rutile TiO_2 thin films with various level of Sn doping (A 0%, B 0.5%, C 1%, D 1.5%)) grown on FTO coated glass (5 dip-hydrolysis cycles, followed by annealing at 600 °C for 1 h) under one sun illumination in 0.1 M NaOH solution with a light-on-light-off frequency of 0.5 Hz. The detailed cathodic photocurrent region of 1% Sn-doped rutile thin film is shown in bottom right corner of caption C.

In the -0.6 to 1.0 V region, anodic photocurrent is present for all samples, photocurrents increase as electrode potential shifts to more positive values. This anodic current is characteristic of PEC water oxidation with an n-type semiconductor photoanode. The n-type semiconductor, at this potential region, has an upward band bending near the S-E interface with a built-in electric field pointing outwards into the electrolyte. Photogenerated holes in the SCL are forced to the electrode surface by the electric field to participate in water oxidation, thus the anodic photocurrent response. With increase in positive potential bias, the upward band bending and SCL width increases, which increase the number of photoactive sites under the influence of built-in electric field, and cause increase in photocurrent.

In the -0.75 to -0.6 V region, cathodic photocurrent is present for all samples. This potential region is equivalent to 0.25 to 0.4 V vs RHE which is impossible for photocatalytic water reduction to hydrogen. As discussed in the previous chapter, this cathodic photocurrent is a result of reduction in leakage electrons due to photogenerated-hole-leakage-electron recombination. This is identified as reduction in cathodic current when light is on. (Figure 5.4 C)

In the -1.5 to -0.75 V region, a capacitive response can be identified as a large forward/reverse current separation. As discussed in the previous chapter, in this potential region, the electric field in the SCL is pointing inwards into the semiconductor bulk, electrons are stored in the SCL. Electrons are majority charge carriers in a n-type semiconductor, the density of which is a few orders of magnitudes higher than minority

charge carriers (holes). The number of stored electrons is higher than the holes in the SCL, thus the pronounced capacitance feature in the cathodic region.

In the 0.75 to 1 V potential region, transition from anodic photocurrent to electrolytic current is seen. This potential region is equivalent to 1.75 to 2 V vs RHE, which is beyond the 0 to 1.23 V vs RHE bias-assisted PEC water splitting window. As explained in the previous chapter, at 1.23 V vs RHE, the alignment of bulk Fermi level, quasi-Fermi level of electrons, and water oxidation level is satisfied. Thus, when applied potential shifts to more positive values (increasing reverse bias), the amount of band bending increase, and eventually the semiconductor will reach reverse breakdown conditions similar to Zener breakdown in p-n junctions. Under this condition, electric field in the SCL enables tunnelling of electrons from the valence to the conduction band of semiconductor electrode, generating numerous free minority carriers (holes) which suddenly increase the anodic electrolytic current. Since the tunnelling of electrons occurs on photoactive sites and non-photoactive site indifferently, tunnelling events compete with photo charge carrier generation. Thus, increasing reverse breakdown current reduces photocurrent, while overall anodic current surges abruptly.

5.3.3 PEC performance comparison

All samples were activated with linear CV scans from -1.5 V to +1.0 V (vs silver chloride electrode) at a rate of 0.02 V/s. A typical set of CV data are presented in Figure 5.5 shows a noticeable discrepancy between scans.

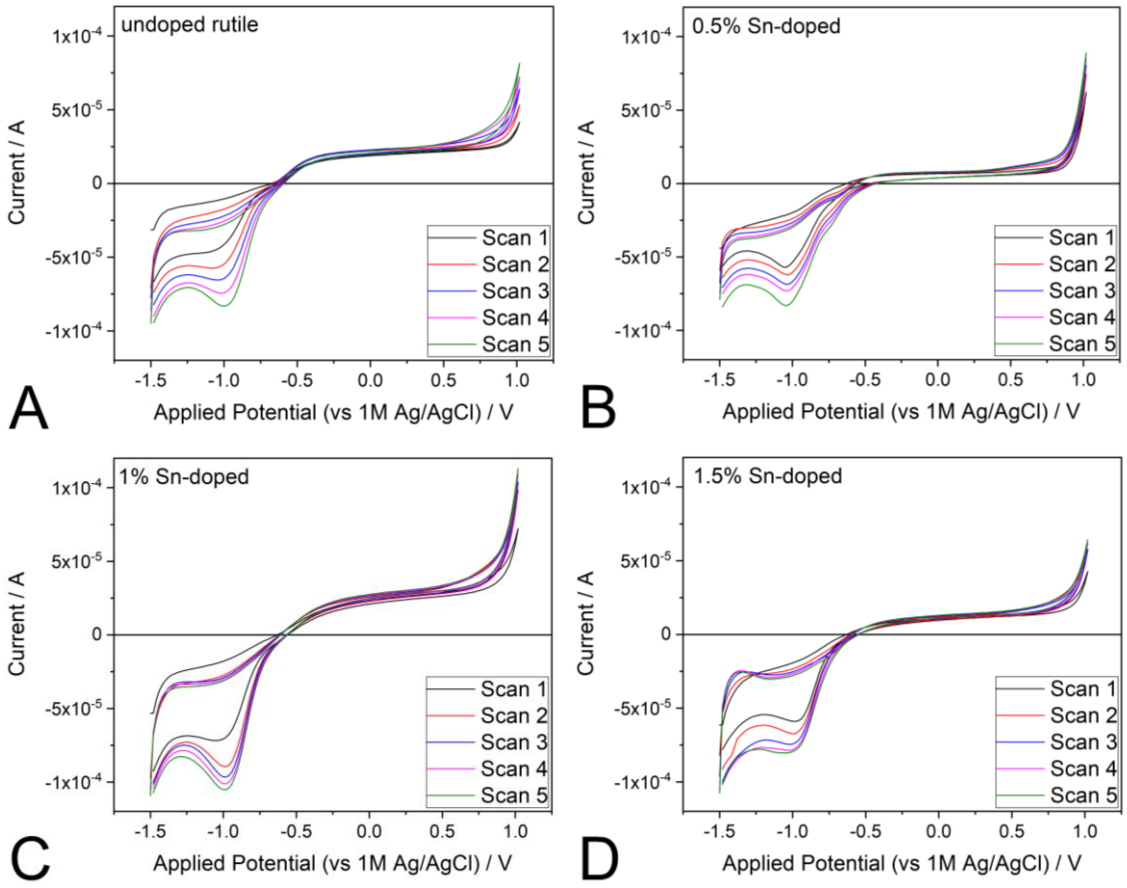


Figure 5.5. 20 mV/s cyclic voltammetry plots of rutile TiO_2 thin films with various level of Sn doping (A 0%, B 0.5%, C 1%, D 1.5%) grown on FTO glass (5 dip-hydrolysis cycles, followed by annealing at 600 °C for 1 h) under one sun illumination in 0.1 M NaOH solution.

During this activation process, an increase in photocurrent (-0.5 V to 1 V) and capacitance (-1.5 V to -0.75 V) is observed. In the 0.75 to 1 V potential region, an abrupt increase in anodic current is present, which was identified as a transition from anodic photocurrent to electrolytic current in the previous section. This feature was not observed for the Sn-doped anatase thin film results in chapter 4. This early onset of electrolytic water oxidation is probably a result of polycrystalline thin film grown on FTO substrate. The 5% Nb: $SrTiO_3$ (001) substrate yields anatase structured thin film with ordered (001) crystal surfaces with large crystal grain size while FTO yields rutile structured thin film with a range of (110), (101), and (211) crystal surfaces and a much smaller crystal grain size. This more

polycrystalline electrode surface of rutile thin films gives rise to increased grain boundaries which facilitate charge transfer across the S-E interface.

CV data in Figure 5.6 shows two consecutive scans of the anodic photocurrent regions with perfect overlap, indicating well-activated electrode surfaces. The noticeable capacitive response is visible as by separation between forward and backward scan currents which was duly discussed in Chapter 4.

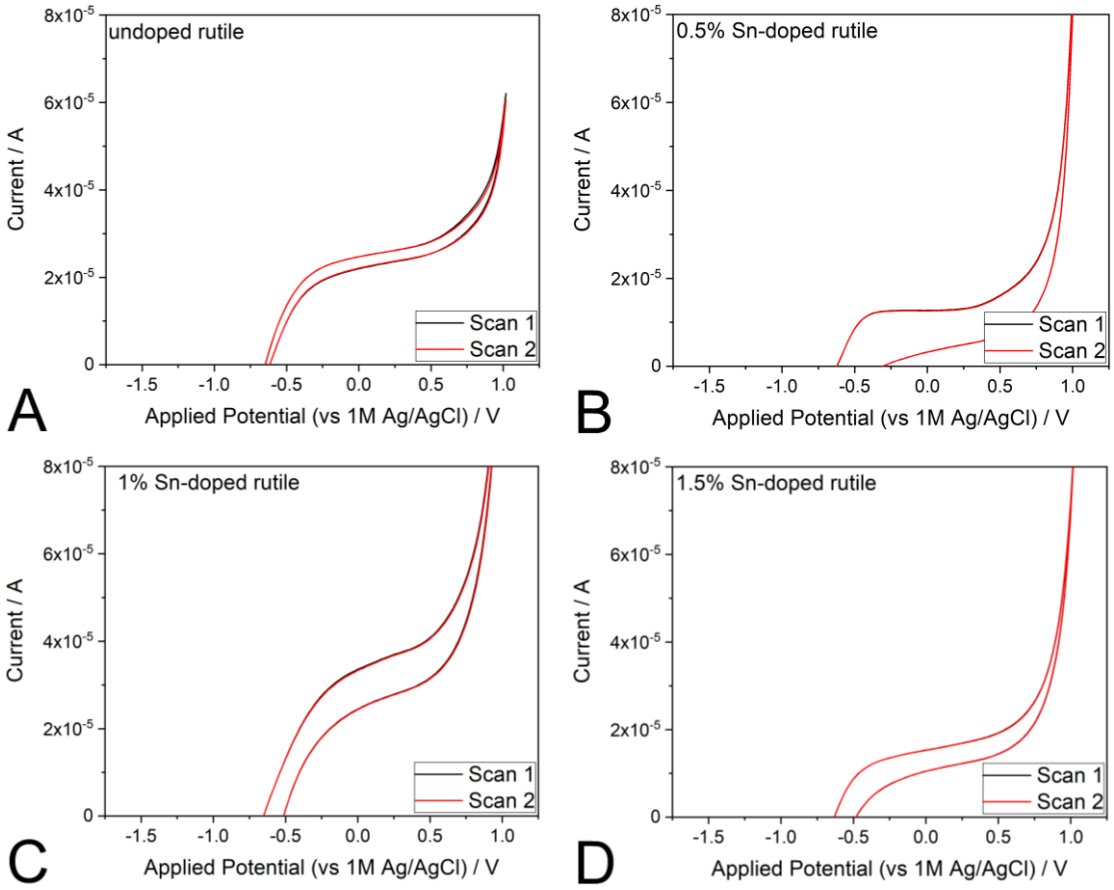


Figure 5.6. 100 mV/s cyclic voltammetry plots of rutile TiO_2 thin films with various level of Sn doping (A 0%, B 0.5%, C 1%, D 1.5%) grown on FTO glass (5 dip-hydrolysis cycles, followed by annealing at 600 °C for 1 h) under one sun illumination in 0.1 M NaOH solution. Only the photocurrent region of the data is shown.

The capacitive feature of Sn-doped samples are more pronounced than un-doped rutile. Under reverse bias (photocurrent region), holes are stored in the SCL. Sn (II) surface sites

act as hole traps increasing hole density in the SCL, which increases SCL capacitance. Capacitor charging/discharging current is non-Faradaic. Assuming charging and discharging current are of the same intensity, they are eliminated by averaging the forward and reverse current. The averaged photocurrent data is shown in Figure 5.7, which is the pure Faradaic current due to photogeneration.

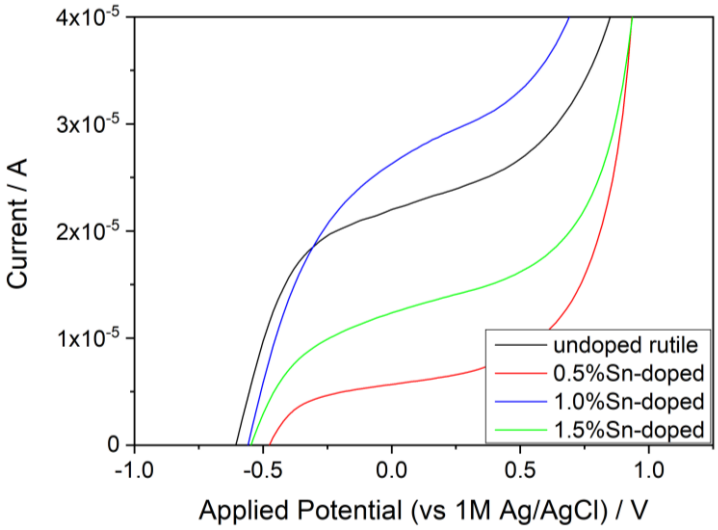


Figure 5.7. Photocurrent plot of rutile TiO_2 thin films with various level of Sn doping (red 0.5%, blue 1.0%, green 1.5%, black 0%) grown on FTO glass (5 dip-hydrolysis cycles, followed by annealing at 600 °C for 1 h) under one sun illumination in 0.1 M NaOH solution.

The applied potential on a working photo-electrode is a key parameter in understanding the properties. RHE scale has become the preferred reference scale for reporting photo-electrode working potentials.[19] Zero volts on the RHE scale reflects the water reduction potential in the actual electrolyte, irrespective of the pH. This is more convenient than SHE scale which requires the H^+ ion at unit activity. Using equation 4.4 in the previous chapter, at pH=13 (0.1 M NaOH electrolyte), the measured potential using 1 M silver chloride electrode ($E_{Ag/AgCl}$) is converted to vs RHE scale (E_{RHE}) using $E_{RHE} = E_{Ag/AgCl} + 0.997\ V$. The photocurrent

plot in Figure 5.7 measured vs 1 M silver chloride reference electrode is converted to vs RHE scale in Figure 5.8.

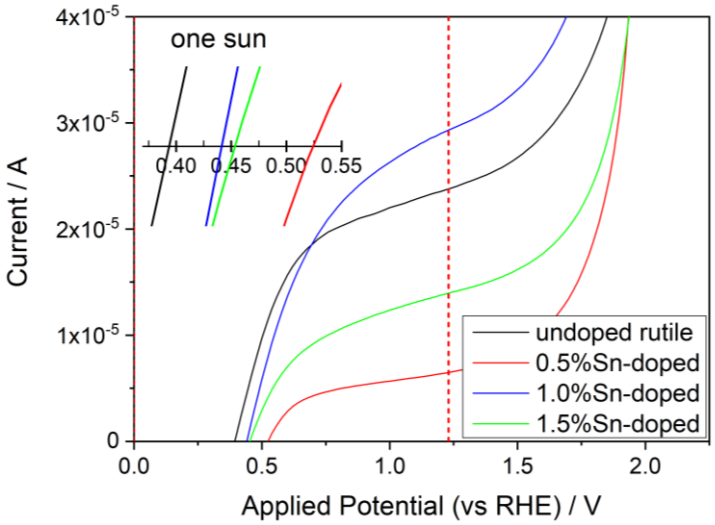


Figure 5.8. Photocurrent plot of rutile TiO_2 thin films with various level of Sn doping (red 0.5%, blue 1.0%, green 1.5%, black 0%) grown on FTO glass (5 dip-hydrolysis cycles, followed by annealing at 600 °C for 1 h) under one sun illumination in 0.1 M NaOH solution. Photocurrent inversion region is enlarged at top left corner. 1 M silver chloride electrode is used as reference, potential converted to vs RHE scale. Water oxidation (1.23 V vs RHE) and reduction (0 V vs RHE) potentials are shown in red dotted lines.

Like many other doped TiO_2 photocurrent results,[20] the photocurrent is not seen at 0 V vs RHE, which means these modified TiO_2 is incapable of sustaining a self-driven water splitting process without external bias. From Figure 5.8, the absence of photocurrent between 0 to 0.5 V vs RHE can be observed. 1 % Sn-doped rutile shows improved photocurrent performance in the external bias assisted PEC potential region (0.7 to 1.23 V vs RHE) compared to undoped rutile. Doping level of 0.5 and 1.5 % Sn showed a negative impact on photocurrent across the entire potential region.

In addition to the full solar spectrum, a visible contribution towards PEC water splitting was investigated using a 400 nm long-pass filtered one sun spectrum. From the results in Figure

5.9, we can see that Sn-doped rutile has shown an overall improvement compared to undoped rutile with 1% Sn-doped rutile delivering the best result.

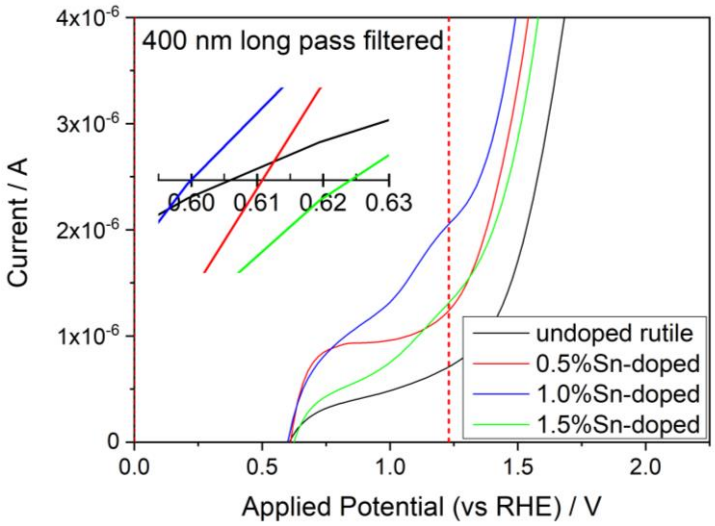


Figure 5.9. Photocurrent plot of rutile TiO_2 thin films with various level of Sn doping (red 0.5%, blue 1.0%, green 1.5%, black 0%) grown on FTO glass (5 dip-hydrolysis cycles, followed by annealing at 600 °C for 1 h) under 400nm long pass filtered one sun illumination in 0.1 M NaOH solution. Photocurrent inversion region is enlarged at top left corner. 1 M silver chloride electrode is used as reference, potential converted to vs RHE scale. Water oxidation (1.23 V vs RHE) and reduction (0 V vs RHE) potentials are shown in red dotted lines.

Considering that under one sun simulated irradiation (Figure 5.8), 0.5 and 1.5 % Sn-doped samples yields a decrease in photocurrent compare to undoped rutile. In Figure 5.9, this photocurrent enhancement of Sn-doped samples under visible illumination suggests Sn doping in rutile TiO_2 lead to a narrowing in band gap which improves visible spectrum response. Band narrowing is due to surface Sn (II), not a bulk property. Increase in reverse bias widens SCL width which provides additional photoactive sites in the photoanode bulk. Thus, under visible spectrum illumination, increasing SCL width beyond surface region provides no increase in photocurrent. The photocurrent of Sn-doped samples reaches plateau

faster under visible illumination (0.2 V, Figure 5.9) than under full spectrum illumination (0.5 V, Figure 5.8) which agrees with this explanation.

Finally, UV contributions towards PEC water splitting were investigated using a 240-395 nm band-pass filtered one sun spectrum. (Figure 5.10)

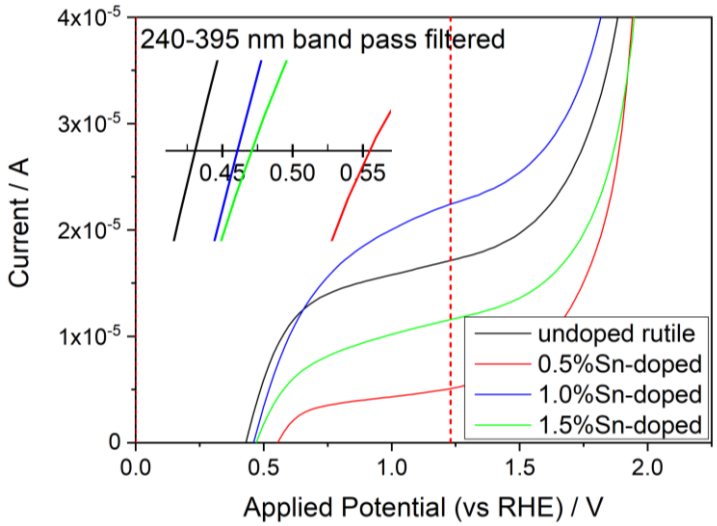


Figure 5.10. Photocurrent plot of rutile TiO_2 thin films with various level of Sn doping (red 0.5%, blue 1.0%, green 1.5%, black 0%) grown on FTO glass (5 dip-hydrolysis cycles, followed by annealing at 600 °C for 1 h) under 240-395 nm band pass filtered one sun illumination in 0.1 M NaOH solution. Photocurrent inversion region is enlarged at top left corner. 1 M silver chloride electrode is used as reference, potential converted to vs RHE scale. Water oxidation (1.23 V vs RHE) and reduction (0 V vs RHE) potentials are shown in red dotted lines.

Photocurrent acquired under visible spectrum (> 400nm) is one magnitude lower compared to the UV spectrum (240-395 nm). This suggests that the bandgap reduction contribution (surface related) is trivial compared to bulk property improvements. Thus, the main PEC photocurrent response is likely due to an increase in photoactive sites through bulk Sn-doping.

Although the band gap of rutile TiO_2 is significantly larger than 1.23 V (the minimum potential difference to drive water oxidation and reduction simultaneously), the separation

between the quasi-Fermi level of electrons and holes is less than this amount. The calculated quasi-Fermi level splitting using Equation 4.3 (Chapter 4) under different illuminations are presented in Table 5.2.

Table 5.2 Calculated quasi-Fermi level splitting of undoped, and 0.5%, 1% and 1.5% Sn-doped rutile thin films under different illumination conditions.

Samples	*quasi-Fermi level splitting / eV*		
Illumination	Full spectrum	240- 395 nm	> 400 nm
Undoped rutile	0.84	0.8	0.62
0.5% Sn-doped	0.71	0.67	0.62
1% Sn-doped	0.79	0.76	0.63
1.5% Sn-doped	0.77	0.76	0.61

Sn-doping reduces quasi-Fermi level splitting under full spectrum and UV spectrum, suggesting reduced concentration of photogenerated holes. But this conflicts with observation of photocurrent increase in the external bias assisted PEC potential region (0.7 to 1.23 V vs RHE), which indicates increase in concentration of photogenerated holes. It has been shown in previous sections that Sn (II) species on the semiconductor surface introduces a Sn 5s- O 2p state just above the valence band. This narrows the band gap while facilitating electrochemical reactions by trapping holes at the surface where they are optimally placed to undergo water oxidation reaction. Thus, the “upward shift” of quasi-Fermi level of holes

due to band gap narrowing on the surface is greater than the "downward shift" of quasi-Fermi level of holes due to increase in photoactive sites. Sn (II) surface doping improves charge transfer across the S-E interface while slightly reducing band gap on the semiconductor surface.

The 1% Sn-doped sample yields the highest photocurrent in the 0.7 to 2 V vs RHE potential region. At 1.23 V vs RHE the photocurrent density of 1% Sn-doped rutile thin film amounts to 1.036 A/m^2 which is a 23% increase compared to undoped rutile thin film. Although bandgap reduction at semiconductor surface is present, the photocurrent improvement is mainly due to increase in bulk photoactive sites through Sn-doping.

5.3.4 Rutile and anatase results compared

In chapter 4, all Sn-doped anatase samples were shown to display an increase in photocurrent compared to undoped anatase, with 10 atomic % doped yielding the best results. However, for Sn-doped rutile samples, only 1 atomic % doped performs better than the undoped rutile. To compare PEC performance of Sn-doped anatase and rutile, photocurrent data of undoped rutile (black dotted), 1% Sn-doped rutile (red dotted), undoped anatase (black), 10% Sn-doped anatase (red) TiO_2 thin film obtained under simulated one sun illumination are overlayed in Figure 5.11.

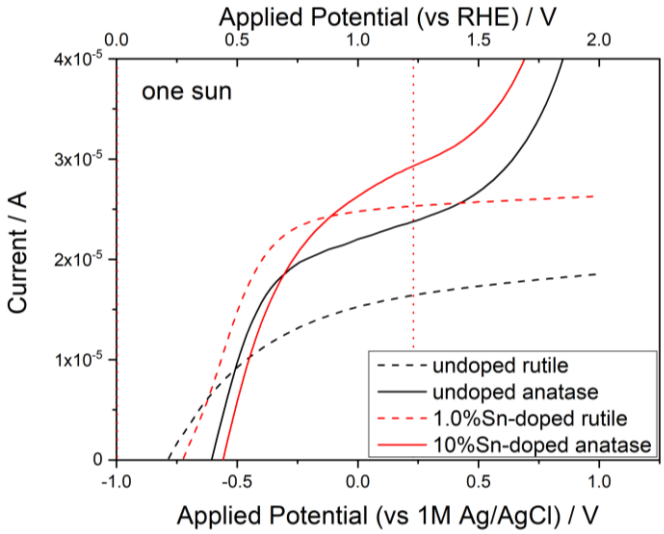


Figure 5.11. Photocurrent plot of undoped rutile (black dotted), 1% Sn-doped rutile (red dotted), pristine anatase (black), 10% Sn-doped anatase (red) TiO_2 thin film with one sun illumination in 0.1 M NaOH solution. Water oxidation (1.23 V vs RHE) and reduction (0 V vs RHE) potentials are shown in red dotted lines.

The increase in photocurrent due to doping is much more significant with anatase (54% increase at 1.23 V vs RHE). However, the Sn-doped rutile sample yields better results at external bias assisted PEC potential region (0.89 to 1.23 V vs RHE). The photocurrent onset potential is positive than 0 V vs RHE, which means that none of these samples can sustain a self-driven PEC water splitting process without external bias. It is interesting to see that PEC performance of undoped rutile is the better than undoped anatase at external bias assisted PEC potential region (0.45 to 1.23 V vs RHE), which is different from previous understanding that anatase is generally found to be the better photocatalyst.[21]

PEC performance of 10% Sn-doped anatase, 1% Sn-doped rutile, undoped anatase and undoped rutile under visible (> 400nm) and UV (240-395 nm) illumination are compared in Figure 5.12 and 5.13 respectively.

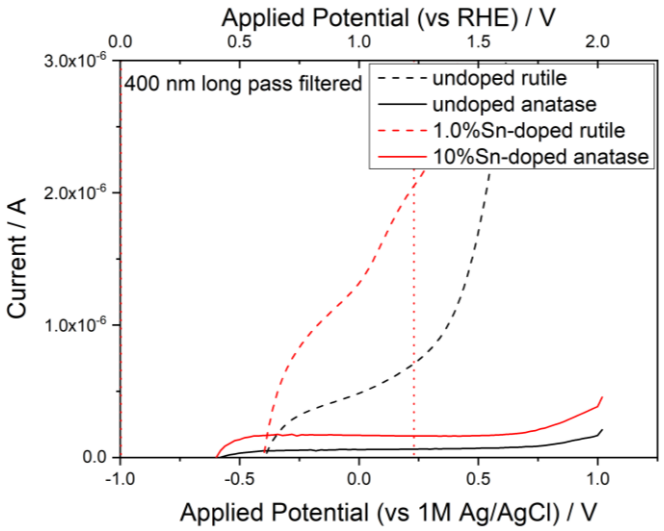


Figure 5.12. Photocurrent plot of undoped rutile (black dotted), 1% Sn-doped rutile (red dotted), pristine anatase (black), 10% Sn-doped anatase (red) TiO_2 thin film under visible (> 400nm filtered one sun) illumination in 0.1 M NaOH solution. Water oxidation (1.23 V vs RHE) and reduction (0 V vs RHE) potential are shown in red dotted lines.

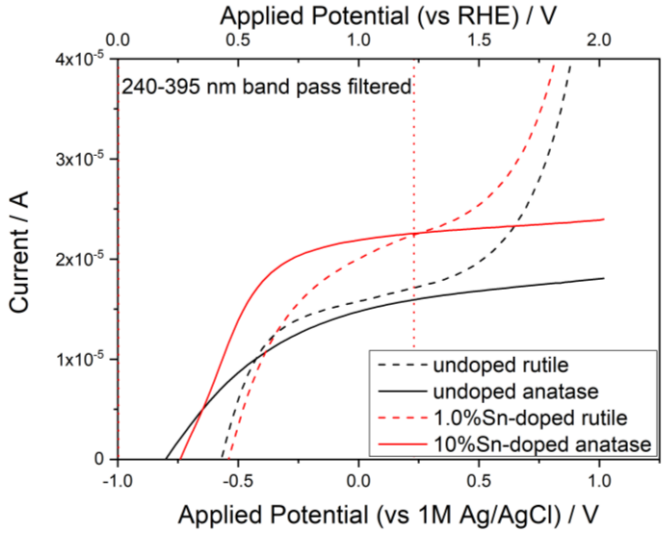


Figure 5.13. Photocurrent plot of undoped rutile (black dotted), 1% Sn-doped rutile (red dotted), pristine anatase (black), 10% Sn-doped anatase (red) TiO_2 thin film under UV (240-395 nm filtered one sun) illumination in 0.1 M NaOH solution. Water oxidation (1.23 V vs RHE) and reduction (0 V vs RHE) potential are shown in red dotted lines.

Sn-doped rutile show much better visible photocurrent response, as expected that rutile TiO_2 have a narrower bandgap than anatase. However, under UV spectrum, the Sn-doped anatase

thin film show overall improved photocurrent response in the external bias assisted PEC potential region (0.25 to 1.23 V vs RHE) and a much lower photocurrent inversion potential.

In conclusion, 1% Sn-doped rutile is the better photoanode under external bias assisted PEC potential region (0.89 to 1.23 V vs RHE) under one sun illumination. While 10 % Sn-doped anatase is the better photoanode under external bias assisted PEC potential region (0.25 to 1.23 V vs RHE) under UV. Rutile is the better PEC water splitting photoanode material at external bias assisted PEC potential region (0.45 to 1.23 V vs RHE), which is different from previous understanding that anatase is generally found to be the better photocatalyst.

5.3.5 Mott-Schottky plot

The variation of the electric potential in the SCL can be calculated by solving Poisson's equation (the detailed process can be found in chapter 1 section 1.3.4):

$$\frac{d^2\phi}{dx^2} = \frac{eN_e}{\varepsilon_r \varepsilon_0}\left(1 - exp\,(\frac{-e\psi}{kT})\right)$$

Where ε_0 is the permittivity of free space, and ε_r is the dielectric constant (relative permittivity) of the semiconductor, and N_e is the charge carrier density. An approximate analytic solution can be derived as the Mott- Schottky equation:

$$\frac{1}{{C_{SCL}}^2} = \frac{2}{\varepsilon_r \varepsilon_0 A^2 e N_e}\left(\psi - \mathrm{V}_{fb} - \frac{kT}{e}\right)$$

where C_{SCL} is the capacitance of SCL, A is the area of the semiconductor-electrolyte interface, N_e is the charge carrier density, ψ is the applied electric potential on the semiconductor and V_{fb} is the flat band potential. However, at this time we would like to use

the slope of Mott-Schottky plot to investigate the charge carrier density differences for different Sn doping levels and under different illumination conditions.

Converted Mott-Schottky data from EIS results of undoped and doping level of 0.5, 1, and 1.5 atomic % Sn rutile thin films in dark condition is plotted in the Figure 5.14 below.

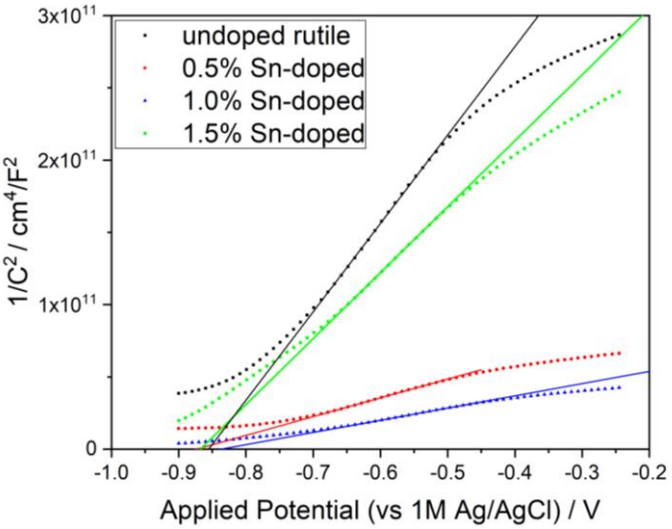


Figure 5.14. Mott−Schottky plot of rutile TiO_2 thin films with various level of Sn doping (red 0.5%, blue 1.0%, green 1.5%, black 0%) grown on FTO glass (5 dip-hydrolysis cycles, followed by annealing at 600 °C for 1 h) dark condition in 0.1 M NaOH solution.

Under dark condition, all the 4 thin film samples shown results with a positive slope, which agrees with typical n-type semiconductor response. Compared to undoped rutile thin film, the Sn-doped rutile thin film samples show more gradual slopes, indicating higher charge carrier densities (slop is negatively correlated with charge carrier density N_e). 1.0% Sn-doped thin film shown the highest charge carrier density under dark conditions. When Sn doping is increased to 1.5%, the charge carrier density drops to undoped TiO_2 level. By introducing a small amount of Sn into the rutile phase of TiO_2, donor density increases which

promotes charge carrier density; further increased Sn doping creates trapping sites that reduce the charge carrier lifetime and acts as recombination sites for electron-hole pairs.

Converted Mott-Schottky data from EIS results of undoped and doping level of 0.5, 1, and 1.5 atomic % Sn rutile thin films under simulated one sun irradiation is plotted in Figure 5.15 below.

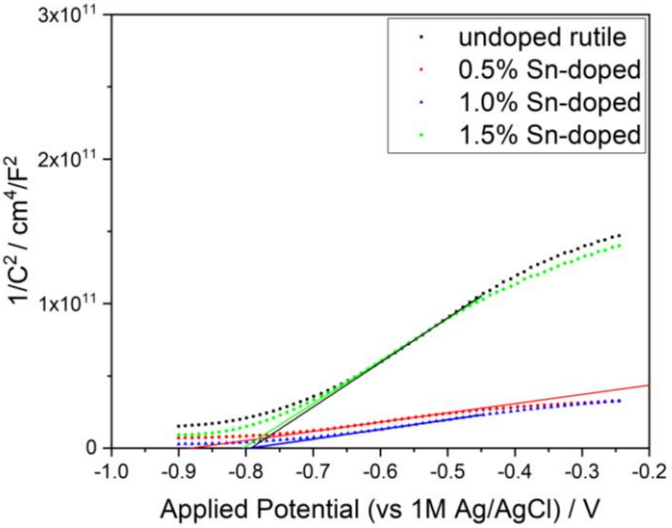


Figure 5.15. Mott−Schottky plot of rutile TiO_2 thin films with various level of Sn doping (red 0.5%, blue 1.0%, green 1.5%, black 0%) thin films grown on FTO glass (5 dip-hydrolysis cycles, followed by annealing at 600 °C for 1 h) one sun illumination in 0.1 M NaOH solution.

Under one sun illumination, all four thin film samples show a reduction in slope indicating increased charge carrier density due to photogenerated electron-holes. The slope of 1.5% Sn-doped thin film showed similar results to undoped rutile indicating reduced charge carrier lifetime due to increased Sn trapping sites. 0.5% and 1% Sn-doped thin films show similar charge carrier density. In section 5.3.3, the quasi-Fermi level splitting under one sun illumination for 0.5% and 1% Sn-doped samples are 0.705 and 0.79 eV respectively. The reason for improved PEC performance of 1% over 0.5% Sn-doped thin film is because of

the larger quasi-Fermi level splitting which provides better energy level alignments at the S-E interface.

5.4 Conclusions

In this chapter, Sn doping was investigated as a potential method for improving PEC water splitting capability of rutile TiO_2 thin film. In order to test the PEC properties of the material, a conductive FTO glass substrate was used. The PEC performance was investigated with a three-electrode setup using CV. The comparison of PEC performance between Sn-doped rutile and anatase were also discussed.

In the first section, ordered Sn-doped rutile TiO_2 thin films were successfully grown on FTO glass substrate using dip-coating method. XRD results show that the as-grown thin films are polycrystalline with a range of (110), (101), and (211) crystal surfaces present. The enrichment of Sn (II) species on the surface was identified using XPS. In the second section, Sn-doped rutile TiO_2 thin film was shown be to a n-type photoanode capable of photocatalytic oxidation of water using light on/off experiment. Transition from anodic photocurrent to electrolytic current is seen in the 0.75 to 1 V (vs 1 M silver chloride electrode) potential region. This is a result of polycrystalline electrode surface having increased grain boundaries which facilitate charge transfer across the S-E interface.

In the third section, PEC improvements due to Sn-doping was investigated with various spectrum of illumination. The photocurrent increased up to 23% (at 1.23 V vs RHE) using 1 atomic % Sn doping, compared to undoped rutile TiO_2, achieving current density of 1.036

A/m^2 with just 5 dip-coating cycles. However, 0.5% and 1.5% Sn-doped rutile TiO_2 showed an overall decrease in photocurrent performance.

In the fourth section, PEC performance of Sn-doped anatase and rutile thin film were compared. 10% Sn-doped anatase thin film showed better photocurrent performance under UV while 1% Sn-doped rutile anatase thin film performed better under simulated one sun illumination and visible spectrum. Sn doping is capable of enhancing PEC performance for both anatase and rutile TiO_2. Rutile is the better PEC water splitting photoanode material at external bias assisted PEC potential region, which is different from previous understanding that anatase is generally found to be the better photocatalyst.

In the fifth section, as indicated by the slope of the Mott-Schottky plot, Sn doping increased charge carrier density in rutile TiO_2 at lower doping levels of 0.5 and 1 atomic %. Increasing doping level to 1.5 % lead to a decrease in charge carrier density to undoped rutile level.

Finally, it is concluded that surface band gap reduction contribution due to surface Sn (II) is insignificant for both anatase and rutile TiO_2. The main contribution to enhanced PEC performance is due to bulk Sn doping which increases photoactive sites.

Reference

1. Walsh, A. & Watson, G. W. Electronic structures of rocksalt, litharge, and herzenbergite SnO by density functional theory. *Phys. Rev. B - Condens. Matter Mater. Phys.* **70**, 1–7 (2004).

2. Xu, M. *et al.* Photocatalytic activity of bulk TiO2 anatase and rutile single crystals using infrared absorption spectroscopy. *Phys. Rev. Lett.* **106**, 1–4 (2011).

3. Sclafani, A. & Herrmann, J. M. Comparison of the photoelectronic and photocatalytic activities of various anatase and rutile forms of titania in pure liquid organic phases and in aqueous solutions. *J. Phys. Chem.* **100**, 13655–13661 (1996).

4. Zhang, Z., Wang, C. C., Zakaria, R. & Ying, J. Y. Role of particle size in nanocrystalline TiOi-based photocatalysts. *J. Phys. Chem. B* **102**, 10871–10878 (1998).

5. RAO, K. V. K., NAIDU, S. V. N. & IYENGAR, L. Thermal Expansion of Rutile and Anatase. *J. Am. Ceram. Soc.* **53**, 124–126 (1970).

6. Czanderna, A. W., Ramachandra Rao, C. N. & Honig, J. M. The anatase-rutile transition: Part 1. - Kinetics of the transformation of pure anatase. *Trans. Faraday Soc.* **54**, 1069–1073 (1958).

7. Yoganarasimhan, S. R. & Rao, C. N. R. Mechanism of crystal structure transformations. Part 3. - Factors affecting the anatase-rutile transformation. *Trans. Faraday Soc.* **58**, 1579–1589 (1962).

8. Wang, C. *et al.* Photosensitization of TiO 2 nanorods with CdS quantum dots for photovoltaic applications: A wet-chemical approach. *Nano Energy* **1**, 440–447 (2012).

9. Oropeza, F. E., Davies, B., Palgrave, R. G. & Egdell, R. G. Electronic basis of visible region activity in high area Sn-doped rutile TiO2 photocatalysts. *Phys. Chem. Chem. Phys.* **13**, 7882 (2011).

10. Padmanabhan, S. C. *et al.* A simple sol - Gel processing for the development of high-temperature stable photoactive anatase titania. *Chem. Mater.* **19**, 4474–4481 (2007).

11. Liao, Y. *et al.* Controllable synthesis of brookite/anatase/rutile TiO 2 nanocomposites and single-crystalline rutile nanorods array. *J. Mater. Chem.* **22**, 7937–7944 (2012).

12. Achilles, C. N., Morris, R. V, Chipera, S. J., Ming, D. W. & Rampe, E. B. X-Ray Diffraction Refrence Intensity Ratios of Amorphous and Poorly Crystalline Phases: Implcatiosn for CHEMIN on the Mars Science Laboratoty Mission. *44th Lunar Planet. Sci. Conf.* 1–2 (2013).

13. Biesinger, M. C., Lau, L. W. M., Gerson, A. R. & Smart, R. S. C. Resolving surface chemical states in XPS analysis of first row transition metals, oxides and hydroxides: Sc, Ti, V, Cu and Zn. *Appl. Surf. Sci.* **257**, 887–898 (2010).

14. Egdell, R. G., Flavell, W. R. & Tavener, P. Antimony-doped tin(IV) oxide: Surface composition and electronic structure. *J. Solid State Chem.* **51**, 345–354 (1984).

15. Cox, P. A. *et al.* Free-electron behaviour of carriers in antimony-doped tin(IV) oxide: A study by electron spectroscopy. *Solid State Commun.* **44**, 837–839 (1982).

16. Gulino, A., Condorelli, G. G., Fragalà, I. & Egdell, R. G. Surface segregation of Sb in doped TiO2 rutile. *Appl. Surf. Sci.* **90**, 289–295 (1995).

17. Cox, P. A., Egdell, R. G., Harding, C., Patterson, W. R. & Tavener, P. J. Surface properties of antimony doped tin(IV) oxide: A study by electron spectroscopy. *Surf. Sci.* **123**, 179–203 (1982).

18. Kwoka, M. *et al.* XPS study of the surface chemistry of L-CVD SnO2 thin films after oxidation. *Thin Solid Films* **490**, 36–42 (2005).

19. Krol, R. & Gratzel, M. *Photoelectrochemical Hydrogen Production*. *Hydrogen Energy System* **102**, (Springer US, 2012).

20. Li, X. *et al.* Engineering heterogeneous semiconductors for solar water splitting. *J. Mater. Chem. A* **3**, 2485–2534 (2015).

21. Luttrell, T. *et al.* Why is anatase a better photocatalyst than rutile? - Model studies on epitaxial TiO2 films. *Sci. Rep.* **4**, 4043 (2015).

Chapter 6 Mn/Co Modified Carbonised Rice Husks for EDLCs

6.1 Introduction

Supercapacitors, also known as electrochemical double layer capacitors (EDLCs) are promising energy storage devices to complement or even replace batteries. The first EDLC design was patented by Becker in 1957 (U.S. Patent 2800616).[1] Compared to batteries, which store energy through Faradaic electrochemical reactions, EDLCs store charges using non-Faradaic double layer capacitance which is explained in detail in the introduction chapter. The advantage of EDLCs over batteries is the extremely large charge/discharge current density which is highly desired in automotive, consumer tech and manufacturing sectors.

At present, various advanced artificial carbon materials can be used as EDLC electrode, owing to high conductivity, high surface area, a rich variety of dimensionality, good corrosion resistance, controlled pore structure, processability and compatibility in composites, etc.[2–5] Despite being made from an element ubiquitous in nature, the production of most state-of-the-art carbon-based materials such as carbon nanotubes (CNTs) and graphene often involves complex, eco-destructive, and resource-consuming processes.[6–9] Instead, green and efficient conversion of abundant and renewable biomass and waste-biomass into functional nanomaterials holds the key to a sustainable future. Moreover, the porous natural structure of biomass material increases the specific area as well as providing a good template for further modification.

Biomass derived EDLC material such as seaweed,[2] cotton pulp,[10] cellulose,[11] flax[12] etc. have been prepared by various strategies and have shown good electrochemical performance. In the work done by previous group members, carbonised filter paper and cotton pulp have obtained good specific capacitance.[10,13] However, these materials are commodities not waste, and the carbonisation temperatures were as high as 1000°C, which is very energy intensive.

Rice husk is biomass waste as a result of rice hulling process which is readily available with large quantities. In this chapter, carbonised rice husks (cRHs) were investigated as a potential material for EDLC applications with reduced carbonisation temperature (400 °C). The specific capacitance is further enhanced with Mn and Co modification using carbonised metal–organic frameworks (MOFs). A drop-coating sample testing procedure on glassy carbon (GC) electrode with Nafion® cover was implemented for electrochemical measurement of smaller quantity materials.

6.2 Experimental

The cRHs and Mn/Co modified cRHs are provided by Korea Institute of Energy Research (KIER). The detailed preparation process is discussed in the experimental chapter of this thesis.

6.2.1 Ball milling

All samples were dry ball milled to fine powder using a Fritsch Pulverisette 7. The 45 ml stainless steel grinding bowl was used with eighteen 10 mm diameter stainless steel balls.

The milling program used was as follows: 200 rpm for 2 min, rest for 2 min and repeat the procedure one more time. 2 g of sample was ground every time.

6.2.2 Drop-coating

Aqueous based drop coating method was used to load a small amount of sample onto the 3 mm diameter GC electrodes (CHI104, CH instruments). The drop coating solution is made by adding the appropriate amount of DI water with the powdered sample to generate a 2 g/L mixture. The mixture was homogenized using sonication. 9 μL of the mixture was extracted immediately after physical agitation and drop coated onto the GC electrode. The mixture was slowly evaporated in room temperature then coated with 9 μL of Nafion® 117 solution (Sigma-Aldrich) are dried in room temperature.

6.3 Results and discussion

6.3.1 Electrolyte selection with GC electrode

The drop-coating technique was introduced to conveniently examine the electrochemical properties of powder-form samples in smaller amounts. This approach uses a GC electrode as the sample holder which is efficient in carrying out electrochemical tests and convenient to clean. Prior to electrochemical characterisation of samples, it is critical to know the maximum usable potential window of GC electrode in the electrolyte.

The thermodynamic potential window of water is known to be 1.23 V. This significantly limits the maximum potential window of EDLC in aqueous electrolyte. Energy stored in EDLC is proportional to the square of applied voltage. Extending the operating potential

window beyond 1.23 V thus becomes a concern when using an aqueous electrolyte. To investigate the operating potential window of GC in different electrolytes, KCl, HCl, LiOH and $NaHCO_3$ were chosen due to their differences in anion and cation mobility combinations (high/high, very-high/high, low/very-high and low/low cation/anion mobility combination). (Table 6.1)

Table 6.1. Relative ion mobility derived from Lange's Handbook of Chemistry.

Symbolic Ion Name	***Full Ion Name***	***Valency***	***Relative Mobility***
K	Potassium	1	1
Li	Lithium	1	0.53
Cl	Chloride	-1	1.04
HCO_3	Bicarbonate	-1	0.61
H	Hydrogen	1	4.76
OH	Hydroxide	-1	2.69
Na	Sodium	1	0.68

1 M aqueous solution of the above-mentioned electrolytes were tested with a three-electrode setup using bare GC electrode (3 mm diameter) as working electrode, Pt wire as counter electrode and 1 M Ag/AgCl as reference electrode. The potential window was investigated with CV with a scan rate of 10 mV/s. The CV results of GC in 1 M KCl, 1 M HCl, 1 M LiOH and 1 M $NaHCO_3$ are shown in Figure 6.1.

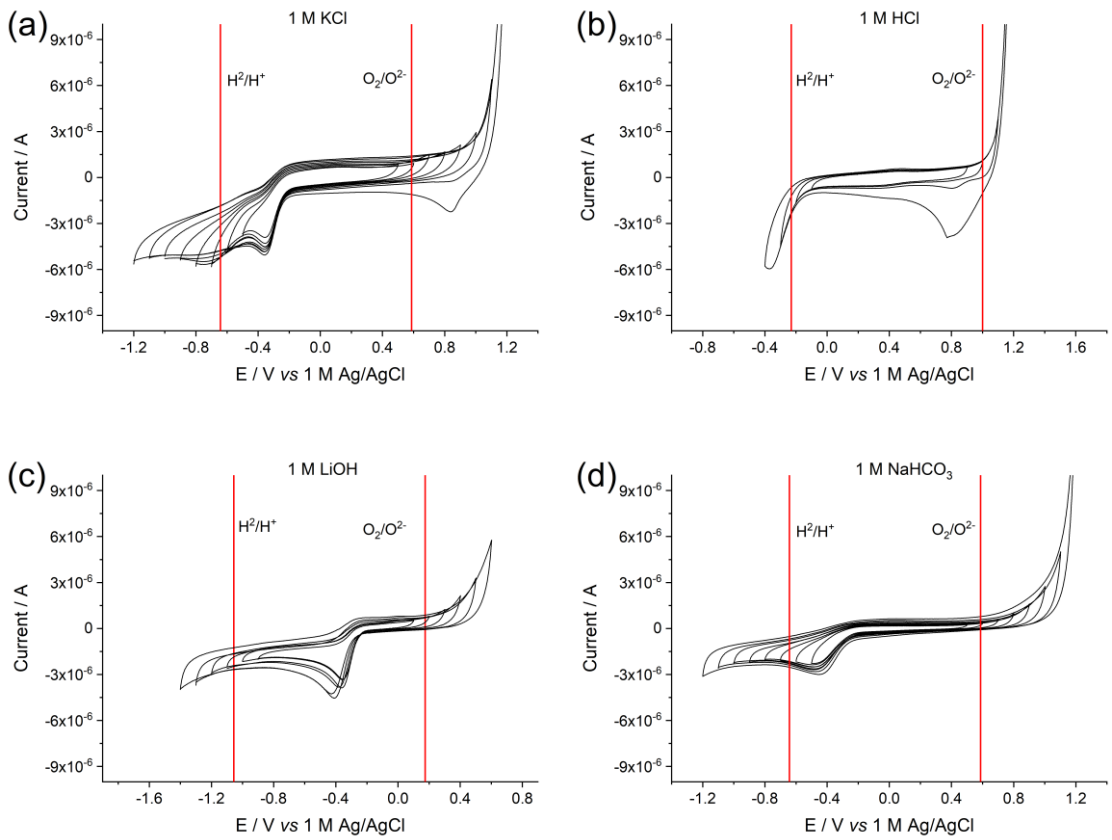


Figure 6.1. CV of bare GC as working electrode in a) 1 M KCl, b) 1 M HCl, c) 1 M LiOH and d) 1 M $NaHCO_3$ aqueous solutions using 1 M silver chloride reference electrode. (Calculated thermodynamic potential window of water in individual electrolyte is shown in red)

From Figure 6.1 it can be seen that apart from the HCl solution, both neutral (KCl and $NaHCO_3$) and alkaline (LiOH) solutions are stable well beyond the thermodynamic potential window of water. A neutral solution of KCl and $NaHCO_3$ could achieve a good potential window of 2.2-2.4 V compared to 2 V using 1M LiOH and 1.2-1.4 V using 1M HCl.

Various articles[14,15] indicate that there is no simple correlation between ion mobility and capacitance; the complexity of ion transport due to ion-ion and ion-carbon interaction, solvation effects, as well as effects of carbon pore size/volume makes it almost impossible to produce a good prediction on the most suitable electrolyte for a specific capacitor material.

In our setup, 2 M KCl was used as an electrolyte for experiments, which has been proven as a reliable electrolyte for carbon materials.[11,16–18] In the following EDLC electrochemical measurements, 0 to 0.8 V vs 1 M silver chloride electrode potential window was used. The good potential window of -1.2 to 1.2 V vs 1 M silver chloride electrode makes it a suitable electrolyte for electrochemical investigation.

6.3.2 Improvements of using Nafion® cover

A drop coating technique was employed to load smaller quantity test samples onto the GC electrode. This technique has displayed shortcomings of losing the coated sample material during electrochemical measurement. This issue was mitigated by covering the sample with Nafion® 117 film. The improvements due to use of Nafion® are discussed in detail in this section.

The drop coating solution is prepared by mixing the appropriate amount of DI water with sample powder to generate a 2 g/L mixture. The mixture was extensively sonicated and cooled to room temperature. Before each drop coating session, the mixture was physically homogenised using a PV-1 vortex mixer (Grant Instruments). 9 μL of the mixture was extracted with a pipette and drop coated onto the GC electrode which forms a half-spherical droplet within the GC contact area. The mixture was slowly evaporated at room temperature.

The consistency of the drop coating testing method was examined by comparing CV data acquired from multiple experiments. The overlaid CV results from three independent instances are shown in Figure 6.2 below with samples **#4**, **#4 ACT** and **#4 Cl**. The **#4** is the

just-carbonised rice husk sample, **#4 ACT** and **#4 Cl** are Mn/Co modified version of **#4** using different carbonised MOFs. (detailed description of samples are discussed in section 6.3.4)

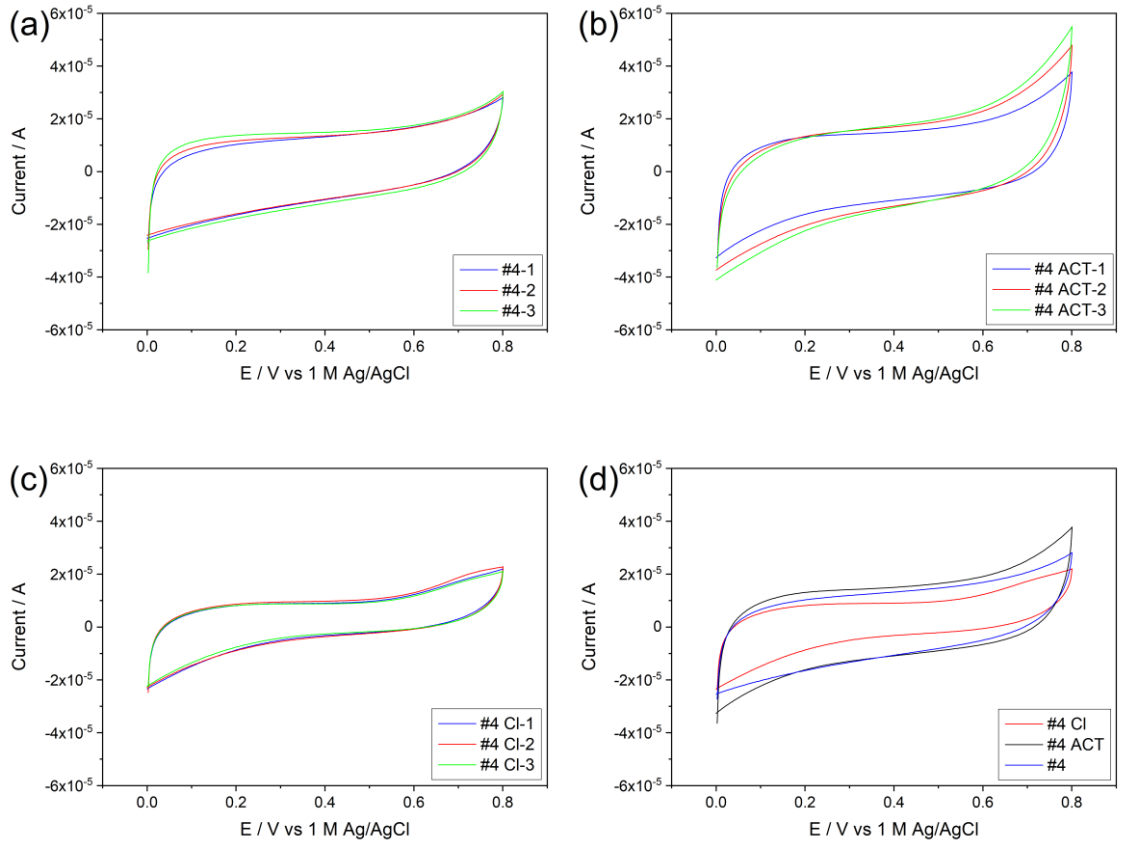


Figure 6.2. CV of 3 different tests of a) cRHs #4, b) carbonised MOFs modified cRHs #4 using acetate precursor (#4 ACT), c) carbonised MOFs modified carbonised cRHs #4 using chloride precursor (#4 Cl) showing good reproducibility, d) overlaid comparison of #4, #4 ACT and #4 Cl in 2 M KCl scanning from 0 to 0.8 V with scan rates of 100 mV/s. (detailed description of sample cRHs #4, #4 ACT and #4 Cl will be discussed in detail in following sections)

Very small discrepency between CV measurements are observed indicating good consistency using the drop coating technique. However, the underwhelming performance of Mn/Co modified sample **#4 Cl** raise concerns. Intuitively, with Mn and Co modification, pseudo-capacitance is introduced which lead to increased specific capacitance. However,

reduced capacitance is observed with Mn/Co modified sample **#4 Cl** when compared against unmodified sample **#4**. It is believed there could be an issue of inadequate contact between coated sample and electrode surface. Moreover, the GC electrode is inserted into the electrolyte facing downwards, and gravitational pull promotes detach of the sample from the GC electrode surface.

In the previous experiment, sample **#4 ACT** has shown decent capacitive performance indicating adequate electrical contact with GC electrode. Thus, sample **#4 ACT** is selected to investigate the issue of sample detach. A quick withdraw/re-immersion test was conducted as follows: after a complete set of CV scans, the GC electrode (loaded with sample) was withdrawn from the electrolyte, then re-immersed, run through the same set of CV scans. This process was repeated multiple times. The overlaid CV data of the 100 mV/s scan from consecutive withdraw/re-immersion test is shown in Figure 6.3.

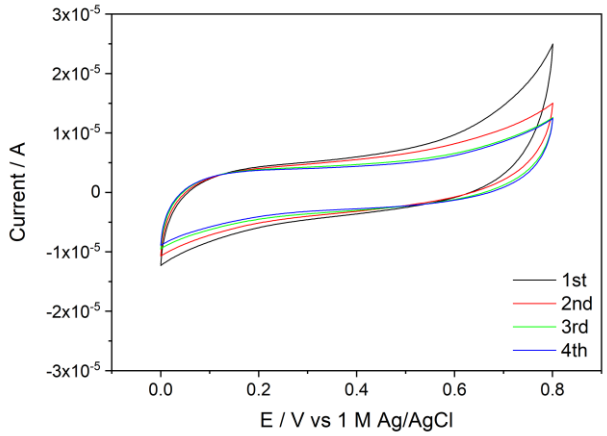


Figure 6.3. CV of cRHs sample **#4 ACT** showing reduction in capacitance with 4 consecutive withdraw/re-immersion of GC electrode with a scan rate of 100 mV/s.

There is a clear trend of a decrease in specific capacitance with each withdraw/re-immersion event indicating a loss of sample material from the GC electrode surface. During the 5th re-immersion test, the entire sample disc detached from the GC electrode surface.

To understand the issue of inadequate electrical contact between coated sample and electrode, the drop coating technique was implemented on a GC plate electrode which has the electrode surface facing upwards in the electrolyte. Gravitational pull assists sample to adhere to the electrode surface for improved electrical contact. The overlaid CV results of samples **#4**, **#4 ACT** and **#4 Cl** measured using GC plate electrode is shown in Figure 6.4.

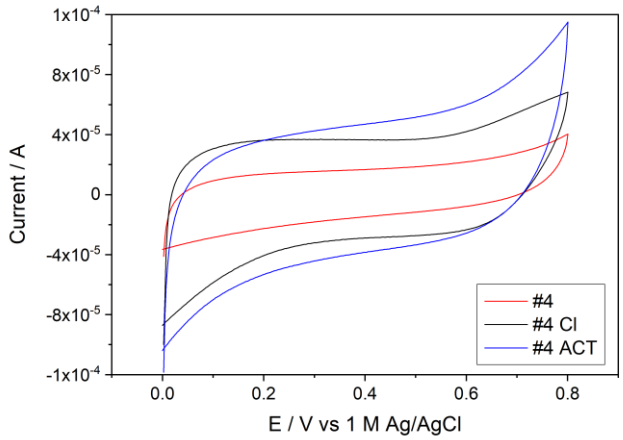


Figure 6.4. CV in 2 M KCl solution scanning from 0 to 0.8 V with scan rates of 100 mV/s for cRHs (**#4**, black), carbonised MOFs modified cRHs #4 with metal chloride precursor (**#4 Cl**, red), carbonised MOFs modified cRHs #4 with metal acetate precursor (**#4 ACT**, blue) using glassy carbon plate electrode setup.

It is clear that Mn/Co modified samples (**#4 ACT**, **#4 Cl**) display an increased specific capacitance compared to unmodified sample (**#4**). In contrast with previous results acquired using GC electrode (Figure 6.2d), there is a significant improvement in capacitive response with Mn/Co modified samples (**#4 ACT**, **#4 Cl**) using GC plate electrode. This finding

confirms there is an issue of inadequate electric contact between sample and GC electrode when electrode surface is facing downwards in the electrolyte.

To settle the above-mentioned two issues, Nafion® 117 film was used as a protective cover to secure the coated samples on the GC electrode during electrochemical investigation. However, the possible complication introduced by Nafion® 117 film must be investigated. 9 µL of Nafion® 117 solution (Sigma-Aldrich) was drop coated on bare GC electrode and dried in ambient condition. The CV measurements of bare and Nafion® 117 coated GC electrode in 2 M KCl electrolyte are shown in Figure 6.5.

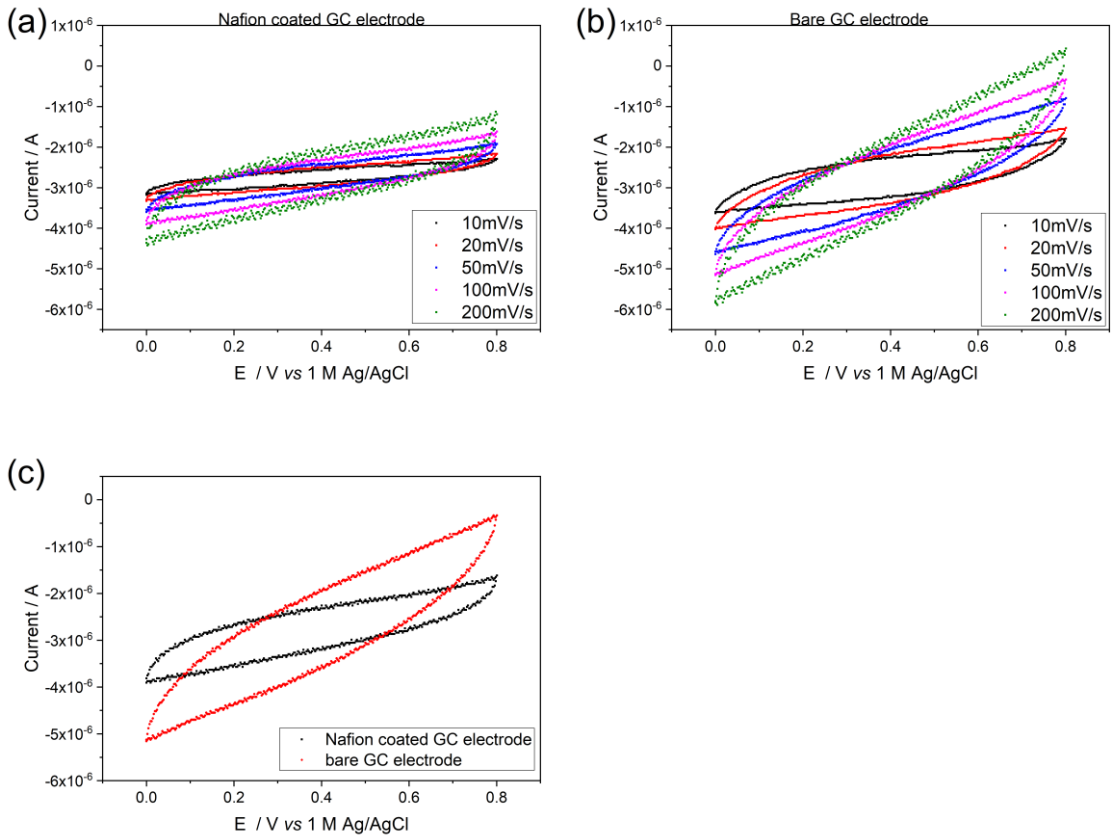


Figure 6.5. CV in 2 M KCl solution scanning from 0 to 0.8 V with scan rates of 10, 20, 50, 100 and 200 mV/s for (a) Nafion® 117 coated bare GC electrode, (b) bare GC electrode and (c) compared at scan rate of 100 mV/s.

The difference in capacitive response of bare and Nafion® 117 coated GC electrode is visible. This is expected since ion mobility in Nafion® 117 is different from the electrolyte.[19,20] However, this difference is inconsequential. The positive/negative capacitive contributions due to Nafion® 117 is one magnitude lower when compared with capacitive response of sample material. (Figure 6.6)

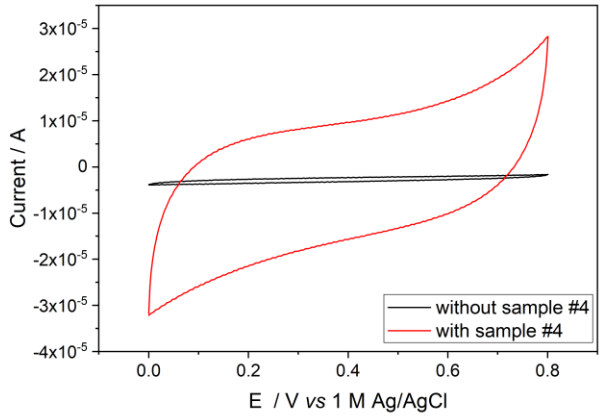


Figure 6.6. CV in 2 M KCl solution scanning from 0 to 0.8 V for Nafion® coated **#4** on GC electrode (red) and Nafion® coated bare GC electrode (black) compared at scan rate of 100 mV/s.

The capacitive improvements of enhanced electrical contact due to Nafion® 117 cover is shown in Figure 6.7. Comparing the measured CV results of samples **#4**, **#4 ACT** and **#4 Cl** with and without Nafion® 117 cover. With Nafion® 117 cover, the capacitive response increase with all samples; and the improvement is especially significant with Mn/Co modified samples (**#4 ACT** and **#4 Cl**).

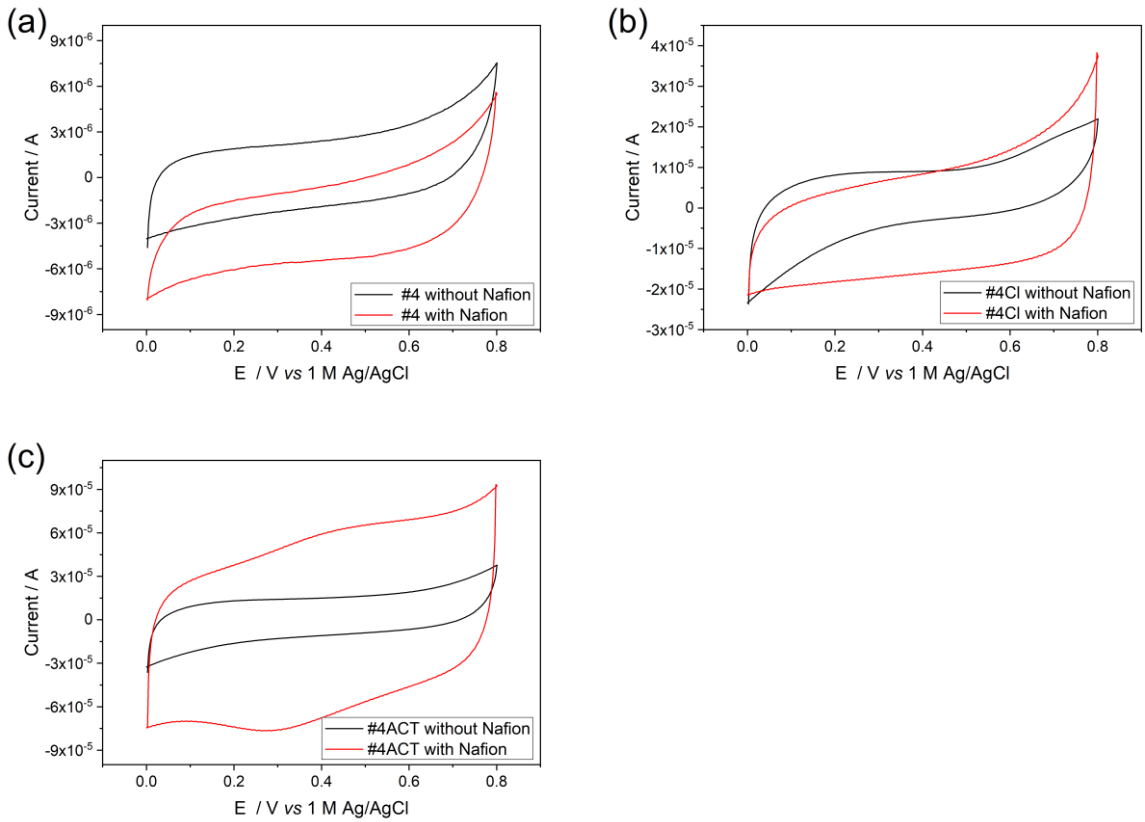


Figure 6.7. CV in 2 M KCl solution scanning from 0 to 0.8 V for (a) cRHs (**#4**), (b) carbonised MOFs modified #4 with metal chloride precursor (**#4 Cl**), (c) carbonised MOFs modified #4 with metal acetate precursor (**#4 ACT**) with and without Nafion® 117 coating using GC electrode compared at scan rate of 100 mV/s.

By adding a protective Nafion® 117 film on top of the drop coated carbon material, the electrical contact with GC electrode is improved significantly to give rise to an enhanced capacitive response using CV measurements. Nafion® cover is deemed an exceptional tool in stabilising carbon material on GC electrode.

6.3.3 Carbonised rice husk

In order to select a suitable carbon template for further Mn/Co modification, the carbonisation temperatures and environment (nitrogen/air) were investigated for rice husks biomass material. The specific capacitance of carbonised rice husks (cRHs) samples obtained under different carbonisation conditions are characterised using the above-

mentioned improved drop coating method with Nafion® cover. CV method was employed to evaluate the specific capacitance of cRHs samples.

The CV data of cRHs samples carbonised at 400 °C (**#4**), 600 °C (**#5**) and 800 °C (**#6**) in nitrogen atmosphere for 3 hours are shown in Figure 6.8 at increasing scan rates ranging from 5 to 200 mV/s.

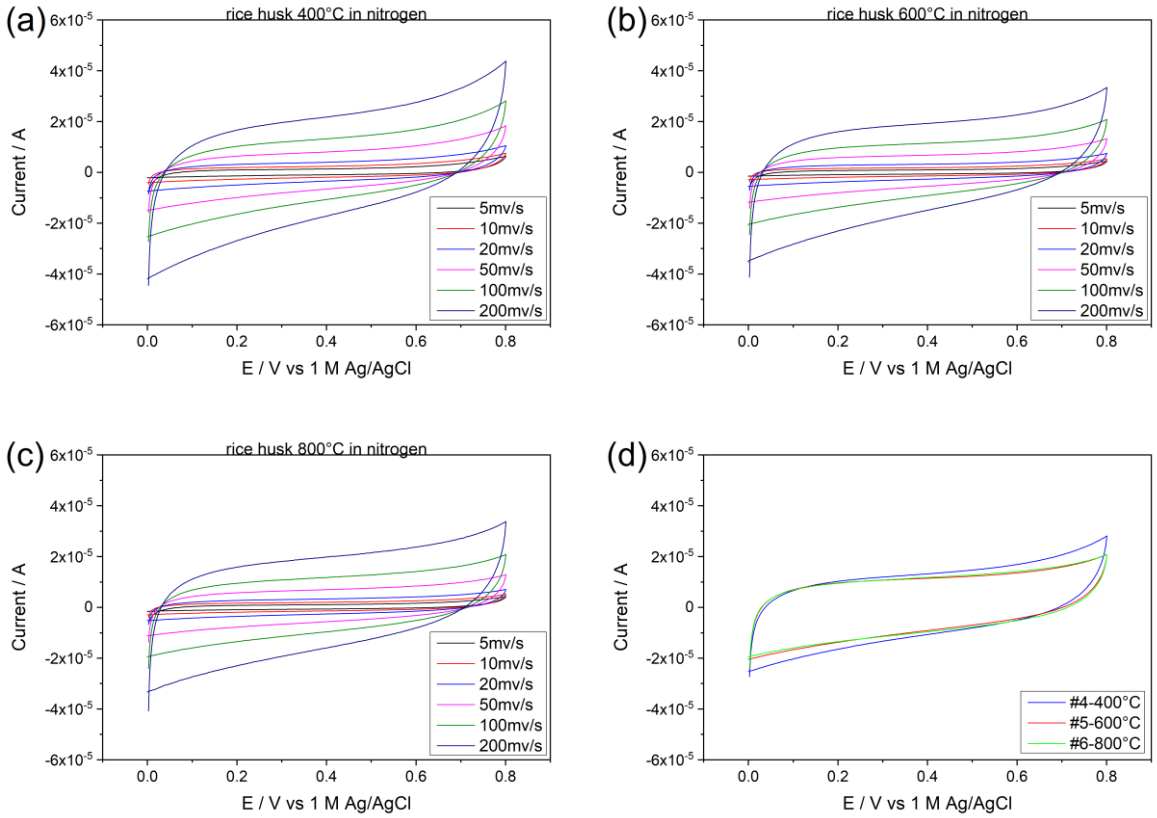


Figure 6.8. CV in 2 M KCl scanning from 0 to 0.8 V with scan rates of 5, 10, 20, 50, 100 and 200 mV/s for cRHs carbonised at (a) 400 °C in nitrogen (**#4**), (b) 600 °C in nitrogen (**#5**), (c) 800 °C in nitrogen (**#6**) and (d) compared at scan rate of 100 mV/s.

At a low scan rate, a quasi-rectangular shape along the current potential axis without obvious redox peak is observed, which is typical for non-Faradaic EDLC behaviour. With increasing scan rate, the curve became more irregular. The distortion in the CV curves at a high scan

rate was a result of the limited diffusion and migration of electrolytes ions in the bulk of materials, as well as the reduced conductivity of the powdered samples.

The CV data of cRHs samples carbonised at 600 °C (**#3**) and 850 °C (**#2**) in air and HCl treated cRHs carbonised at 850 °C in air (**#1**) for 3 hours are shown in Figure 6.9 at increasing scan rates ranging from 5 to 200 mV/s.

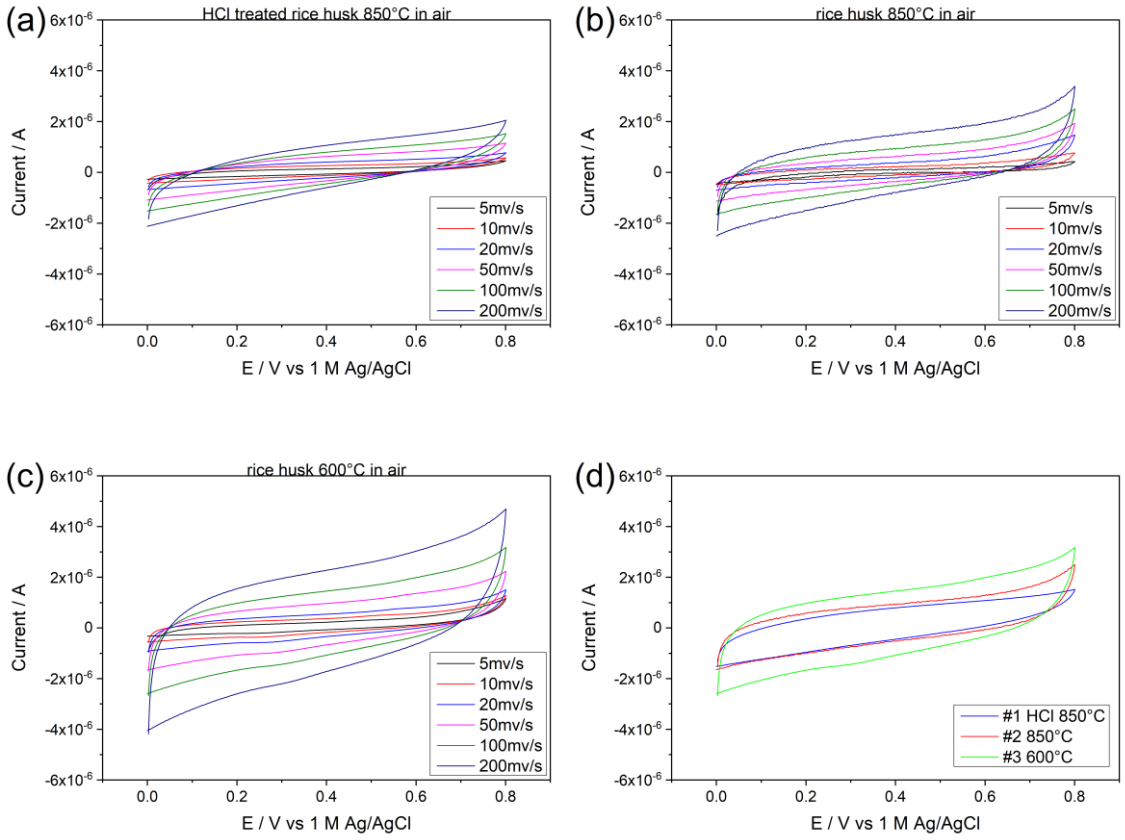


Figure 6.9. Cyclic voltammograms in 2 M KCl electrolyte scanning from 0 to 0.8 V with scan rates of 5, 10, 20, 50, 100 and 200 mV/s for cRHs (a) HCl treated and carbonised at 850 °C in air (**#1**), (b) carbonised at 850 °C in air (**#2**), (c) carbonised at 600 °C in air (**#3**) and (d) compared at scan rate of 100 mV/s.

The charge-discharge current of samples carbonised in air is a magnitude lower compared to sample carbonised under nitrogen atmosphere. This suggests carbonisation with presence

of oxygen reduces capacitive performance of the material. The corresponding specific capacitances of all cRHs samples are summarised in Table 6.2.

Table 6.2. Calculated specific capacitance using 10 mV/s CV data.

Sample	***Carbonisation method***	***Specific capacitance (F/g)***
#1	850 °C air (with HCl)	0.88
#2	850 °C air	0.86
#3	600 °C air	1.33
#4	400 °C in nitrogen	11.54
#5	600 °C in nitrogen	8.61
#6	800 °C in nitrogen	8.71

The capacitive performance of cRHs carbonised in air is generally inferior compared to cRHs that were carbonised in nitrogen atmosphere. Increase in carbonisation temperature reduces capacitive performance. The highest specific capacitance was achieved at 400 °C under nitrogen atmosphere for 3 hours (sample **#4**), which is consequently used as carbon template for Mn/Co modification.

6.3.4 Mn/Co modified cRHs

It has been shown that metal oxides (MO) such as manganese and cobalt oxide increases the capacitive performance of the substrate carbon materials.[21–25] Herein, Mn/Co bi-metallic MOFs is employed to load Mn and Co metals on cRHs (sample **#4**), and then carbonised to generate MO@cRHs structure to enhance the capacitive performance of cRHs. The Mn/Co bi-metallic MOFs, MOFs@cRHs before carbonisation and after carbonisation (MO@cRHs

product) are characterised using a range of physical techniques. The capacitive performance of MO@cRHs are compared using CV.

The bi-metallic MOF-74 with mixed Mn(II) and Co(II) were prepared by a one-pot solvothermal reaction.[26] The bimetallic crystalline products synthesized from $Co(NO_3)_2$/Mn(acetate)$_2$ and $Co(NO_3)_2$/$MnCl_2$ exhibit the same XRD patterns, which is well consistent with a calculated XRD profile of MOF-74. (Figure 6.10)

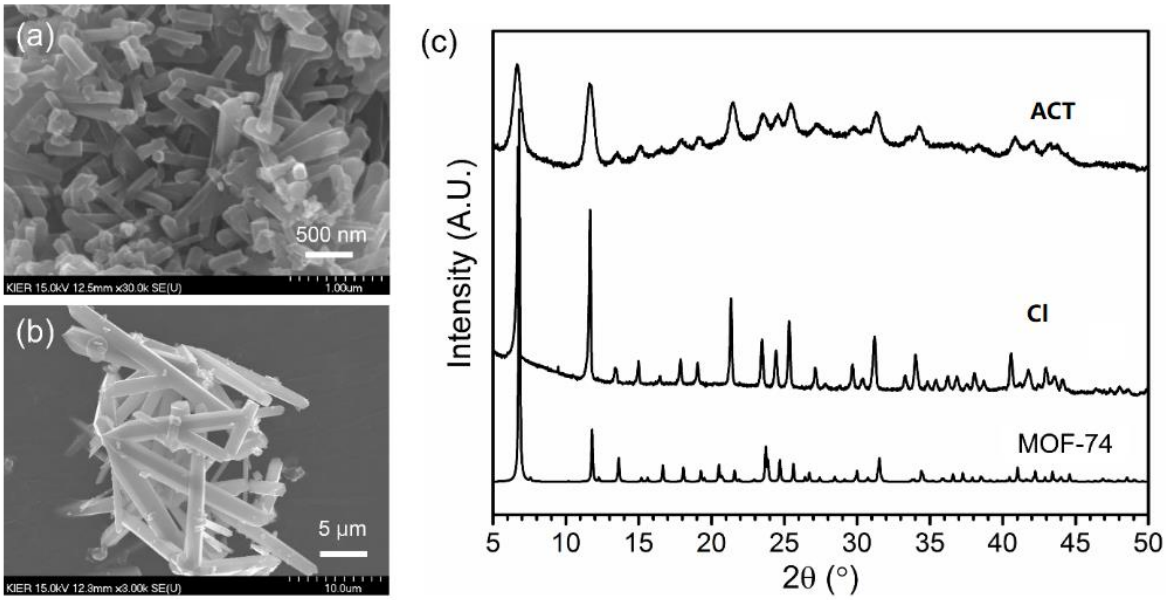


Figure 6.10. SEM images of (a) $Co(NO_3)_2$/Mn(acetate)$_2$-derived **ACT** sample and (b) $Co(NO_3)_2$/$MnCl_2$-derived **Cl** sample, (c) XRD profiles of **ACT** (top) and **Cl** (middle) and calculated XRD pattern of MOF-74 (bottom).

The XRD peak width and intensity of the $Co(NO_3)_2$/Mn(acetate)$_2$-derived MOFs (**ACT**) was significantly broader and lower than those of $Co(NO_3)_2$/$MnCl_2$-derived MOFs (**Cl**) which imply crystal size of **ACT** sample is smaller than **Cl** according to the Scherrer equation. SEM images showed that **Cl** sample has hexagonal rod shapes with a micrometre size, while **ACT** sample has similar but shorter rod shapes with several hundred nanometres. Crystal

shape and size were significantly influenced by metal precursors. The different crystal sizes of **ACT** and **Cl** can be explained by considering the nucleophilicity of the counter anions to the metal cations. Acetate during the crystallization of **ACT** is less solvated than chloride during that of **Cl** in polar and aprotic solvents such as DMF, which is the major solvent, indicating a higher nucleophilic reactivity of acetate to Co^{2+} and Mn^{2+} ions.[27,28] Therefore, metal complexes with acetate are slow to dissociate and participate in the crystallization of **ACT**, and hence generates smaller crystals than that of **Cl**. Co/Mn ratios of **ACT** sample and **Cl** sample determined by EDX analysis were 1.1 and 1.0, respectively.

To incorporate MOFs onto cRHs, both **ACT** and **Cl** were in-situ crystallized in the presence of cRHs (sample **#4**). SEM analysis revealed that **ACT** and **Cl** were grown within the channels of cRHs. SEM and XRD analysis of as-synthesized MOFs@cRHs are shown in Figure 6.11.

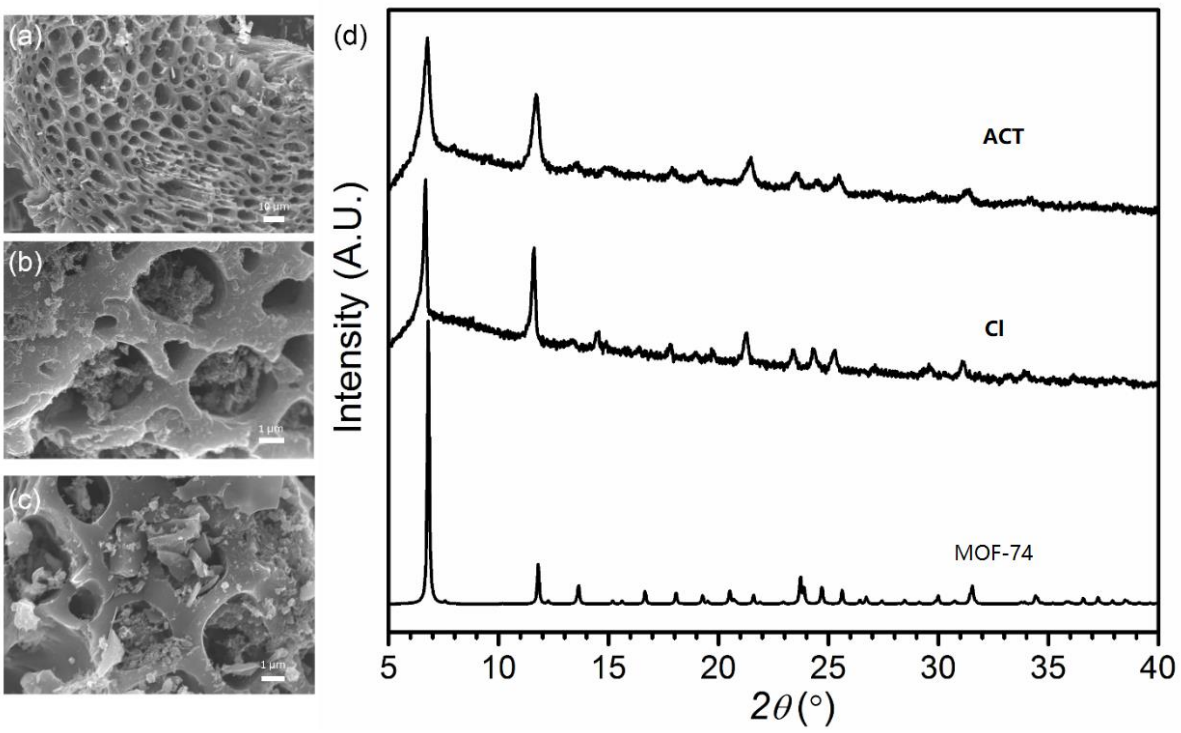


Figure 6.11. SEM images of (a) cRHs at 400 °C (#4) and (b) ACT@cRHs, (c) Cl@cRHs and (d) measured powder XRD profiles of ACT@cRHs (top), Cl@cRHs (middle) and calculated XRD pattern of MOF-74 (bottom).

The size of **ACT** formed inside the channels of cRHs is smaller than that of **Cl**. EDX reveal that Co/Mn ratios of **ACT**@cRHs and **Cl**@cRHs are 1.1 and 1.0, respectively, which is consistent with pure MOFs. XRD profiles of **ACT**@cRHs and **Cl**@cRHs also confirmed that both samples have an identical phase to those of MOF-74.

To synthesize conductive pseudocapacitive materials derived from MOFs, the MOFs@cRHs samples were carbonised at 700 °C for 6 hours under nitrogen atmosphere. The carbonised MOFs@cRHs samples (**#4 ACT** and **#4 Cl**) show little difference in morphology. In Figure 6.12, SEM images show that carbonised MOFs remained in channels of cRHs.

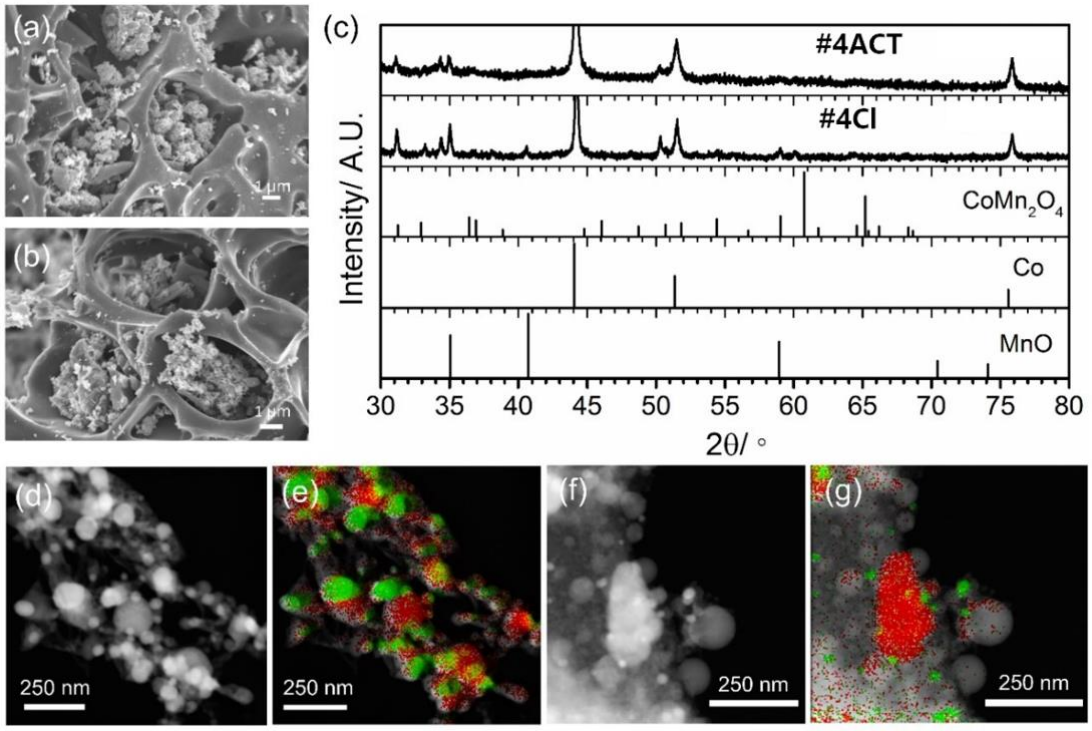


Figure 6.12. SEM images of (a) carbonised ACT@cRHs (**#4 ACT**) and (b) carbonised Cl@cRHs (**#4 Cl**), and (c) measured powder XRD profiles of carbonised ACT@cRHs (**#4**

ACT, top) and carbonised Cl@cRHs (**#4 Cl**, bottom). EDX mapping of **#4 ACT** (d,e) and **#4 Cl** (f,g) are shown with Mn in green and Co in red.

XRD profiles reveals that **#4 ACT** and **#4 Cl** have three crystalline phases corresponding to cubic Co, cubic MnO and tetragonal $CoMn_2O_4$. The MnO (111), (200), (220), (311), and (222) reflections were present in the XRD pattern at 2θ=34.9°, 40.6°, 58.8°, 70.3 and 73.8° respectively.[29] The Co metal (111), (200) and (220) reflections at 2θ=44.26°, 51.57° and 75.93° are also obvious.[30] The remaining peaks at 2θ=31.5°, 33.2° and 50.3° correspond to (200), (103) and (204) reflections of tetrahedral $CoMn_2O_4$ respectively.

The surface chemical composition of **#4**, **#4 ACT** and **#4 Cl** derived from XPS survey scan are shown in Table 6.3. There is no trace of Mn and Co in the bare cRHs sample **#4** which confirms that Mn and Co loading is due to carbonised MOFs. Composition analysis revealed that carbon and oxygen were present in all three samples, as expected, however potassium was found only in the unmodified cRHs. It is likely that during MOFs loading process potassium is leached out from cRHs. A large amount of silicon (~10%) was also found to be present in **#4** which is common in plants. Living plants absorbs silica from soil, and the silica accumulates around cellulose microcompartments in the roots, branches, and seeds by biomineralization synthesis. The silicon content drops to 2.4% in **#4 Cl** since cRHs is no longer the sole contribution of carbon material and MOFs does not contain any silicon, the reduced percentage of silicon makes sense. As for the lack of surface silicon in **#4 ACT**, it is likely the acetate used in the precursor freed the immobilised silicon in the form of silica from the cRHs surface during hydrothermal synthesis. As a charge recombination centre, silicon is found to reduce capacitance in biomass-derived carbon materials.[31] This reduction

in surface silicon is later shown as one of the reasons for the better specific capacitance of **#4 ACT** compared to **#4 Cl**.

Table 6.3. Surface chemical composition of samples in atomic percent derived from XPS survey scan.

Sample	**C**	**O**	**Mn**	**Co**	**Si**	**K**	**N**	**Cl**
#4	60	28.8	0	0	9.8	1.4	0	0
#4 ACT	57.3	28.3	7.2	6.4	0	0	0.8	0
#4 Cl	69.8	19.5	3.7	2.8	2.4	0	0.9	0.9

Table 6.4. Calculated surface chemical composition ratio against carbon derived from XPS survey scan.

Sample	**Mn/C**	**Co/C**	**(Mn+Co)/C**
#4	n/a	n/a	n/a
#4 ACT	0.126	0.113	0.238
#4 Cl	0.053	0.040	0.094

Calculating the ratio of Mn and Co against C show more than two times more Mn and Co loading with sample **#4 ACT** compared to sample **#4 Cl**. (Table 6.4) This is likely due to larger crystal size of **Cl** blocks the channels of the cRHs and lead to lowered MOFs loading. This increased Mn and Co loading is later shown as the main reason in the better specific capacitance of **#4 ACT** compared to **#4 Cl**. XPS spectra of **#4** (black), **#4 ACT** (blue) and **#4 Cl** (red) samples are shown in Figure 6.13 below.

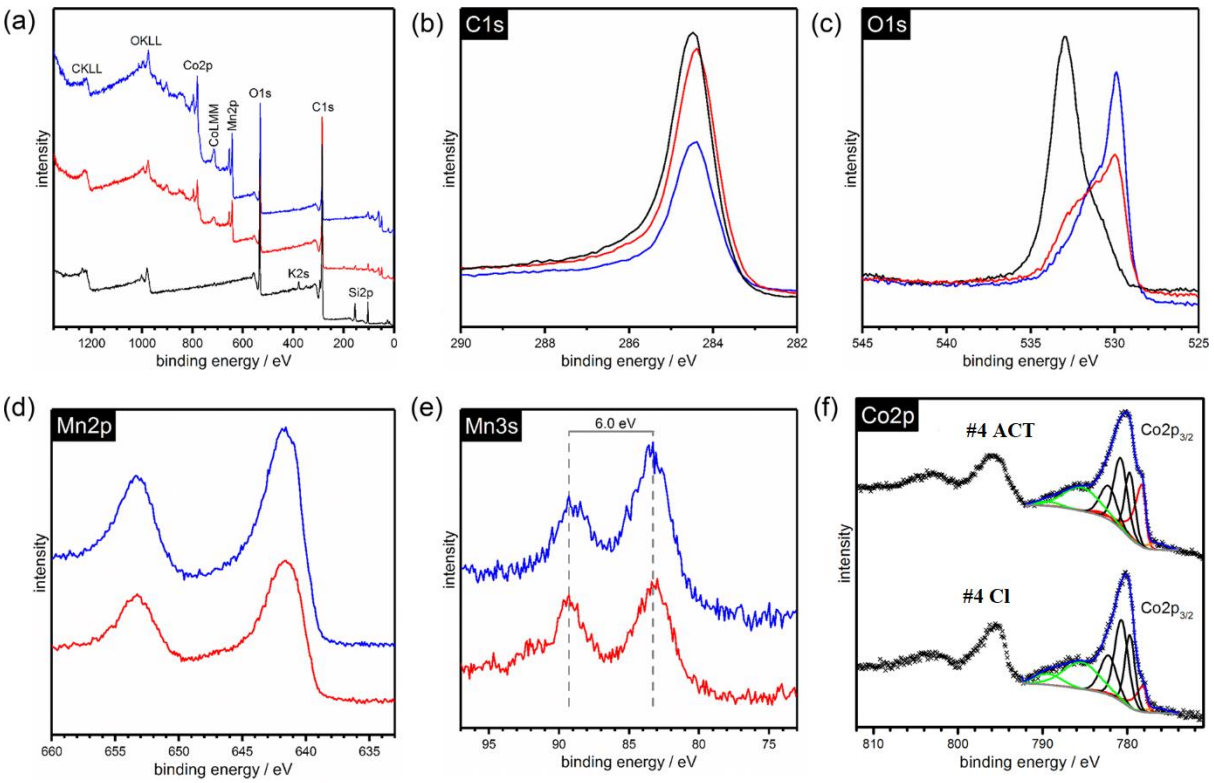


Figure 6.13. XPS spectra of a) **#4** (black), **#4 ACT** (blue) and **#4 Cl** (red), b) C1s region, c) O 1s region, d) Mn 2p region, e) Mn 3s region showing peak splitting of 6 eV, and f) deconvolution of the Co $2p_{3/2}$ region.

From XPS data in Figure 6.13, it is identified that the presence of Mn (II) at the Mn 3s region showing Mn 3s peak splitting of 6.0 eV. This is in good agreement with the XRD data. The O 1s XPS spectra is quite interesting showing very different oxygen species between cRHs (**#4**) from carbonised MOFs@cRHs samples (**#4 ACT**, **#4 Cl**). In **#4** the O 1s peak is centred at 532.9 eV (Figure 6.13d, black lines) which can be attributed to SiO_2. The atomic percent of Si in **#4** is 9.75 (Table 6.3) which implies that most of the oxygen found in the XPS spectra of cRHs can be attributed to SiO_2, given the 1:2 Si:O stoichiometry. Both **#4 ACT** and **#4 Cl** have their most intense peak centred at 529.9 eV which can be assigned to metal oxides. In the Co 2p region significant amount of Co (II) co-exists with Co metal. Deconvolution of the Co $2p_{3/2}$ region in Figure 6.13f reveals a shoulder feature at ~778.3 eV

(the most pronounced red peak) which can be unequivocally assigned to Co metal in both the **#4 ACT** and **#4 Cl**.[32] Similarly, a small contribution from the Co LMM Auger can also be seen at lower binding energy of the Co metal peak (fitted peak in orange). The remaining fitted peaks in black and green can be assigned to $CoMn_2O_4$ and their satellites respectively. Typically, Co (II) peaks come at a higher binding energy than Co (III), whilst the converse is true of the satellite features.[33] The fitting of the Co $2p_{3/2}$ region was carried out as described by Biesinger and coworkers.[32] The mixed bimetallic $CoMn_2O_4$ species was fitted by considering the fitting parameters used for Co_3O_4 which is also a mixture of Co (II) and Co (III) cations. However, the area was not constrained as the ratio of Co (II) and Co (III) ions is unknown. Lastly, a background offset for the deconvolution was found unable to improve the peak fitting of the Co $2p_{3/2}$ region. From XRD data, CoO presence is almost negligible. XPS is a surface sensitive technique, the surface Co oxide protective layer gives a misleadingly large composition compared to the bulk material which is mostly made up of Co metal as shown in pronounced Co metal XRD peak intensities.

The porous texture of the various carbons has been analysed by nitrogen adsorption at 77K using a BELSORP-MAX instrument. Samples were activated at 250°C prior to N_2 adsorption isotherm measurements. The specific surface area was calculated from the nitrogen adsorption isotherms by applying the BET equations. Micropore volume was determined using deBoer t-Plot. BET surface area of Mn/Co MOFs fabricated using acetate (**ACT**), and chloride (**Cl**) precursor are 234 and 724 m^2/g respectively, which agrees with other research.[34] However, after carbonisation in nitrogen at 700 °C for 6 hours, the MOFs

structure is destroyed thus provides little improvement in the specific surface area for cRHs template (**#4**). The carbonised MOFs@cRHs structure shown similar BET surface area to template cRHs **#4** while total pore volume reduced significantly. This reduction in total pore volume is due to carbonised MOFs filled the channels of cRHs taking up space and reducing overall pore volume. The total pore volume **#4 ACT** is slightly higher than that of **#4 Cl**. This increased total pore volume is later shown as one of the reasons in the better specific capacitance of **#4 ACT** compared to **#4 Cl**. The N_2 adsorption isotherms show a quick saturation at low pressure followed by slow increase at high pressure indicating the coexistence of micropores and mesopores. The pore size distributions (PSDs) estimated by non-local density functional theory (NLDFT) show two characteristic pores at 1 nm (micropore) and 9 nm (mesopore). The mesopore volume of **#4 ACT** is much higher than that of **#4 Cl**. Consequently, it is expected that a higher mesopore volume will result in an increase in overall capacitance due to the diffusion of electrolyte ions into the pores.

Table 6.5: BET specific surface and pore volume of MOFs modified cRHs samples

Samples	**S_{BET} (N_2) (m^2/g)**	**V_{Total} (cm^3/g) P/P_0=0.99**	**$V_{Micropore}$[a] (cm^3/g)**	**$V_{Mesopore}$[b] (cm^3/g)**
#4	121	0.2824	0.2019	0.0805
ACT	234	0.2792	0.0609	0.2183
#4 ACT	136	0.1160	0.0386	0.0792
Cl	724	0.3921	0.2230	0.1691
#4 Cl	137	0.0808	0.0411	0.0397

[a]Determined by deBoer t-plot.

[b]Mesopore volume = Total pore volume – micropore volume

CV method was employed to evaluate the specific capacitance of each sample. CV data of **#4**, **#4 ACT** and **#4 Cl** sample with increasing scan rates from 10 to 200 mV/s are shown in Figure 6.14.

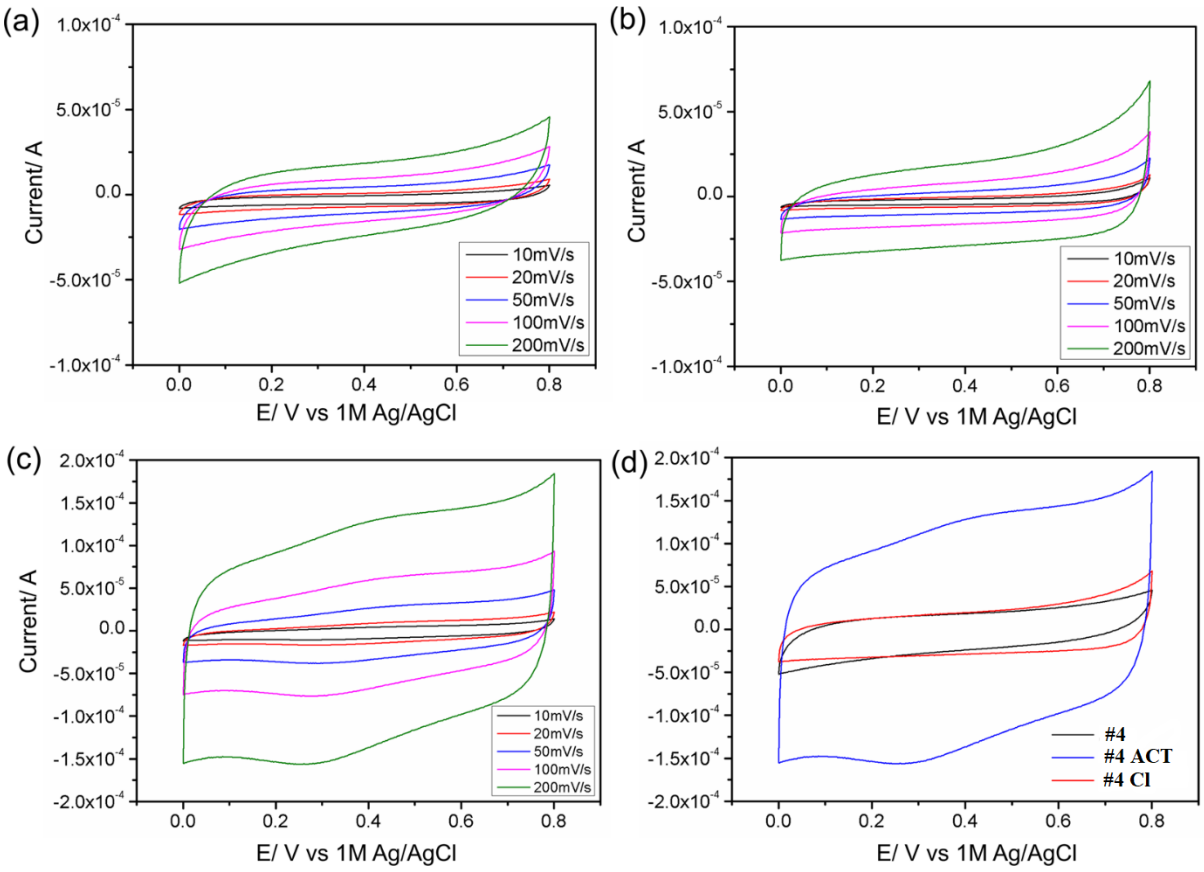


Figure 6.14. CV in 2 M KCl solution scanning from 0 to 0.8 V with scan rates of 10, 20, 50, 100 and 200 mV/s of (a) cRHs (**#4**), (b) carbonised MOFs modified cRHs #4 using metal chloride precursor (**#4 Cl**), (c) carbonised MOFs modified cRHs #4 using metal acetate precursor (**#4 ACT**), and (d) merged CV curves of all samples at scan rates of 200 mV/s, 1 M silver chloride electrode was used as reference.

At lower scan rates, a quasi-rectangular shape along the current/potential axis without obvious redox peaks is observed, which is typical for electric double-layer capacitive behaviour. With the increase in scan rate, the CV curves became more irregular. The distortion of the CV curves at higher scan rates was due to the limited diffusion and migration of ions in electrolytes. Also, the poor conductivity of the cRHs in loose powder

form cause losses at higher charge/discharge current. The CV curve of **#4 ACT** is more symmetrical and exhibits larger currents than **#4 Cl** as a result of reversible pseudocapacitance which can be attributed to the changing of oxidation states of cobalt and manganese in $CoMn_2O_4$ as described by Eq 6.1 and 6.2 below.[35]

$$CoMn_2O_4 + H_2O + OH^- \rightleftarrows Co(O)OH + 2Mn(O)OH + e^- \quad 6.1$$

$$Mn(O)OH + Co(O)OH + 2OH^- \rightleftarrows MnO_2 + CoO_2 + 2H_2O + 2e^- \quad 6.2$$

Similarly, MnO can be oxidized to Mn(O)OH and hence take part in the pseudocapacitance as described by Eq 6.2. However, it should be noted that Co metal, which is present in the samples, will also be oxidized but is unlikely to contribute to the pseudocapacitive performance of the material.

The specific capacitances of **#4**, **#4 ACT** and **#4 Cl** samples derived from various scan rates are summarised in Table 6.6. The results indicate that **#4 Cl** yields little to no improvements over **#4**, while **#4 ACT** show a significant increase in capacitive performance across all scan rates. Moreover, the capacitive performance for **#4 ACT** maintains across all scan rates, suggesting ideal capacitive behaviour, while the capacitances of **#4**, and **#4 Cl** decrease with increasing scan rates. The decreasing trend is due to the slow formation of the electric double-layer as a result of the limited diffusion of the electrolyte ions within the pores.[36]

Table 6.6. Specific capacitance of samples #4, #4 ACT and #4 Cl at various scan rates.

Scan rate	**#4 specific capacitance (F/g)**	**#4 Cl specific capacitance (F/g)**	**#4 ACT specific capacitance (F/g)**
C_m (10 mV/s)	13.1	9.4	30.3

C_m *(50 mV/s)*	8.2	7.1	28.4
C_m *(100 mV/s)*	6.7	6.8	30.7
C_m *(200 mV/s)*	5.6	6.8	32.8

The high electrochemical performance of **#4 ACT** is proposed to be due to 1) the higher loading amount of metal oxide, 2) a larger mesopore volume and 3) removal of surface silicon. **#4 ACT** has two times more Mn and Co loading which enhances pseudocapacitive property, the increase in metal oxide uptake was a consequence of the smaller crystallite size of **ACT** allowing for facile uptake into the cRHs channels. The higher mesopore volume allowed for increased surface area and hence greater EDLC. Finally, as shown in XPS, surface silicon is removed from cRHs surfaces which improves charge storage capability. Complete removal of silicon from cRHs should further enhance the capacitance which could be of interest for future work.

The electrochemical stability of **#4 ACT** was investigated by galvanostatic charge-discharge (GCD) for 3000 cycles from 0 to 0.8 V at a current density of 1 A/g.

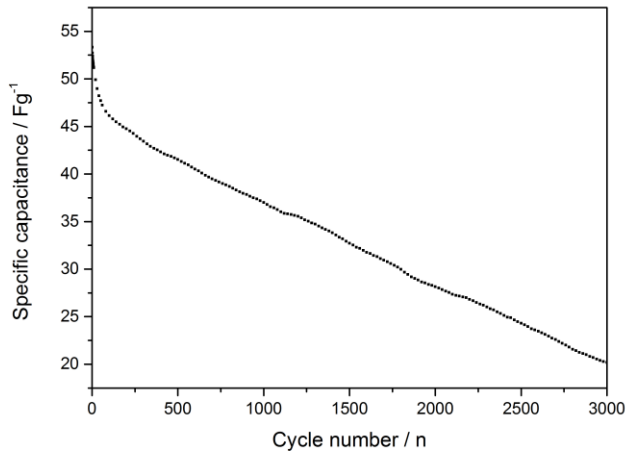


Figure 6.15. GCD cyclability at charging/discharging current density of 1 A/g and scanning potential from 0 to 0.8 V with 1 M Ag/AgCl reference electrode.

The calculated specific capacitance dropped from 47 F/g to 20 F/g over 3000 cycles. This drop in specific capacitance maybe due to leaching of metal cations which lead to the gradual loss of pseudocapacitance. This suggest immobilisation of metal cations using protective coating such as TiO_2 is critical in retaining pseudocapacitance of material, which may be interest for future work.

6.6 Conclusion

Carbonised rice husk waste material can be used as a potential biomass-derived carbon material for EDLC electrode. The capacitive performance of carbonised rice husk is further enhanced with Mn and Co modification using carbonised metal–organic frameworks (MOFs).

Firstly, various aqueous electrolyte was tested as a potential candidate for EDLC electrolyte. A neutral solution of 1 M KCl and 1 M $NaHCO_3$ could achieve a good potential window of 2.2-2.4 V compared to 2 V using 1M LiOH and 1.2-1.4 V using 1M HCl. Secondly, a drop-coating method was devised for EDLC testing suitable for smaller material quantity. The loss of sample during electrochemical measurement was solved by covering GC electrode surface with Nafion® 117. Thirdly, cRHs fabricated under different carbonisation conditions were tested with 400 °C carbonised in nitrogen (**#4**) showing best specific capacitance of 11.54 F/g which is consequently used as cRHs template for further modification.

Finally, in order to incorporate Mn and Co onto the cRHs template, two different-sized bimetallic Co/Mn-MOFs were directly grown in the channels of pre-activated cRHs, which is a conductive host, by changing the Mn (II) precursors. As confirmed by SEM and PXRD analysis, acetate precursor prepared MOFs (**ACT)** has much smaller crystal size and grain size than those of chloride precursor prepared MOFs (**Cl)** although both have an identical phase. TGA data revealed that **ACT** with smaller crystal size has higher loading amount than **Cl** inside RHs since the larger crystal size of **Cl** can block the channels of the RHs and lead to lower loading capacities. The carbonisation of MOFs@cRHs generates $CoMn_2O_4$, Co and MnO mixtures inside the cRHs channels, which work as pseudocapacitive nanomaterials. The high capacitance of **#4 ACT** across all scan rates is attributed to high loading amount of metal/metal oxide in cRHs, higher mesopore volume, good electrical contact and removal of surface silicon compared with **#4 Cl**. The smaller crystallite size of **ACT** MOFs compared to **Cl** MOFs prevents the blockage of micrometer-scale channels of RHs, and increase the loading amount of **ACT** and the mesopore volume.

In conclusion, the crystal size control of MOFs in cRHs is crucial to improve the electrochemical performance of pseudocapacitive nanomaterials. Metal acetate precursor derived sample **#4 ACT** yields a consistent specific capacitance of around 30 F/g irrespective of CV scan rate. In order to further improve the pseudocapacitance of Mn/Co modified cRHs both silicon removal and metal cation immobilisation are suitable options which may be of interest for future works.

Reference

1. Becker, H. I. Low voltage electrolytic capacitor. (1957).

2. Bichat, M. P., Raymundo-Piñero, E. & Béguin, F. High voltage supercapacitor built with seaweed carbons in neutral aqueous electrolyte. *Carbon N. Y.* **48**, 4351–4361 (2010).

3. Simon, P. & Gogotsi, Y. Materials for electrochemical capacitors. *Nature Materials* (2008). doi:10.1038/nmat2297

4. Zhai, Y. *et al.* Carbon materials for chemical capacitive energy storage. *Adv. Mater.* **23**, 4828–4850 (2011).

5. Béguin, F., Presser, V., Balducci, A. & Frackowiak, E. Carbons and electrolytes for advanced supercapacitors. *Adv. Mater.* **26**, 2219–2251 (2014).

6. Wu, Z. S., Parvez, K., Feng, X. & Müllen, K. Graphene-based in-plane micro-supercapacitors with high power and energy densities. *Nat. Commun.* **4**, (2013).

7. Sheberla, D. *et al.* Conductive MOF electrodes for stable supercapacitors with high areal capacitance. *Nat. Mater.* **16**, 220–224 (2017).

8. Lin, T. *et al.* Nitrogen-doped mesoporous carbon of extraordinary capacitance for electrochemical energy storage. *Science (80-.).* **350**, 1508–1513 (2015).

9. Feng, D. *et al.* Robust and conductive two-dimensional metal−organic frameworks with exceptionally high volumetric and areal capacitance. *Nat. Energy* **3**, 30–36 (2018).

10. Jiang, L. *et al.* Hybrid system of nickel–cobalt hydroxide on carbonised natural cellulose materials for supercapacitors. *J. Solid State Electrochem.* **22**, 387–393 (2018).

11. Jiang, L. *et al.* Natural Cellulose Materials for Supercapacitors. *Electrochim. Acta* **192**, 251–258 (2016).

12. He, S. & Chen, W. Application of biomass-derived flexible carbon cloth coated with MnO2 nanosheets in supercapacitors. *J. Power Sources* (2015). doi:10.1016/j.jpowsour.2015.06.051

13. Jiang, L. *et al.* Cellulose-Derived Supercapacitors from the Carbonisation of Filter Paper. *ChemistryOpen* **4**, 586–589 (2015).

14. Fic, K., Lota, G., Meller, M. & Frackowiak, E. Novel insight into neutral medium as electrolyte for high-voltage supercapacitors. *Energy Environ. Sci.* **5**, 5842–5850 (2012).

15. Forse, A. C., Merlet, C., Griffin, J. M. & Grey, C. P. New perspectives on the charging mechanisms of supercapacitors. *J. Am. Chem. Soc.* **138**, 5731–5744 (2016).

16. Lee, H. Y. & Goodenough, J. B. BRIEF COMMUNICATION Supercapacitor Behavior with KCl Electrolyte. *J. Solid State Chem.* **223**, 220–223 (1999).

17. Hong, M. S., Lee, S. H. & Kim, S. W. Use of KCl aqueous electrolyte for 2 V manganese oxide/activated carbon hybrid capacitor. *Electrochem. Solid-State Lett.* **5**, 227–230 (2002).

18. Jiang, L. *et al.* Nickel treatment of biomass-derived nanocarbon for energy devices. *Carbon N. Y.* **130**, 724–729 (2018).

19. Stenina, I. A., Sistat, P., Rebrov, A. I., Pourcelly, G. & Yaroslavtsev, A. B. Ion mobility in Nafion-117 membranes. *Desalination* **170**, 49–57 (2004).

20. Okada, T. *et al.* Ion and water transport characteristics of Nafion membranes as electrolytes. *Electrochim. Acta* **43**, 3741–3747 (1998).

21. Xia, X. H., Tu, J. P., Wang, X. L., Gu, C. D. & Zhao, X. B. Mesoporous Co3O4monolayer hollow-sphere array as electrochemical pseudocapacitor material. *Chem. Commun.* **47**, 5786–5788 (2011).

22. Patel, M. N. *et al.* Hybrid MnO2-disordered mesoporous carbon nanocomposites: Synthesis and characterization as electrochemical pseudocapacitor electrodes. *J. Mater. Chem.* **20**, 390–398 (2010).

23. Weng, Y. T. *et al.* Spatially Confined MnO<inf>2</inf> Nanostructure Enabling Consecutive Reversible Charge Transfer from Mn(IV) to Mn(II) in a Mixed Pseudocapacitor-Battery Electrode. *Adv. Energy Mater.* **5**, 1–10 (2015).

24. Augustyn, V., Simon, P. & Dunn, B. Pseudocapacitive oxide materials for high-rate electrochemical energy storage. *Energy Environ. Sci.* **7**, 1597–1614 (2014).

25. Huang, L. *et al.* Nickel-cobalt hydroxide nanosheets coated on NiCo2O4nanowires grown on carbon fiber paper for high-performance pseudocapacitors. *Nano Lett.* **13**, 3135–3139 (2013).

26. Wang, L. J. *et al.* Synthesis and characterization of metal-organic framework-74 containing 2, 4, 6, 8, and 10 different metals. *Inorg. Chem.* **53**, 5881–5883 (2014).

27. Parker, A. J. The effects of solvation on the properties of anions in dipolar aprotic solvents. *Q. Rev. Chem. Soc.* **16**, 163–187 (1962).

28. Parker, A. J. Protic-dipolar aprotic solvent effects on rates of bimolecular reactions. *Chem. Rev.* **69**, 1–32 (1969).

29. SASAKI, S., FUJINO, K. & TAKÉUCHI, Y. X-Ray Determination of Electron-Density Distributions in Oxides, MgO, MnO, CoO, and NiO, and Atomic Scattering Factors of their Constituent Atoms. *Proc. Japan Acad. Ser. B Phys. Biol. Sci.* **55**, 43–48 (1979).

30. Hull, A. W. X-Ray crystal analysis of thirteen common metals. *Phys. Rev.* **17**, 571–588 (1921).

31. Huang, Y. *et al.* Promising biomass-derived hierarchical porous carbon material for high performance supercapacitor. *RSC Adv.* **7**, 10385–10390 (2017).

32. Biesinger, M. C., Lau, L. W. M., Gerson, A. R. & Smart, R. S. C. Resolving surface chemical states in XPS analysis of first row transition metals, oxides and hydroxides: Sc, Ti, V, Cu and Zn. *Appl. Surf. Sci.* **257**, 887–898 (2010).

33. Burke, A. R&D considerations for the performance and application of electrochemical capacitors. *Electrochim. Acta* **53**, 1083–1091 (2007).

34. Díaz-García, M., Mayoral, Á., Díaz, I. & Sánchez-Sánchez, M. Nanoscaled M-MOF-74 materials prepared at room temperature. *Cryst. Growth Des.* **14**, 2479–2487 (2014).

35. Ren, L. *et al.* Facile synthesis of flower-like CoMn2O4 microspheres for electrochemical supercapacitors. *RSC Adv.* **5**, 30963–30969 (2015).

36. Zequine, C. *et al.* High per formance and flexible supercapacitors based on carbonized bamboo fibers for wide temperature applications. *Sci. Rep.* **6**, (2016).

Chapter 7 Conclusions

7.1 N doped TiO_2 powder

N doped TiO_2 product can be easily obtained using an efficient evaporation process. The novel 2-propanol/HNO_3 based one pot sol-gel evaporation method was developed and optimized. The preparation process was optimized regarding roasting time and mortar grinding. This facile preparation process can produce highly N doped TiO_2 nanoparticles at low temperature. The annealing temperature of 300 °C yields the best results. Annealing temperature beyond 400 °C lead to complete loss of nitrogen incorporation. 2 mL of concentrated nitric acid per 25 mL precursor solution yields best results. It is possible that going beyond 2 mL could further improve MB degradation capability, which may be of interest for future study.

With the adaptation of CasaXPS software, a novel MB absorption spectrum peak deconvolution technic is proposed. This adaptation is not only limited to UV-Vis spectrum peak deconvolution, any peak deconvolution process can also benefit from this adaption including but not limited to Raman, FTIR, reflectance. Analysing deconvoluted data, a better indicator of MB degradation is identified. Total absorption area yields better pseudo-first-order reaction linearity than using maximum absorption peak height (MB monomer). This is especially true for exotic absorption spectra change with uneven peak reduction rate.

In the case of N-doped TiO_2, it appears that the photocatalytic degradation of MB by N-doped TiO_2 takes place via the sequential decomposition of methyl groups from MB to azure

A/B/C and further mineralisation. N-doping enables photocatalytic response under visible spectrum. Samples prepared using 2 mL concentrated nitric acid in 25 mL 2-propanol solution (0.5 M Ti concentration) and annealed at 300 °C for 10 hrs yield best photocatalytic results under visible spectrum irradiation.

7.2 Sn doped TiO_2 thin films

Sn doped anatase TiO_2 thin film can be grown on 5%Nb:$SrTiO_3$ (001) substrate using dip-coating method. Incorporating Sn into anatase TiO_2 lattice causes an expansion of the unit cell, while the crystalline structure is maintained. Using Sn doped anatase TiO_2 thin film as PEC photo anode, yields an overall increase in photocurrent. Compared to undoped anatase TiO_2, the photocurrent of Sn-doped TiO_2 thin film increased substantially, up to ~60% (1.23 V vs RHE at pH 13) using 10 atomic % Sn doping. The main contribution to PEC performance is UV, suggesting insignificant bandgap reduction with Sn doping. The overall increase in photocurrent should be due to an increase in photoactive sites caused by Sn doping.

Sn doped rutile TiO_2 thin film can be grown on FTO substrate using dip-coating method. Compared to undoped rutile TiO_2, the photocurrent of 1% Sn-doped rutile TiO_2 thin film increased up to ~20% under reverse bias (1.23 V vs RHE at pH 13). However, 0.5% and 1.5% Sn-doped rutile TiO_2 showed an overall decrease in photocurrent performance. As indicated by the slope of the Mott-Schottky plot, Sn doping increased donor density. The reduction in photocurrent is likely due to trap sites introduced by Sn doping.

PEC performance of Sn doped anatase and rutile thin film were compared. 10% Sn doped anatase thin film showed better photocurrent performance under UV while 1% Sn doped rutile anatase thin film performed better under simulated one sun illumination and visible spectrum. The main contribution to PEC performance is still due to the UV spectrum. The overall increase in photocurrent should be due to an increase in photoactive sites caused by Sn doping.

The underlying principle of water oxidation and reduction using a semiconductor photoanode-cathode-based PEC device was explored, and the reason for RHE scale is explained with multiple examples of PEC designs. This serves as a standard model in interpreting electrochemical data of photoanode/photocathode in a three-electrode setup.

7.3 Carbonised Co/Mn MOFs modified cRHs

Rice husk waste material can be used as a potential biomass-derived carbon material for EDLC electrode. Two different-sized bimetallic Co/Mn MOFs were grown in the channels of cRHs for improved EDLC performance. By changing the Mn(II) precursors, acetate precursor prepared MOFs (**ACT)** has much smaller crystal size and grain size than those of chloride precursor prepared MOFs (**Cl)**. The electrochemical performance of carbonized **ACT**@cRHs with cRHs sample **#4 (#4ACT)** is superior to that of carbonized **Cl** @cRHs with cRHs sample **#4** (**#4 Cl)** though they have a similar surface area. High capacitance of **#4 ACT** across all scan rates is attributed to high loading amount of metal/metal oxide in cRHs, high mesopore volume and good electrical contact. Smaller crystals size of **ACT** compared to **Cl** prevents the blockage of micrometer-scale channels of RHs. Therefore, the

crystal size control of MOFs in cRHs is crucial to improve the electrochemical performance of pseudocapacitive nanomaterials.

A drop-coating method was devised for EDLC testing using smaller material quantity. cRHs fabricated under different carbonisation conditions were tested with 400 °C carbonised in nitrogen (**#4**) showing best specific capacitance of 11.54 F/g. Metal acetate precursor derived sample **#4 ACT** yields a consistent specific capacitance of around 30 F/g irrespective of scan rate.